UNIVERSIDAD DE VALENCIA - CSIC

DEPARTAMENTO DE FÍSICA ATÓMICA, MOLECULAR Y NUCLEAR

INSTITUTO DE FÍSICA CORPUSCULAR

Beta Decay of T_z = -1 nuclei and Comparison with Charge Exchange Reaction Experiments

TESIS DOCTORAL

FRANCISCO GABRIEL MOLINA PALACIOS

Febrero de 2011

Dra. Berta Rubio Barroso, Profesor de Investigación del Consejo Superior de Investigaciones Científicas (CSIC)

CERTIFICA:

Que la presente memoria ***"Beta Decay of T_z = -1 nuclei and Comparison with Charge Exchange Reaction Experiments"*** ha sido realizada bajo su dirección en el Instituto de Física Corpuscular (Centro Mixto Universidad de Valencia - CSIC) por **Francisco Gabriel Molina Palacios** y constituye su Tesis doctoral dentro del programa de doctorado del Departamento de Física Atómica, Molecular y Nuclear.

Y para que así conste, en cumplimiento con la legislación vigente, presenta ante el Departamento de Física Atómica, Molecular y Nuclear la referida memoria, firmando el presente certificado en Burjassot (Valencia) a 21 de Febrero de 2011.

A mis padres, Gabriel Molina Pinto y Gladys Palacios Pérez

CONTENTS

1 Introduction **1**
- 1.1 β decay . . . 1
- 1.2 Fermi theory of beta decay . . . 3
  - 1.2.1 Fermi and Gamow-Teller decay. Definition of the strengths . . . 4
- 1.3 Isotopic spin of the nucleon . . . 5
- 1.4 Isospin symmetry . . . 6
- 1.5 Experimental studies of the Gamow-Teller transition strengths . . . 6
  - 1.5.1 Charge exchange reactions ($T_z = +1 \rightarrow T_z = 0$) . . . 8
  - 1.5.2 The *merged analysis* . . . 8
- 1.6 $B(GT)$ studies for the T=1 fp-shell nuclei . . . 9
  - 1.6.1 CE reactions (^{3}He, t), T$_z$=+1 $\rightarrow$ 0 results . . . 10

2 T$_z$=-1 ^{54}Ni Measurements at LISOL **17**
- 2.1 The Production of ^{54}Ni . . . 17
- 2.2 The LISOL Separator . . . 17
  - 2.2.1 Gas Cell . . . 18
  - 2.2.2 Resonant Laser Ionisation . . . 19
  - 2.2.3 Sextupole Ion Guide . . . 20
- 2.3 Radiation Detectors . . . 21
- 2.4 The Tape System . . . 22
- 2.5 The Data Acquisition System . . . 22
- 2.6 Data Analysis . . . 24

3 Analysis and Results of LISOL Experiment **25**
- 3.1 γ Calibrations . . . 26
- 3.2 Control Measurements during the Experiment . . . 26
- 3.3 Data Analysis . . . 27
- 3.4 Half-life Analysis . . . 30
- 3.5 High Energy Gamow-Teller states . . . 39

4 T_Z=-1 ^{54}Ni,^{50}Fe ^{46}Cr and ^{42}Ti Measurements at RISING 41
4.1 Description of the Experiment . . . 42
4.1.1 The Accelerator complex and the reaction used . . . 42
4.1.2 The Fragment Separator . . . 43
4.1.3 Particle Identification at FRS . . . 46
4.1.4 The Active Stopper . . . 50
4.1.5 RISING Ge Array . . . 54
4.2 Experiment: General Description . . . 55
4.2.1 Experiment Description . . . 55
4.3 Data Description and Calibrations . . . 56
4.3.1 DAQ, Trigger and Structure of the data . . . 56
4.3.2 Beta Calibrations . . . 57
4.3.3 Gamma Calibrations . . . 67

5 Results of GSI Experiment Analysis 75
5.1 Gamma Analysis . . . 75
5.1.1 ^{54}Ni run, γ-analysis . . . 76
5.1.2 ^{50}Fe run, γ-analysis . . . 92
5.1.3 ^{46}Cr run, γ-analysis . . . 94
5.1.4 ^{42}Ti run γ-analysis . . . 95
5.2 β-decay half-life analysis . . . 96
5.2.1 Immediate time correlations . . . 97
5.2.2 All Betas/All Implantations (ABAI) time correlations . . . 97
5.2.3 Possible sources of systematic error in the half-life determination . 102
5.2.4 β half-life results . . . 105
5.3 β half-life by γ-implantations time correlations . . . 116
5.3.1 Implant-β-delay γ correlation . . . 116
5.3.2 β half-life from β-delayed γ-implantation correlation . . . 117
5.4 β branching and ground state feeding . . . 126
5.5 Gamow-Teller transition Strength . . . 130

6 Discussions and Conclusions 133
6.1 B(GT) compared with the Extreme Single Particle Model . . . 138
6.1.1 Extreme Single Particle Calculations . . . 139
6.2 Comparison with Charge Exchange reaction results . . . 142
6.2.1 T=1, mass 54 . . . 148
6.2.2 T=1, mass 50 . . . 149
6.2.3 T=1, mass 46 . . . 150
6.2.4 T=1, mass 42 . . . 151
6.3 M1 $1^+ \rightarrow 1^+$ transitions in the daughter nuclei . . . 152

7 Resumen en Castellano 153
7.1 Introducción . . . 153
7.1.1 Estudio de la B(GT$^+$) en desintegraciones β . . . 154
7.1.2 Estudio de la B(GT-) en reacciones de intercambio de carga . . . 154
7.2 Reacciones de intercambio de carga RCNP . . . 155
7.3 Simetría de Isoespín en núcleos con la misma masa A . . . 156

7.4 Transiciones Gamow-Teller en la capa fp 157
7.4.1 Transiciones Gamow-Teller en el colapso del núcleo de una supernova 157
7.4.2 Medidas de $B(GT)$ en núcleos con T=1 en la capa fp 158
7.4.3 Resultados: Reacciones (^{3}He, t), T$_z$=+1 $\rightarrow$ 0 159
7.4.4 Resultados: Desintegración β^+, T$_z$=-1 $\rightarrow$ 0 164
7.5 Discusiones y Conclusiones 207
7.5.1 Comparación de las fuerzas de transición Gamow-Teller $B(GT)$, obtenidas mediante reacciones de intercambio de carga (CE) y mediante experimentos de desintegración β 207
7.5.2 Ausencia de transiciones M1 $1^+ \rightarrow 1^+$ en l núcleo hijo. 209

A FRS Calibration **211**
A.1 Time of Flight Calibration 212

B B(GT) Results from CE-Reaction measurements at RCNP, Osaka. **213**

C Appendix A: Addback Routine **217**
C.1 Algorithm 217
C.2 Addback code 220

D Appendix B: RISING Ge Array Efficiency **223**

E Appendix C: Simulation of the background of wrong correlations **235**
E.1 Simulation uniformly-distributed random implantations 235
E.2 Simulation Gaussian-distributed random implantations 238

LIST OF FIGURES

1.1 Schematic illustration of the isospin symmetry transitions in mirror nuclei with T_z= 0, ±1, ±2. (a) Level scheme in real energy space. (b) Level scheme in isospin space, neglecting the Coulomb displacement energies. The symmetric structure is evident. Analogue states are connected by segmented lines [Ada07a]. 7

1.2 Comparison between energy resolution of the results of the CE reaction ^{58}Ni$(p,n)^{58}$Cu [RS94] (ΔE $\sim$ 400 keV) and recent measurements of the CE reaction ^{58}Ni$(^3\mathrm{He},t)^{58}$Cu [Fuj07a] (ΔE $\sim$ 35 keV). 8

1.3 Chart of nuclides. In the figure are shown some of the fp-shell nuclei. The lines shows those nuclei with $T_z = \frac{N-Z}{2} = 0, \pm 1$. The usual colour code in the nuclear chart is: red for β^+-decaying nuclei, blue β^--decaying nuclei, and black for stable nuclei. 10

1.4 Scheme of the charge exchange reaction experiment at RCNP in Osaka, Japan [Ada07a]. 12

1.5 High resolution triton spectrum for the ^{42}Ca$(^3\mathrm{He},t)^{42}$Sc charge exchange reaction [Ada07b]. The excitation energy of the levels in the final ^{42}Sc nucleus and the $B(GT)$ values extracted from this measurement are shown in Appendix B. 13

1.6 High resolution triton spectrum for the ^{46}Ti$(^3\mathrm{He},t)^{46}$V charge exchange reaction [Ada06]. The excitation energy of the levels in the final ^{46}V nucleus and the $B(GT)$ values extracted from this measurement are shown in Appendix B. 14

1.7 High resolution triton spectrum for the ^{50}Cr$(^3\mathrm{He},t)^{50}$Mn charge exchange reaction [Fuj05a]. The excitation energy of the levels in the final ^{46}V nucleus and the $B(GT)$ values extracted from this measurement are shown in Appendix B. 15

1.8 High resolution triton spectrum for the ^{54}Fe$(^3\mathrm{He},t)^{54}$Co charge exchange reaction [Ada07b]. The excitation energy of the levels in the final ^{54}Co nucleus and the $B(GT)$ values extracted from this measurement are shown in Appendix B. 16

2.1 Leuven Ion Separator On Line [Pau09]. 18
2.2 Atomic level scheme and the different ways to ionise an atom. 19
2.3 Scheme of the sextupole ion guide (SPIG). 20
2.4 Top and side view of the setup of β and γ detectors at the Louvain la Neuve facility. 21
2.5 Schematic view of the detector and type system setup. 22
2.6 Schematics showing core contacts and segment contacts in a Miniball Cluster. 23

3.1 ^{54}Ni and ^{54}Co^{g,m} decay schemes. 25
3.2 Veto Condition: If a β particle is detected in one of the side plastic detectors, the corresponding γs are accepted if they are detected in the opposite MINIBALL cluster. If the β particle goes through the middle β detector, the γ rays are accepted if they happen in the two most distant crystals of each MINIBALL cluster 28
3.3 Difference between the no-veto (up) and veto (down) laser on Ni, mass A=54 β gated γ spectra 29
3.4 A=54 laser on Co β-γ spectrum 31
3.5 A=54 mass, laser on Ni β-γ spectrum 32
3.6 Expanded view of the A=54 laser on Ni and laser on Co spectra. 33
3.7 ID Curve during a macrocycle time (400 ms implantation and 600 ms decay) solving the differential equations system with Maple10. ^{54}Ni is shown in red and ^{54}Co is shown in green. 34
3.8 Implantation-decay curve of ^{54}Ni. Each point represents the area of the fitted Gaussian for the 937 keV γ-ray, subtracting a linear background in the neighbouring region. 36
3.9 Implantation-decay curve of ^{54}Ni. Each point represents the area of a Gaussian with fixed width and centroid at 937 keV, after subtracting a long linear background taken from 800 to 1100 keV. 37
3.10 Implantation-decay curve of ^{54}Ni. Each point represents the area of the 937 keV peak in the double Gaussian fit with a linear background subtraction, in the range from 800 to 1100 keV. 38
3.11 ^{54}Ni spectrum in the vicinity of 3375 keV. 39

4.1 General layout of the FRS separator and the various detectors where the ion is identified before its implantation in a DSSSD. 41
4.2 Complete overview of the GSI facilities. UNILAC, SIS18 Synchrotron and the FRS. 42
4.3 Complete scheme of the Fragment Separator at GSI. All experimental areas are shown. Our experimental setup was placed at S4. 44
4.4 Simple scheme of a degrader: for different ions with different Z values, the velocity after the degrader is different. 45
4.5 Drawing of the Degrader System at the S2 focal plane consisting of a wedge, a ladder and wedge-shaped disks. 46
4.6 FRS Degrader scheme. In achromatic mode, the ions are spatially focus at the last focal plane at F4. In monoenergetic mode, the ions after the degrader had the same momentum. 47

4.7 Schematic view of the time-of-flight (TOF) measurement. When an ion passes through the scintillators sci21 and sci41, two signals are produced per detector. The difference of the average of these signals gives the time-of-flight of the ion. Figure from V.Ricciardi [Ric04]. 48

4.8 This figure shows (i)schematic drawing of the multi-wire detector, and (ii) the position of each multi-wire in the FRS line 49

4.9 MUSIC80: Ionisation chamber. 49

4.10 Identification plot for the reaction fragments separated and identified up to sci41 in the ^{54}Ni experiment setup. $Z^*$and A/Q^* are the correct Z and A/Q values for the ^{54}Ni; for the other identified nuclei small differences may exist. 50

4.11 Identification plot for the reaction fragments separated and identified up to sci41 in the ^{50}Fe experiment setup. $Z^*$and A/Q^* are the correct Z and A/Q values for the ^{50}Fe; for the other identified nuclei small differences may exist. 51

4.12 Identification plot for the reaction fragments separated and identified up to sci41 in the ^{46}Cr experiment setup. $Z^*$and A/Q^* are the correct Z and A/Q values for the ^{46}Cr; for the other identified nuclei small differences may exist. 51

4.13 Identification plot for the reaction fragments separated and identified up to sci41 in the ^{42}Ti experiment setup. $Z^*$and A/Q^* are the correct Z and A/Q values for the ^{42}Ti; for the other identified nuclei small differences may exist. 52

4.14 Active Stopper used during the RISING Stopped Beam campaign: Micron Semiconductor Ltd. Double Sided Silicon Strip Detector (DSSSD), 16 front and 16 back strips with a $1\times50\times3.125$ mm^3 active volume each. . . 52

4.15 Schematic figure of the end of the FRS separator after the fourth dipole magnet. 54

4.16 The RISING Germanium Array and the DSSSD Silicon active stopper. . . 54

4.17 Scheme of RISING electronics. 56

4.18 Sum of all M2 DSSSD Y-Strips calibrated in energy for the decay events. The red lines show the selected decay energy range in the present analysis: (264,1590 keV). 58

4.19 Sum of all M2 DSSSD Y-Strips aligned for implantation events. The red lines show the selected implantation range in the present analysis: (2560,3442 A.U). 58

4.20 Identification plot of the reaction fragments separated and identified including the implantation condition in M2, during the ^{54}Ni experimental run. The window used to select the ^{54}Ni implants is shown. The total number of ^{54}Ni ions implanted in M2 and selected in the window was 3,853,587 ions. $Z^*$and A/Q^* are the correct Z and A/Q values for the ^{54}Ni; for the other identified nuclei small differences may exist. 60

4.21 Identification plot for the reaction fragments separated and identified including the implantation condition in M2, during the ^{50}Fe experimental run. The window used to select the ^{50}Fe implants is shown. The total number of ^{50}Fe ions implanted in M2 and selected in the window was 2,526,305 ions. $Z^*$and A/Q^* are the correct Z and A/Q values for the ^{50}Fe; for the other identified nuclei small differences may exist. 60
4.22 Identification plot for the reaction fragments separated and identified including the implantation condition in M2, during the ^{46}Cr experimental run. The window used to select the ^{46}Cr implants is shown. The total number of ^{46}Cr ions implanted in M2 and selected in the window was 1,793,477 ions. $Z^*$and A/Q^* are the correct Z and A/Q values for the ^{46}Cr; for the other identified nuclei small differences may exist. 61
4.23 Identification plot for the reaction fragments separated and identified including the implantation condition in M2, during the ^{42}Ti experimental run. The window used to select the ^{42}Ti implants is shown. The total number of ^{42}Ti ions implanted in M2 and selected in the window was 373,231 ions. $Z^*$and A/Q^* are the correct Z and A/Q values for the ^{42}Ti; for the other identified nuclei small differences may exist. 61
4.24 Implantations of ^{54}Ni ions in the DSSSDs (see text). 63
4.25 Implantations of ^{50}Fe ions in the DSSSDs (see text) 64
4.26 Implantations of ^{46}Cr ions in the DSSSDs (see text) 65
4.27 Implantations of ^{42}Ti ions in the DSSSDs (see text) 66
4.28 RISING experimental efficiency curve in single crystal and add-back mode. 69
4.29 Comparison of the simulated efficiency for a point-like source and an extended source (see text). 70
4.30 Geometry of the RISING Ge array for the Active Stopper Campaign implemented in the Montecarlo simulation. The pertinax box with the 6 DSSSD configuration was included in the simulation. 71
4.31 Geant4 simulated efficiency in addback and single crystal modes varying the geometrical radius of the Ge array. 72
4.32 Experimental and simulated γ-efficiencies using addback and single efficiency. The experimental values for: 1) ^{152}Eu source are shown in red squares, 2) ^{133}Ba-^{137}Cs-^{60}Co mixed source are shown in blue squares, 3) ^{226}Ra source are shown in green squares, and 4) ^{56}Co source are shown in brown squares. The simulated points are shown in black squares. The efficiency curve from Eq. 4.8 -p.68- is shown in red. The evaluation of the efficiency curves for Single Crystal and Addback are detailed in Appendix D -p.223-. 73

5.1 ^{54}Ni β-delayed γ-events in the coincidence gate of 100 μs. In the analysis software the β-γ coincidence gate of 250 ns was set in the 86.5-89.0 [100ns] time interval. 76
5.2 ^{54}Ni addback β-delayed γ-spectrum Part 1. Energy range: 0-1000 keV. . . 78
5.3 ^{54}Ni addback β-delayed γ-spectrum Part 3. Energy range: 2000-3000 keV. 78
5.4 ^{54}Ni addback β-delayed γ-spectrum Part 5. Energy range: 4000-5000 keV. 78
5.5 ^{54}Ni addback β-delayed γ-spectrum Part 2. Energy range: 1000-2000 keV. 79

5.6 ^{54}Ni addback β-delayed γ-spectrum Part 4. Energy range: 3000-4000 keV. 79
5.7 ^{54}Ni addback β-delayed γ-spectrum Part 6. Energy range: 5000-6000 keV. 79
5.8 ^{50}Fe addback β-delayed γ-spectrum Part 1. Energy range: 0-1000 keV. . . 82
5.9 ^{50}Fe addback β-delayed γ-spectrum Part 3. Energy range: 2000-3000 keV. 82
5.10 ^{50}Fe addback β-delayed γ-spectrum Part 5. Energy range: 4000-5000 keV. 82
5.11 ^{50}Fe addback β-delayed γ-spectrum Part 2. Energy range: 1000-2000 keV. 83
5.12 ^{50}Fe addback β-delayed γ-spectrum Part 4. Energy range: 3000-4000 keV. 83
5.13 ^{50}Fe addback β-delayed γ-spectrum Part 6. Energy range: 5000-6000 keV. 83
5.14 ^{46}Cr addback β-delayed γ-spectrum Part 1. Energy range: 0-1000 keV. . 86
5.15 ^{46}Cr addback β-delayed γ-spectrum Part 3. Energy range: 2000-3000 keV. 86
5.16 ^{46}Cr addback β-delayed γ-spectrum Part 5. Energy range: 4000-5000 keV. 86
5.17 ^{46}Cr addback β-delayed γ-spectrum Part 2. Energy range: 1000-2000 keV. 87
5.18 ^{46}Cr addback β-delayed γ-spectrum Part 4. Energy range: 3000-4000 keV. 87
5.19 ^{46}Cr addback β-delayed γ-spectrum Part 6. Energy range: 5000-6000 keV. 87
5.20 ^{42}Ti addback β-delayed γ-spectrum Part 1. Energy range: 0-1000 keV. . . 90
5.21 ^{42}Ti addback β-delayed γ-spectrum Part 3. Energy range: 2000-3000 keV. 90
5.22 ^{42}Ti addback β-delayed γ-spectrum Part 5. Energy range: 4000-5000 keV. 90
5.23 ^{42}Ti addback β-delayed γ-spectrum Part 2. Energy range: 1000-2000 keV. 91
5.24 ^{42}Ti addback β-delayed γ-spectrum Part 4. Energy range: 3000-4000 keV. 91
5.25 ^{42}Ti addback β-delayed γ-spectrum Part 6. Energy range: 5000-6000 keV. 91
5.26 Good and wrong correlations using the All Betas/All Implantation method. The red area corresponds to the good correlations. The blue area contains the wrong correlation events which correspond to correlations with random events. 98
5.27 Schematic picture of the "Same" (good and wrong correlations can be found) and "Opposite" (wrong correlations only can be found) pixel correlations. 99
5.28 Same (red) and opposite (blue) pixel time correlations corresponding to the full statistics for ^{54}Ni in a $\pm$50 s time correlation window 99
5.29 Same (red) and opposite (blue) pixel time correlations corresponding to the full statistics for ^{54}Ni in a $\pm$50 s time correlation window. Opposite pixel correlations are normalised by a factor of 1.11206. The same (red) and opposite (blue) correlation curves are indistinguishable except for the interval associated with the activity under study. 100
5.30 Same (red) and opposite (blue) pixel time correlations corresponding to the full statistics for ^{54}Ni in a $\pm$50 s time correlation window. The normalised opposite-pixel spectrum is subtracted from the same-pixel spectrum bin by bin. Each 10ms bin includes the error bar associated with the subtraction 101
5.31 True correlations fitted by Eq. 5.2 -p.101- in black. Mother beta-decay curve in red, daughter beta growth and decay curve in blue. In this case the minimisation of the function was done using the least squares method 102
5.32 Time difference between the beginning of the spill and the time-stamp of a decay trigger or implantation trigger during the measurement of the ^{54}Ni. The time-region selected was 2500-8000 [ms] 103

5.33 Time difference between the beginning of the spill and the time-stamp of a decay or implantation trigger during the measurement of the ^{50}Fe setup. The time-region selected was 2500-6500 [ms] 104

5.34 Time difference between the beginning of the spill and the time-stamp of a decay or implantation trigger during the measurement of the ^{46}Cr setup. The time-region selected was 3000-8000 [ms] 104

5.35 Time difference between the beginning of the spill and the time-stamp of a decay or implantation trigger during the measurement of the ^{42}Ti setup. The time-region selected was 2000-7000 [ms] 105

5.36 ^{54}Ni β-decay half-life for implant-beta correlations using a least squares minimisation. The red curve represents the decay of the mother nucleus ^{54}Ni and the blue curve represents the growth and decay curve of the ^{54}Co superallowed β emitting daughter nucleus. The daughter half-life is $T^d_{1/2}$= 193.271(63) ms [HT09], and is a fixed parameter in the fit. 108

5.37 ^{54}Ni β-decay half-life for implant-beta correlations using a maximum likelihood minimisation. The red curve represents the decay of the mother nucleus ^{54}Ni and the blue curve represents the growth and decay curve of the ^{54}Co superallowed β emitting daughter nucleus. The daughter half-life is $T^d_{1/2}$= 193.271(63) ms [HT09], and is a fixed parameter in the fit. 109

5.38 ^{50}Fe β-decay half-life for implant-beta correlations using a least squares minimisation. The red curve represents the decay of the mother nucleus ^{50}Fe and the blue curve represents the growth and decay curve of the ^{50}Mn daughter superallowed β emitting nucleus. The daughter half-life is $T^d_{1/2}$= 283.21(11) ms [HT09], and is a fixed parameter in the fit. 110

5.39 ^{50}Fe β-decay half-life for implant-beta correlations using a maximum likelihood minimisation. The red curve represents the decay of the mother nucleus ^{50}Fe and the blue curve represents the growth and decay curve of the ^{50}Mn superallowed β emitting daughter nucleus. The daughter half-life is $T^d_{1/2}$= 283.21(11) ms [HT09], and is a fixed parameter in the fit. 111

5.40 ^{46}Cr β-decay half-life for implant-beta correlations using a least squares minimisation. The red curve represents the decay of the mother nucleus ^{46}Cr and the blue curve represents the growth and decay curve of the ^{46}V superallowed β emitting daughter nucleus. The daughter half-life is $T^d_{1/2}$= 422.50(11) ms [HT09], and is a fixed parameter in the fit. 112

5.41 ^{46}Cr β-decay half-life for implant-beta correlations using a maximum likelihood minimisation. The red curve represents the decay of the mother nucleus ^{46}Cr and the blue curve represents the growth and decay curve of the ^{46}V superallowed β emitting daughter nucleus. The daughter half-life is $T^d_{1/2}$= 422.50(11) ms [HT09], and is a fixed parameter in the fit. 113

5.42 ^{42}Ti β-decay half-life for implant-beta correlations using a least squares minimisation. The red curve represents the decay of the mother nucleus ^{42}Ti and the blue curve represents the growth and decay curve of the ^{42}Sc superallowed β emitting daughter nucleus. The daughter half-life is $T^d_{1/2}$= 680.72(26) ms [HT09], and is a fixed parameter in the fit. 114

5.43 ^{42}Ti β-decay half-life for implant-beta correlations using a maximum likelihood minimisation. The red curve represents the decay of the mother nucleus ^{42}Ti and the blue curve represents the growth and decay curve of the ^{42}Sc superallowed β emitting daughter nucleus. The daughter half-life is $T^d_{1/2}$= 680.72(26) ms [HT09], and is a fixed parameter in the fit. 115
5.44 ^{54}Ni β-delayed γ-events in the coincidence gate of 100 μs. The software coincidence gate of 250 ns was set in the 86.5-89.0 [100ns] time range. . . 118
5.45 Correlation time vs. γ-energy for correlations in the same pixel in the ^{54}Ni experiment. 118
5.46 Correlation time vs. γ-energy for correlations in the opposite pixel in the^{54}Ni experiment. 119
5.47 All γ-implantation time correlations for the ^{54}Ni setup. In red the same-pixel correlations. In blue the wrong correlations. Normalisation Factor 1.11152. Integration from 6 sec to 20 sec 119
5.48 Same-pixel γ-implant correlations and wrong correlations normalised. . . 120
5.49 ^{54}Ni γ-ray energy spectrum with Same-pixel (red) and wrong correlations (Blue) normalised using the same factor as in Fig. 5.48 -p.120- 120
5.50 A clean ^{54}Ni γ-ray energy spectrum, i.e. without contaminants or randoms for correlations in the same pixel. 121
5.51 ^{54}Ni, ^{50}Fe, ^{46}Cr and ^{42}Ti clean γ-energy spectra, i.e. without contaminants or randoms for correlations in the same pixel. 122
5.52 ^{54}Ni γ-ray energy spectrum with Same-pixel (red) and wrong correlations (Blue). 123
5.53 ^{54}Ni γ-ray energy spectrum with same-pixel (red) and wrong correlations (Blue) normalised. 123
5.54 ^{54}Ni γ-ray energy spectrum with same-pixel (red) and wrong correlations (Blue) subtracted. This spectrum shows the real ^{54}Ni gamma spectrum without contaminants and randoms, but the implantation and the beta in coincidence with the gammas are correlated in the same pixel. 124
5.55 Fits to the β-delayed first-excited-state-γ for the ^{54}Ni, ^{50}Fe, ^{46}Cr and ^{42}Ti.125

6.1 ^{54}Ni β-decay scheme. All the values given in this figure originate from the present work except for the Q_β-value which is taken from [Aud03] and the daughter half-life, taken from [HT09]. 134
6.2 ^{50}Fe β-decay scheme. All the values given in this figure originate from the present work except for the Q_β-value which is taken from [Aud03] and the daughter half-life, taken from [HT09]. 135
6.3 ^{46}Cr β-decay scheme. All the values given in this figure originate from the present work except for the Q_β-value which is taken from [Aud03] and the daughter half-life, taken from [HT09]. 136
6.4 ^{42}Ti β-decay scheme using the Q-value reported by T.Kurtukian-Nieto et al [Kur09]. All the values given in this figure originate from the present work except for the Q_β-values which are taken from [Kur09] and the daughter half-life, taken from [HT09]. 137
6.5 ^{54}Ni β-decay in the single particle scheme 139
6.6 ^{50}Fe β-decay in the single particle scheme 140
6.7 ^{46}Cr β-decay in the single particle scheme 140

6.8 ^{42}Ti β-decay single particle scheme. 141

6.9 Comparison between the absolute Gamow-Teller Strength from β-decay $B(GT+)$, shown in red triangles, and the normalised Gamow-Teller strength from charge exchange reactions $B(GT-)$, for the mass 54 with total isospin T=1. The half-life value shown in blue was obtained from the normalised $B(GT-)$ using Eq. 1.22 -p.9-. 144

6.10 Comparison between the absolute Gamow-Teller Strength from β-decay $B(GT+)$, shown in red triangles, and the normalised Gamow-Teller strength from charge exchange reactions $B(GT-)$, for the mass 50 with total isospin T=1. The half-life value shown in blue was obtained from the normalised $B(GT-)$ using Eq. 1.22 -p.9-. 145

6.11 Comparison between the absolute Gamow-Teller Strength from β-decay $B(GT+)$, shown in red triangles, and the normalised Gamow-Teller strength from charge exchange reactions $B(GT-)$, for the mass 46 with total isospin T=1. The half-life value shown in blue was obtained from the normalised $B(GT-)$ using Eq. 1.22 -p.9-. 146

6.12 Comparison between the absolute Gamow-Teller Strength from β-decay $B(GT+)$, shown in red triangles, and the normalised Gamow-Teller strength from charge exchange reactions $B(GT-)$, for the mass 42 with total isospin T=1. The half-life value shown in blue was obtained from the normalised $B(GT-)$ using Eq. 1.22 -p.9-. 147

7.1 Espectros de energía de reacciones de intercambio de carga a 0°. Comparación entre medidas de la reacción ^{58}Ni$(p,n)^{58}$Cu llevadas a cabo en los 80 [RS94] (ΔE $\sim$ 400 keV) y las medidas recientes de la reacción ^{58}Ni$(^3$He$,t)^{58}$Cu [Fuj07a] (ΔE $\sim$ 35 keV). 155

7.2 Estructura de la simetría de isoespín en núcleos isóbaros con T$_z$= 0, $\pm$1, $\pm$2. (a) Esquema de niveles en el espacio real de energías. (b) Esquema de niveles sustrayendo la energía Coulombiana de desplazamiento. La estructura simétrica es evidente. Los estados análogos estan conectados mediante líneas discontínuas [Ada07a]. 156

7.3 Carta de Nucleidos. En la figura se muestran algunos núcleos de la capa fp. Las líneas muestran los núcleos con tercera componente de isoespín $T_z = \frac{N-Z}{2} = 0, \pm 1$. El código de colores usual en la carta de nucleidos es: rojo para núcleos que se desintegran β^+, azul para núcleos que se desintegran β-, negro para núcleos radioactivamente estables. 158

7.4 Esquema del experimento de reacción de intercambio de carga en RCNP Osaka, Japón. 159

7.5 Resultados de la reacción ^{42}Ca$(^3$He$,t)^{42}$Sc de alta resolución [Ada07b]. Las tablas con las energías de excitación y el valor de la fuerza de transición Gamow-Teller medida en esta reacción puede verse en el Apéndice B. 160

7.6 Resultados de la reacción ^{46}Ti$(^3$He$,t)^{46}$V de alta resolución [Ada06]. Las tablas con las energías de excitación y el valor de la fuerza de transición Gamow-Teller medida en esta reacción puede verse en el Apéndice B. . . . 161

7.7 Resultados de la reacción ^{50}Cr(^{3}He, t)^{50}Mn de alta resolución [Fuj05a]. Las tablas con las energías de excitación y el valor de la fuerza de transición Gamow-Teller medida en esta reacción puede verse en el Apéndice B. 162
7.8 Resultados de la reacción ^{54}Fe(^{3}He, t)^{54}Cr de alta resolución [Ada07b]. Las tablas con las energías de excitación y el valor de la fuerza de transición Gamow-Teller medida en esta reacción puede verse en el Apéndice B. 163
7.9 Esquema de LISOL. 165
7.10 Espectro de energía γ del ^{54}Ni 166
7.11 Curva de implantación y desintegración del ^{54}Ni. Cada punto representa el area de una función Gaussiana ajustada al γ de 937 keV, sustrayendo un fondo líneal en la región cercana. 167
7.12 Curva de implantación y desintegración del ^{54}Ni. Cada punto representa el area de una función Gaussiana ajustada al γ de 937 keV, sustrayendo un fondo líneal obtenido en la región de sólo fondo 800 keV - 1100 keV. . 168
7.13 Curva de implantación y desintegración del ^{54}Ni. Cada punto representa el area de una función Gaussiana ajustada al γ de 937 keV. El fondo fue sustraido a ajustando una segunda Gaussiana al rayo γ suma a 922 keV más un fondo líneal tomado entre 800 to 1100 keV. 169
7.14 Esquema general del separador de fragmentos FRS y los distintos detectores utilizados para la identificación del ión implantado en los detectores de silicio DSSSD. 170
7.15 Espectro γ del set-up del ^{54}Ni, Parte 1. Rango de Energía: 0-1000 keV. . 172
7.16 Espectro γ del set-up del ^{54}Ni, Parte 3. Rango de Energía: 2000-3000 keV.172
7.17 Espectro γ del set-up del ^{54}Ni, Parte 5. Rango de Energía: 4000-5000 keV.172
7.18 Espectro γ del set-up del ^{54}Ni, Parte 2. Rango de Energía: 1000-2000 keV.173
7.19 Espectro γ del set-up del ^{54}Ni, Parte 4. Rango de Energía: 3000-4000 keV.173
7.20 Espectro γ del set-up del ^{54}Ni, Parte 6. Rango de Energía: 5000-6000 keV.173
7.21 Espectro γ del set-up del ^{50}Fe Parte 1. Rango de Energía: 0-1000 keV. . . 174
7.22 Espectro γ del set-up del ^{50}Fe Parte 3. Rango de Energía: 2000-3000 keV. 174
7.23 Espectro γ del set-up del ^{50}Fe Parte 5. Rango de Energía: 4000-5000 keV. 174
7.24 Espectro γ del set-up del ^{50}Fe Parte 2. Rango de Energía: 1000-2000 keV. 175
7.25 Espectro γ del set-up del ^{50}Fe Parte 4. Rango de Energía: 3000-4000 keV. 175
7.26 Espectro γ del set-up del ^{50}Fe Parte 6. Rango de Energía: 5000-6000 keV. 175
7.27 Espectro γ del set-up del ^{46}Cr, Parte 1. Rango de Energía: 0-1000 keV. . 176
7.28 Espectro γ del set-up del ^{46}Cr, Parte 3. Rango de Energía: 2000-3000 keV.176
7.29 Espectro γ del set-up del ^{46}Cr, Parte 5. Rango de Energía: 4000-5000 keV.176
7.30 Espectro γ del set-up del ^{46}Cr, Parte 2. Rango de Energía: 1000-2000 keV.177
7.31 Espectro γ del set-up del ^{46}Cr, Parte 4. Rango de Energía: 3000-4000 keV.177
7.32 Espectro γ del set-up del ^{46}Cr, Parte 6. Rango de Energía: 5000-6000 keV.177
7.33 Espectro γ del set-up del ^{42}Ti, Parte 1. Rango de Energía: 0-1000 keV. . 178
7.34 Espectro γ del set-up del ^{42}Ti, Parte 3. Rango de Energía: 2000-3000 keV.178
7.35 Espectro γ del set-up del ^{42}Ti, Parte 5. Rango de Energía: 4000-5000 keV.178
7.36 Espectro γ del set-up del ^{42}Ti, Parte 2. Rango de Energía: 1000-2000 keV.179
7.37 Espectro γ del set-up del ^{42}Ti, Parte 4. Rango de Energía: 3000-4000 keV.179
7.38 Espectro γ del set-up del ^{42}Ti, Parte 6. Rango de Energía: 5000-6000 keV.179

7.39 Correlaciones temporales de implantación y desintegración en el mismo píxel (en rojo) y en píxeles opuestos (en azul) correspondientes a toda la estadística del ^{54}Ni, en una ventana de correlación de ±50 s 184
7.40 Vida media de la desintegración del ^{54}Ni usando minimización por mínimos cuadrados. La curva roja representa la actividad del núcleo padre ^{54}Ni y la curva azul representa la actividad del núcleo hijo ^{54}Co. La vida media del núcleo hijo es $T^d_{1/2}$= 193.271(63) ms [HT09] (parámetro fijo del ajuste). 187
7.41 Vida media de la desintegración del ^{54}Ni usando minimización por máxima verosimilitud. La curva roja representa la actividad del núcleo padre ^{54}Ni y la curva azul representa la actividad del núcleo hijo ^{54}Co. La vida media del núcleo hijo es $T^d_{1/2}$= 193.271(63) ms [HT09] (parámetro fijo del ajuste). 188
7.42 Vida media de la desintegración del ^{50}Fe usando minimización por mínimos cuadrados. La curva roja representa la actividad del núcleo padre ^{50}Fe y la curva azul representa la actividad del núcleo hijo ^{50}Mn. La vida media del núcleo hijo es $T^d_{1/2}$= 283.21(11) ms [HT09] (parámetro fijo del ajuste). 189
7.43 Vida media de la desintegración del ^{50}Fe usando minimización por máxima verosimilitud. La curva roja representa la actividad del núcleo padre ^{50}Fe y la curva azul representa la actividad del núcleo hijo ^{50}Mn. La vida media del núcleo hijo es $T^d_{1/2}$= 283.21(11) ms [HT09] (parámetro fijo del ajuste). 190
7.44 Vida media de la desintegración del ^{46}Cr usando minimización por mínimos cuadrados. La curva roja representa la actividad del núcleo padre ^{46}Cr y la curva azul representa la actividad del núcleo hijo ^{46}V. La vida media del núcleo hijo es $T^d_{1/2}$= 422.50(11) ms [HT09] (parámetro fijo del ajuste). 191
7.45 Vida media de la desintegración del ^{46}Cr usando minimización por máxima verosimilitud. La curva roja representa la actividad del núcleo padre ^{46}Cr y la curva azul representa la actividad del núcleo hijo ^{46}V. La vida media del núcleo hijo es $T^d_{1/2}$= 422.50(11) ms [HT09] (parámetro fijo del ajuste). 192
7.46 Vida media de la desintegración del ^{42}Ti usando minimización por mínimos cuadrados. La curva roja representa la actividad del núcleo padre ^{42}Ti y la curva azul representa la actividad del núcleo hijo ^{42}Sc. La vida media del núcleo hijo es $T^d_{1/2}$= 680.72(26) ms [HT09] (parámetro fijo del ajuste). 193
7.47 Vida media de la desintegración del ^{42}Ti usando minimización por máxima verosimilitud. La curva roja representa la actividad del núcleo padre ^{42}Ti y la curva azul representa la actividad del núcleo hijo ^{42}Sc. La vida media del núcleo hijo es $T^d_{1/2}$= 680.72(26) ms [HT09] (parámetro fijo del ajuste). 194
7.48 Vidas medias de los núcleos ^{54}Ni, ^{50}Fe, ^{46}Cr y ^{42}Ti, evolución temporal del rayo γ asociado al primer estado excitado en los correspondientes núcleos hijos. 195
7.49 ^{54}Ni, ^{50}Fe, ^{46}Cr and ^{42}Ti clean γ-energy spectra, i.e. without contaminants or randoms for correlations in the same pixel. 196
7.50 Esquema de niveles de la desintegración β del ^{54}Ni. Todos los resultados de esta figura provienen del análisis de nuestro experimento, excepto el valor Q_β [Aud03] y la vida media del núcleo hijo [HT09]. 203

7.51 Esquema de niveles de la desintegración β del ^{50}Fe. Todos los resultados de esta figura provienen del análisis de nuestro experimento, excepto el valor Q_β [Aud03] y la vida media del núcleo hijo [HT09]. 204
7.52 Esquema de niveles de la desintegración β del ^{46}Cr. Todos los resultados de esta figura provienen del análisis de nuestro experimento, excepto el valor Q_β [Aud03] y la vida media del núcleo hijo [HT09]. 205
7.53 Esquema de niveles de la desintegración β del ^{42}Ti. Todos los resultados de esta figura provienen del análisis de nuestro experimento, excepto el valor Q_β [Kur09] y la vida media del núcleo hijo [HT09]. 206

C.1 Drawing of the interaction of a γ-ray with energy E_γ, with two germanium crystals, depositing part of its energy in both of them. $E_\gamma = E_1+E_2$ . . . 218

D.1 RISING efficiency curve using the Addback routine 233
D.2 Efficiency curve using the sum of single crystals 234

E.1 ABAI correlations using simulated implantation and beta events in a $\pm$50s time window. The implantations were obtained using a uniform random distribution in the first 10 s of the spill period of 13 s. The beta-events were simulated using an exponential distribution with $T_{1/2}$= 114.1 ms (experimental ^{54}Ni half-life). We simulated 300 implantations per spill and the total simulation time was 10 min. 236
E.2 ABAI correlations using simulated implantation and beta events in a $\pm$50s time window. The implantations were obtained using a uniform random distribution in the first 10 s of the spill period of 13 s.The beta-events were simulated using an exponential distribution with $T_{1/2}$= 114.1 ms (experimental ^{54}Ni half-life). We simulated 300 implantations per spill and the total simulation time was 1 h. 236
E.3 ABAI correlations using simulated implantation and beta events in a $\pm$50s time window. The implantations were obtained using a uniform random distribution in the complete spill period of 13 s. The beta-events were simulated using an exponential distribution with $T_{1/2}$= 114.1 ms (experimental ^{54}Ni half-life). We simulated 300 implantations per spill and the total simulation time was 10 min. 237
E.4 ABAI correlations using simulated implantation and beta events in a $\pm$50s time window. The implantations were obtained using a uniform random distribution in the complete spill period of 13 s. The beta-events were simulated using an exponential distribution with $T_{1/2}$= 114.1 ms (experimental ^{54}Ni half-life). We simulated 300 implantations per spill and the total simulation time was 1 h. 237
E.5 ABAI correlations using simulated implantation and beta events in a $\pm$50s time window. The implantations were obtained using a Gaussian random distribution in the first 10sec of the spill period. The beta-events were simulated using an exponential distribution with $T_{1/2}$= 114.1 ms (experimental ^{54}Ni half-life). We simulated 300 implantations per spill and the total simulation time was 10 min. 238

E.6 ABAI correlations using simulated implantation and beta events in a ±50s time window. The implantations were obtained using a Gaussian random distribution in the first 10sec of the spill period. The beta-events were simulated using an exponential distribution with $T_{1/2}$= 114.1 ms (experimental ^{54}Ni half-life). We simulated 300 implantations per spill and the total simulation time was 1 h. 239
E.7 Expansion of Figure E.6. 239
E.8 ABAI correlations using simulated implantation and beta events in a ± 20s time window. The implantations were obtained using a Gaussian random distribution in the first 10sec of the spill period. The beta-events were simulated using an exponential distribution with $T_{1/2}$= 114.1 ms (experimental ^{54}Ni half-life). We simulated 20 implantations per spill and the total simulation time was 10 h. 240
E.9 Expansion of Figure E.8. 240

LIST OF TABLES

4.1 Experimental Settings for the production of the different fragments. . . . 43
4.2 Experimental Settings for the separation of the fragments. 43
4.3 Trigger of the data acquisition system and the detector signals recorded. The implantation trigger was an AND signal of sci41 and an OR DSSSD strips, and the decay trigger was an OR signal of the DSSSD strips. . . . 57
4.4 Ratio of the selected fragment, in the window, implanted in M2 shown in Figs. 4.20-4.23 -pp.60 to 61-, and total including the rest of the ions implanted in M2. The rates of implantation of all the fragments implanted in M2 are also shown. 59

5.1 List of γ-ray energies for the ^{54}Ni setup at RISING in Single Crystal mode (sum of all crystals). 80
5.2 List of γ-ray energies for the ^{54}Ni setup at RISING in Add-back mode. (^{1}) ^{52}Co β^{+}/^{53}Co p-decay 81
5.3 List of γ-ray energies for the ^{50}Fe setup at RISING in Single Crystal mode (sum of all crystals). 84
5.4 List of γ-ray energies for the ^{50}Fe setup at RISING in Add-back mode. . 85
5.5 List of γ-ray energies for the ^{46}Cr setup at RISING in Single Crystal mode (sum of all crystals). 88
5.6 List of γ-ray energies for the ^{46}Cr setup at RISING in Add-back mode. . 89
5.7 List of γ-ray energies for the ^{42}Ti setup at RISING in Single Crystal mode (sum of all crystals). 92
5.8 List of γ-energies for the ^{42}Ti setup at RISING in Add-back mode. 93
5.9 Statistics for the different runs in DSSSD M2. The counting rate per pixel was calculated for the 64 beam-centred pixels in M2. 97
5.10 Half-life measurements with ABAI correlations in M2, with the complete statistics and using a selected range within the spill period. 105

5.11 β-decay half-life results and comparison with values in the literature. $T^{LS}_{1/2}$ is the half-life obtained using a least square minimisation, $T^{ML}_{1/2}$ is the half-life obtained using a maximum likelihood minimisation and $T^{Av}_{1/2}$ is the average of $T^{LS}_{1/2}$ and $T^{ML}_{1/2}$. The error in $T^{Av}_{1/2}$ is the simple average of the $T^{LS}_{1/2}$ and $T^{ML}_{1/2}$ errors. 106

5.12 β-decay ($T^{\beta}_{1/2}$) and β-delayed first-excited-state-γ ($T^{\beta-\gamma}_{1/2}$) half-life results and comparison with half-life values from the literature (Lit. $T_{1/2}$). 124

5.13 ^{54}Ni β branching ratio. The total number of ^{54}Ni nuclei which were produced and β-decay giving a signal in the M2 DSSSD, N_0^{β}, was taken from the fit to the β-decay half-life (see Figs. 5.36 and 5.37 -pp.108 and 109-, N_0^{β}= 838204.8(686.3)). The number of ^{54}Ni nuclei produced and β-decays populating the first excited state in ^{54}Co and the γ detected in the RISING array, $N_0^{1st.exct.state}$, was taken from the fit of the β-delayed γ half-life (see Fig. 5.55 -p.125-, $N_0^{1st.exct.state}$ = 24535.1(268.5)). The Branching Ratio was obtained using Eq. 5.4 and 5.5 -p.127-. 128

5.14 ^{50}Fe β branching ratio. The total number of ^{50}Fe nuclei which were produced and β-decay giving a signal in the M2 DSSSD, N_0^{β}, was taken from the fit to the β-decay half-life (see Figs. 5.38 and 5.39 -pp.110 and 111- , N_0^{β}= 330691.7(508.5)). The number of ^{50}Fe nuclei which were produced and β-decay giving a signal in the M2 DSSSD populating the first excited state in ^{50}Mn and the γ detected in the RISING array, $N_0^{1st.exct.state}$, was taken from the fit of the β-delayed γ half-life (see Fig. 5.55 -p.125-, $N_0^{1st.exct.state}$ = 13391.5(187.0)). The Branching Ratio was obtained using Eq. 5.4 and 5.5 -p.127-. 128

5.15 ^{46}Cr β branching ratio. The total number of ^{46}Cr nuclei which were produced and β-decay giving a signal in the M2 DSSSD, N_0^{β}, was taken from the fit to the β-decay half-life (see Figs. 5.40 and 5.41 -pp.112 and 113-, N_0^{β}= 310096.1(1009.3)). The number of ^{46}Cr nuclei which were produced and β-decay giving a signal in the M2 DSSSD populating the first excited state in ^{46}V and the γ detected in the RISING array, $N_0^{1st.exct.state}$, was taken from the fit of the β-delayed γ half-life (see Fig. 5.55 -p.125-, $N_0^{1st.exct.state}$ = 6198.0(190.0)). The Branching Ratio was obtained using Eq. 5.4 and 5.5 -p.127-. 129

5.16 ^{42}Ti β branching ratio. The total number of ^{42}Ti nuclei which were produced and β-decay giving a signal in the M2 DSSSD, N_0^{β}, was taken from the fit to the β-decay half-life (see Figs. 5.42 and 5.43 -pp.115 and 115-, N_0^{β}= 74565.7(250.9)). The number of ^{42}Ti nuclei which were produced and β-decay giving a signal in the M2 DSSSD populating the first excited state in ^{42}Sc and the γ detected in the RISING array, $N_0^{1st.exct.state}$, was taken from the fit of the β-delayed γ half-life (see Fig. 5.55 -p.125-, $N_0^{1st.exct.state}$ = 7631.3(134.3)). The Branching Ratio was obtained using Eq. 5.4 and 5.5 -p.127-. 129

5.17 Experimental results: Beta half-life ($T_{1/2}^{\beta\text{exp}}$), estimated T_F, with the corresponding Q-value from Audi et al. [Aud03]. In the case of ^{42}Ti we also used a recently measured Q-value from T.Kurtukian-Nieto et al. [Kur09]. In the fifth column we give the experimental g.s. to g.s. feeding and in the sixth column the expected g.s. feed = $T_{1/2}^{\beta\text{exp}}/T_F$ 130

5.18 Gamow-Teller transition strength to the excited states in ^{54}Co in the β^+-decay of ^{54}Ni, using the Q$_\beta$-value from [Aud03]. 131

5.19 Gamow-Teller transition strength to the excited states in ^{50}Mn in the β^+-decay of ^{50}Fe, using the Q$_\beta$-value from [Aud03]. 131

5.20 Gamow-Teller transition strength to the excited states in ^{46}V in the β^+-decay of ^{46}Cr, using the Q$_\beta$-value from [Aud03]. 131

5.21 Gamow-Teller transition strength to the excited state in ^{42}Sc in the β^+-decay of ^{42}Ti, using the Q$_\beta$-value from [Kur09]. 132

5.22 Gamow-Teller transition strength to the excited state in ^{42}Sc in the β^+-decay of ^{42}Ti, using the Q$_\beta$-value from [Aud03]. 132

6.1 Single Particle Gamow-Teller matrix element $|\langle i|\sigma\tau_+|f\rangle|^2$, where l is the angular momentum (s=0,d=1,f=2,g=3,h=4). 138

6.2 Comparison of measured Gamow-Teller strength in β-decay experiments $B(GT+)_{\text{exp}}$ with the prediction of the extreme single particle method $B(GT+)_{\text{ESPM}}$. The quenching factor q is the ratio of these two quantities. In the ^{42}Ti case the two different results for the experimental B(GT) value, using the Q-values from Kurtukian-Nieto [Kur09] and Audi [Aud03], are shown. 141

6.3 Comparison of the Gamow-Teller strength values from Charge Exchange reactions (B(GT-)$_{CE}$) and β-decay experiments B(GT+)$_\beta$ for mass 54. The B(GT-)$_{CE1}$ are the B(GT) from CE reactions normalised to the first excited state B(GT+). The B(GT-)$_{CE2}$ are the B(GT) from CE reactions normalised to the total strength in the Q$_\beta$ window. The B(GT-)$_{CE3}$ are the B(GT) from CE reactions normalised using the *merged analysis*. The R^2-value was taken from the systematic dependence of R^2 and A. In this case R^2=8.9(9). 148

6.4 Comparison of the Gamow-Teller strength values from Charge Exchange reactions (B(GT-)$_{CE}$) and β-decay experiments B(GT+)$_\beta$ for mass 50. The B(GT-)$_{CE1}$ are the B(GT) from CE reactions normalised to the first excited state B(GT+). The B(GT-)$_{CE2}$ are the B(GT) from CE reactions normalised to the total strength in the Q$_\beta$ window. The B(GT-)$_{CE3}$ are the B(GT) from CE reactions normalised using the *merged analysis*. The R^2-value was calculated using the half-life value obtained from the analysis of the present experiment. 149

6.5 Comparison of the Gamow-Teller strength values from Charge Exchange reactions (B(GT-)$_{CE}$) and β-decay experiments B(GT+)$_\beta$ for mass 46. The B(GT-)$_{CE1}$ are the B(GT) from CE reactions normalised to the first excited state B(GT+). The B(GT-)$_{CE2}$ are the B(GT) from CE reactions normalised to the total strength in the Q$_\beta$ window. The B(GT-)$_{CE3}$ are the B(GT) from CE reactions normalised using the *merged analysis*. The R^2-value was taken from the systematic dependence of R^2 and A. In this case R^2=7.8(9). 150

6.6 Comparison of the Gamow-Teller strength values from Charge Exchange reactions (B(GT-)$_{CE}$) and β-decay experiments B(GT+)$_\beta$ for mass 42. The B(GT-)$_{CE1}$ are the B(GT) from CE reactions normalised to the first excited state B(GT+). The B(GT-)$_{CE2}$ are the B(GT) from CE reactions normalised to the total strength in the Q$_\beta$ window. The B(GT-)$_{CE3}$ are the B(GT) from CE reactions normalised using the *merged analysis*. The R^2-value was taken from the systematic dependence of R^2 and A. In this case R^2=5.5(3). 151

6.7 Half-life obtained from the CE-reactions normalising by the first excited state $B(GT+)$ ($T_{1/2}^{\mathrm{CE1}}$) and by the total strength in the Q$_\beta$-window ($T_{1/2}^{\mathrm{CE2}}$), using Eq. 1.22 -p.9-, in comparison with the β-decay half-life obtained from this work. 151

7.1 Resultados de medidas experimentales en la literatura de los núcleos en la capa fp con T$_z$=-1. 164

7.2 Lista de las energías γ vistas en la desintegración del ^{54}Ni en RISING, usando el modo Add-back. (^{1}) ^{52}Co $\beta^+/^{53}$Co p-decay. 180

7.3 Lista de las energías γ vistas en la desintegración del ^{50}Fe en RISING, usando el modo Add-back. 181

7.4 Lista de las energías γ vistas en la desintegración del ^{46}Cr en RISING, usando el modo Add-back. 182

7.5 Lista de las energías γ vistas en la desintegración del ^{42}Ti en RISING, usando el modo Add-back. 183

7.6 Resultados de vida media de la desintegración β y su comparación con los valores de la literatura. $T_{1/2}^{\mathrm{LS}}$ es la vida media obtenida usando mínimos cuadrados, $T_{1/2}^{\mathrm{ML}}$ es la vida media obtenida usando máxima verosimilitud y $T_{1/2}^{\mathrm{Av}}$ es el promedio de $T_{1/2}^{\mathrm{LS}}$ y $T_{1/2}^{\mathrm{ML}}$. 185

7.7 Vidas medias obtenidas mediante correlaciones implantación-β (T$_{1/2}^{\beta}$) y vidas medias obtenidas mediante correlaciones implantación-β-$\gamma^{\mathrm{1er.estado.excitado}}$ (T$_{1/2\beta-\gamma}$) y la comparación con los resultados de la literatura (Lit. T$_{1/2}$). 186

7.8 Población de los estados excitados del ^{54}Co en la desintegración del ^{54}Ni. El número total de ^{54}Ni implantados que se desintegran β, N_0^β, proviene del ajuste de la vida media en las Figs. 7.40 y 7.41, N_0^β= 838204.8(686.3). El número de ^{54}Ni implantados que se desintegran β y que además pueblan el primer estado excitado en ^{54}Co, $N_0^{\gamma_1}$, proviene del ajuste de la vida media en la Fig. 7.48, $N_0^{\gamma_1}$ = 24535.1(268.5). 199

7.9 Población de los estados excitados del ^{50}Mn en la desintegración del ^{50}Fe. El número total de ^{50}Fe implantados que se desintegran β, N_0^β, proviene del ajuste de la vida media en las Figs. 7.42 y 7.43, N_0^β= 330691.7(508.5). El número de ^{50}Fe implantados que se desintegran β y que además pueblan el primer estado excitado en ^{50}Mn, $N_0^{\gamma_1}$, proviene del ajuste de la vida media en la Fig.7.48, $N_0^{\gamma_1}$ = 13391.5(187.0). 199

7.10 Población de los estados excitados del ^{46}V en la desintegración del ^{46}Cr. El número total de ^{46}Cr implantados que se desintegran β (N_0^β), proviene del ajuste de la vida media en las Figs. 7.44 y 7.45, N_0^β=310096.1(1009.3). El número de ^{46}Cr implantados que se desintegran β y que además pueblan el primer estado excitado en ^{46}V, $N_0^{\gamma_1}$, proviene del ajuste de la vida media en la Fig.7.48, $N_0^{\gamma_1}$ = 6198.0(190.0). 200

7.11 Población de los estados excitados del ^{42}Sc en la desintegración del ^{42}Ti. El número total de ^{42}Ti implantados que se desintegran β, N_0^β, proviene del ajuste de la vida media en las Figs. 7.46 y 7.47, N_0^β=74565.7(250.9). El número de ^{42}Ti implantados que se desintegran β y que además pueblan el primer estado excitado en ^{42}Sc, $N_0^{\gamma_1}$, proviene del ajuste de la vida media en la Fig.7.48, $N_0^{\gamma_1}$ = 7631.3(134.3). 200

7.12 Resultados experimentales: Vida media desintegración β ($T_{1/2}^{\mathrm{exp.}\beta}$), población al estado fundamental del núcleo hijo de nuestro experimento (Pobl.e.f.(Exp.)), valor Q_β según referencias. 201

7.13 Resultados de la fuerza de la transición Gamow-Teller a los estados excitados del ^{54}Co en la desintegración β^+ del ^{54}Ni. 201

7.14 Resultados de la fuerza de la transición Gamow-Teller a los estados excitados del ^{50}Mn en la desintegración β^+ del ^{50}Fe. 202

7.15 Resultados de la fuerza de la transición Gamow-Teller a los estados excitados del ^{46}V en la desintegración β^+ del ^{46}Cr. 202

7.16 Resultados de la fuerza de la transición Gamow-Teller a los estados excitados del ^{42}Sc en la desintegración β^+ del ^{42}Ti. Valores calculados usando el valor Q_β [Kur09] 202

7.17 Resultados de la fuerza de la transición Gamow-Teller a los estados excitados del ^{42}Sc en la desintegración β^+ del ^{42}Ti. Valores calculados usando el valor Q_β [Aud03]. 202

7.18 Comparación entre los valores de la fuerza Gamow-Teller obtenidos mediante reacciones de intercambio de carga B(GT-)$^{\mathrm{CE}}$ y experimentos de desintegración β B(GT$^+$)$^\beta$ en la masa 42. Usando el valor Q_β [Kur09] . . 207

7.19 Comparación entre los valores de la fuerza Gamow-Teller obtenidos mediante reacciones de intercambio de carga B(GT-)$^{\mathrm{CE}}$ y experimentos de desintegración β B(GT$^+$)$^\beta$ en la masa 42, usando el valor Q_β [Aud03]. . . 207

7.20 Comparación entre los valores de la fuerza Gamow-Teller obtenidos mediante reacciones de intercambio de carga B(GT-)$^{\mathrm{CE}}$ y experimentos de desintegración β B(GT$^+$)$^\beta$ en la masa 46. 208

7.21 Comparación entre los valores de la fuerza Gamow-Teller obtenidos mediante reacciones de intercambio de carga B(GT-)$^{\mathrm{CE}}$ y experimentos de desintegración β B(GT$^+$)$^\beta$ en la masa 50. 208

7.22 Comparación entre los valores de la fuerza Gamow-Teller obtenidos mediante reacciones de intercambio de carga B(GT-)$^{\mathrm{CE}}$ y experimentos de desintegración β B(GT$^+$)$^{\beta}$ en la masa 54. 209

B.1 States observed in the ^{42}Ca(^{3}He, t)^{42}Sc reaction below 4 MeV excitation energy. For the $L = 0$ states, B(GT) are given. 213
B.2 States observed in the ^{46}Ti(^{3}He, t)^{46}V reaction below 4.5 MeV excitation energy. For the $L = 0$ states, except for the $J^\pi = 0^+$ g.s. (IAS), GT transition strengths B(GT) are given. 214
B.3 States observed in the ^{50}Cr(^{3}He, t)^{50}Mn reaction below $E_x = 4.6$ MeV. For the $L = 0$ states, B(GT) values are given. 215
B.4 States observed in the ^{54}Fe(^{3}He, t)^{54}Co reaction for $E_x \leq 8$ MeV. For the identified $L = 0$ states, GT transition strengths B(GT) are given. 216

C.1 Example of Add-Back procedure 219

D.1 ^{133}Ba Single Crystal mode gamma rays 223
D.2 ^{152}Eu Single Crystal mode gamma rays 224
D.3 ^{226}Ra Single Crystal mode gamma rays 224
D.4 ^{133}Ba Addback mode 225
D.5 ^{152}Eu Addback mode 225
D.6 ^{226}Ra Addback mode 226
D.7 List of Addback and Single Crystal efficiencies each 100[keV], from the evaluation of Z.Hu [Hu98] efficiency curve. First Part. 227
D.8 List of Addback and Single Crystal efficiencies each 100[keV], from the evaluation of Z.Hu [Hu98] efficiency curve. Second Part. 228
D.9 Evaluation of the efficiency curve for the addback simulation for different radii of the RISING array. Columns 2-5 shows the efficiency value for the different simulated radii. Columns 6-8 shows the percentage difference between two simulated radii with 1cm difference. First Part 229
D.10 Evaluation of the efficiency curve for the addback simulation for different radii of the RISING array. Columns 2-5 show the efficiency value for the different simulated radii. Columns 6-8 shows the percentage difference between two simulated radii with 1cm difference. Second Part. 230
D.11 Evaluation of the efficiency curve for the single crystal simulation for different radii of the RISING array. Columns 2-5 shows the efficiency value for the different simulated radii. Columns 6-8 shows the percentage difference between two simulated radii with 1cm difference. First Part. . 231
D.12 Evaluation of the efficiency curve for the single crystal simulation for different radii of the RISING array. Columns 2-5 shows the efficiency value for the different simulated radii. Columns 6-8 shows the percentage difference between two simulated radii with 1cm difference. Second Part. 232

PREFACIO

Esta tesis comprende el estudio experimental de la desintegración β de cuatro núcleos con tercera componente de isoespín T_z=-1 en la capa nuclear fp. El objetivo principal de este trabajo es comparar estas cuatro desintegraciones con el proceso espejo estudiado en reacciones de intercamio de carga del tipo (^{3}He,t) en el Centro de Investigación de Física Nuclear RCNP en Osaka, Japón.
Los experimentos de desintegración β fueron realizados en dos laboratorios europeos: LISOL en el Centro de Investigación del Ciclotrón CRC en Louvain-la-Neuve, Belgica, y en Separador de FRagmentos, RISING-FRS en la Instalación de Iones Pesados GSI en Darmstadt, Alemania. Estos dos laboratorios emplean dos métodos de separación completamente distintos. Mientras que LISOL utiliza la técnica ISOL de separación luego de una reacción de fusión evaporación, en el GSI los iones se separan en vuelo luego de una reacción de fragmentación. Como veremos en los resultados, para estudiar núcleos de vidas medias del orden de cientos de ms, la reacción de fragmentación resulta más adecuada.

El experimento de desintegración β realizado en LISOL está descrito en el Capítulo 2 -p.17- (en inglés) y en la Sección 7.4.4 -p.164- del resumen en castellano (ver Capítulo 7 -p.153-). El experimento de desintegración β realizado en GSI está descrito en el Capítulo 4 -p.41- (en inglés) y en la Sección 7.4.4 -p.170-.

En el Capítulo 1 -p.1- (en inglés) y en la Sección 7.1 -p.153- del resumen en castellano, se describe el proceso de desintegración β, en particular las desintegraciones del tipo Fermi y Gamow-Teller; también se definen las fuerzas de transición Fermi $B(F)$ y Gamow-Teller $B(GT)$, dos cantidades muy importantes y necesarias para la comparación con los resultados de las reacciones de intercambio de carga.

La motivación de nuestro experimento esta explicada en la Sección 1.6 -p.9- (en inglés) y en la Sección 7.4.2 del resumen en castellano. Los resultados de los experimentos realizados en LISOL y en GSI están en los Capítulos 3 -p.25- y 5 -p.75-, respectivamente (en inglés) y en la Sección 7.4.4 -p.164- del resumen en castellano. La discusión y conclusiones del análisis de estos experimentos, se encuentran en el Capítulo 6 -p.133- (en inglés) y en la Sección 7.5 -p.207- del resumen en castellano.

ABSTRACT

This thesis covers an experimental study of the beta-decay of four T_z=-1 nuclei. The main purpose of this work is to compare these four decays with the mirror process studied in the (^{3}He,t) charge exchange reaction at RCNP in Osaka, Japan.
The experimental work was carried out at two different laboratories, LISOL at the Centre de Recherches du Cyclotron CRC in Louvain-la-Neuve, Belgium and RISING-FRS at the Gesellschaft für SchwerIonenforschung GSI in Darmstadt, Germany. The two facilities employ completely different methods of ion separation. The former uses the ISOL separation technique and the latter experiment uses fragmentation reactions and in-flight separation. As we will see from the results, for nuclei with very short half-lives such as those studied in this thesis, the fragmentation method is more appropriate.
The LISOL experiment is described in Chapter 2 -p.17- and the GSI experiment in Chapter 4 -p.41-.
In Chapter 1 -p.1- we give an overall description of the β-decay process, in particular the Fermi and Gamow-Teller decays and we also define the Fermi strength $B(F)$ and the Gamow-Teller strength $B(GT)$, two very important quantities needed for comparison with the charge exchange reaction results.
The motivation for our experiments is explained in Section 1.6 -p.9-. The results of the LISOL and GSI experiments are given in Chapter 3 -p.25- and in Chapter 5 -p.75- respectively. The discussion of the analysis and the conclusions are given in Chapter 6.

CHAPTER 1

INTRODUCTION

1.1 β decay

The history of beta-decay began in 1896 with the discovery of radioactivity by Antoine Henri Becquerel [Bec96]. In the years 1899 and 1900 he identified β radiation as one component of radioactivity, and demonstrated that β rays are composed of electrons, comparing it with the properties of cathode rays. Unfortunately the rapidity with which β rays were identified after their discovery did not lead to an equally rapid interpretation of the β decay process. At that moment physicists knew that certain substances have the same chemical properties but different radioactive properties (isotopes). As experiments improved, the interpretations of the β decay phenomenon became more and more confusing. Chadwick in 1914 [Cha14], using a magnetic spectrometer, discovered the continuous spectrum of the β particles. Thus it was known that the electron spectra had mono-energetic lines and a continuous component, in contrast with alpha and gamma ray spectra, which were known to consist of mono-energetic lines only. Chadwick further demonstrated that most of the events were part of the continuous component, the rest being mono-energetic electrons from electron conversion. The interpretation of the continuous electron spectrum was a major subject of debate. In 1914 Rutherford thought that the β electrons were all emitted from the nucleus with the same energy, but lost different fractions of this energy in collisions with the surrounding atoms, depending on the source thickness. But the main point was made by Lise Meitner in 1922. She realised that a quantised nucleus could not emit electrons of continuous energy. The known features of α and γ spectra were correctly interpreted as due to transitions of nuclei from one quantum state to another. Thus the continuous electron spectrum was a unique feature of β decay.
The measurement of the masses of different isotopes was the main determinant of the conclusion that the neutral mass existed inside the nucleus, but the common thought was that this neutrality was due to the neutralisation of the proton with an atomic

electron which falls into the nucleus. However, the uncertainty principle only allows electrons inside the nucleus with an energy greater than ∼100 MeV [1] (the maximum energy of electrons in the continuous β-spectrum is around 10 MeV). Consequently the electrons could not exist "a priori" in the nucleus.

In 1927 a crucial experiment was performed by Ellis and Wooster [EW27], in which they measured the total energy released in the disintegration of a ^{210}Bi source inside a calorimeter thick enough to stop all the emitted electrons. The endpoint of the electron β spectrum was known to be E_o=1.05 MeV, and the mean energy, $\bar{E}$, of the β electrons was known to be 390 keV. The calorimeter should have measured a total energy of 1.05 MeV if Rutherford's reasoning was correct. In fact they observed $\bar{E} = 344 \pm 34$ keV, which corresponded very well with the mean energy of the emitted electrons. The experiment was repeated in Berlin with an improved calorimeter by Meitner and Orthman in 1930 and the result was $\bar{E}$=337 $\pm$ 20 keV. These results were conclusive, Rutherford was wrong, but the results were difficult to interpret at the time.
In β decay not only was energy apparently not conserved, but the momentum and angular momentum were not conserved either. Pauli in 1931 proposed the idea of a very penetrating neutral particle of very small mass and spin 1/2 being emitted simultaneously with the electron. Then the β decay became a 3-body decay[Pau33]; the problem of the conservation of energy, momentum and spin was solved. This proposal was made before Chadwick's discovery in 1932 of the neutral elementary particle, the neutron, and it was Fermi who named Pauli's particle as the *neutrino*. In this way the process of emission of electrons from the nucleus was explained and scientifically accepted.
In 1934 Irene and Frédéric Joliot-Curie observed the emission of positive electrons (later called positrons) in radioactive decay. And in 1938 Alvarez observed electron capture from the innermost electronic orbits.
This brings us to our present knowledge of β-decay which takes the following forms;

1.- β^- **decay**: In this process a neutron (n) in the nucleus is converted into a proton (p) due to the Weak Interaction, emitting an electron (e^-) and an anti-neutrino ($\bar{\nu}$).

$$n \rightarrow p + e^- + \bar{\nu} \tag{1.1}$$

2.- β^+ **decay**: In this process a proton (p) in the nucleus is converted into a neutron (n) due to the Weak Interaction emitting a positron (e^+) and a neutrino (ν).

$$p \rightarrow n + e^+ + \nu \tag{1.2}$$

3.- **Electron Capture**: In the electron capture process, also called inverse β^+ decay, an electron (e^-) from the inner shell of the atom is captured by the nucleus, converting a proton (p) into a neutron (n) and emitting a neutrino (ν).

$$p + e^- \rightarrow n + \nu \tag{1.3}$$

[1] This rough calculation was made considering the size of the nucleus ∼ 1 [fm], but now we know that the size of the nucleus is ∼ 6 [fm], and considering this value the uncertainty principle allows electrons inside the nucleus with energies ∼ 16 MeV

1.2 Fermi theory of beta decay

In 1934 Fermi developed a theory of the β decay process to include the neutrino, presumed to be massless [2] as well as charge-less, dealing with the calculation of the transition probability of the process of β decay. This cannot be done starting from any other theory. A completely new force had to be introduced to explain the β transition which converts a neutron into a proton (or vice versa) and at the same time produces an electron (positron) and an anti-neutrino (neutrino). Such a force was introduced by Fermi, using the analogy with electromagnetism.
The transition probability in the β decay process can be given in terms of the first-order, time-dependent perturbation theory, later called the *Fermi Golden Rule*,

$$\lambda = \frac{2\pi}{\hbar}|\langle f|H_\beta|i\rangle|^2\rho_f \tag{1.4}$$

where $\langle f|H_\beta|i\rangle$ is the matrix element of the beta interaction H_β between the initial state $|i\rangle$ and the final state $|f\rangle$ of the complete system (nucleus and other relevant light particles), and ρ_f is the density of states in the final system. The final state of the system is specified by the electron and neutrino momenta and energies, (p_e, E_e) and (p_ν, E_ν), with $E_\nu = cp_\nu$. If E_f denotes the energy in the final system, we have

$$\rho_f dE_f = V^2\frac{p_e^2 dp_e d\Omega_e}{(2\pi\hbar)^3}\frac{p_\nu^2 dp_\nu d\Omega_\nu}{(2\pi\hbar)^3} \tag{1.5}$$

where V is a spherical volume in the momentum space and

$$E_f = E_e + E_\nu = E_e + p_\nu c \tag{1.6}$$

Without fixing the directions of the momenta, we have

$$\rho_f = V^2(4\pi)^2\frac{p_e^2 dp_e p_\nu^2}{(2\pi\hbar)^6}\frac{dp_\nu}{dE_f} \tag{1.7}$$

Fermi did not know the mathematical form of the interaction H_β in β decay. But in considering all possible forms consistent with special relativity, he showed that H_β could be replaced by an operator O_x which could, mathematically, take the form of a vector(V), scalar(S), pseudo-scalar(P), axial vector (A) or tensor (T). So, for beta-decay,

$$\langle f|H_\beta|i\rangle = W_{fi} = \sum_x g_x \int d\vec{r}\left[\Phi_f^*\psi_e^*\psi_\nu^*\right]O_x\Phi_i \tag{1.8}$$

where Φ_f, ψ_e and ψ_ν are the final wave functions of the nucleus, the electron and the neutrino. The value of g_x determines the *strength* of the interaction. The electron and neutrino are treated like free-particles, thus their wave functions have the form,

$$\psi_e(\vec{r}) = \frac{1}{\sqrt{V}}e^{i\vec{p_e}\cdot\vec{r}/\hbar}, \qquad \psi_\nu(\vec{r}) = \frac{1}{\sqrt{V}}e^{i\vec{p_\nu}\cdot\vec{r}/\hbar} \tag{1.9}$$

If we expand the exponentials and use the fact that over the nuclear volume $pr \ll 1$, we have the allowed approximation. If we replace the electron and neutrino wave functions

[2] Nowadays we think that the neutrino has some mass, although very small

in Eq. 1.8 -p.3- and use the allowed approximation, the matrix element is now $gM_{fi} = g\int d\vec{r}\Phi_f^* O\Phi_i$, so the decay rate is

$$\lambda = \frac{g^2}{2\pi^3\hbar^7}\int \frac{dp_\nu}{dE_f} p_e^2 p_\nu^2 |M_{fi}|^2 dp_e \tag{1.10}$$

for a fixed E_e the term $\frac{dp_\nu}{dE_f} = 1/c$. On the other hand, if we define Q as the total decay energy, the momentum of the neutrino is $p_\nu = (Q - T_e)/c$. The decay rate is now

$$\lambda = \frac{g^2}{2\pi^3\hbar^7 c^3}\int dp |M_{fi}|^2 p^2 (Q - T_e)^2 \tag{1.11}$$

but here we are not taking into account the interaction between the beta particle and the Coulomb field in the daughter nucleus. In order to take this effect into account an additional factor was added to the decay rate, $F(Z', p)$ where Z' is the atomic number of the daughter nucleus. The total decay rate is now

$$\lambda = \frac{g^2|M_{fi}|^2}{2\pi^3\hbar^7 c^3}\int_0^{p_{max}} p^2 (Q - T_e)^2 F(Z', p) dp. \tag{1.12}$$

This integral only depends on Z' and the maximum electron energy E_0, and it is represented as

$$f(Z', E_0) = \frac{1}{m_e^5 c^7}\int_0^{p_{max}} p^2 (Q - T_e)^2 F(Z', p) dp \tag{1.13}$$

where the constants have been included to make f dimensionless. This function is known as the *Fermi integral* and it is tabulated for values of Z' and E_0 [WB74].
As $\lambda = 1/t_{1/2}$, we have,

$$ft_{1/2} = \frac{2\pi^3\hbar^7}{g^2 m_e^5 c^4 |M_{fi}|^2} \tag{1.14}$$

The equation 1.14 gave the comparative half-life or *ft value*.

1.2.1 Fermi and Gamow-Teller decay. Definition of the strengths

In the allowed approximation the electron and the neutrino are created at the origin ($r = 0$). As the orbital angular momentum is zero($l = 0$), the only change in the angular momentum is due to the spins of the electron ($s_e = 1/2$) and neutrino ($s_\nu = 1/2$). If the two spins are anti parallel ($S = 0$), there is no change in the nuclear spin: $\Delta I = |I_i - I_f| = 0$. This is known as *Fermi Decay* (F). If the electron and neutrino spins are parallel ($S = 1$), they carry away an angular momentum of 1, therefore I_i and I_f must be coupled through a vector of length 1: $\vec{I}_i = \vec{I}_f + \vec{1}$. This is possible for $\Delta I = 0$ or 1 (except for $I_i = 0$ and $I_f = 0$, when only Fermi transitions can contribute). This is known as *Gamow-Teller Decay* (GT). They are governed by different operators which we will call O_F and O_{GT} in an obvious notation.

The matrix elements of F and GT decays must be written separately. The matrix elements for Fermi Decay, following equation 1.8 -p.3- , is

$$M_{fi} = M_F = g_V \int d\vec{r}\Phi_f^* O_F \Phi_i \tag{1.15}$$

and for the Gamow-Teller Decay

$$M_{fi} = M_{GT} = g_A \int d\vec{r} \Phi_f^* O_{GT} \Phi_i \tag{1.16}$$

The Fermi operator is expressed as $O_F = \sum_{i=1}^{A} \tau_{\pm}(i)$ where τ_+ (τ_-) is the isospin ladder operator converting the proton(neutron) wave function into a neutron(proton) wave function. For Gamow-Teller decay the corresponding operator is $O_{GT} = \sum_{i=1}^{A} \vec{\sigma}(i)\tau_{\pm}(i)$ where $\vec{\sigma}(i)$ are the Pauli matrices, which also act on the i-th nucleon. Now we can rewrite Eq. 1.14 -p.4- in terms of the Fermi and Gamow-Teller matrix elements.

$$ft_{1/2} = \frac{K}{|M_F|^2 + \frac{g_A^2}{g_V^2}|M_{GT}|^2} = \frac{K}{B(F) + \frac{g_A^2}{g_V^2}B(GT)}, \quad \text{where} \quad K = \frac{2\pi^3\hbar^7}{g_V^2 m_e^5 c^4} \tag{1.17}$$

and $B(F)$ and $B(GT)$ are the dimensionless Fermi and Gamow-Teller strengths.

The transition strengths $B(GT)$ are directly obtained from β-decay *ft values* which are derived from measurements of the Q_β value, the half-life and the branching ratio of the transition of interest.

In a β-decay, the partial half-life $t_{1/2}$ multiplied by the f-factor is related to the $B(GT)$ and the Fermi transition strength $B(F)$, as we saw in Eq. 1.17 -p.5- , which has to be corrected by a Coulomb factor,

$$ft_{1/2} = \frac{K}{B(F)(1-\delta_c) + \lambda^2 B(GT)} \tag{1.18}$$

where K=6143.6 ± 1.6 [HT09], $\lambda = g_A/g_V$=-1.270 ± 0.003 [HT06], δ_c is the Coulomb correction factor[TH02]. The Fermi strength can be calculated theoretically, and its value is $B_F = |N - Z|$ [3]; on the contrary, $B(GT)$ has to be taken from experiment.
Uncertainties in the experimental $B(GT)$ values originate from uncertainties in the decay Q-value, the total half-life $T_{1/2}$ and the branching ratios. The accurate determination of the feeding ratios to higher excited states is more difficult due to the smaller f-factors.

1.3 Isotopic spin of the nucleon

The charge symmetry and charge Independence of the nuclear interaction and the near equality of the masses of the neutron and the proton strongly suggest that they can be considered as the same particle (the nucleon) in two different *charge* states [Sta63, RN67, BM98].
In analogy with the reorientation of the two degenerate states of the electron spin under the effect of a magnetic field in real space, a nucleon can differentiate the two degenerate *isospin states* or *charge states* in the *isospin space* or *charge space*. A nucleon with third isospin component $T_z = -1/2$ (down) is defined as a proton, and a nucleon with third

[3] Except for the superallowed $0^+ \rightarrow 0^+$ transitions where B_F=2.

isospin component $T_z = +1/2$ (up) is defined as a neutron [4]. The isospin obeys the usual rules for angular momentum vectors. The isospin vector τ has a length of $\sqrt{\tau(\tau+1)}\hbar$ and with 3-axis projections $\tau_z = m_\tau \hbar$.
For a system of several nucleons, the isospin follows the same coupling rules as the ordinary angular momentum vectors. The 3-axis component of the total isospin vector, T_z, is the sum of the 3-axis components of the individual nucleons, and for any nucleus

$$T_z = \sum_{i=1}^{A} t_z(i) = \frac{1}{2}(N - Z) \tag{1.19}$$

expressed in units of $\hbar$ [Kra88].

1.4 Isospin symmetry

The assumption that the attractive nuclear force is independent of the charge of the interacting nucleons is one of the bases of our understanding of nuclear physics. This assumption hides a simple and elegant symmetry: The isospin symmetry (or charge symmetry).

The use of isospin gives us a simple way to classify nuclei according to the third component of their isospin.
A state in a nucleus with $N = Z$ corresponds to a particular configuration of neutrons and protons. If an identical state cannot be constructed in the neighboring nucleus with $N - 1$ neutrons and $Z + 1$ protons by exchanging a neutron for a proton then the original state must have isospin $T = 0$, because it can only be constructed in a nucleus with $N - Z = 0$, which has projection $T_z = 0$. The $N = Z$ nucleus can also have a state with $T = 1$, which, can be constructed identically in the $N \pm 1$, $Z \mp 1$ systems (see Fig. 1.1 -p.7-) [DWI06].

1.5 Experimental studies of the Gamow-Teller transition strengths

The $T_z = +1$ to $T_z = 0$ transitions can be studied in charge exchange (CE) reactions ((p, n)-type [Tad87], [Hag94] or (^{3}He, t)-type [Fuj01], [Zeg06]), and the $T_z = -1$ to $T_z = 0$ transitions can be investigated in β-decay experiments as shown in Fig. 1.1 -p.7-. Their comparison can provide information on isospin symmetry. Such studies have only been performed in detail so far for light nuclei, such as the $A = 26$ system (^{26}Mg, ^{26}Al and ^{26}Si) [Fuj03]. One major constraint on these studies in light nuclei is that β decays

[4] The isospin assignment for a neutron and a proton, which is adopted here, is conventional in nuclear physics and has the advantage that the heavy nuclei with large neutron excess have their isospin aligned in the direction of the positive z axis in the isospin space. In elementary particle physics, the inverse sign conversion is usually adopted [BM98].

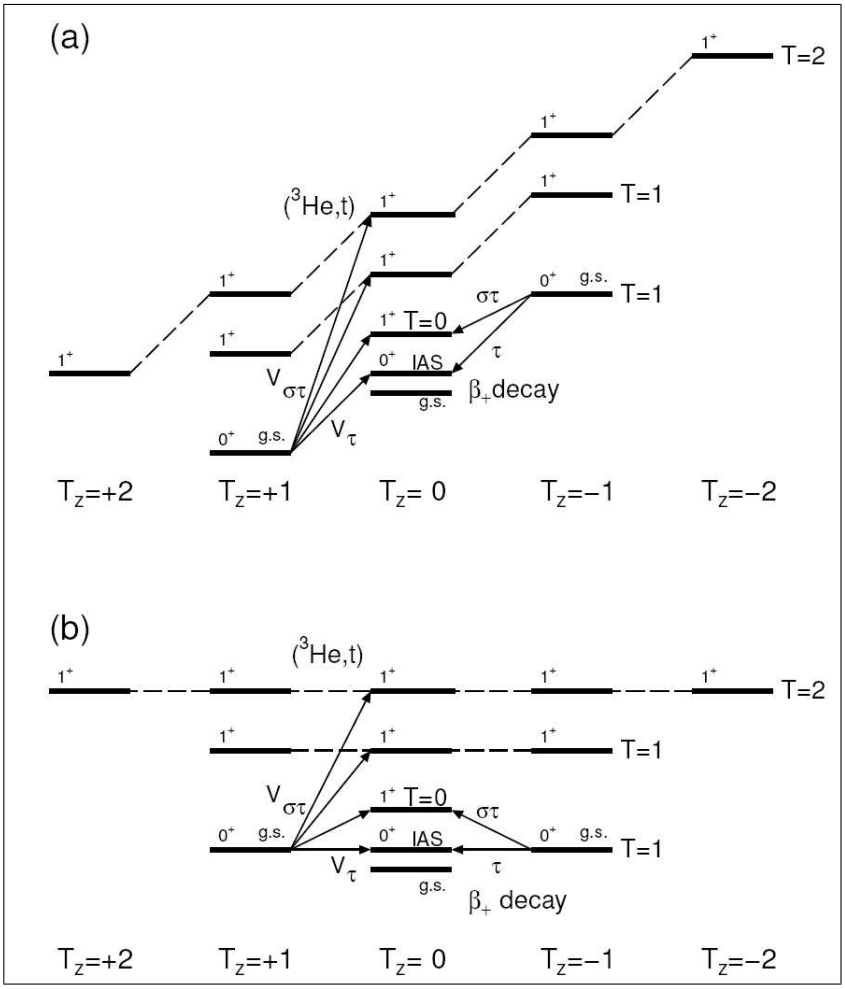

Figure 1.1: Schematic illustration of the isospin symmetry transitions in mirror nuclei with T_z= 0, ±1, ±2. (a) Level scheme in real energy space. (b) Level scheme in isospin space, neglecting the Coulomb displacement energies. The symmetric structure is evident. Analogue states are connected by segmented lines [Ada07a].

can access only a few low-lying states due to the restriction imposed by the Q_β-window. Among the $T_z = -1 \rightarrow 0$ candidates, i.e. those where the mirror T_z=+1 is stable and charge exchange reactions are possible, the analogue transitions in the fp-shell nuclei are well suited to an accurate study of isospin symmetry. The reason is that due to relatively large Q_β values, the β-decay studies should allow $B(GT)$ measurements up to high excitation energies in the daughter nuclei.

1.5.1 Charge exchange reactions ($T_z = +1 \rightarrow T_z = 0$)

It is known that the CE reactions, such as (p, n) or (^{3}He,t) reactions, at intermediate incident energies are valuable tools for $B(GT-)$ studies up to high excitation energies in the final nucleus, since they are not limited by the Q_β window as in β-decay. It has been found that in CE reactions performed at angles around 0^o and intermediate energies ($E_{in} > 100$ MeV/nucleon) there is an approximate proportionality between the differential cross section at 0^o and the $B(GT-)$ values [Goo80], [Tad87],

$$\frac{d}{d\Omega}\sigma_{CE}(0^o) \propto K^{CE} N_{\sigma\tau}^{CE} |J_{\sigma\tau}(q=0)|^2 B(GT-) = \hat{\sigma}^{GT}(0^o) B(GT-) \tag{1.20}$$

where $|J_{\sigma\tau}(q=0)|^2$ is the volume integral of the effective interaction $V_{\sigma\tau}$ at momentum transfer $q = 0$, K^{CE} is a kinematic factor, $N_{\sigma\tau}^{CE}$ is a distortion factor defined by the ratio between the distorted wave and plane wave cross sections, and $\hat{\sigma}^{GT}(0^o)$ is the unit cross section for a GT transition at 0^o.

The charge exchange reaction studies have greatly improved in recent years, because the poor energy resolution in the pioneering (p, n) work has now been overcome by the use of the (^{3}He,t) reaction [Fuj05b], [Fuj06].

The first studies of the $B(GT-)$ in charge exchange reactions were performed in the 80s, in laboratories like the Indiana University Cyclotron (IUCF) [RS94], using beam energies in the range of 100-200 MeV at 0^o. However, the energy resolution was ∼400 keV.

Since the year 2000, high resolution experiments of the type (^{3}He,t) have been developed at the Research Centre of Nuclear Physics (RCNP) in Osaka, Japan, where the typical energy resolution is ∼35 keV [Fuj07a].

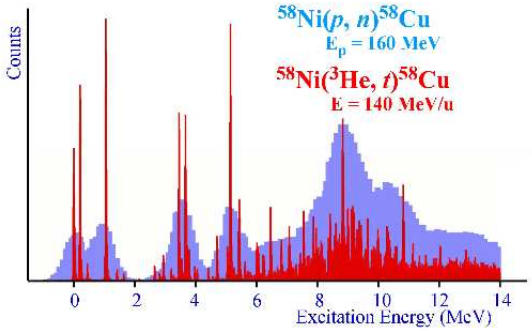

Figure 1.2: Comparison between energy resolution of the results of the CE reaction ^{58}Ni$(p, n)^{58}$Cu [RS94] (ΔE ∼ 400 keV) and recent measurements of the CE reaction ^{58}Ni(^{3}He, $t)^{58}$Cu [Fuj07a] (ΔE ∼ 35 keV).

With these energy resolution improvements, it is possible to study the Gamow-Teller transition strengths $B(GT-)_i$ from charge exchange reactions and compare it with the absolute Gamow-Teller transition strengths $B(GT+)_i$ from β-decay experiments.

1.5.2 The *merged analysis*

In the (^{3}He, t) measurements studying the corresponding GT transition, relative transition strengths to these higher excited states can be obtained accurately. The expected feeding ratios in the β-decay can be deduced using these values and f-factors calculated using the decay Q_β-value. These feeding ratios can then be converted into

absolute $B(GT)$ values by the normalisation process using the total half-life of the β-decay.
The inverse of the total β-decay half-life $T_{1/2}$ is the sum of the inverse of the partial half-life t_F of the Fermi transition to the Isobaric Analogue State (IAS) and the inverse of the partial half lives (t_i) of GT transitions to the i-th GT states.

$$\frac{1}{T_{1/2}} = \frac{1}{t_F} + \sum_{i=GT} \frac{1}{t_i} \tag{1.21}$$

Applying eq. 1.18 -p.5- one can eliminate both t_F and the t_i, so that

$$\frac{1}{T_{1/2}} = \frac{1}{K}\left(B(F)(1-\delta_c)f_F + \sum_{i=GT} \lambda^2 B(GT)_i f_i \right) \tag{1.22}$$

where f_F and f_i are the f-factors of the β-decay to the IAS and to the i-th GT states, respectively, $B(GT)_i$ is the $B(GT)$ value of the transition to the i-th GT state, and $B(F) = |N - Z|$.
In order to relate the strengths of GT and Fermi transitions in a CE reaction, the ratio R^2 of unit GT and Fermi cross sections at 0^o is introduced.

$$R^2 = \frac{\hat{\sigma}^{GT}}{\hat{\sigma}^F} = \frac{\sigma_i^{GT}}{B(GT)_i} \frac{B(F)(1-\delta_c)}{\sigma^F} \tag{1.23}$$

Due to the isospin symmetry, this ratio R^2 is expected to be the same for all the $T_z = \pm 1 \rightarrow 0$ transitions. Eliminating $B(GT)_i$ by using R^2, we get

$$\frac{1}{T_{1/2}} = \frac{B(F)(1-\delta_c)}{K\sigma^F}\left(\sigma^F f_F + \frac{\lambda^2}{R^2} \sum_{i=GT} \sigma_i^{GT} f_i \right) \tag{1.24}$$

In the merging method, $B(F)$ and δ_c are known and depend on which nucleus we are working with, σ^F and σ^{GT} are obtained from CE reaction experiments, f_i and f_F are obtained from calculations and the total half-life $T_{1/2}$ is obtained from β-decay experiments.

In summary, the relative values of $B(GT-)_i$ can be obtained from the CE reaction. Subsequently, if we have an accurate value for $T_{1/2}$ from β decay studies, we can use the CE information to extract absolute $B(GT-)_i$ values to all the states observed in the reaction, and compare them with the absolute $B(GT+)_i$ values obtained directly from β-decay measurements. This comparison will be done at the end of this work.

1.6 $B(GT)$ studies for the T=1 fp-shell nuclei

The comparison of the Gamow-Teller transition strength $B(GT-)$ obtained by charge exchange reactions and the $B(GT+)$ obtained by β-decay measurements in T=1 f-shell nuclei, has two big advantages from the experimental point of view,

1.- The T_z=+1 f-shell nuclei, i.e. ^{42}Ca, ^{46}Ti, ^{50}Cr and ^{54}Fe, are stable nuclei. Therefore it is possible to construct targets and study them in reactions of the type $(^3\mathrm{He}, t)$ (see Fig. 1.3).

2.- The T_z=-1 f-shell nuclei, i.e. ^{42}Ti, ^{46}Cr, ^{50}Fe and ^{54}Ni, β^+-decays and their Q_β-values [Aud03, Kur09] are in the range of 7 to 9 MeV which allows us access to high excitation energy in the daughter nucleus (see Fig. 1.3).

1.6.1 CE reactions (^{3}He, t), T_z=+1 → 0 results

The charge exchange reaction experiments have been carried out at the RCNP facilities in Osaka, Japan. The analysis of these experiments were part of the PhD thesis of Dr. Tatsuya Adachi [Ada07a].

The experiment

A ^{3}He beam is accelerated to 140 MeV/u from the Ring Cyclotron (K=400 MeV) to the stable target (see Fig. 1.4). A nuclear reaction occur inside the scattering chamber where the target is placed. The incident ^{3}He exchanges a proton with a neutron of the target (namely ^{42}Ca, ^{46}Ti, ^{50}Cr or ^{54}Fe), producing triton ^{3}H.

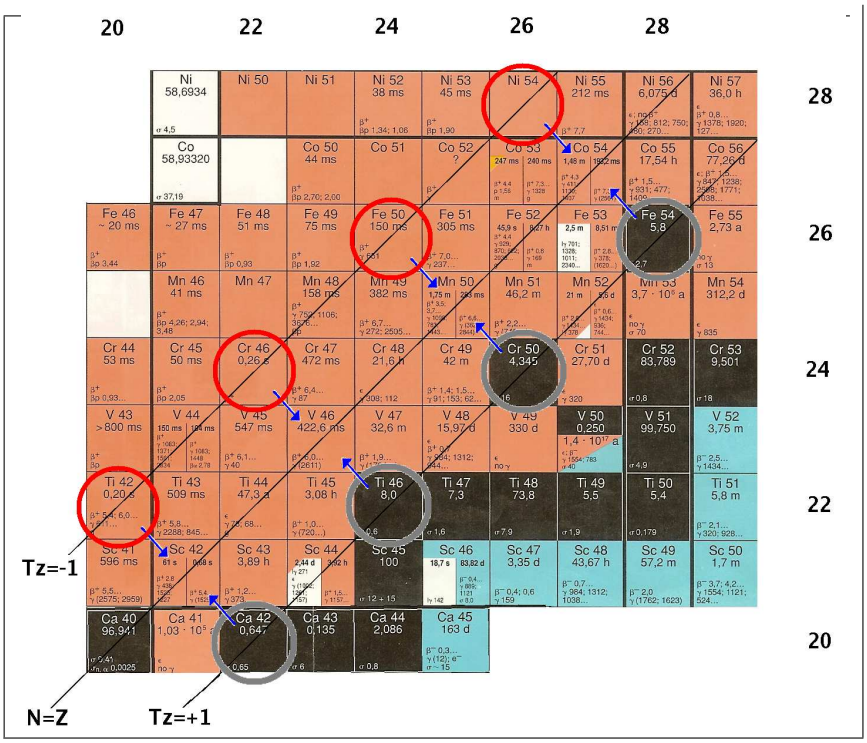

Figure 1.3: Chart of nuclides. In the figure are shown some of the fp-shell nuclei. The lines shows those nuclei with $T_z = \frac{N-Z}{2} = 0, \pm 1$. The usual colour code in the nuclear chart is: red for β^+-decaying nuclei, blue β^--decaying nuclei, and black for stable nuclei.

After the scattering chamber the "Grand Raiden" spectrometer (momentum res-

olution $p/\Delta p$ = 37000 and magnetic rigidity Bρ= 5.4 Tm) at 0^o, bends the triton trajectories depending on their the momentum/energy after the reaction.
In the last focal plane a set of two multi-wire chambers and two scintillator detectors are placed in order to identify and track the position and angle of incidence of the incoming particle.
The resulting triton spectra are shown in Figs. 1.5-1.8 -pp.13 to 16-. The labels indicate the excitation energy in the final T_z=0 nucleus.

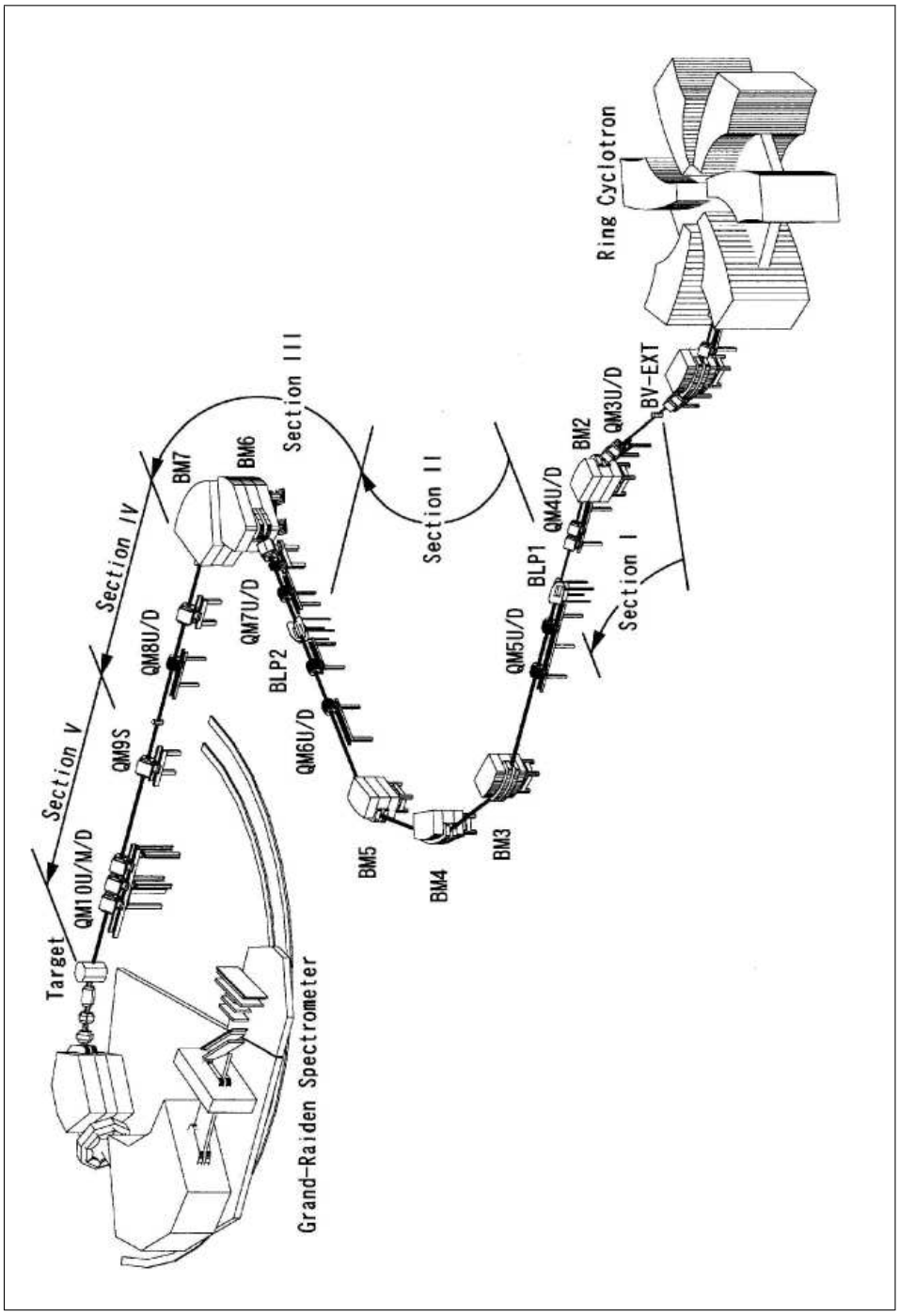

Figure 1.4: Scheme of the charge exchange reaction experiment at RCNP in Osaka, Japan [Ada07a].

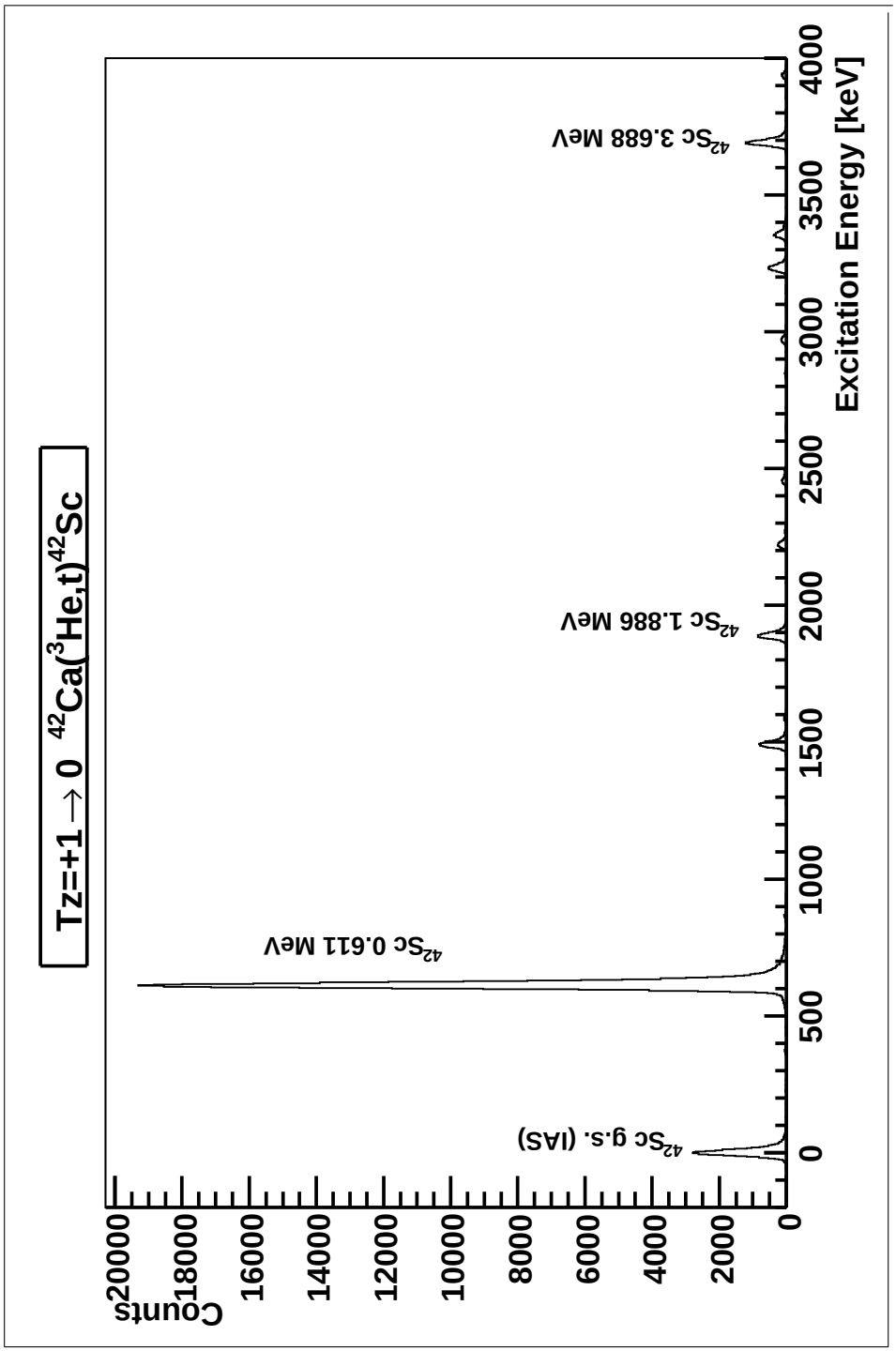

Figure 1.5: High resolution triton spectrum for the ^{42}Ca(^{3}He, t)^{42}Sc charge exchange reaction [Ada07b]. The excitation energy of the levels in the final ^{42}Sc nucleus and the $B(GT)$ values extracted from this measurement are shown in Appendix B.

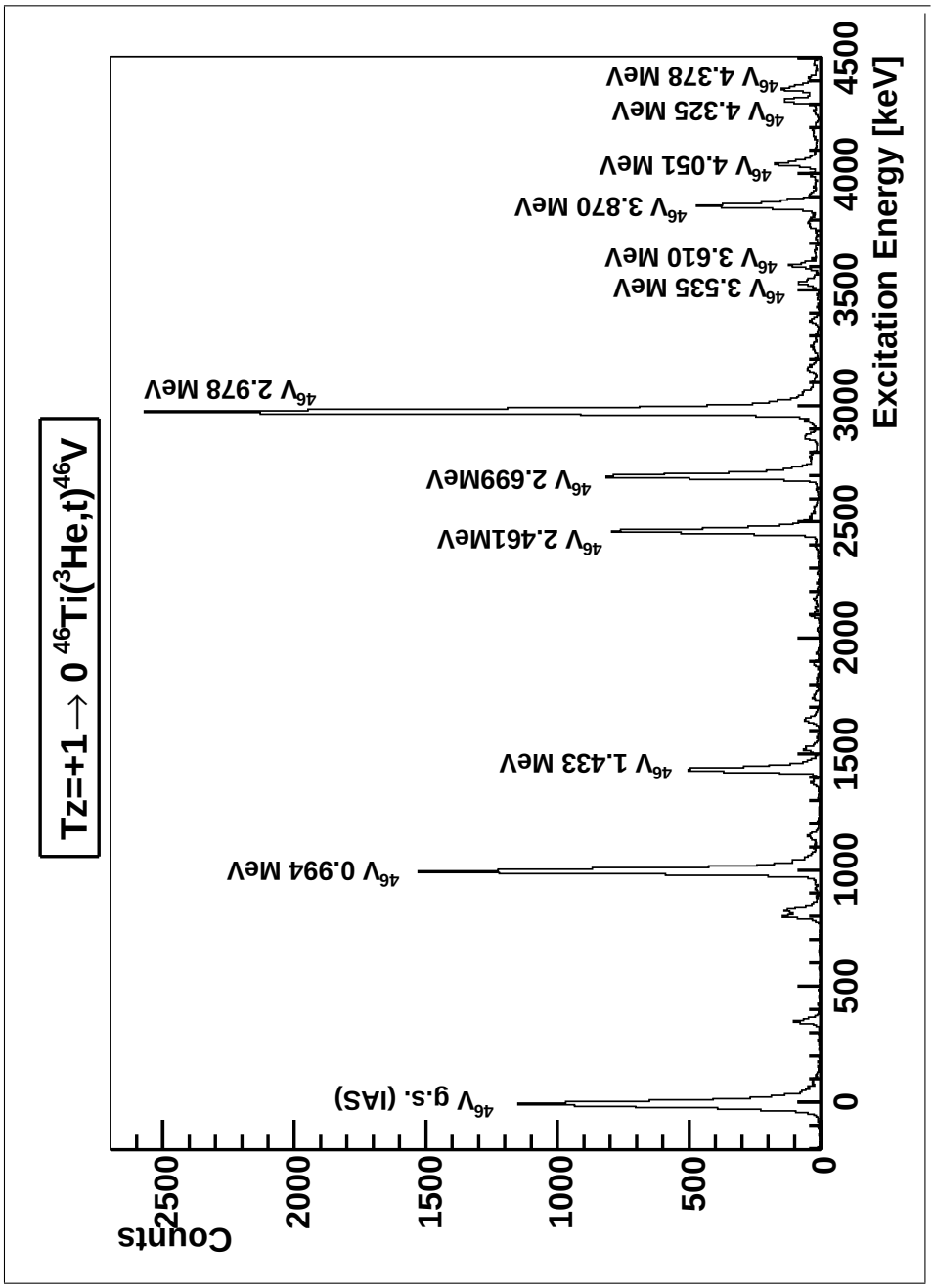

Figure 1.6: High resolution triton spectrum for the ^{46}Ti(^{3}He, t)^{46}V charge exchange reaction [Ada06]. The excitation energy of the levels in the final ^{46}V nucleus and the $B(GT)$ values extracted from this measurement are shown in Appendix B.

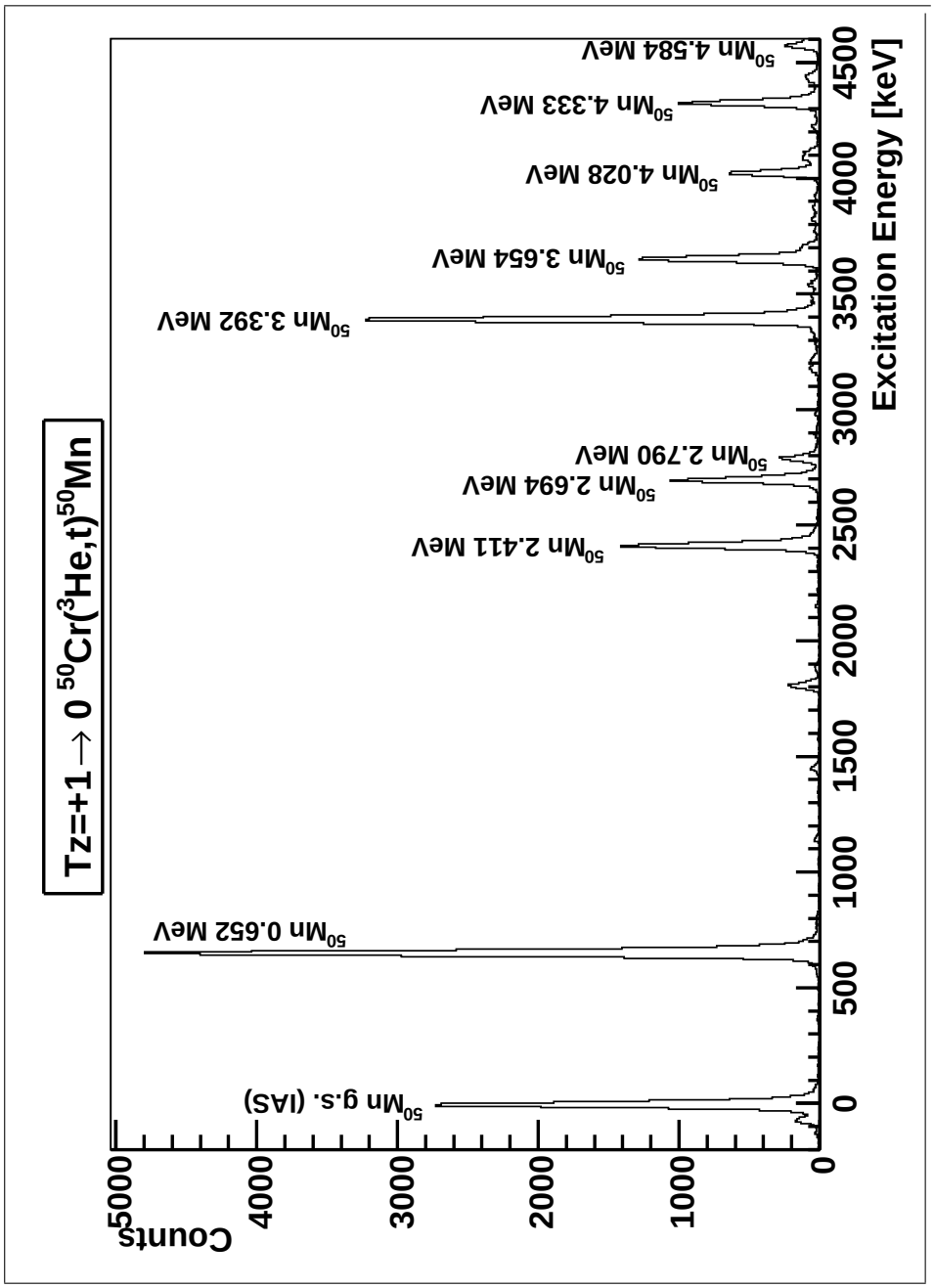

Figure 1.7: High resolution triton spectrum for the ^{50}Cr(^{3}He, t)^{50}Mn charge exchange reaction [Fuj05a]. The excitation energy of the levels in the final ^{46}V nucleus and the $B(GT)$ values extracted from this measurement are shown in Appendix B.

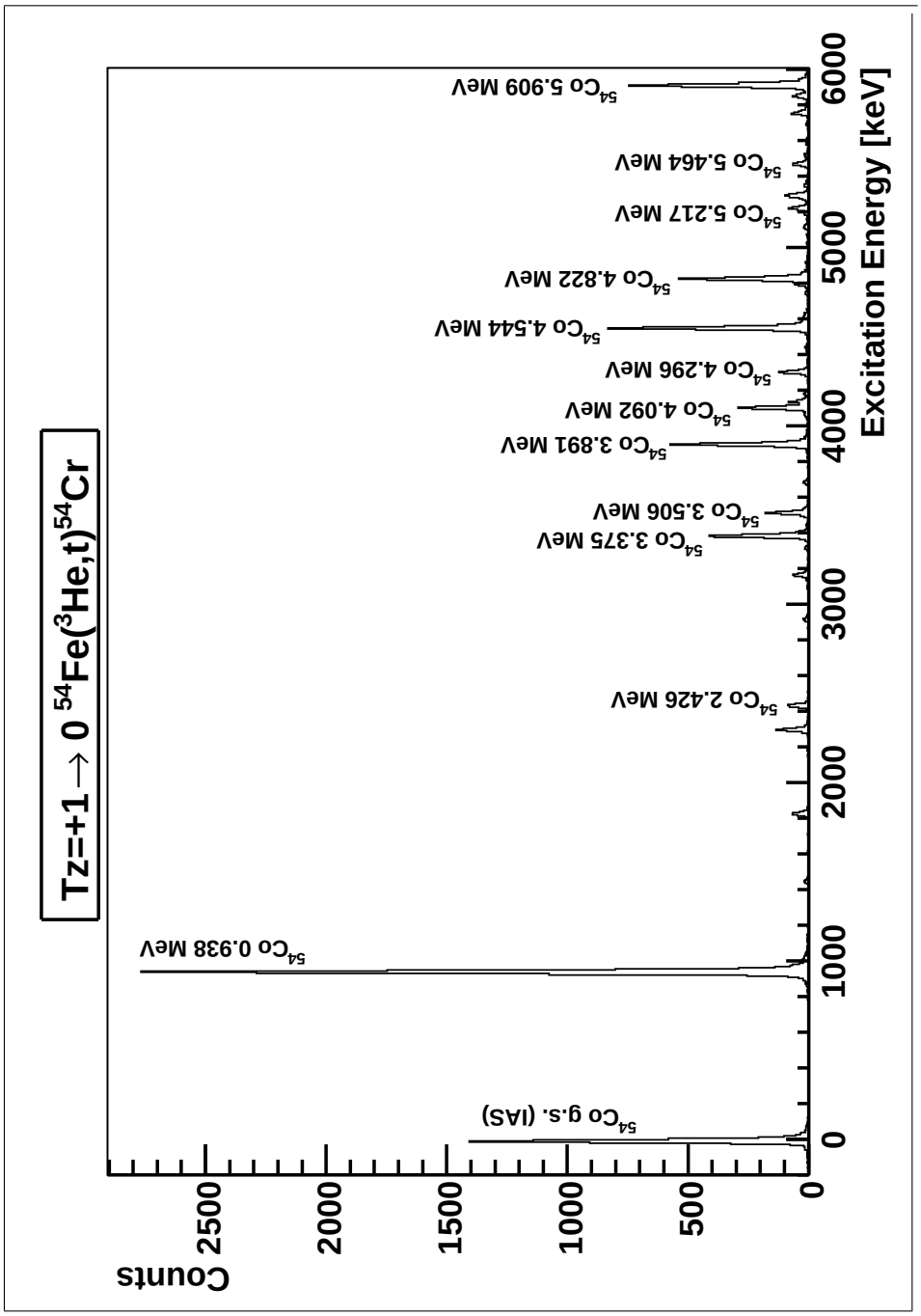

Figure 1.8: High resolution triton spectrum for the ^{54}Fe(^{3}He, t)^{54}Co charge exchange reaction [Ada07b]. The excitation energy of the levels in the final ^{54}Co nucleus and the $B(GT)$ values extracted from this measurement are shown in Appendix B.

CHAPTER 2

T_Z=-1 ^{54}NI MEASUREMENTS AT LISOL

The first experiment to measure the ^{54}Ni beta-decay was carried out at the Leuven Isotope Separator On Line (LISOL) at Centre de Recherche du Cyclotron at Louvain La Neuve (Belgium) in April 2006.

2.1 The Production of ^{54}Ni

The ^{54}Fe target, located in a gas cell, was bombarded with a primary ^{3}He beam at 45 MeV coming from the CYCLONE110 cyclotron. Several radioactive nuclei were created in this fusion evaporation reaction but since we have an on-line mass separator we are only concerned about the production, selection and mass separation of the ^{54}Ni and ^{54}Co nuclei.

The decay of ^{54}Ni is difficult to study at an ISOL facility because its production is always overwhelmed by the direct production of its daughter nucleus ^{54}Co. Indeed the calculated production cross section for the ^{54}Ni has a maximum of 30 μbarn at an energy of 45 MeV for the ^{3}He beam. At the same energy the ^{54}Co has a production cross section of 5 $m$barn (166 times bigger)[Reu99a].

2.2 The LISOL Separator

The products of the ^{54}Fe(^{3}He,2np)^{54}Co and ^{54}Fe(^{3}He,3n)^{54}Ni reactions recoil into the gas cell. A laser beam selectively ionises either Ni or Co atoms. The resonant ions are extracted and accelerated by a DC electrical field and directed to the mass separator which separates the singly-charged, A=54 mass ions by A/Q. In the following we give a detailed explanation of the different components of the LISOL device (see Fig.2.1).

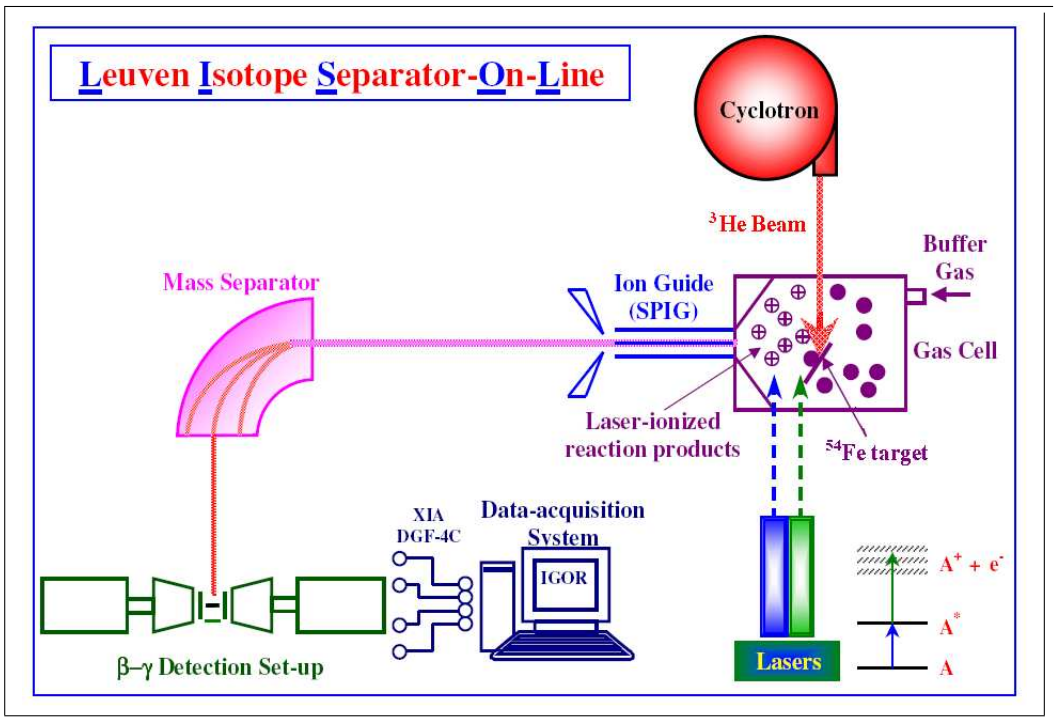

Figure 2.1: Leuven Ion Separator On Line [Pau09].

2.2.1 Gas Cell

The gas cell is a gas catcher source and is the first component of the so-called Laser Ion Source (LIS). The nuclear reaction on the target occurs inside the gas cell filled with a noble gas flowing through it. The reaction products are stopped, thermalised and neutralised in the noble gas. This avoids chemical reactions with the nuclei produced. The body of the cell is made of stainless steel and is electro-polished to reduce the level of roughness at the surface.

In order to optimise its efficiency and its selectivity for the ion of interest, a LIS has to fulfil some important requirements such as (a) the reaction products, recoiling out of the target, have to be stopped in the buffer gas, (b) all reaction products must be neutralised before arriving in the laser ionisation zone, (c) avoiding as much as possible the interaction of the ion of interest with impurities in the buffer gas to avoid the formation of neutral molecules, (d) the evacuation time should be shorter than the mean diffusion time to the wall in order to avoid sticking of the reaction products to the wall, (e) the evacuation time should be shorter than the lifetime of the isotope of interest, (f) the time between two subsequent laser pulses should be shorter than the evacuation time of the ions produced in the laser ionisation region and (g) the survival time of the laser produced ions has to be longer than their evacuation time.

2.2.2 Resonant Laser Ionisation

After the thermalisation and neutralisation of the reaction products we need to select and extract the ion of interest. The resonant laser ionisation technique is used to ionise a specific element.

Two tunable dye lasers are pumped by two excimer Xe-Cl (308 nm) lasers. The atoms thermalised in the ground state level are excited in two steps. The first step laser λ_1 excites the atom to an intermediate level. The second step laser λ_2 may ionise and excite the atom to the continuum, to an auto-ionising state or to a Rydberg state where it is ionised by collision with the buffer gas (See Fig. 2.2 -p.19-).
The two dye laser beams are focused by lenses and directed by prisms to the gas cell

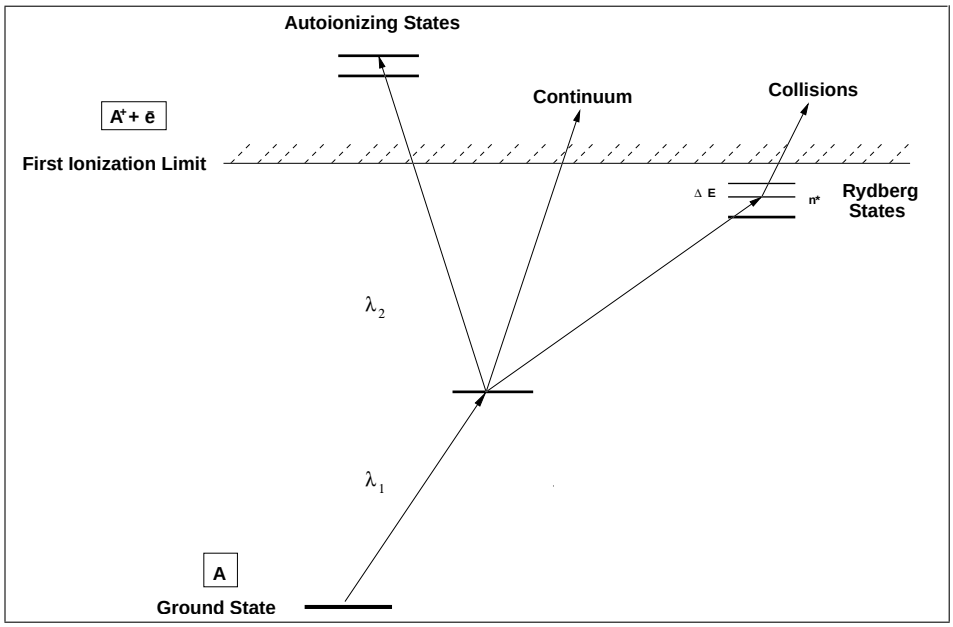

Figure 2.2: Atomic level scheme and the different ways to ionise an atom.

located at 15 m from the optical setup. In order to focus the two beams at an optical distance of 15 m a screen is located at that distance but not in the same position as the gas cell.
To choose the most efficient resonance wavelength of the two dye laser beams, a fraction of each beam is deflected and directed to a reference cell in a vacuum chamber. An atomic beam is produced by evaporating the element investigated from a resistively-heated crucible.
After the laser ionisation, the ionised atoms and compound molecules [Kud01] are attracted by a potential difference and ejected from the gas cell.

2.2.3 Sextupole Ion Guide

Once the selected atom is ionised it can re-combine with the impurities (normally H_2O) in the gas cell forming molecules [Kud01]. These compound molecules are heavier than a single atom so the isotope of interest is lost in the subsequent mass separation step. This problem can be solved if a sextupole ion guide is located at the exit hole of the gas cell [dB97].

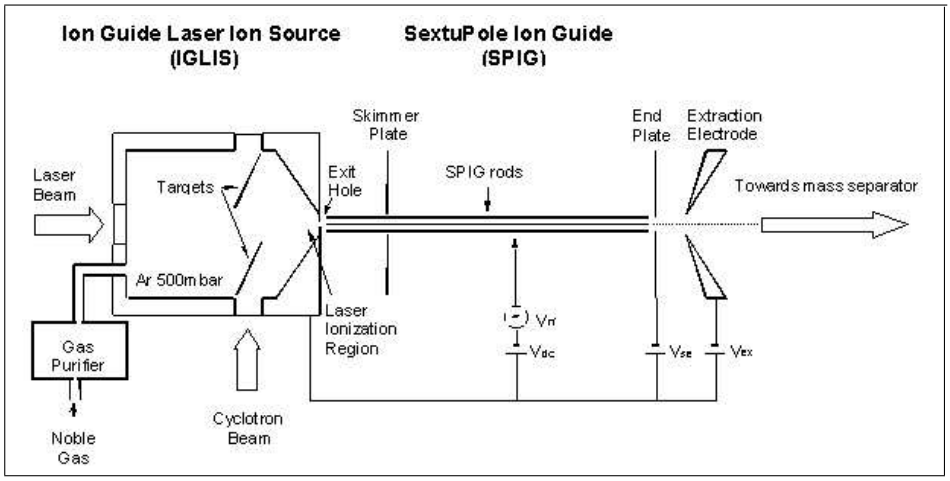

Figure 2.3: Scheme of the sextupole ion guide (SPIG).

The **S**extu**P**ole **I**on **G**uide SPIG, as shown in Fig. 2.3 -p.20-, consists of six silver rods (1.5 mm diameter and 124 mm length) cylindrically mounted and forming a hexagonal structure parallel to the beam path. An oscillating radio frequency voltage (V_{rf}) is applied to the rods, with every rod in anti-phase with the neighbouring rods. The amplitude and the frequency of the rf signal are chosen in order to confine the ions in the centre of the SPIG. Hence the gas coming out of the gas cell can expand through the gaps between the rods, while the ions are radially confined and transported to an extraction electrode with the velocity of the gas jet.
In addition to the rf voltage, a DC voltage is applied between the rods and the gas cell exit (grounded). Hence a molecule could dissociate and liberate the ion of interest, thus increasing the selection production efficiency of the LIS.

After that, the selected ion is mass-separated in a mass separator. The mass separator is a 55^o dipole magnet of 1.5 m radius. The ions are separated according to the mass-over-charge ratio since they are, in general, in a single charge state, normally 1^+. Hence they are separated in mass. The ion beam of the selected mass is implanted into a tape located in the middle of two Miniball germanium detectors (see Fig. 2.4 -p.21-), as described in the next section.

2.3 Radiation Detectors

In the β decay of ^{54}Ni we expect to have three type of radiation: betas, neutrinos and gammas. It is difficult and impractical to detect the neutrinos but we can make a sensitive setup to detect β radiation and γ-rays. For the γ-ray detection we used two MINIBALL Ge cluster detectors and for the β particles we used plastic detectors. Three 1.3 mm thick plastic β detectors were placed around the implantation point (tape ending, see Figs. 2.4 and 2.5 -p.21 and 22-). In most of the cases the β particle only deposits part of its energy in the thin plastic. These detectors were used to determine if a β particle passed through the detector or not. No energy was registered.

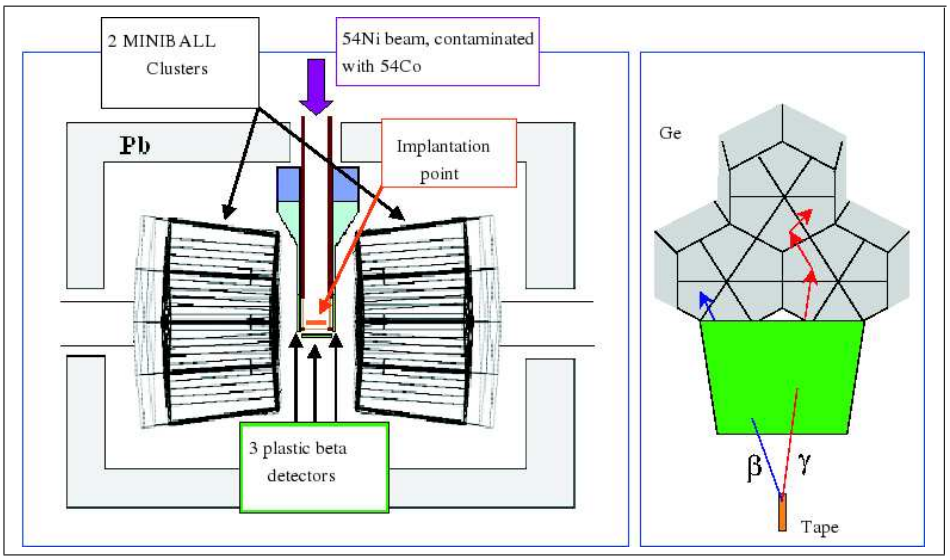

Figure 2.4: Top and side view of the setup of β and γ detectors at the Louvain la Neuve facility.

Two MINIBALL clusters were located as close as possible to two of the scintillators. Each MINIBALL detector is a cluster of three hyper-pure germanium crystals, each of them six-fold segmented. The crystals and the capsules are tapered in a hexagonal shape to fit three of them side-by-side in a single cryostat. A positive high voltage is applied to a lithium-diffused central contact, which penetrates deep inside the germanium. Six boron-implanted contacts on the surface of each crystal constitute the segmented outer contacts. An incident γ-ray interacts with the Ge crystal and transfers its energy either totally (photoelectric effect) or partially (Compton scattering or pair creation) to an electron, this electron loses its kinetic energy, creating a number of electron-hole pairs. Within the fully depleted region of germanium between the contacts, the charge created goes to the corresponding electrode. Thus, the electrons go to the central contact (core signal), and the holes go to the outer contacts (segment signal) (See Fig. 2.6 -p.23-) . The charge collected on the crystal contacts is integrated by charge-sensitive resistor

feedback preamplifiers, developed and produced by the Institute of Nuclear Physics in Cologne, a member institute of the MINIBALL Collaboration [Iva07].

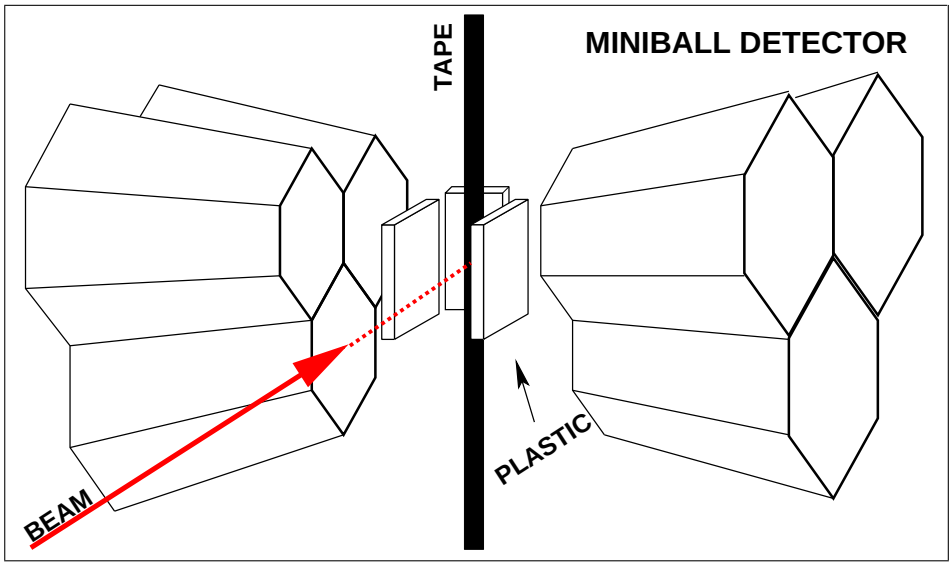

Figure 2.5: Schematic view of the detector and type system setup.

2.4 The Tape System

After the mass separation, the ions are implanted on a thin 1.25 cm wide aluminium-coated mylar tape. The thickness of the tape is chosen to stop the beam completely. The tape rewinding system is located below the detectors. The tape from one of the two coils goes up, intercepts the beam path, goes up again and turning fully down, comes again below the detector level and finally ends in the second coil (see Fig. 2.5 -p.22-). After the measurement the part of the tape where the ions were implanted is moved down to a safe distance away from the detectors, to avoid the background produced by the activity of long-lived ions close to stability. The whole tape system is kept in the same vacuum as the beam transport line. There are three thin mylar windows in the chamber around the implantation area to reduce the attenuation of the radiation of interest.
A schematic picture of the detector setup and the tape system is shown in Fig. 2.5 -p.22-.

2.5 The Data Acquisition System

The preamplified signals are provided to the analogue inputs of the DGF-4C modules [LLC]. The DGF (Digital Gamma Finder) can measure the amplitude and the shape of the incoming pulses simultaneously. The energy information is extracted directly from

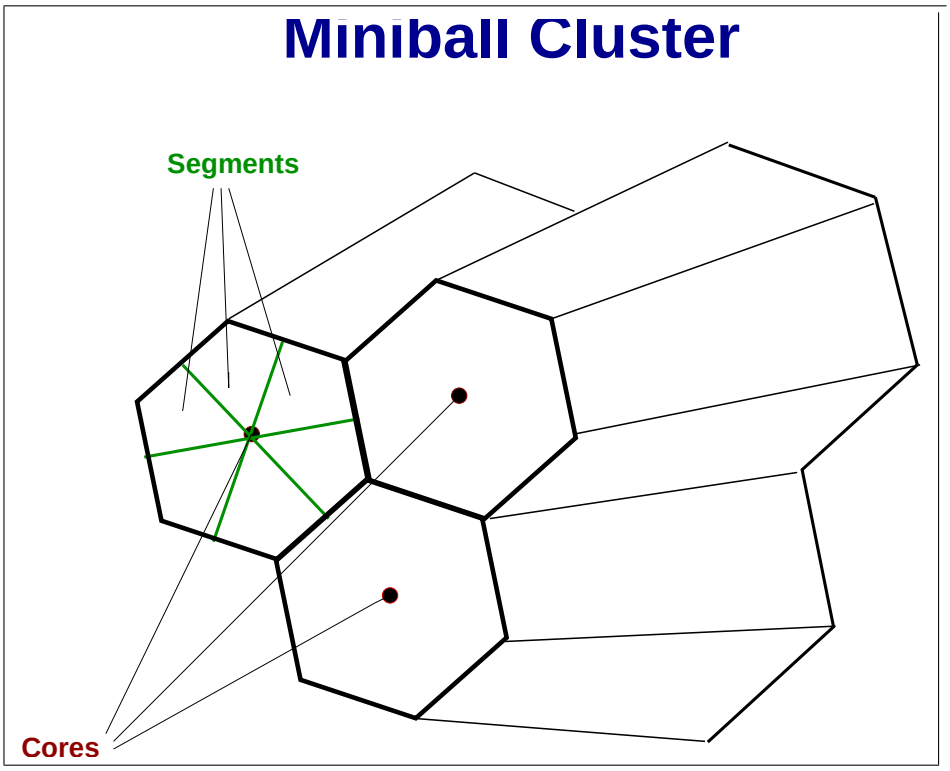

Figure 2.6: Schematics showing core contacts and segment contacts in a Miniball Cluster.

the preamplified signal height and the time information is obtained from a built-in high-precision internal clock after the event validation.
In our detector system we have 21 signals from each MINIBALL γ detector (3 signals from the cores and 18 segments) and another 3 signals from the three plastic scintillator β detectors. All of these γ and β signals triggered the acquisition.
Since an incident γ ray is registered by the core and some of the segments of the same crystal, there is a time correlation between the signals from one crystal. Further on there should be no segment signal unless there is a signal from the corresponding crystal core. For these reasons, the DGF modules are split into trigger groups, in which each group represents one crystal and the core channel is the main trigger of the group. The logic signals from the β detectors are provided to one DGF module and their inputs are set independently. To estimate the total acquisition live time, a pulser signal feeds one channel of a DGF module. The live time is given by the ratio between the registered pulser signals to the number of pulses provided by the pulser, which is also part of the acquisition trigger.

2.6 Data Analysis

A new C++ software code has been created by Oleg Ivanov and Dieter Pauwels from Katholieke Universiteit Leuven, to read and analyse the data acquired by the detection setup. The object oriented ROOT package developed at CERN is used for building the output histograms. While building the singles spectra is a simple procedure, the β-nγ and nγ coincidences, where n represents the number of γ-detectors (crystals), are based on the event time stamps. These coincidences are stored in ROOT trees for further analysis [Iva07].

CHAPTER 3

ANALYSIS AND RESULTS OF LISOL EXPERIMENT

The aim of this experiment was to study the GT transitions in the β-decay of ^{54}Ni analogous to the GT transitions in the ^{54}Fe(^{3}He,t) reaction. The main objectives are to measure 1) the total half-life $T_{1/2}$ of ^{54}Ni with high accuracy, 2) the decay branching ratios of the ^{54}Ni to the ground state and to the first GT state and, if possible 3) the decay to at least one extra GT excited state in ^{54}Co.

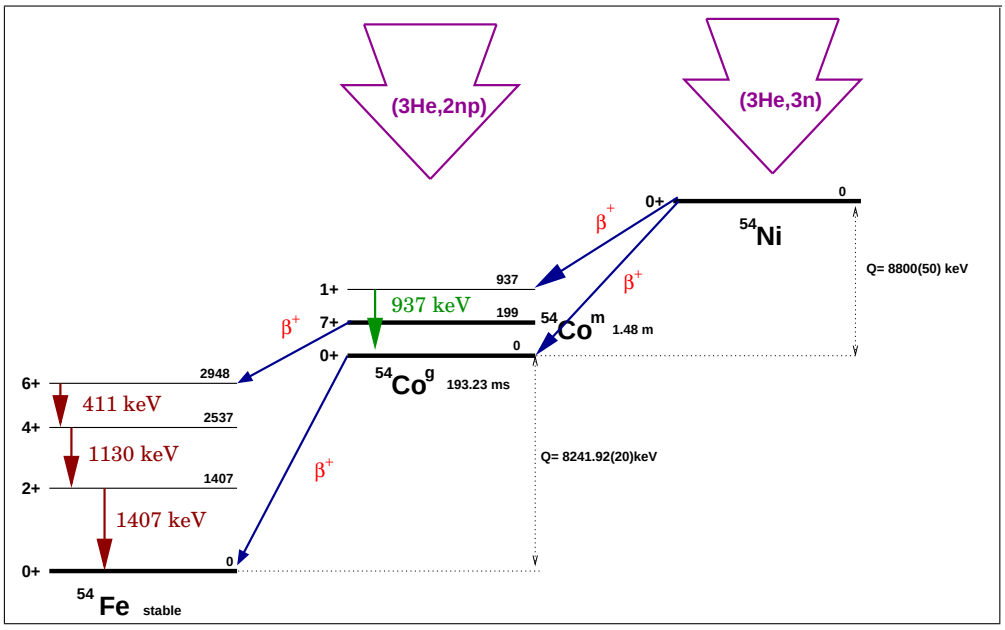

Figure 3.1: ^{54}Ni and ^{54}Co^{g,m} decay schemes.

Fig. 3.1 -p.25- shows the known decay schemes of ^{54}Ni and ^{54}Co^{g,m} prior to our experiment [Reu99a]. The β^+ decay of ^{54}Ni feeds the ground state of ^{54}Co and at least one excited state ($J^{\Pi}=1^+$) with an energy of 937 keV. The decay of ^{54}Co^m is accompanied by a triple γ cascade of 411 keV, 1130 keV and 1408 keV γ rays. The ^{54}Co ground state decays 100% to the ground state of ^{54}Fe.

3.1 γ Calibrations

The resolution measurements for the MINIBALL detectors were carried out using a ^{60}Co source. The measured resolutions for all MINIBALL crystals at 1.3 MeV are shown in the next table for the so-called "Heidelberg" and "Leuven" cluster detectors.

Heidl.A	3.4 keV	LeuvenA	3.3 keV
Heidl.B	2.7 keV	LeuvenB	3.1 keV
Heidl.C	2.8 keV	LeuvenC	3.0 keV

A ^{152}Eu source was used before the experiment, for the on-line analysis energy calibration. Afterwards, for off-line analysis, an internal energy calibration was performed using the ^{54}Co^m gamma cascade present in our experiment for each ROOT file created after more or less each hour of running time.

3.2 Control Measurements during the Experiment

For all the calibrated spectra, several control measurements were performed before and during the experiment in order to optimise the production and mass separation of ^{54}Ni and ^{54}Co^{g,m}.

1.- **Laser tuning on Co and Ni**: To optimise the selection of Co and Ni ions by laser resonance in the gas cell, we looked at the ratio in intensity of the 411 keV and 511 keV γ-ray lines from the decay of ^{54}Co^{g,m} in the singles and $\beta-\gamma$ coincidence spectra with a fixed mass 54 in the mass separator. The cyclotron current and the tape steps were also fixed. Short measurements of 100 seconds with and without laser resonance were made.

2.- **Mass tuning**: Once the selectivity was optimised, we proceeded to tune the mass selection on the separator with laser resonance on Co looking at the integral of the 411 keV line in the singles and $\beta-\gamma$ spectra, taking short measurements of 100 seconds.

3.- **Gas Buffer Pressure and Cyclotron Current**: With the mass optimised and with laser resonance on Co, the optimal gas buffer pressure was found by looking again at the 411 keV line in the singles and $\beta-\gamma$ spectra, taking short measurements of 100 seconds. After this the cyclotron current was tuned following the same procedure as described above.

4.- **Tape Step and Implantation-Decay Macrocycle**: In the previous ^{54}Ni β decay experiment carried out by I.Reusen et al. [Reu99b], [Reu99a] the measured half-life was 106(12) ms. Based on this knowledge, a 400 ms and 600 ms

implantation-decay macrocycle was chosen for this experiment. The collected source was moved away every six macrocycles using the tape transport system. The reason for not moving the source away every macrocycle was to minimise the time lost during the tape rewinding.

In the following table the starting settings are summarised.

Mass (A)	54
Cyclotron Current	4.0 μA
Gas Buffer Pressure	760 mbar
ID Macrocycle	400 ms / 600 ms
Tape Movement Period	6 Macrocycles

These settings were checked and, if necessary, modified during the experiment in order to increase the selectivity and mass separation of the ion of interest.

3.3 Data Analysis

After seven days of experiment, the data taking time with laser resonance on Ni was 115 hours. The time used for the laser resonance on Co was 16 hours. The total number of counts in the 411 keV $^{54}Co^{m}$ decay radiation in the laser on Ni total spectrum was 94,817 while the number of counts in the 411 keV peak in the laser on Co total spectrum was 46,903. Finally, the settings adjustment time was 2.5 hours. Singles and β-γ coincidence spectra were constructed in ROOT trees to facilitate the on-line analysis. These pre-processed data were also used for the off-line analysis.
In general the data analysis was done with the β-γ coincidence spectra. As we are interested in the high energy excited states in the daughter nucleus, a veto condition (see Fig. 3.2 -p.28-) was imposed in order to reduce the background produced by the penetration of β particles into the MINIBALL crystal. The main idea is that if a β particle is detected in a plastic detector, the gamma detector situated behind it is not used. In Fig. 3.3 -p.29- we see the difference between the spectra with the no-veto condition, which has 5,984 counts in the 937 keV peak and with the veto condition, which has 3,886 counts in the 937 keV peak. Although the upper spectrum has higher statistics, the lower one has a better peak-to-total ratio.

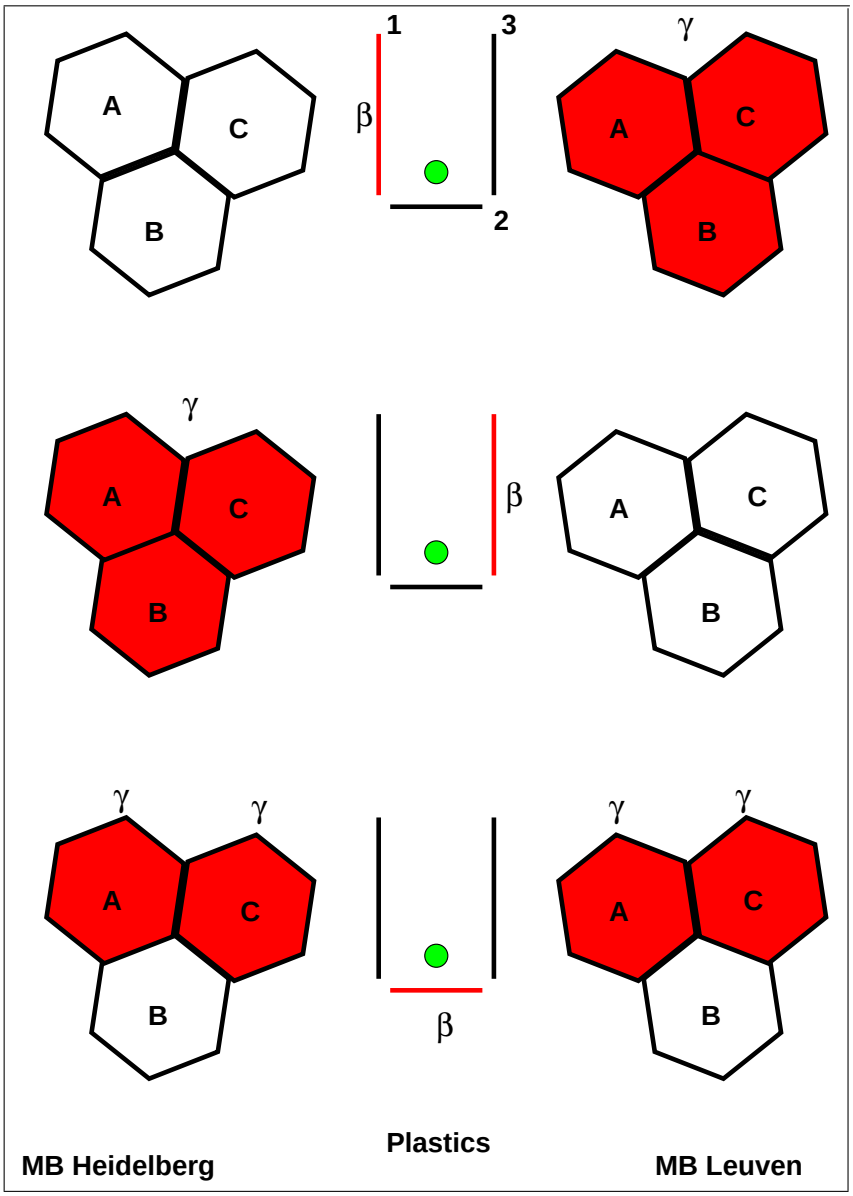

Figure 3.2: Veto Condition: If a β particle is detected in one of the side plastic detectors, the corresponding γs are accepted if they are detected in the opposite MINIBALL cluster. If the β particle goes through the middle β detector, the γ rays are accepted if they happen in the two most distant crystals of each MINIBALL cluster

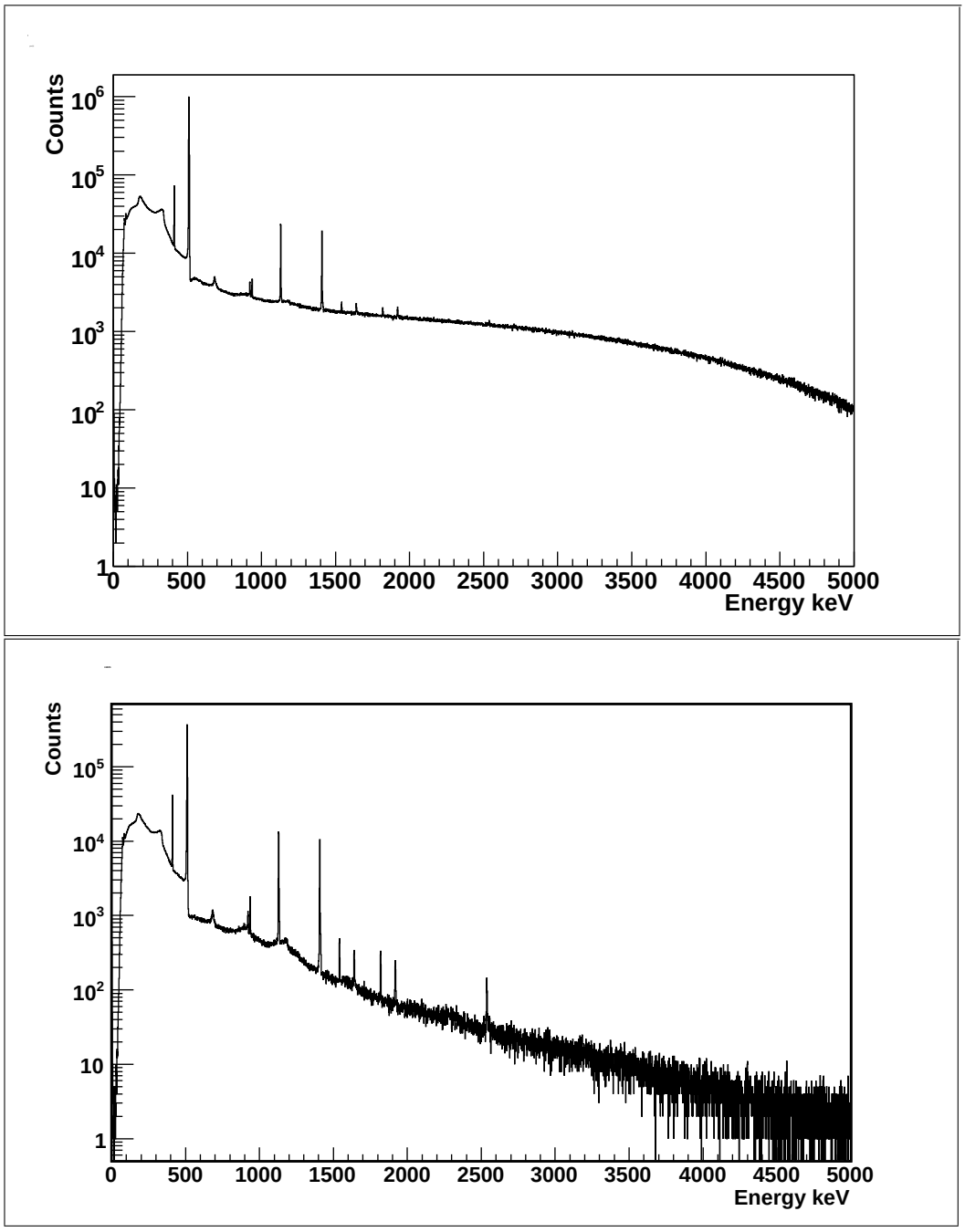

Figure 3.3: Difference between the no-veto (up) and veto (down) laser on Ni, mass A=54 β gated γ spectra

Figs.3.4 and 3.5 -pp.31 to 32- represent the total γ-spectra of mass 54 activity with the laser set on resonance for Ni and Co respectively. Both of them were constructed with the no-β penetration, veto condition. In the laser on Ni spectrum we can observe the 937 keV γ-ray known in the decay of ^{54}Ni. The gamma cascade lines 411 keV, 1130 keV and 1408 keV from the ^{54}Co^m decay and the 922 keV sum peak (411 keV + 511 keV) are also present. See Fig. 3.6 -p.33- for the low energy part of the spectra. In the laser set on Co spectrum, the same cascade lines and sum peaks are present but not the 937 keV line.

3.4 Half-life Analysis

From the previous experiment [Reu99b] we know that the ^{54}Ni half-life is 106(12) ms, thus if we take into account the macrobeam structure (400 ms of implantation and 600 ms of decay) and the microbeam structure due to the mass separator time behaviour during the implantation which was 50 ms OFF and 50 ms ON, we can model our *Implantation Decay Curve* ID, simply by solving the decay differential equations.

$$\frac{d}{dt}N_1(t) = P(t) - \lambda_1 N_1(t) \qquad N_1(0) = 0 \tag{3.1}$$

$$\frac{d}{dt}N_2(t) = \lambda_1 N_1(t) - \lambda_2 N_2(t) \qquad N_2(0) = 0 \tag{3.2}$$

$$P(t) = \sum_{i=1}^{4} a(H(t - 50(2i-1)) - H(t - 100i))$$

$$H(t-b) = \begin{cases} 0 & \text{if } t < b \\ 1 & \text{if } t \leq b \end{cases}$$

where N_1 is the ^{54}Ni activity, N_2 is the ^{54}Co activity, λ_1 and λ_2 are the respective decay constants and $P(t)$ is the implantation rate of ^{54}Ni, taking into account the microbeam structure. $H(t)$ is the Heaviside step function and a is the constant implantation rate when $P(t) \neq 0$.
Solving the differential equation with the initial conditions for $N_1(t)$ and $N_2(t)$ using Maple10, we obtain the *implantation decay curves* for ^{54}Ni and ^{54}Co (see Fig. 3.7 -p.34-).

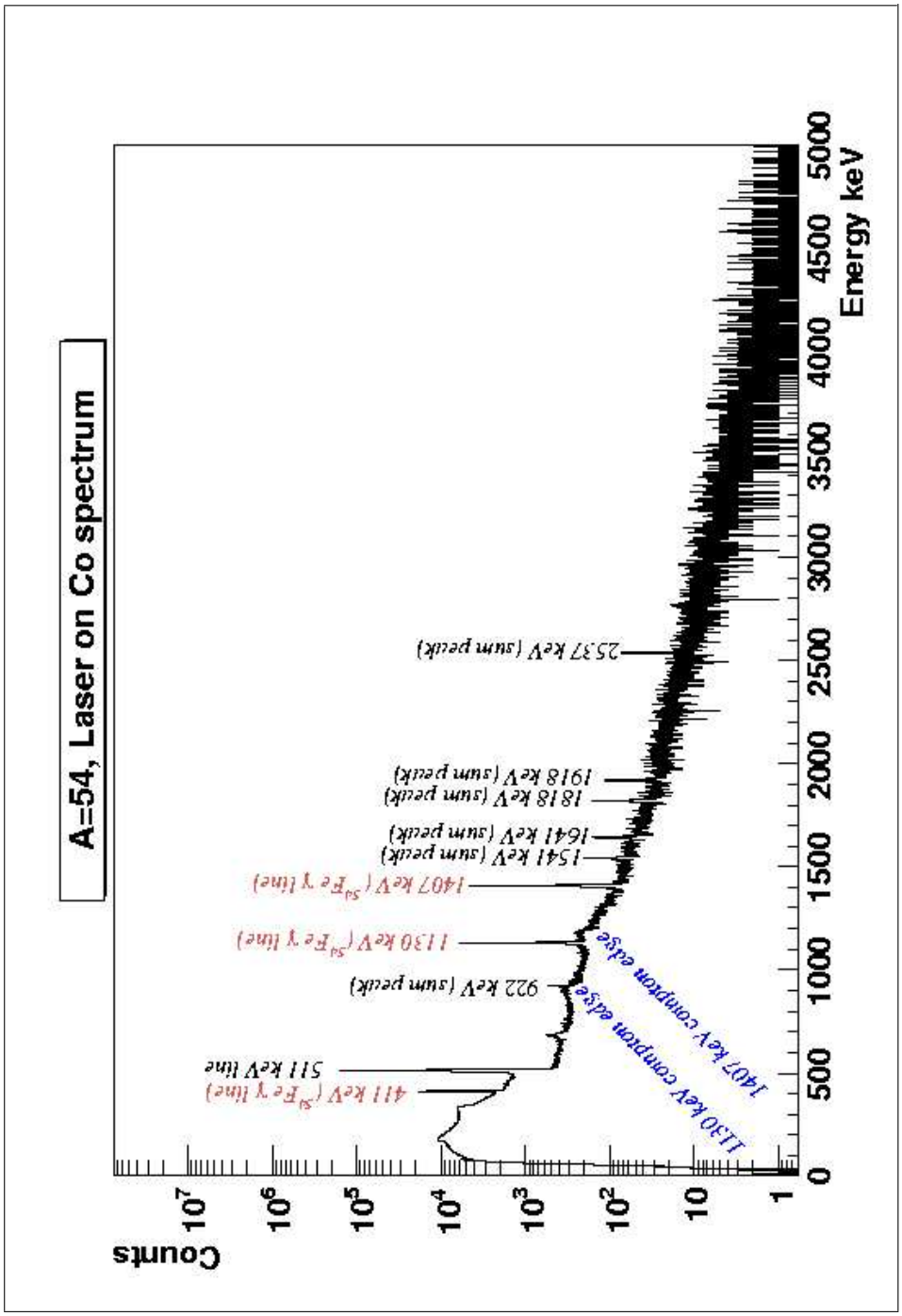

Figure 3.4: A=54 laser on Co β-γ spectrum

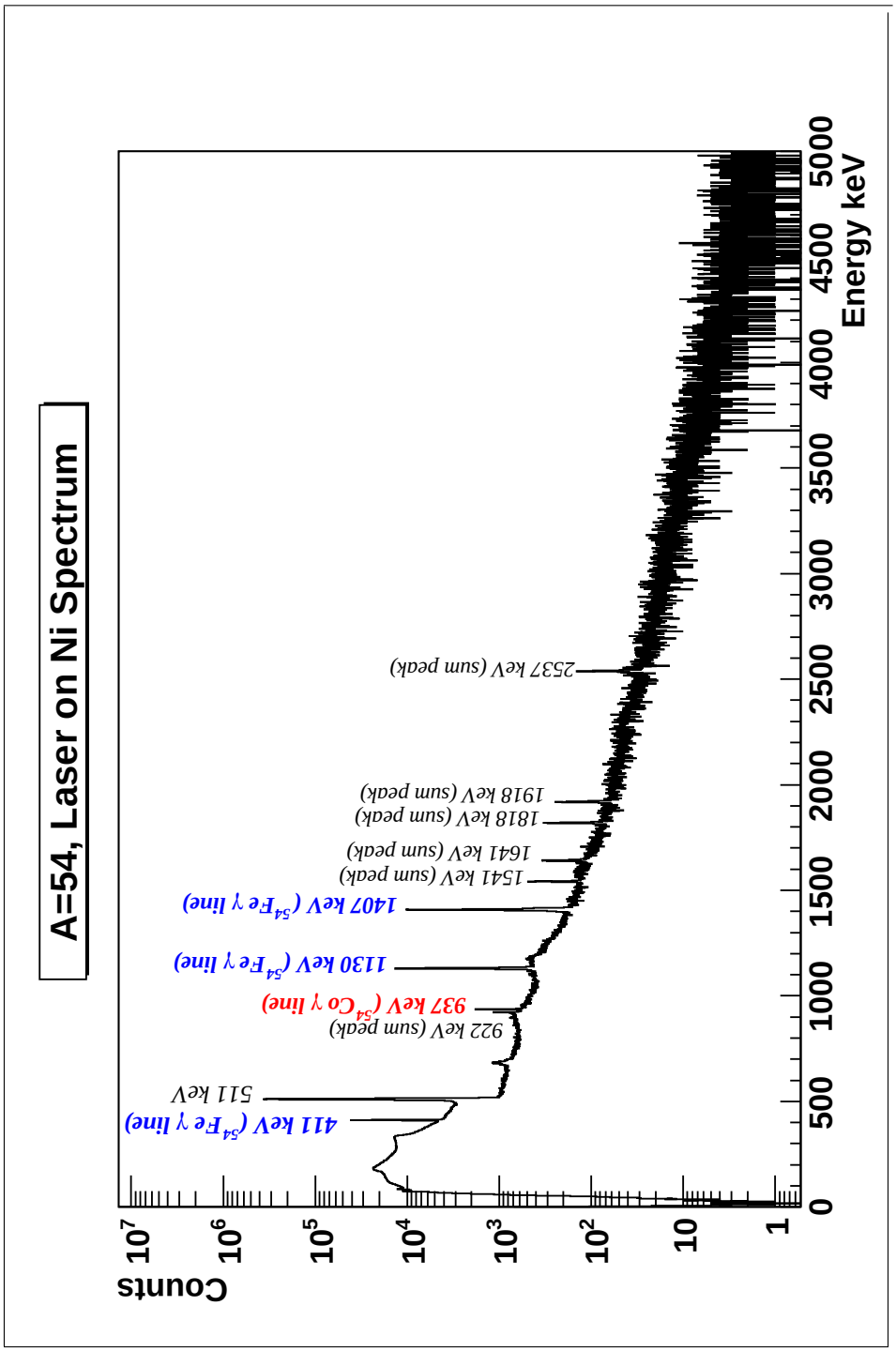

Figure 3.5: A=54 mass, laser on Ni β-γ spectrum

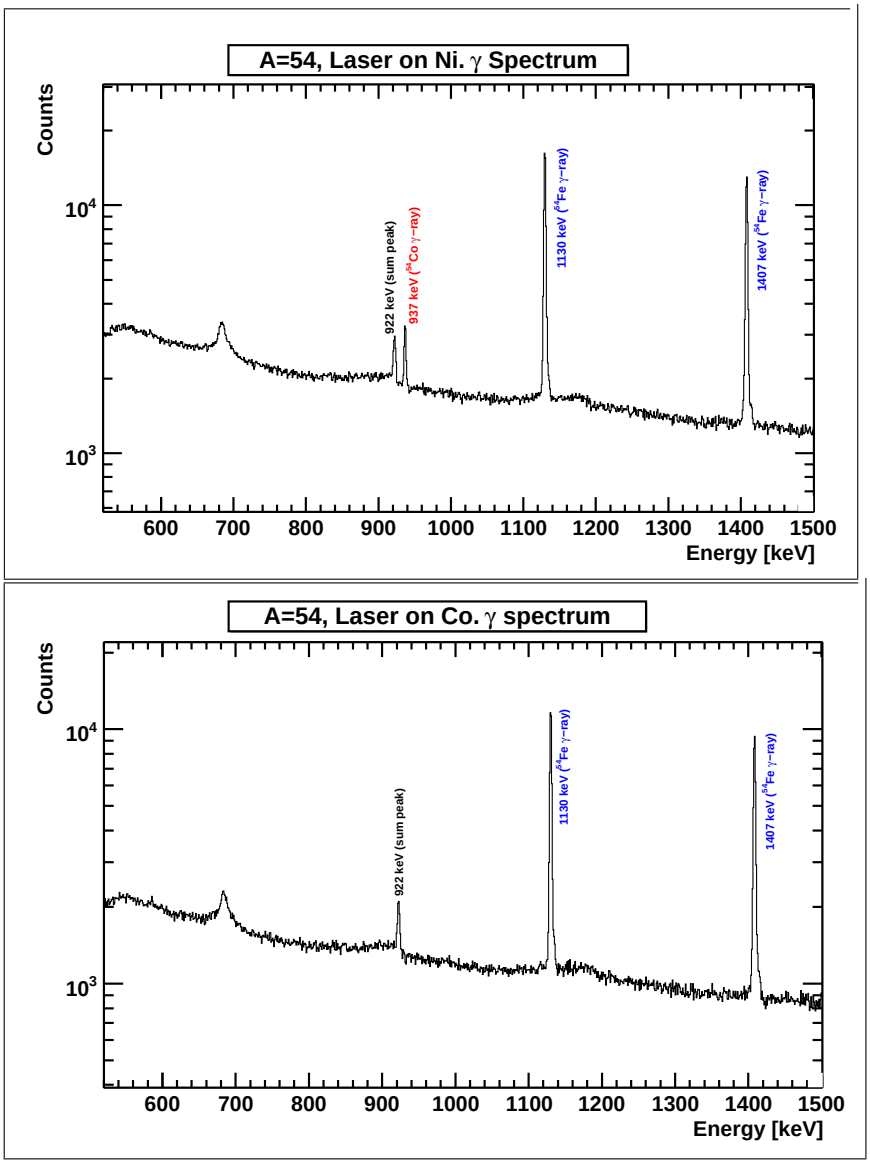

Figure 3.6: Expanded view of the A=54 laser on Ni and laser on Co spectra.

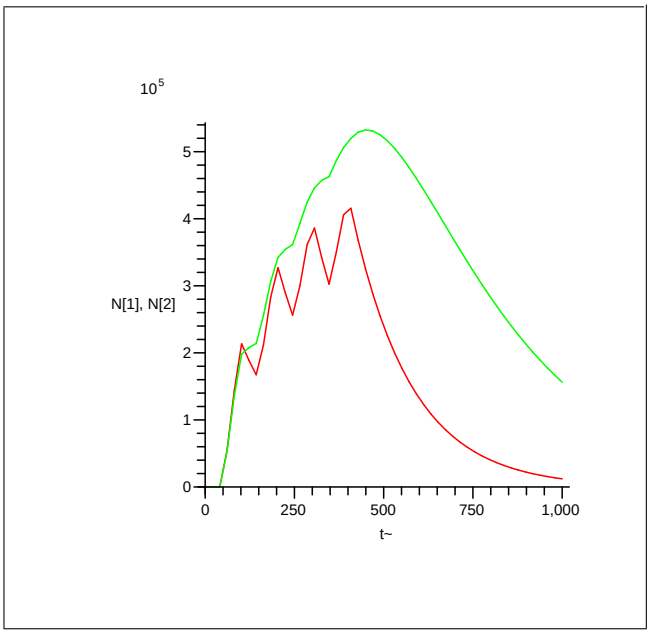

Figure 3.7: ID Curve during a macrocycle time (400 ms implantation and 600 ms decay) solving the differential equations system with Maple10. ^{54}Ni is shown in red and ^{54}Co is shown in green.

On the other hand, from our experiment we obtain a β gated γ-spectrum, thus we can reproduce the ID curve looking at the time evolution of the 937 keV peak during one macrocycle. The time behaviour of the 937 keV γ-ray was analysed using 50 ms time intervals in order to be consistent with the beam ON - beam OFF structure of the beam.

The half-life of ^{54}Ni can be deduced from the time behaviour of the area of the 937 keV peak after background subtraction in the laser on Ni γ spectrum.

As a first approach to obtaining the half-life we integrated the peak using a Gaussian shape centred on 937 keV, subtracting a linear background close to the Gaussian (centroid $\pm$ twice FWHM region). The integrated Gaussian areas are plotted in Fig.3.8 -p.36- and the implantation-decay curve is fitted. The last 4 points corresponding to 200 ms, were not considered in the fit, because the intensity of the 937 keV peak became of the same order as the background. The error obtained for each point in the curve was obtained from the Gaussian fit of the 937 keV γ-ray time behaviour, which uses the ROOT minimisation package MINUIT [1]. The half-life of the ^{54}Ni was obtained by fitting the ID curve and obtaining a value of $T_{1/2}^{\beta-\gamma} = 114.9 \pm 6.0$ ms. The half-life error,

[1] MINUIT calculates an error matrix with the fitted parameters. This error matrix is the inverse of the second derivative matrix of the best parameter values (the function minimum) and the diagonal elements of the error matrix are the square roots of the individual parameter errors, including the effect of correlation with the other parameters.

is obtained from the parameter minimisation using MINUIT.

Another attempt to deduce the half-life as precisely as possible was made by fitting double Gaussian functions, one on the 922 keV sum peak (511 keV + 411 keV, see Fig. 3.5) and the other Gaussian on the 937 peak. The last was fitted with a fixed width which was obtained by the fit in the total γ spectrum with all the statistics. The so-called long background (linear background taken from 800 keV to 1100 keV) was used to subtract the background in the region of interest, in order to reduce background fluctuations in the vicinity of the 937 peak. A reduced error bar is obtained with this method in comparison with the first attempt. Again, the error obtained by fitting a double Gaussian for each experimental point in Fig. 3.8 -p.36- is calculated with the ROOT minimisation package MINUIT. It is also clear from this fit that the last points do not behave in the way expected and should therefore be ignored in the $T_{1/2}$ fit. This tells us that due to the lack of statistics (peak indistinguishable from the background) at the end of the macrocycle, we can eliminate those points. The value of the half-life of the ^{54}Ni for this case was $T_{1/2}^{\beta-\gamma}$= 113.8 ± 4.4 ms. The half-life error was obtained from the fit of the implantation-decay curve including the micro structure using again the ROOT minimisation package MINUIT.

A third method to measure the half-life of the ^{54}Ni was to integrate directly the 937 keV peak (no fitting procedure) and subtract the long linear background. The error bar is a statistical error obtained from the integration of the 937 keV peak. If we again neglect the last 200 ms of the macrocycle, the half-life value was $T_{1/2}^{\beta-\gamma}$= 113.7 ± 4.6 ms(See Fig. 3.10 -p.38-). The half-life error was obtained from the fit of the implantation-decay curve including the micro structure again using the ROOT minimisation package MINUIT.

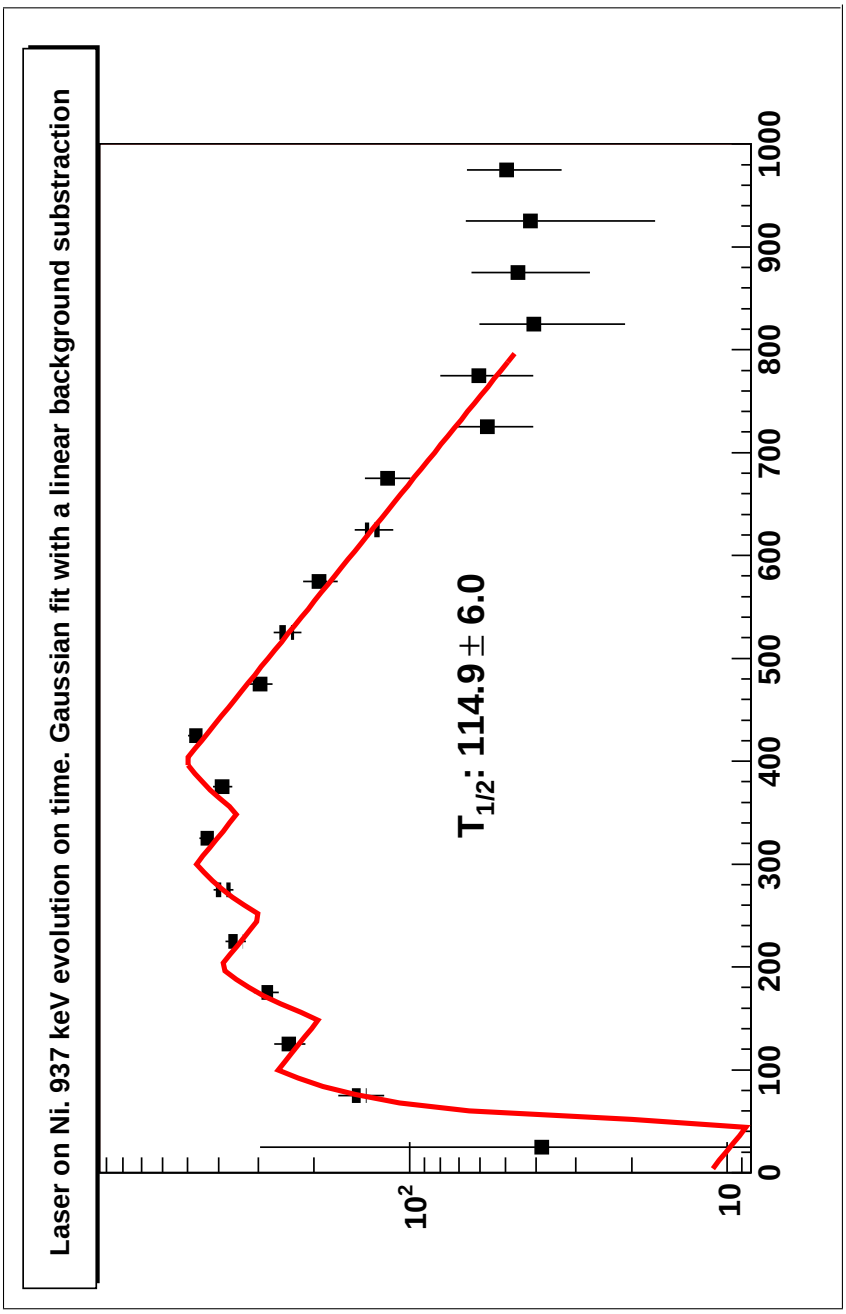

Figure 3.8: Implantation-decay curve of ^{54}Ni. Each point represents the area of the fitted Gaussian for the 937 keV γ-ray, subtracting a linear background in the neighbouring region.

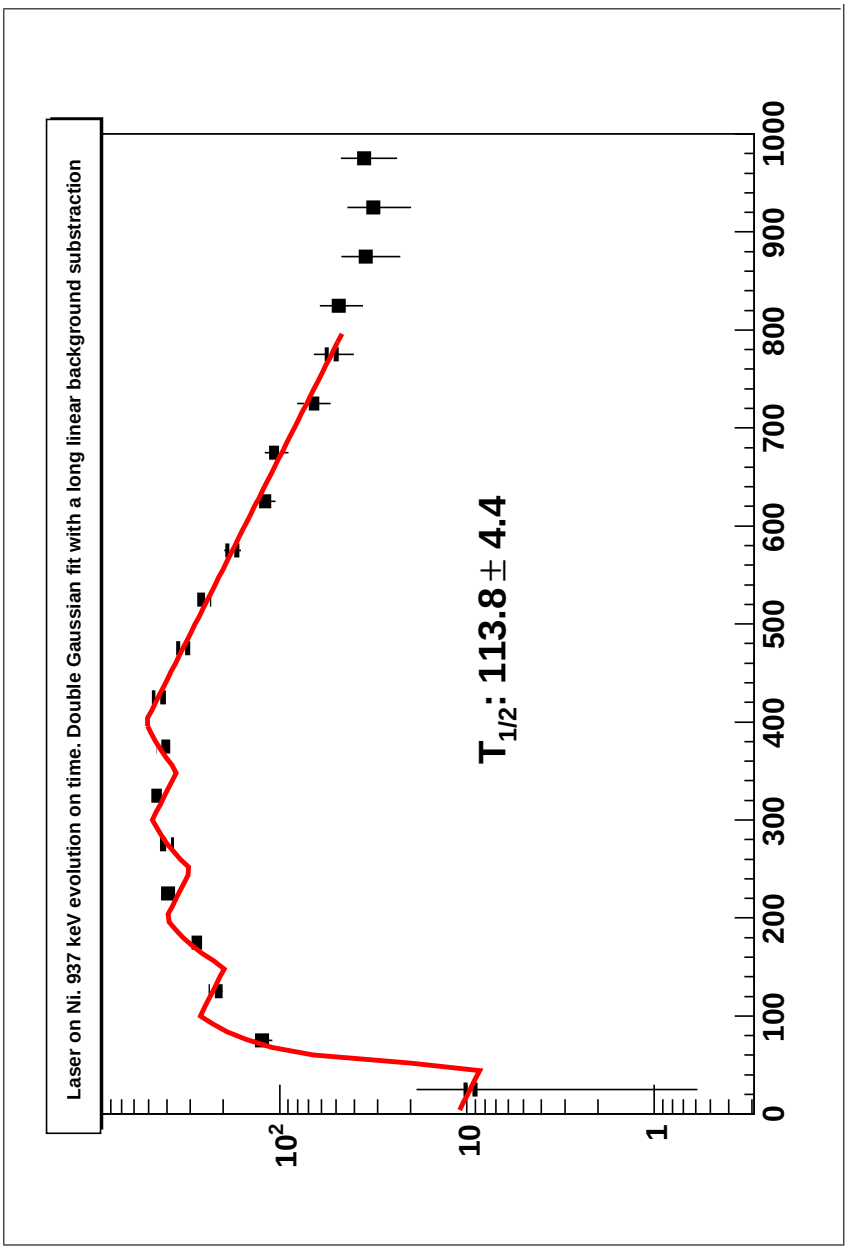

Figure 3.9: Implantation-decay curve of ^{54}Ni. Each point represents the area of a Gaussian with fixed width and centroid at 937 keV, after subtracting a long linear background taken from 800 to 1100 keV.

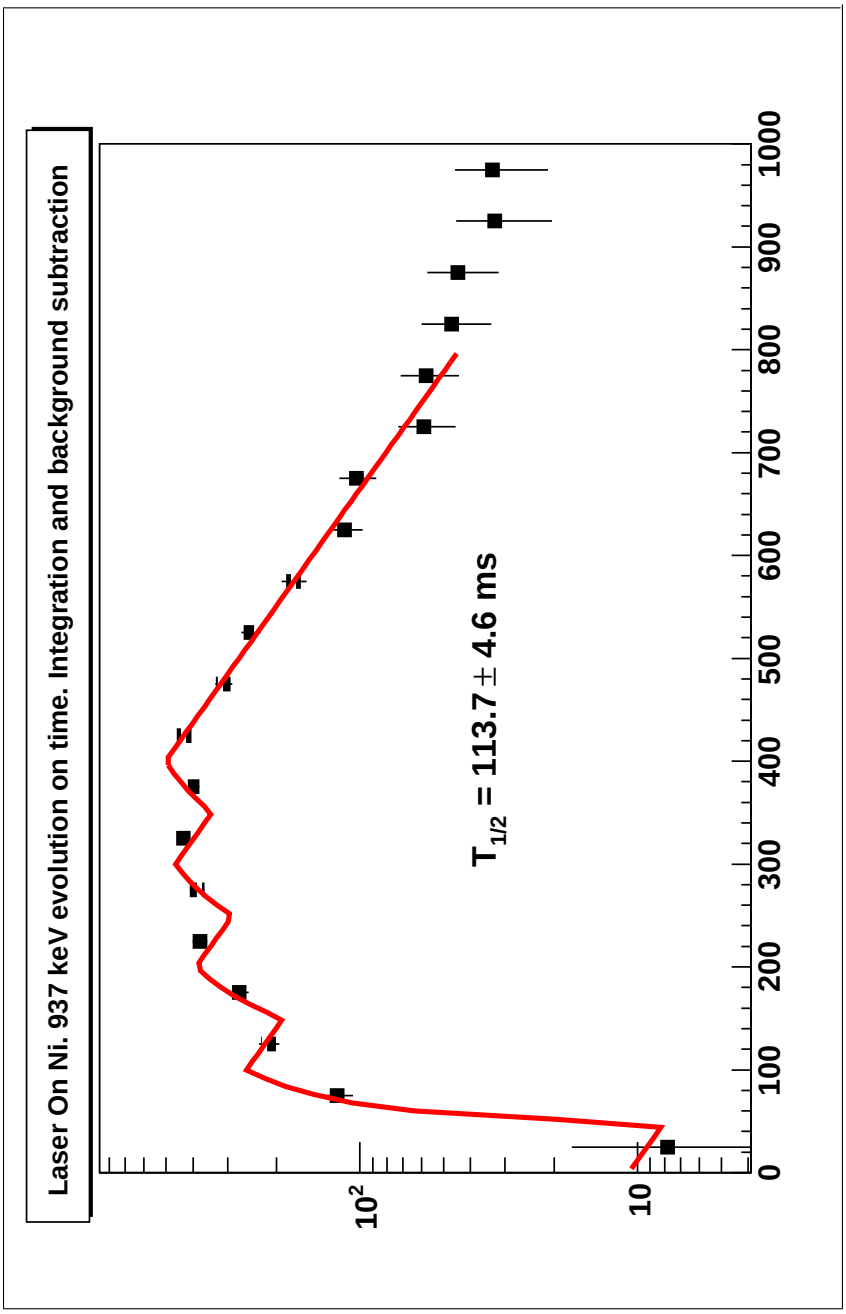

Figure 3.10: Implantation-decay curve of ^{54}Ni. Each point represents the area of the 937 keV peak in the double Gaussian fit with a linear background subtraction, in the range from 800 to 1100 keV.

3.5 High Energy Gamow-Teller states

In Fig. 1.8 -p.16- we present the energy spectra obtained in the ^{54}Fe(^{3}He,t)^{54}Co charge exchange reaction [Fuj07b]. In addition to the $0^+ \rightarrow 0^+$ Fermi transition and the first $0^+ \rightarrow 1^+$ Gamow-Teller transition, other high energy states are populated in the reaction. Because in the β decay case we have a Q-value window up to 8.8 MeV we also expected to populate some of these states. Because of the expected drop in β-branching due to the f factor and the drop of the γ-ray detection efficiency at high γ-energies, the detection of the γ-rays de-exciting these levels is difficult, among all the possibilities we expect to see the 3375 keV peak more easily than the other higher lying states. We therefore searched for the 3375 keV peak.

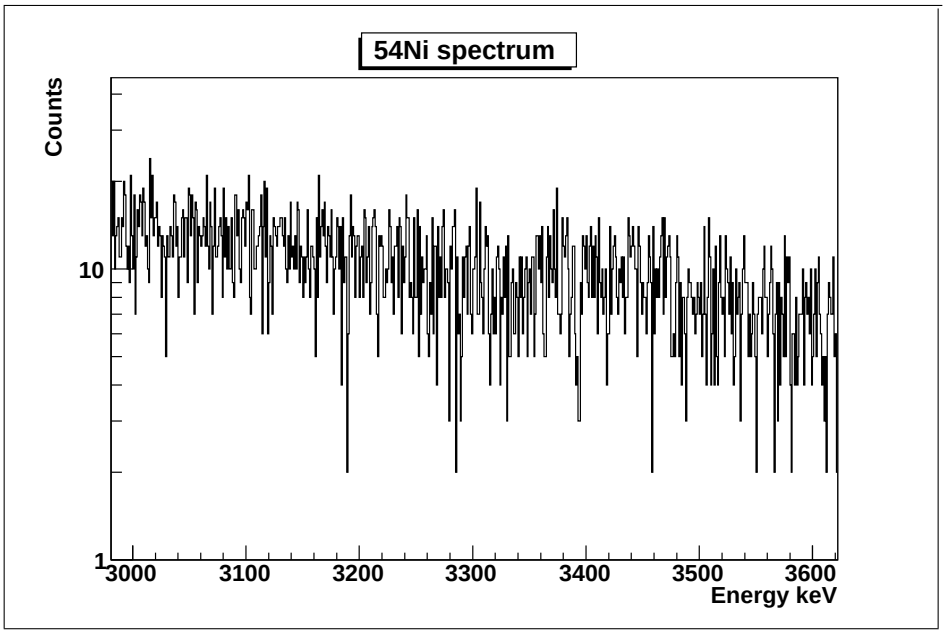

Figure 3.11: ^{54}Ni spectrum in the vicinity of 3375 keV.

In the Fig.3.11 -p.39- the 3375 keV region is plotted, but no γ lines are distinguishable from the background.

CHAPTER 4

T_Z=-1 ^{54}NI,^{50}FE ^{46}CR AND ^{42}TI MEASUREMENTS AT RISING

A second β-decay experiment was carried out at the Gesellschaft für Schwerionenforschung (facility for heavy-ion research), GSI, situated near Darmstadt in the state of Hessen in Germany. It was part of the **RISING** (**R**are **IS**otope **IN**vestigation at **G**SI) Stopped beam campaign [GdAW01] carried out in July 2007.
In this case not only ^{54}Ni, but also ^{50}Fe, ^{46}Cr and ^{42}Ti were measured. They were produced as fragmentation products of ^{58}Ni, accelerated in the UNILAC and SIS18 synchrotron accelerator colliding with a Be target. The products of the reaction were separated in the fragment separator (FRS), characterised in A/Q and Z and implanted at the final focal plane of the separator. Here the β particles emitted in the decay were measured as well as the γ-rays.

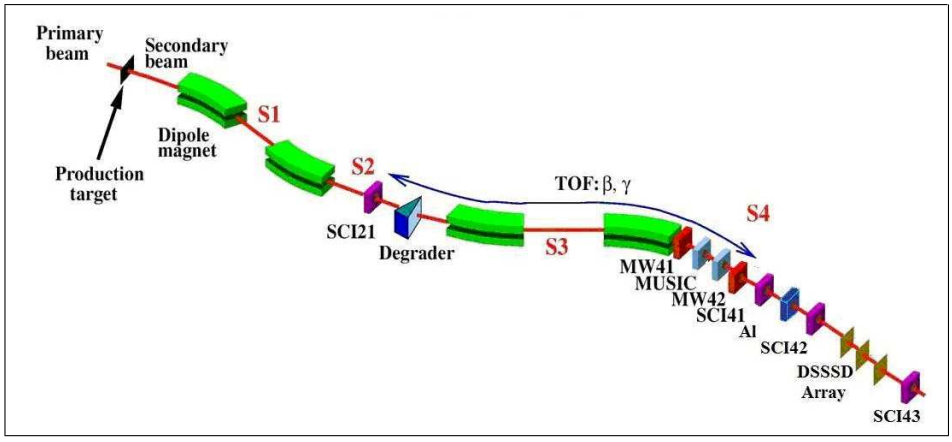

Figure 4.1: General layout of the FRS separator and the various detectors where the ion is identified before its implantation in a DSSSD.

A general layout of the experiment is presented in Figs. 4.1 -p.41-, 4.15 -p.54- and 4.30 -p.71- and the different stages of the experiment are described in the following sections.

4.1 Description of the Experiment

4.1.1 The Accelerator complex and the reaction used

The ion acceleration at GSI starts in the UNILAC [unia] (see Fig. 4.2 -p.42-). Stable ions from hydrogen (Z=1) to uranium (Z=92) can be accelerated in this device up to energies of 18 MeV per nucleon, which can be adjusted in a last linear acceleration stage to give a final energy range between 2 to 18 MeV per nucleon [unib]. For higher energies, the UNILAC ion beam is injected into the heavy ion synchrotron SIS18, where ions can reach final energies up to 2 GeV per nucleon, which is equivalent to about 90% of the speed of light [sis]. The SIS18 has a circumference of 216 m with 24 bending magnets and 36 magnetic lenses, with a maximum magnetic rigidity of $B\rho$=18 Tm.

Once the desired energy is defined, the stable beam is extracted either quickly -in less

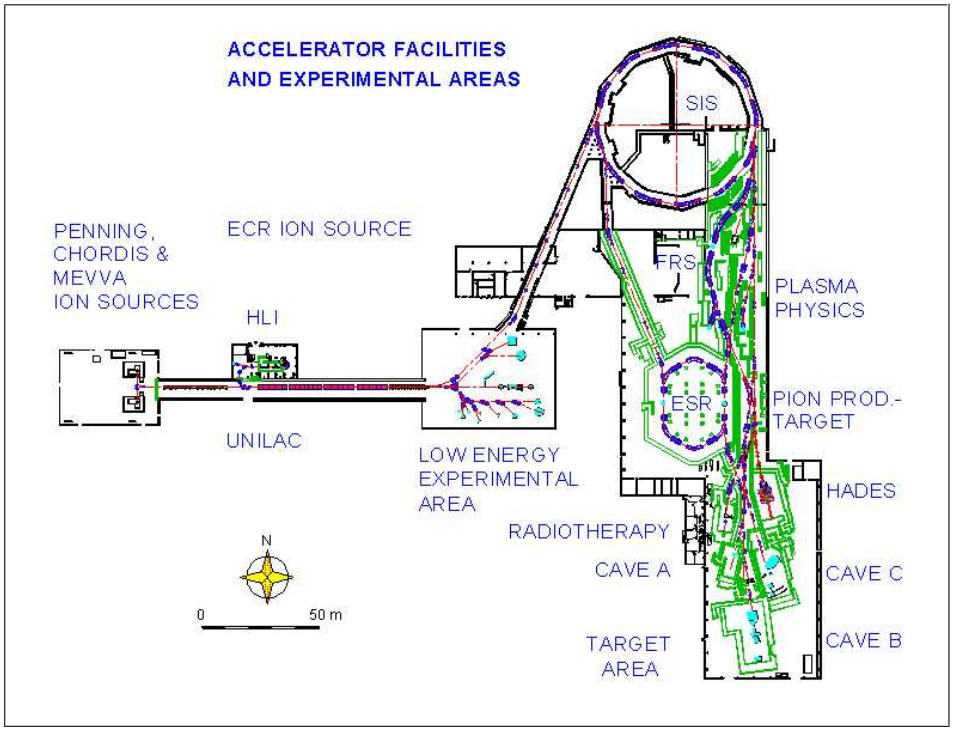

Figure 4.2: Complete overview of the GSI facilities. UNILAC, SIS18 Synchrotron and the FRS.

than a microsecond- or slowly -over a period up to 10 seconds-. Slow extraction is used for most experiments in the fragment separator FRS. After the extraction, the beam is

focused on a stable target, where two kind of nuclear reactions can take place, either projectile fragmentation or induced fission (or a combination of both) [M̈92], depending on the primary beam and the target, and the energy of the collision. After the reaction a secondary beam including radioactive and stable nuclei is produced. In the present case the T_z=-1 ^{54}Ni, ^{50}Fe, ^{46}Cr and ^{42}Ti nuclei were produced by the fragmentation of a ^{58}Ni beam accelerated to 680 MeV/u on a 400 mg/cm^2 Be target. The primary beam spill length was 10 sec with an intensity of ∼3x10^9 particles per spill and the repetition cycle was ∼13 sec. Table 4.1 and Table 4.2 -p.43- give a summary of the experimental conditions for the different selected fragments.

Beam	Energy	Av.Intensity	Spill Period	Target (Thickness)	Fragment
^{58}Ni	680 MeV/u	2.1×10^9 ppSp	13.0s (10s/3.0s)	^{nat}Be (4011 mg/cm^2)	^{54}Ni
^{58}Ni	680 MeV/u	4.6×10^9 ppSp	13.3s (10s/3.3s)	^{nat}Be (4011 mg/cm^2)	^{50}Fe
^{58}Ni	680 MeV/u	3.4×10^9 ppSp	13.3s (10s/3.3s)	^{nat}Be (4011 mg/cm^2)	^{46}Cr
^{58}Ni	680 MeV/u	3.3×10^9 ppSp	13.3s (10s/3.3s)	^{nat}Be (4011 mg/cm^2)	^{42}Ti

Table 4.1: Experimental Settings for the production of the different fragments.

Frag.	Bρ_1 [Tm]	S2 Deg.Thick.	θ_{S2} (Achro.)	Bρ_2[Tm]	S4 Deg.Thick.	Time Meas.
^{54}Ni	7.4963	6500 mg/cm^2	8.67 mrad	5.4125	3430 mg/cm^2	2151 min
^{50}Fe	7.4962	6500 mg/cm^2	8.59 mrad	5.6066	4470 mg/cm^2	1402 min
^{46}Cr	7.4893	6500 mg/cm^2	8.52 mrad	5.7817	5500 mg/cm^2	1140 min
^{42}Ti	7.4748	6500 mg/cm^2	8.43 mrad	5.9409	7010 mg/cm^2	531 min

Table 4.2: Experimental Settings for the separation of the fragments.

4.1.2 The Fragment Separator

The reaction fragments were filtered using the $B\rho$-ΔE-$B\rho$ technique (explained later in this section) and a series of slits at the FRS. The signals produced by each individual ion were recorded in various components of the FRS. This allowed an off-line identification of each single ion which arrived at the implantation detector and also provided a trigger.
In the following we will describe the FRS working principle as well as the particle identification components.

The FRagment Separator, FRS (see Fig. 4.3 -p.44-), is a 74 m long, in-flight magnetic spectrometer consisting mainly of four 30^o dipole magnets with a set of quadrupoles before and after each dipole. The first two dipole magnets are used as first ($B\rho$) filter for the secondary ions produced in the reaction. In the middle of the spectrometer, at S2 (see Fig 4.1 -p.41-), a specially shaped degrader (see Fig. 4.5 -p.46-) is placed which allows an energy filter ΔE. Finally a second pair of dipole magnets acts again as a $B\rho$ filter. This three stage separation method ($B\rho - \Delta E - B\rho$) allows a proper selection of the nucleus of interest [Gei92].

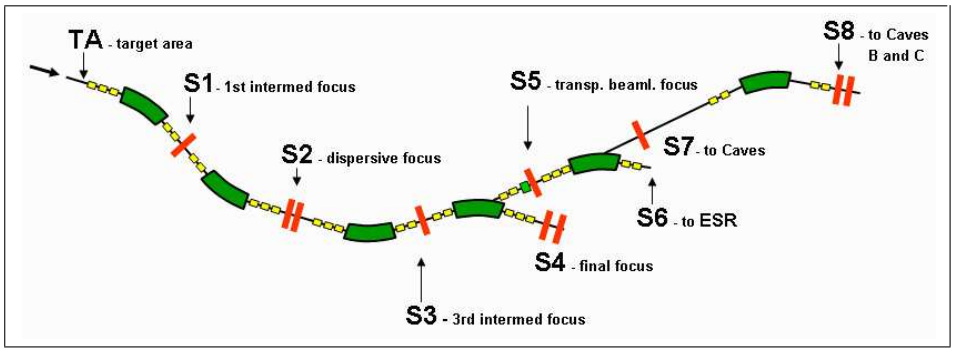

Figure 4.3: Complete scheme of the Fragment Separator at GSI. All experimental areas are shown. Our experimental setup was placed at S4.

The $B\rho - \Delta E - B\rho$ method

A heavy ion with mass m and charge q which moves with a velocity $\vec{v}$ in a magnetic field $\vec{B}$ experiences the Lorentz force given by

$$\frac{d}{dt}(m\vec{v}) = \vec{F}_L = q\vec{v} \times \vec{B} \tag{4.1}$$

Inside an FRS magnetic dipole, the magnetic field is homogeneous and perpendicular to the momenta of the heavy ions. If no other force is involved, the centripetal force balances with the Lorentz force,

$$qvB = \frac{mv^2}{r} \qquad \rightarrow \qquad B\rho = \frac{m}{q}v \tag{4.2}$$

where ρ is the trajectory of the heavy ion with mass m and charge q. Moreover, as shown in the introduction of Section 4.1 -p.42-, the energies of the heavy ions are relativistic, so the same formula can be expressed in relativistic terms in the following way, momentum is defined as $p = \beta\gamma Auc$ with the velocity $\beta = v/c$, the Lorentz factor $\gamma = \sqrt{1/(1-\beta^2)}$, the speed of light c and the atomic mass u. If heavy ions are fully stripped, i.e. without any electron $q = Ze$,

$$\frac{A}{Z} = \frac{B\rho e}{\beta\gamma uc} \tag{4.3}$$

Thus, each fragment with a defined A and Z, is spatially separated depending on its magnetic rigidity $B\rho$ and velocity β. At the FRS it is possible to reduce the accepted $B\rho$ range by including horizontal slits[1] at the exit of the magnetic dipoles. If two ions with the same magnetic rigidity enter the dipole at the same position but with different angle, they will end up at different positions after the magnet. To correct this angular dependence, quadrupole and sextupole magnets are placed after and before each dipole.

The second stage of this method (ΔE) is the wedge. This part has two purposes a) to correct for differences in energy in the secondary beam arriving at this point, by

[1] piece of material, usually Cu, thick enough to stop an ion

letting the ions with higher energy pass through more material than those with lower energy, b) to separate ions with different Z using the energy loss in the material. The energy loss per distance travelled by a charged particle in a material, as a function of the square of their charge, Q^2, is given by the Bethe-Bloch formalism [Bet32],

$$-\frac{dE}{dx} = \frac{4\pi}{m_e c^2}\frac{\tilde{Z}N_a\varrho Z^2}{\tilde{A}\beta^2}\left(\frac{e^2}{4\pi\epsilon_0}\right)^2\left[\ln\left(\frac{2m_e c^2\beta^2}{I(1-\beta^2)}\right)-\beta^2\right] \tag{4.4}$$

where $\tilde{Z}$, $\tilde{A}$, ϱ and I are the atomic number, mass, density and mean excitation potential of the absorbing material, m_e is the electron mass and N_a is the Avogadro number. Then under the assumption that all fragments have the same velocity after the reaction, we can separate different Z values by making the ions pass through a piece of material, where they lose energy (and velocity) according to the value of Z (See Fig. 4.4 -p.45-).

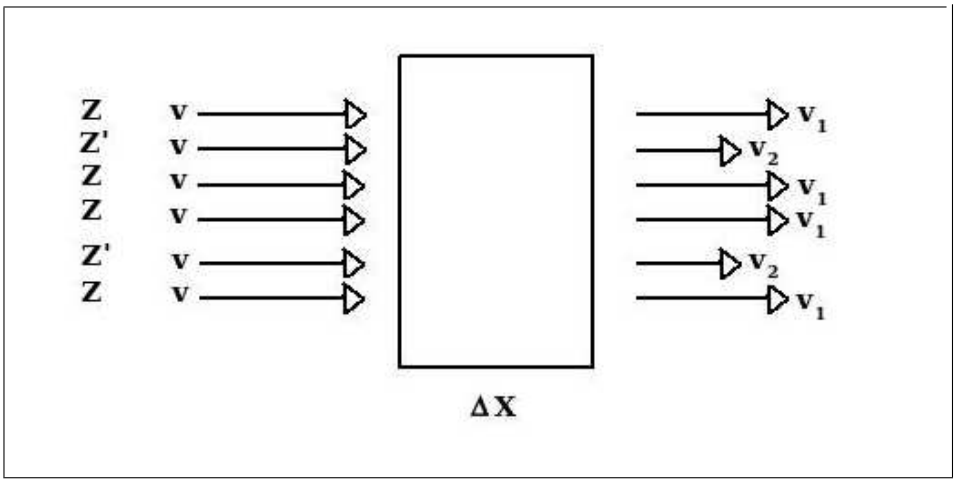

Figure 4.4: Simple scheme of a degrader: for different ions with different Z values, the velocity after the degrader is different.

In the FRS setup the degrader system consists of three different parts: A.- a wedge-shaped disk degrader pair, B.- a set of plane plates (usually called ladder), and C.- a wedge-shaped plane degrader pair (See Fig. 4.5 -p.46-). The ladder and the plane wedge (A.- and C.-) are the homogeneous part of the degrader, i.e their thickness is independent of the X-position[2]. With the wedges any thickness between 270 and 6750 mg/cm^2 of aluminium can be set up. The ladder consists of five aluminium plates, each of them with a fixed thickness. If the degrader disk is used, another 737 mg/cm^2 of aluminium can be added to the beam line. By changing the disk's slope, i.e. rotation along the beam axis, different ion optical settings can be archieved. In the mono-energetic mode, the degrader system is set to compensate for the momentum spread of the selected ion

[2]Considering the Z-direction as the direction of the beam; thus, X-direction and Y-direction are the orthogonal horizontal and vertical-directions respectively

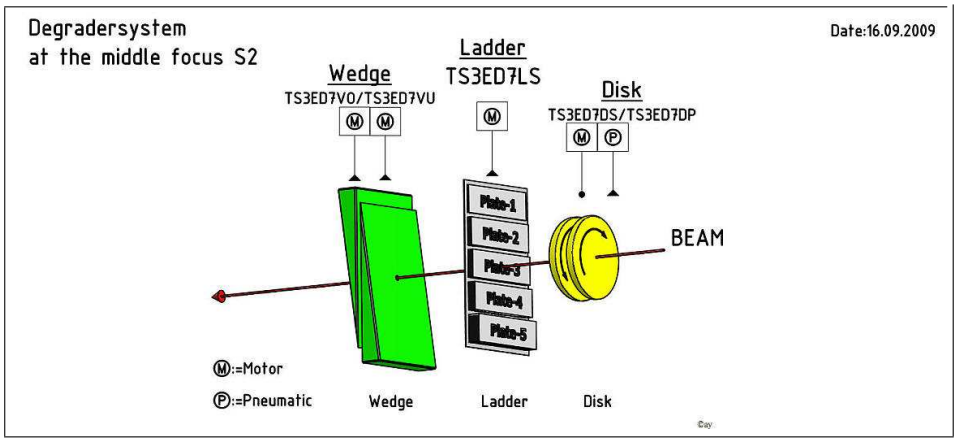

Figure 4.5: Drawing of the Degrader System at the S2 focal plane consisting of a wedge, a ladder and wedge-shaped disks.

(energy focusing), in consequence they are finally implanted at a well-defined depth in the DSSSD detector; in the achromatic mode, the degrader system is set to compensate for the X-position spread (position focusing). A schematic drawing of both modes is presented in Fig. 4.6 -p.47-. In our case we used a fully achromatic mode. In Table 4.2 the S2 degrader thickness and the disk angle θ_{S2} used for the different settings is shown. At the third stage of the method, i.e the second $B\rho$, a second pair of magnetic dipoles separates the fragments according to their momentum ($B\rho \propto Av$). The spatial distribution remains the same as at the intermediate focal plane.

4.1.3 Particle Identification at FRS

An essential part of every experiment at the FRS is the identification of the fragment. Firstly it is possible to select the desired ion knowing the proper A/Z value and tuning the proper magnetic field in the dipoles, but after the ion interacts with the matter at S2, it is necessary to track it by means of particle detectors which can measure the time-of-flight, position and energy loss of the fragments up to the final focusing plane at S4.

Scintillator Detectors

Four plastic scintillator detectors are placed in different sectors of the FRS. Three of them, sci21, sci41 and sci42 are used for time-of-flight measurements while sci43, placed at the end of the FRS at S4, is used as a veto (See Fig.4.1 -p.41-). The reason for using plastic scintillators is because of their good time response.

In our setup, sci41 gives the start signal to the TAC while sci21 gives the stop signal, for the amplitude of the TAC output signal provides the time-of-flight (TOF) parameters. The inverse logic is used in order to avoid too many "wrong starts", recording only the

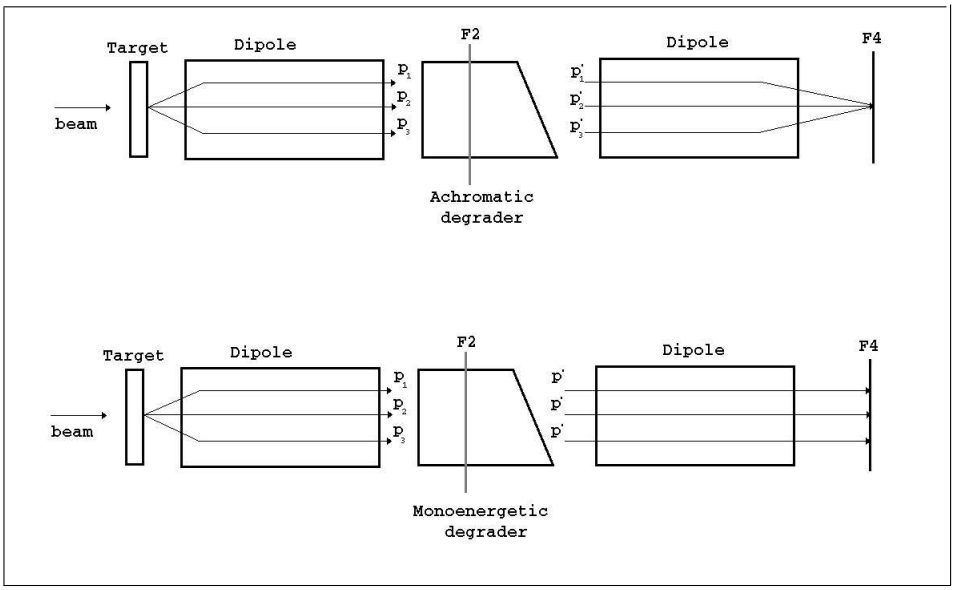

Figure 4.6: FRS Degrader scheme. In achromatic mode, the ions are spatially focus at the last focal plane at F4. In monoenergetic mode, the ions after the degrader had the same momentum.

signals for the ions which survived till section S4 and reduce the deadtime. The time difference of signals from right and left PMs of sci21 and sci41 are also measured in the same way for position correction purposes. On the other hand sci42 is placed behind the last plane wedge degrader at S4 to measure the survival of the ions in the slowing-down process. Sci43 is installed at the end of the FRS, behind the active stoppers and is used to detect the non-implanted ions.
The electronic circuit associated with these TAC signals for the scintillator detectors is explained in Fig. 4.7 -p.48-.

Multi-wire Proportional Counter Detectors

The multi-wire proportional counter detector MWPC is an XY-position sensitive detector (See Fig. 4.8 -p.49-) used (i) to centre the primary beam on the optical axis after inserting the target and degrader (ii) to calibrate the position sensitive sci21 and sci42 detectors, and (iii) to correct the position of the ion in the MUSIC energy signals. A MWPC detector consists of a gas chamber filled with CO_2/Argon mixture and three thin wire grids. When a charged particle passes through the detector, it produces an electron avalanche which drifts to the anode wires providing an electrical signal corresponding to the position of the ion with a typical position resolution of 0.5 mm [Ste91].

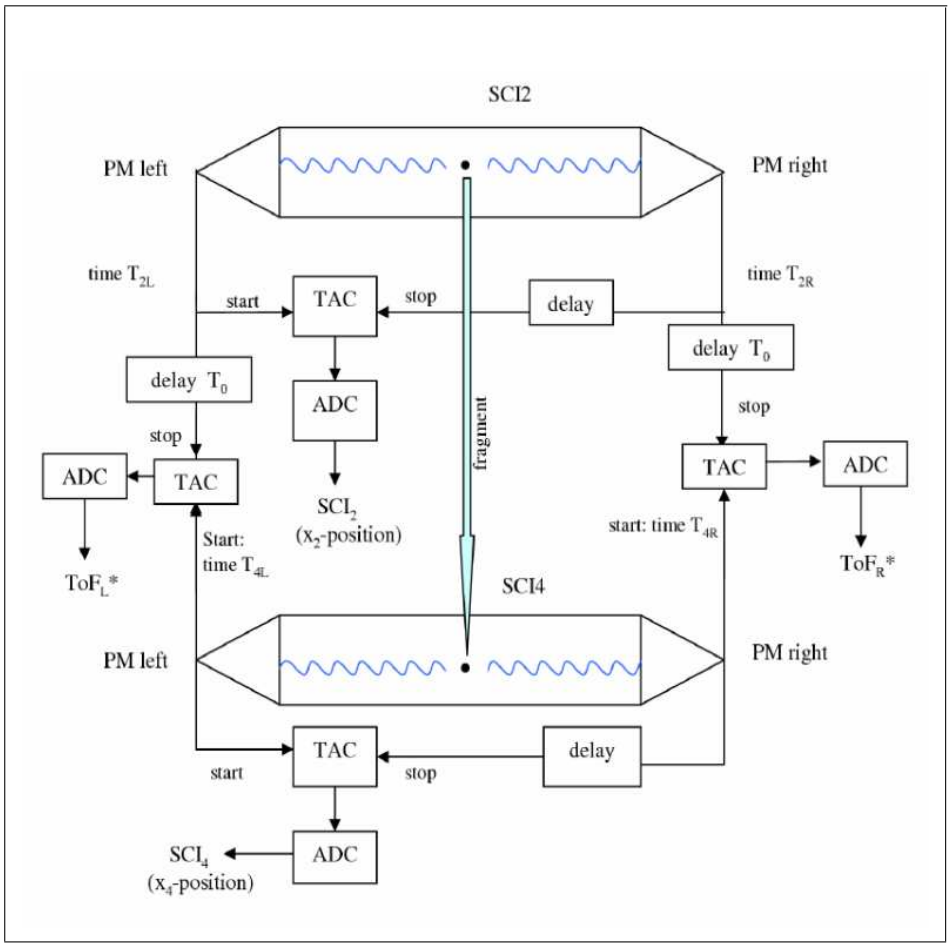

Figure 4.7: Schematic view of the time-of-flight (TOF) measurement. When an ion passes through the scintillators sci21 and sci41, two signals are produced per detector. The difference of the average of these signals gives the time-of-flight of the ion. Figure from V.Ricciardi [Ric04].

MUSIC Detector

The MUltiple Sampling Ionisation Chamber (MUSIC) is an ionisation chamber which measures the energy loss of the ion passing through it. This chamber consists of a cathode, a Frisch grid and eight independent anode strips as shown in Fig. 4.9 -p.49-. The MUSIC is operated with a constant gas flow of pure CF_4 at atmospheric pressure and at room temperature. The active area of a MUSIC chamber is 200 mm $\times$ 80 mm and the active length is 400 mm. The anode strips are read out with an optimised charge sensitive preamplifier and shaper combination for particle rates up to 200kHz. Since the number of electrons generated in the gas is proportional to the square of the charge

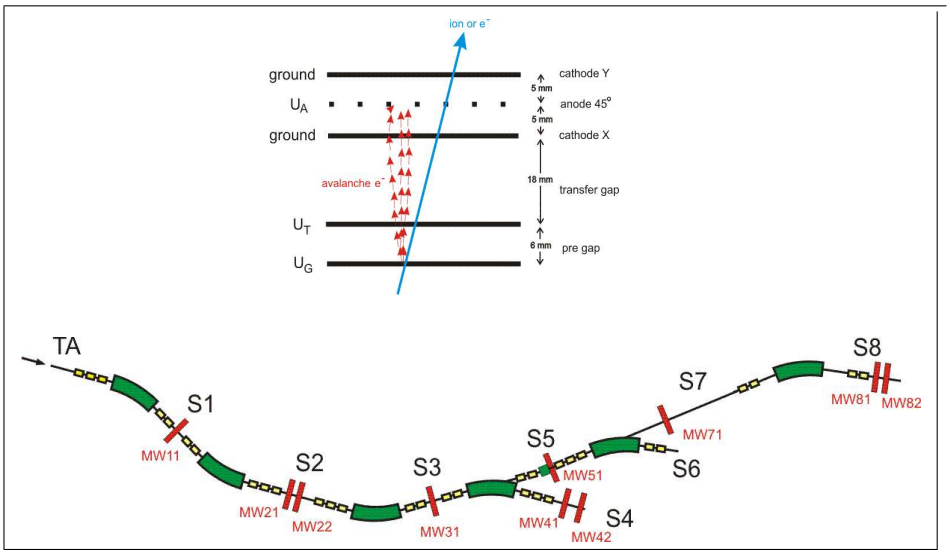

Figure 4.8: This figure shows (i)schematic drawing of the multi-wire detector, and (ii) the position of each multi-wire in the FRS line

of the penetrating ion (see Eq. 4.4 -p.45-), the output voltage signal of the shaper is a measure of the atomic number Z of the ion [SS00]. In this experiment two MUSIC ionisation chambers were used.

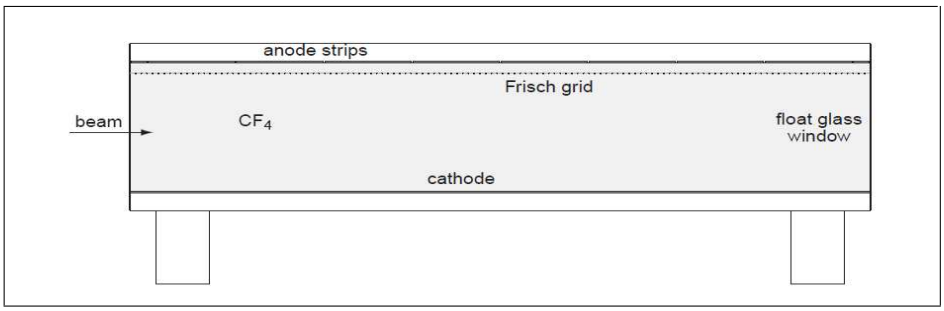

Figure 4.9: MUSIC80: Ionisation chamber.

With the TOF measured with scintillation detectors sc21 and sc41 ($TOF \propto \frac{1}{v}$), the energy loss measured with the two MUSIC ionisation chambers (ΔE $\propto Z^2$) and the $B\rho$ from the dipole magnets ($B\rho \propto A/Q$) it is possible to construct an ion-by-ion identification plot.
In Figs. 4.10 -p.50-, 4.11 -p.51-, 4.12 -p.51- and 4.13 -p.52- the identification plots for ^{54}Ni, ^{50}Fe, ^{46}Cr and ^{42}Ti are shown. These plots were obtained from the calculated values of Z and A/Q using the TOF, ΔE and $B\rho$ measurements. The Z and the A/Q values were re-calibrated run-by-run in order keep the identification of the desired nuclei

(^{54}Ni, ^{50}Fe, ^{46}Cr and ^{42}Ti) in the same position. It is also important to remark that these are the separated and identified ions up to the scintillator sci41 (see Fig. 4.1 -p.41-) but not all of these ions survive until the last focal plane of the FRS at S4 and are implanted in the DSSSD. More explicitly secondary reactions can take place in the Al degrader between sci41 and sci42, and in the DSSSD detectors themselves. How many of the identified ions at sci41 survive after implantation in the DSSSD is normally called the "survival probability".

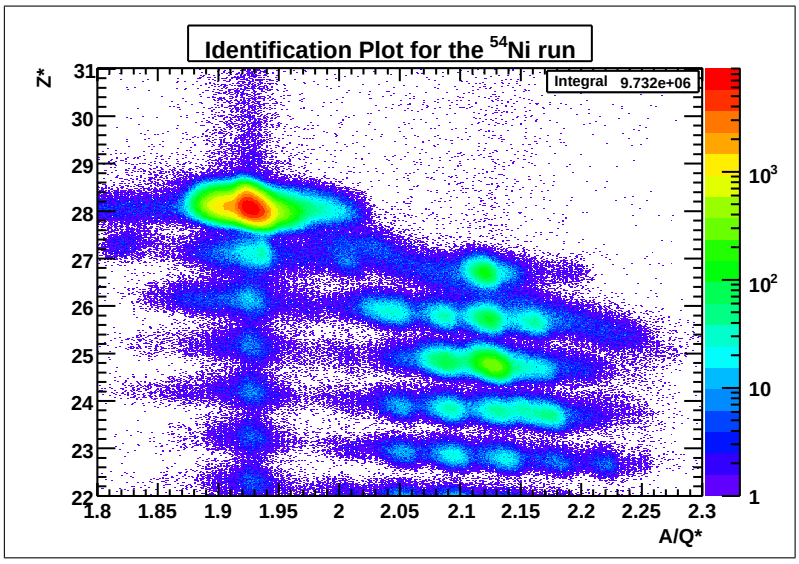

Figure 4.10: Identification plot for the reaction fragments separated and identified up to sci41 in the ^{54}Ni experiment setup. $Z^*$and A/Q^* are the correct Z and A/Q values for the ^{54}Ni; for the other identified nuclei small differences may exist.

4.1.4 The Active Stopper

During the RISING Stopped beam campaign [GdAW01] two kinds of experiment were carried out, where the main difference was the kind of detector used to stop the beam. For the first series of experiments a so-called passive stopper was used [Pie07a]. Different materials were used as the passive stopper, such as Beryllium and Cooper, but no implantation signal was obtained from them. The passive stopper was used to ensure that the ion was stopped at the centre of the RISING array. Then the gamma-rays were observed in a time period less than a μs after the implantation [3]. They were assigned as de-excitations of isomeric states in the implanted ions.

[3]Several articles were publish for the passive stopper campaign [Loz08], [Reg07], [Pie07b], [Jun07], [Gar08], [Rud08a], [Rud08b], [Ste08] and [Cac09].

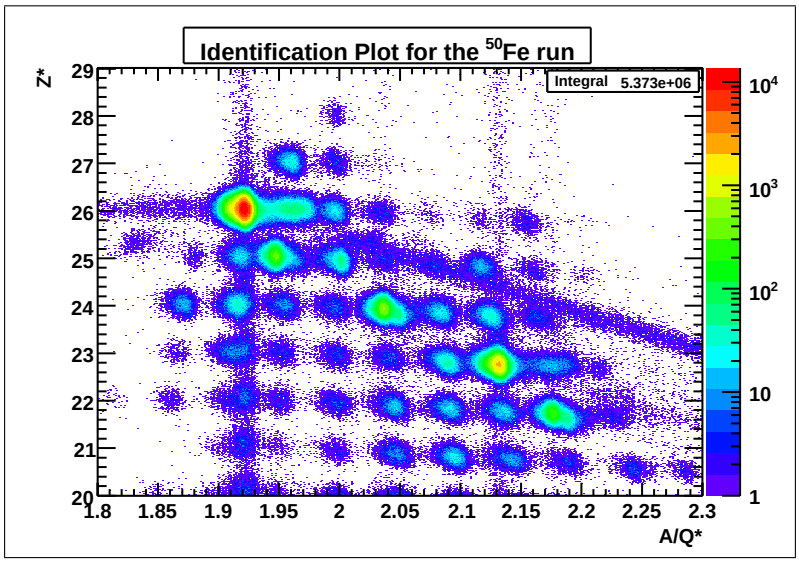

Figure 4.11: Identification plot for the reaction fragments separated and identified up to sci41 in the ^{50}Fe experiment setup. $Z^*$and A/Q^* are the correct Z and A/Q values for the ^{50}Fe; for the other identified nuclei small differences may exist.

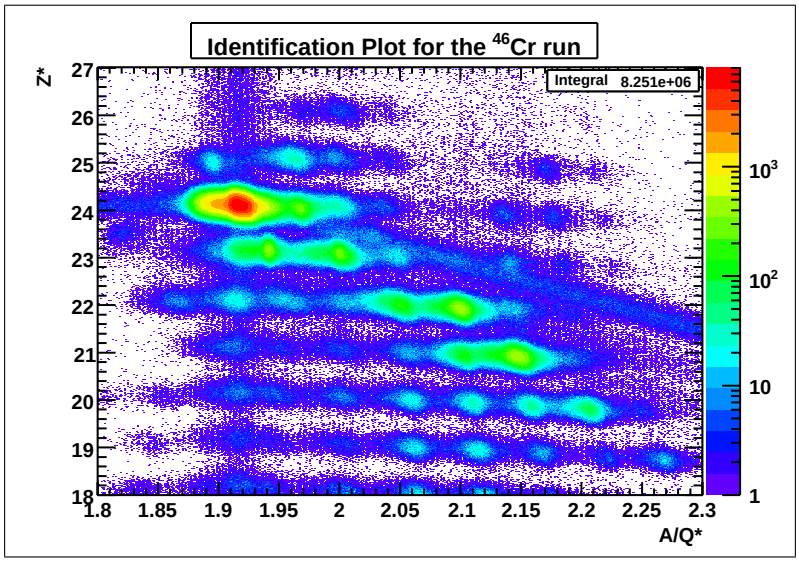

Figure 4.12: Identification plot for the reaction fragments separated and identified up to sci41 in the ^{46}Cr experiment setup. $Z^*$and A/Q^* are the correct Z and A/Q values for the ^{46}Cr; for the other identified nuclei small differences may exist.

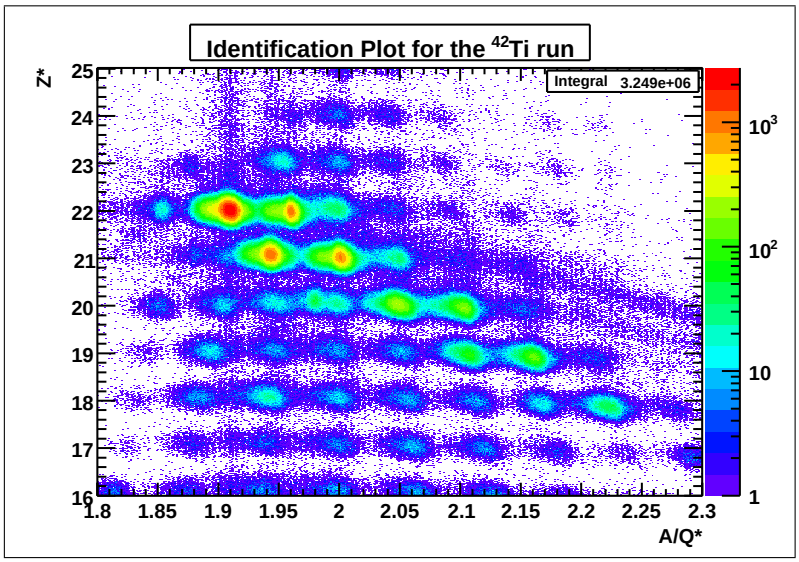

Figure 4.13: Identification plot for the reaction fragments separated and identified up to sci41 in the ^{42}Ti experiment setup. $Z^*$and A/Q^* are the correct Z and A/Q values for the ^{42}Ti; for the other identified nuclei small differences may exist.

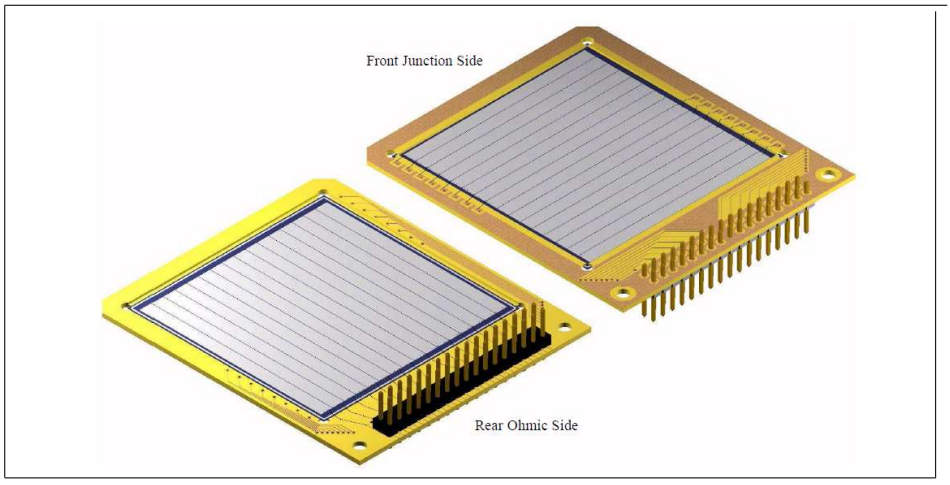

Figure 4.14: Active Stopper used during the RISING Stopped Beam campaign: Micron Semiconductor Ltd. Double Sided Silicon Strip Detector (DSSSD), 16 front and 16 back strips with a 1×50×3.125 mm^3 active volume each.

For the active stopper experiments such as the one presented here, which was the second and final set of experiments for the Stopped Beam campaign, the aim was not just to measure the properties of isomeric-states. In this experiment in particular, the

main interest was to measure the implantation position and its subsequent β-decay. For that purpose six Micron Semiconductor Ltd. [ltd]. model W1(DS)-1000 DC coupled double-sided silicon strip detectors (DSSSD) 1 mm thick were used. Each detector consisted of 16 front strips and 16 back strips, each of width 3.125 mm. As each strip is bonded to a pin of the connector, it is possible to obtain an individual signal per each strip(see Fig. 4.14 -p.52-). Back strips and front strips are orthogonal to each other, so it is possible to construct a 256 pixel grid per DSSSD comparing front and back side signals by software. This pixellation of the active stopper, allows a better determination of the position of the implanted ion.

The Electronics

The *Mesytec* MPR-32 preamplifier [mGcKa] is a 32-channel input logarithmic preamplifier which was used for the 16 front and 16 back strips of a single DSSSD. The logarithmic preamplifier provides a linear range of 2.5 or 10 MeV, which covers 70% of the total range of amplification. The last 30% of the range covers the energy range from 10 MeV to 3 GeV in a logarithmic amplification to avoid the saturation of the implantation signal in the ADC after amplification [mGcKa, Kum09].

The MPR-32 was combined with two *Mesytec* STM-16 shaping-/ timing filter amplifiers with discriminators [mGcKb]. The STM was controlled by an MRC-1 control unit which works as a bus master and it was prepared for the remote control of (i) individual discriminator thresholds (0-40% of the maximum range of 4V) and (ii) gains of coupled pairs of signals. The communication with the control PC is done via RS-232 serial interface. Each analogue output signal from the STM-16 was fed to a CAEN V785 VME-ADC module [S.p].

The active stoppers were placed at the S4 FRS focal plane (see Fig. 4.15 and Fig. 4.16(a) -pp.54 and 54-) inside a vessel made out of Pertinax (phenolic-formaldehyde cellulose-paper PF CP 2061) with entrance and exit windows of black Pocalon C foil of thickness 20 μm (see Fig. 4.16(b) -p.54-). The pertinax wall was 2mm thick, corresponding to an aluminium equivalent for γ-transmission of 0.7 mm.
The active stopper detectors were in a dry nitrogen environment, at atmospheric pressure, in a particular configuration: (i) First row: 3 DSSSDs named L1 (Left first row), M1 (Middle first row) and R1 (Right first row) looking at the beam direction. (ii) Second row: 2 DSSSDs named M2, R2 and (iii) Third row: 1 DSSSD named L2 but in position "M3" [4] (see Fig. 4.15 -p.54-). This configuration was decided on according to the LISE simulation results for this particular setup where it was calculated that the majority of the ions are be stopped in the second row M2 detector, and the maximum spread of the selected ions is approximately 5 cm (the area of a DSSSD detector is 5×5 cm^2).

[4]During the RISING Stopped Beam campaign in July 2007 three experiments were performed. The active stopper configuration for the first experiment was two rows of three DSSSDs each. For the second and third experiment the detectors were re-organised as shown in Fig. 4.15 -p.54- but the look-up-tables and the names in the on-line analysis program were not changed. This is the reason why the DSSSD in position M3 is called L2.

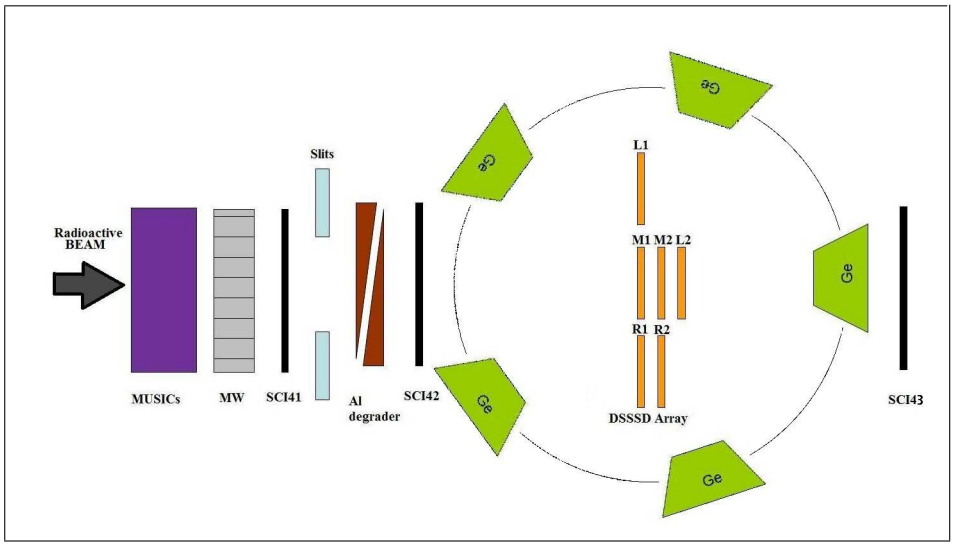

Figure 4.15: Schematic figure of the end of the FRS separator after the fourth dipole magnet.

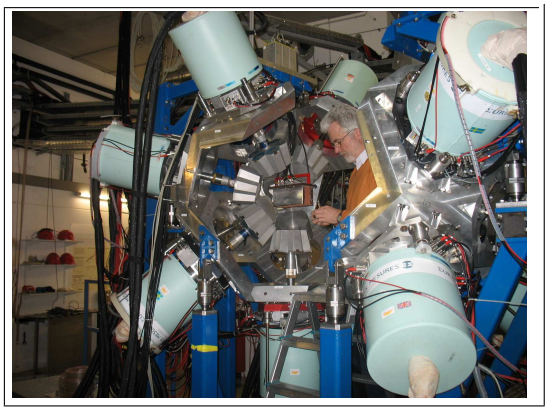

(a) Preparation of the active stopper DSSSD and RISING before the experiment.

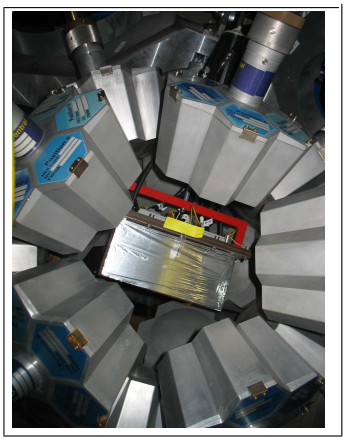

(b) Active Stopper vessel: Pertinax box

Figure 4.16: The RISING Germanium Array and the DSSSD Silicon active stopper.

4.1.5 RISING Ge Array

The RISING stopped beam set-up consisted of 15 Euroball Cluster detectors [Ebe92] in a 4π geometry, divided in three rings of 5 clusters each, at 51^o, 90^o and 129^o with

respect to the beam axis. The distance from the front face of the Ge detectors to the middle position of the M2 active stopper is ∼23 cm. Each cluster consists of 7 hexagonal germanium crystals[Wil96]. Normally the measured γ-ray photo-peak efficiency for the array in this geometry for sources situated in the centre of the focal plane was approximately 15% at 661 keV. In this experiment an exhaustive measurement of the γ-ray efficiency was performed including comparison with Monte Carlo simulations. A full discussion of the efficiency measurements and simulations can be found in Section 4.3.3 -p.67-.

In order to process the time and energy information from RISING, two different sets of electronics were used. Each Ge-crystal had two parallel pre-amplifier outputs [5]. One was sent to a digital branch, consisting of 30 Digital Gamma Finders (DGF-4C) from XIA electronics [LLC]. Each of the 4 channels of a DGF trigger is first validated by a GFLT (General First Level Trigger) provided by either, the sci41 plastic scintillator (implantations) or an OR signal of the DSSSD (β-events). The master trigger, implantation or decay signal, is sent to the DGFs in order to synchronise the DGF clocks. Furthermore, the time differences between an implantation and a γ-event or a β-event and a γ-event were given by the DGF γ-time signal. Thus it is possible to correlate an implanted nucleus in an isomeric state with the subsequent γ-rays or a β-decay with the characteristic γ-rays. The DGF-4C module has a time resolution of 25 ns and a maximum coincidence window of 400 μs. The implant-γ or β-γ correlation gate is adjusted off-line. A typical value for the β-delayed γ-ray coincidence window is in the range of few hundreds of ns.

4.2 Experiment: General Description

Large facilities such as GSI operate with several working groups which interact with each other during an experiment. The accelerator group provides the primary beam in optimal conditions to the different experimental areas, but their work ends there. The selection, alignment and calibration of the beam in order to bring the selected ion to the implantation DSSSD detector in the S4 area is the responsibility of the FRS group and the RISING group. In this section a general description of the experiment and the calibration work carried out by the FRS and RISING groups, is presented.

4.2.1 Experiment Description

The reaction fragments were separated and identified in-flight, ion-by-ion, at the FRS as explained in Section 4.1.2 -p.43-.

[5] One of the output from the Ge-crystal preamplifier is sent to an analogue timing branch, consisting of an electronic circuit TFA-CFD- 2 TDC. The first TDC module is called the *short range* TDC, providing a coincidence gate up to 1 μs with a time resolution of 0.31 ns. This short range is used for short-lived isomeric lifetime measurements. The second module is called the *long range* TDC and had a maximum coincidence window of 800 μs with a time resolution of 0.73 ns. This long range is used for long-lived isomeric lifetime measurements. Both trigger (implantation and decay trigger) are delayed 10 μs and sent to the TDCs to avoid unnecessary data being processed in the acquisition.

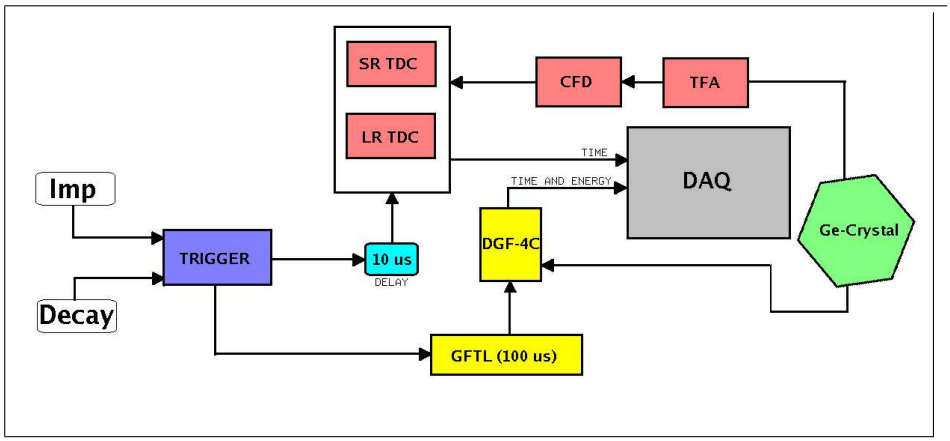

Figure 4.17: Scheme of RISING electronics.

The time-of-flight was measured using two plastic scintillators sci21 and sci41, and the energy loss was measured with two MUSIC ionisation chambers. Multiwire detectors were used for angular correction of the ion trajectory. See Fig. 4.1 -p.41- and for details Section 4.1.3 -p.46-.
The separated ions were implanted in one of six Double Sided Silicon Strip Detectors (DSSSD) of the array (each detector consisted of 16 x and 16 y strips and $50 \times 50 \times 1$ mm^3 volume). The separator was operated in achromatic mode; the implanted ions are spatially separated in the focal plane. As a consequence, several types of ion beside the nucleus of interest survived the several filters and were implanted in the implantation detector. The ions implanted could be separated in A and Z off-line using the time-of-flight, the $B\rho$ of the magnets and the energy loss signal. This separation can be clearly appreciated in Figs. 4.10-4.13 -pp.50 to 52-.
The β-decay signals were detected in the DSSSD detectors as well. As explained before, a logarithmic amplifier was used in order to amplify the energy signals produced by the β-particles and the energy signals produced by the implants. The correlation analysis was done by demanding that the β-signal occurred in the same pixel as the implant. Surrounding the implantation setup was the RISING array for γ-ray detection. The aluminium energy degrader was adjusted so that most of the desired ions were implanted in the central DSSSD detector M2.

4.3 Data Description and Calibrations

4.3.1 DAQ, Trigger and Structure of the data

The VME Data AcQuisition (DAQ) at RISING is based on a single branch within the GSI Multi-Branch System (MBS) framework. The different processes are shared between two processors in order to improve the data recording time. The data sender is an RIO-3 processor included in the VME crate. The RIO-3 is responsible for the read out ADCs, TDCs and other digitisers and eventually sends the data by means of

TCP/IP to a data receiver (a PC), which formats the events and controls the storage on disk.
In the present experiment, the FRS CAMAC crate and the USER VME crate were included the DAQ. They were triggered by a GSI trigger module, which controlled the timing cycle of the hardware readout.
Two different triggers were defined, (1) an *implantation trigger* constructed with a signal of **sci41** , and (2) a *decay trigger* constructed with the **OR signal from all six DSSSD strips**. The data were written on disk according to the trigger signal from the trigger box as described in Table 4.3 -p.57-.

Information written in disk	Imp. trigger	Decay trigger
FRS detectors	√	X
All DSSSD Strips	√	√
RISING crystals	√	√
Scaler	√	√

Table 4.3: Trigger of the data acquisition system and the detector signals recorded. The implantation trigger was an AND signal of sci41 and an OR DSSSD strips, and the decay trigger was an OR signal of the DSSSD strips.

The on-line visualisation of the data was performed with the CRACOW graphics user interface program [Gre07]. It consists of two separate programs: the event analyser (SPY) and the on-line spectra viewer (CRACOW). Conditions created in CRACOW are applied to the sorted data by SPY, creating in an easy way the on-line spectra.

Analysis Program

The raw data were sorted off-line firstly using CRACOW, where it is possible to introduce calibration coefficients to obtain calibrated parameters. These calibrated parameters (energy, position, time, etc.) are recorded event-by-event in a ROOT tree [roo]. A specific C++ program was created for the data analysis of the present experiment, where it is possible to create conditions, correlations between the different calibrated branches of the ROOT tree, and obtain histograms.
The data sorting, analysis and simulations were done using eight 2.5 Ghz processors Intel(R) Xeon(R), 8 Gb ram, 64bit Scientific Linux server.

4.3.2 Beta Calibrations

One of the main goals of the present analysis is to obtain a precise value for the β-decay half-lives. Using a DSSSD detector it was possible to distinguish an implantation-event and a decay-event by means of the trigger information (implantation or decay trigger), furthermore it is possible to select a proper energy range where the beta or implantation signal was expected (See Fig. 4.18 -p.58- and Fig. 4.19 -p.58-). Actually, an energy calibration was performed only for β-events using a ^{207}Bi source in the linear range of the logarithmic pre-amplifier. For an implantation-event it was not possible to make a proper energy calibration at such energies ($\sim$GeV) so we aligned the 16 Y- and X-strips per DSSSD using a pulser signal as input to the preamplifier.

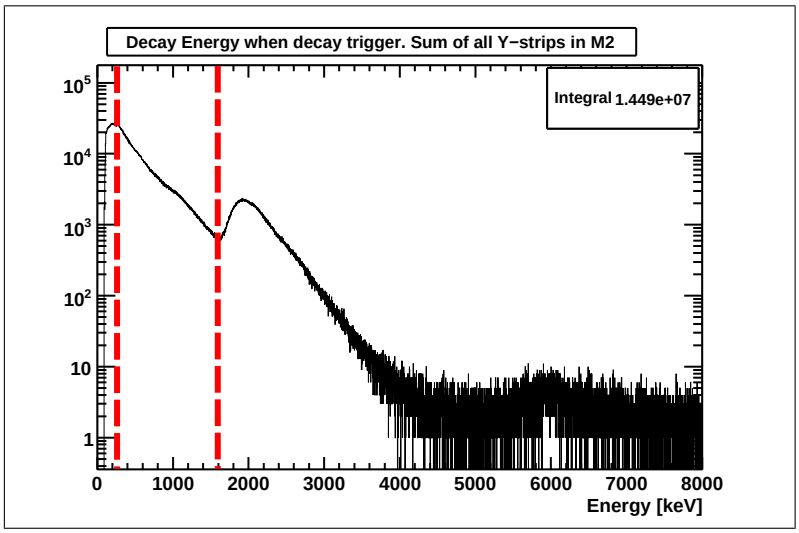

Figure 4.18: Sum of all M2 DSSSD Y-Strips calibrated in energy for the decay events. The red lines show the selected decay energy range in the present analysis: (264,1590 keV).

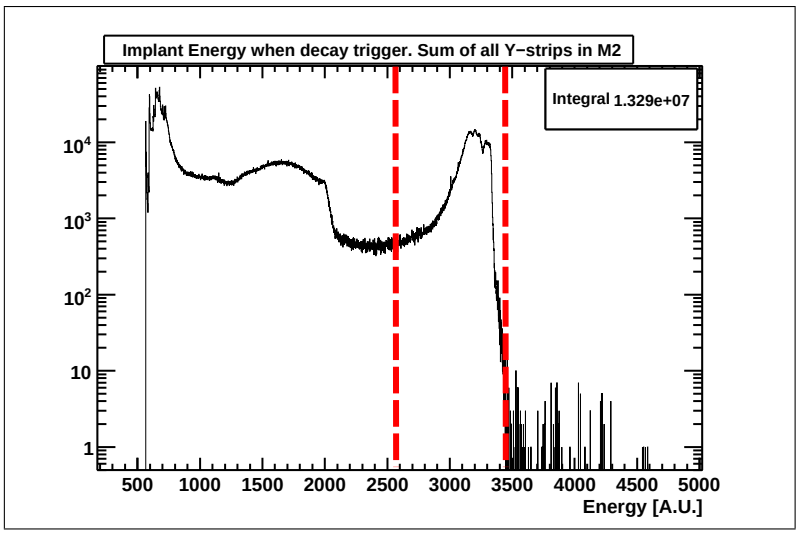

Figure 4.19: Sum of all M2 DSSSD Y-Strips aligned for implantation events. The red lines show the selected implantation range in the present analysis: (2560,3442 A.U).

As an implantation event can deposit a huge amount of energy in the active stopper it is possible that more than one strip fires per event. This makes the position identification in a DSSSD of an implantation-event difficult. On the other hand, β par-

ticles can penetrate more than one pixel. Consequently a *maximum energy criterion* was established, for both the implantation-event and the decay-event: The strip with the maximum energy is the strip to which that event belongs. In this way we should obtain an unique combination of X and Y strips per event in the DSSSD. This software procedure was called pixellisation of the DSSSD. Moreover, each event registered by the acquisition had a unique time stamp given by the TITRIS-VME [JH06] module with an accuracy of 20 ns.
In summary, each event in a DSSSD single strip is identified by the type of trigger and by the energy deposited in the DSSSD. Then this event could be identified in one of the 256 pixels by the *maximum energy criterion*. Finally a time stamp given by the TETRIS-VME module is assigned to each event-pixel registered.

Now we can identify the implanted ions in a DSSSD including the implantation condition in the DSSSD energy range using the identification plot already shown in Figs. 4.10- 4.13 -pp.50 to 52- they are shown in Figs. 4.20 - 4.23 -pp.60 to 61-. In these new identification plots it is possible to see exactly which ion is implanted and the ratio between the selected ion (shown in Figs. 4.20- 4.23 -pp.60 to 61-) in comparison with the all implanted ions. From Table 4.4 -p.59- we see that in all the cases studied in this work, the selected ion is the predominant implanted ion in the M2 detector.

Frag.	Frag. in the window vs Rest of ions	Total rate of imp. in M2
^{54}Ni	60.4%	50.4 ions/sec
^{50}Fe	90.3%	33.8 ions/sec
^{46}Cr	57.9%	45.3 ions/sec
^{42}Ti	57.8%	20.7 ions/sec

Table 4.4: Ratio of the selected fragment, in the window, implanted in M2 shown in Figs. 4.20-4.23 -pp.60 to 61-, and total including the rest of the ions implanted in M2. The rates of implantation of all the fragments implanted in M2 are also shown.

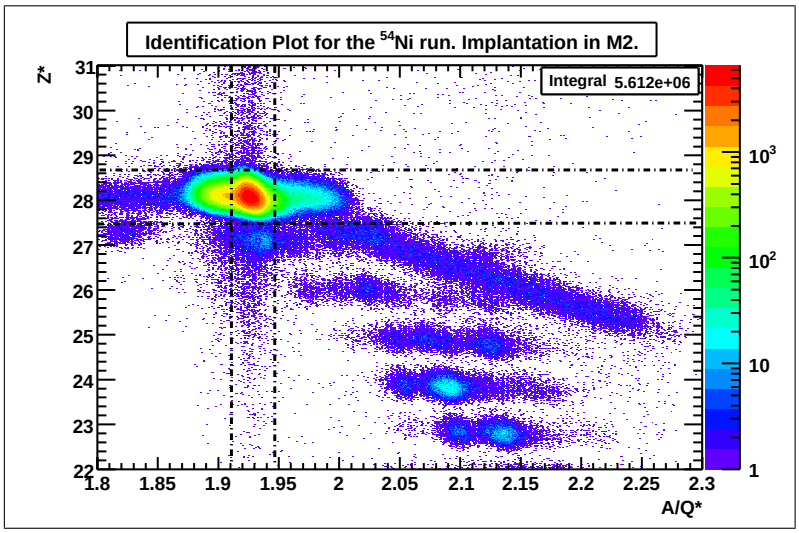

Figure 4.20: Identification plot of the reaction fragments separated and identified including the implantation condition in M2, during the ^{54}Ni experimental run. The window used to select the ^{54}Ni implants is shown. The total number of ^{54}Ni ions implanted in M2 and selected in the window was 3,853,587 ions. $Z^*$and A/Q^* are the correct Z and A/Q values for the ^{54}Ni; for the other identified nuclei small differences may exist.

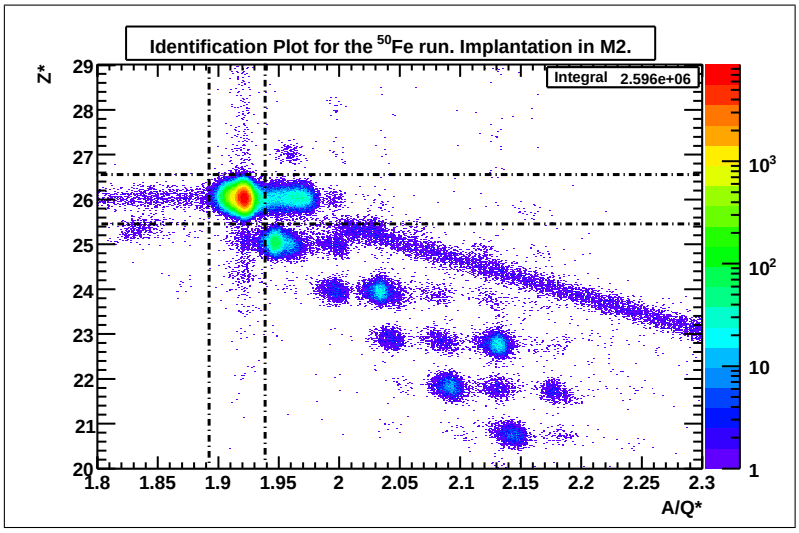

Figure 4.21: Identification plot for the reaction fragments separated and identified including the implantation condition in M2, during the ^{50}Fe experimental run. The window used to select the ^{50}Fe implants is shown. The total number of ^{50}Fe ions implanted in M2 and selected in the window was 2,526,305 ions. $Z^*$and A/Q^* are the correct Z and A/Q values for the ^{50}Fe; for the other identified nuclei small differences may exist.

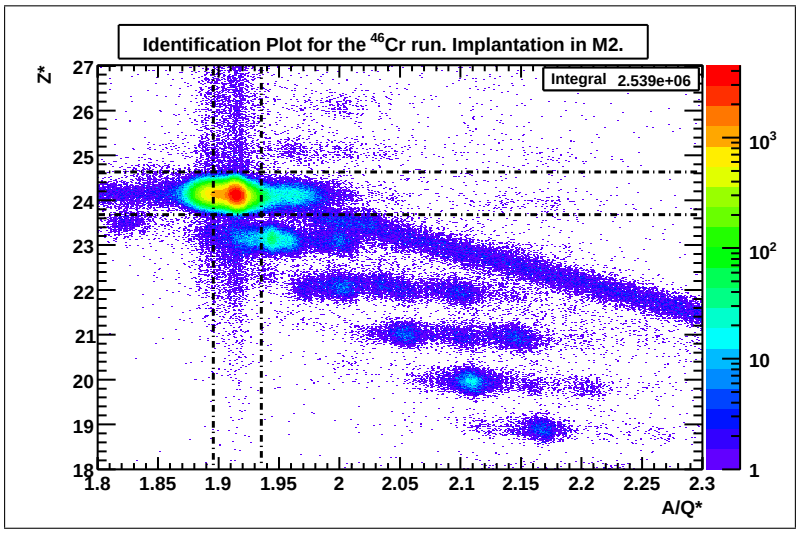

Figure 4.22: Identification plot for the reaction fragments separated and identified including the implantation condition in M2, during the ^{46}Cr experimental run. The window used to select the ^{46}Cr implants is shown. The total number of ^{46}Cr ions implanted in M2 and selected in the window was 1,793,477 ions. $Z^*$and A/Q^* are the correct Z and A/Q values for the ^{46}Cr; for the other identified nuclei small differences may exist.

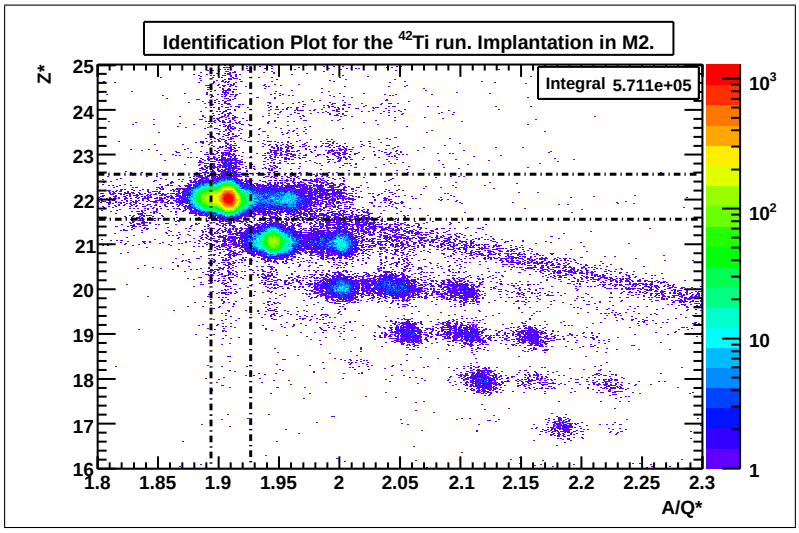

Figure 4.23: Identification plot for the reaction fragments separated and identified including the implantation condition in M2, during the ^{42}Ti experimental run. The window used to select the ^{42}Ti implants is shown. The total number of ^{42}Ti ions implanted in M2 and selected in the window was 373,231 ions. $Z^*$and A/Q^* are the correct Z and A/Q values for the ^{42}Ti; for the other identified nuclei small differences may exist.

In addition to the new identification plots gated with the implantation detectors we can look at the spatial location of the selected ion in the M1, M2 (focal plane) and L2 DSSSD detectors. For that purpose we gate on the selected ion on the identification plot and look at the DSSSD strips requiring a *clean implantation* in each detector, which means (see Fig. 4.15 -p.54-) (i) for detector M1: Implantation in detector M1 but not in M2 or L2 (ii) for detector M2: implantation in detector M2 but not in detector L2 only, and (iii) for detector L2: implantation in detector L2.

Fig. 4.24 -p.63- shows the implantation spacial distribution of ^{54}Ni in the detectors M1, M2 and L2. We can see that most of the ions, 74.6%, are implanted in the detector M2. 14.1% of the ions are stopped in the first detector M1, and the rest are stopped in L2.

Fig. 4.25 -p.64- shows the implantation distribution for ^{50}Fe in the detectors M1, M2 and L2. Most of the ions, 81.6%, are implanted in the detector M2. 5.3% of the ions are stopped in the first detector M1, and the remaining 13.1% are stopped in the last detector L2.

The case of ^{46}Cr is slightly different. Fig. 4.26 -p.65- shows that 49.9% of the ions identified as ^{46}Cr are implanted in the detector M2. 35.9% of the ions are stopped in the first detector M1, and the remaining 14.2% are implanted in detector L2.

For ^{42}Ti the situation is similar to the ^{46}Cr case. In Fig. 4.27 -p.66- we can see that 54.3% of the ions identified as ^{42}Ti are implanted in the detector M2. 28.8% are stopped at the first detector M1, and 16.9% of the ions are implanted in the last detector L2.

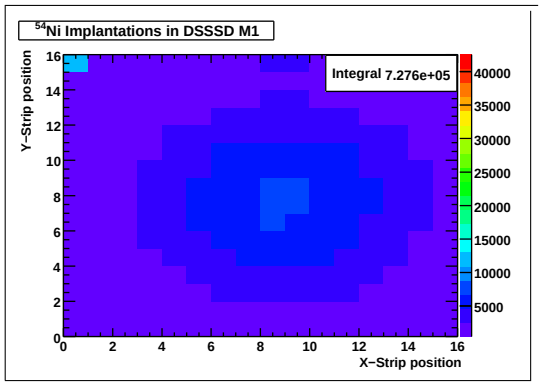

(a) Clean implantation of ^{54}Ni in detector M1

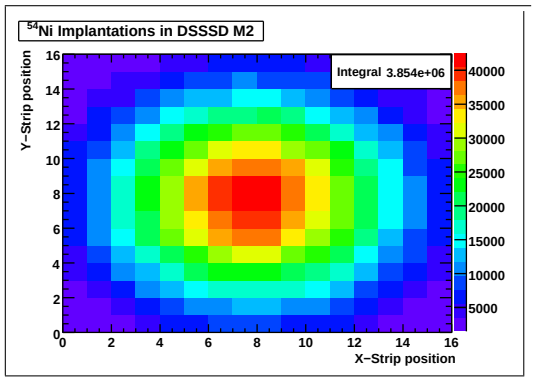

(b) Clean implantation of ^{54}Ni in detector M2

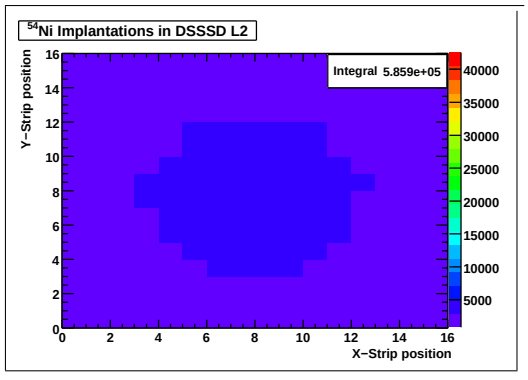

(c) Clean implantation of ^{54}Ni in detector L2

Figure 4.24: Implantations of ^{54}Ni ions in the DSSSDs (see text).

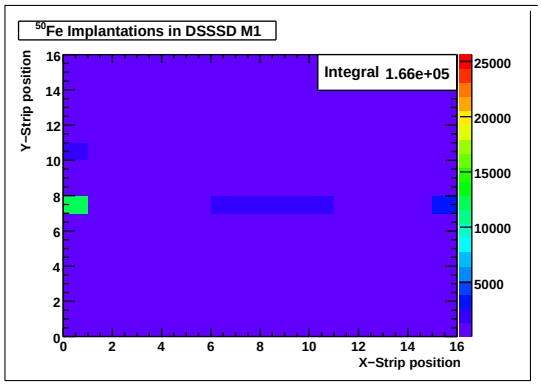

(a) Clean implantation of ^{50}Fe in detector M1

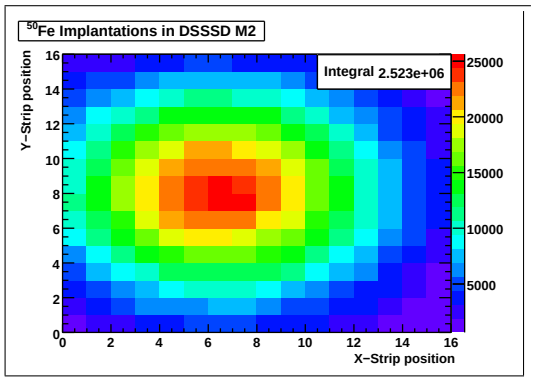

(b) Clean implantation of ^{50}Fe in detector M2

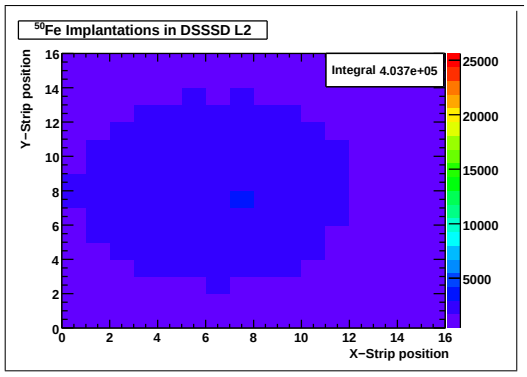

(c) Clean implantation of ^{50}Fe in detector L2

Figure 4.25: Implantations of ^{50}Fe ions in the DSSSDs (see text)

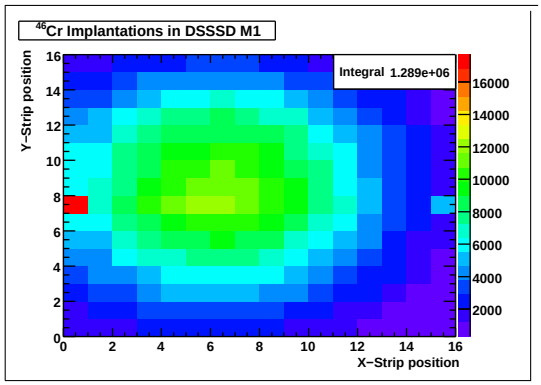

(a) Clean implantation of ^{46}Cr in detector M1

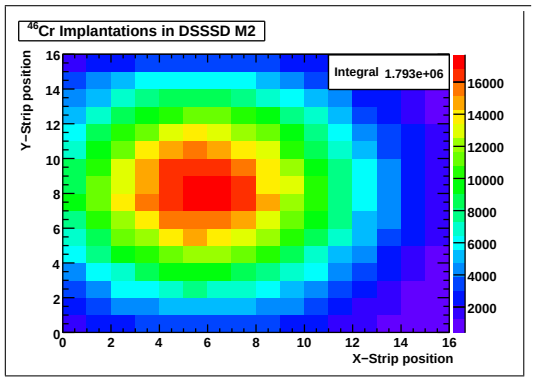

(b) Clean implantation of ^{46}Cr in detector M2

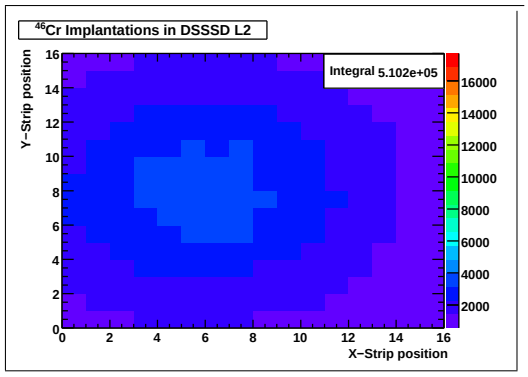

(c) Clean implantation of ^{46}Cr in detector L2

Figure 4.26: Implantations of ^{46}Cr ions in the DSSSDs (see text)

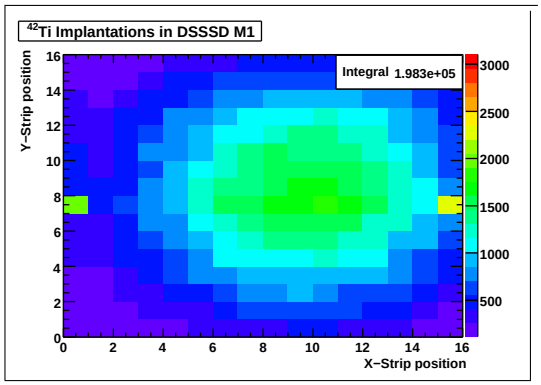

(a) Clean implantation of ^{42}Ti in detector M1

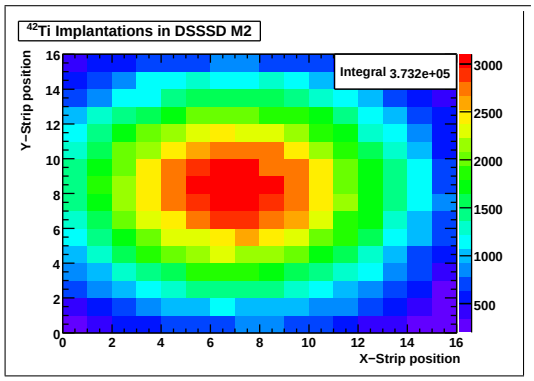

(b) Clean implantation of ^{42}Ti in detector M2

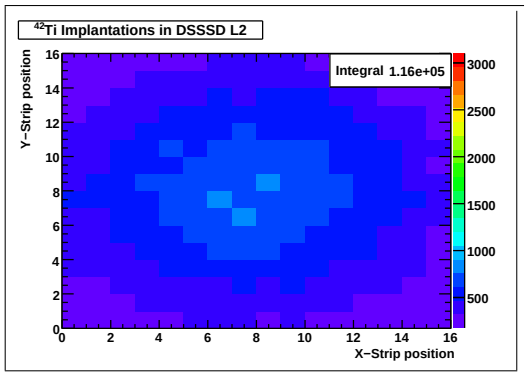

(c) Clean implantation of ^{42}Ti in detector L2

Figure 4.27: Implantations of ^{42}Ti ions in the DSSSDs (see text)

4.3.3 Gamma Calibrations

γ-energy calibrations

Before the experiment began, the RISING array was calibrated using a ^{152}Eu standard source. We also performed periodic control measurements during the experiment using ^{152}Eu as well as ^{133}Ba sources. After the experiment we measured with ^{226}Ra, ^{60}Co and ^{137}Cs. With all the γ-energies from these sources we made an off-line calibration of each of the 105 crystals. In some cases we introduced recalibration coefficients from our own internal sources, ^{54}Ni, ^{50}Fe and other cases where the gamma intensities are known.

RISING Efficiency Calibration

As we mentioned in Section 1.6 -p.9- one of the aims of performing these measurements is to obtain the feeding probability to each state populated in the daughter nuclei. Precise measurements of the efficiency of the germanium array are essential to derive these quantities. The error in the Ge-array efficiency contributes directly to the error in the extracted gamma intensities which will be used to deduce the feeding probability and in turn the Gamow-Teller Strength.
Six standard efficiency sources were measured (^{152}Eu, ^{133}Ba, ^{60}Co,^{137}Cs, ^{56}Co and ^{226}Ra) providing 48 experimental points for efficiency calibration. These measurements were made after the experiment. The M2 detector was removed and replaced by a *dummy* detector with a point-like source in the middle.

The γ efficiency ($\epsilon_\gamma(E_\gamma, t_M)$) is defined as the ratio between the total number of gamma-rays detected ($N\gamma_{det}(E_\gamma, t_M)$) and the total number of gammas emitted ($N\gamma_{emit}(E_\gamma, t_M)$) within the time of measurement (t_M).

$$\epsilon_\gamma(E_\gamma) = \frac{N\gamma_{det}(E_\gamma, t_M)}{N\gamma_{emit}(E_\gamma, t_M)} \tag{4.5}$$

In order to perform a proper efficiency measurement, the data acquisition system was triggered by a 500 Hz pulser which opened two gates: a 400 μs gate for the acquisition itself (t_{ag}) and another gate of 100 μs for the GFLT (General First Level Trigger) of each DGF-4C RISING modules (t_{Re}). Due to the activities of the gamma sources used ($\sim$100 KBq), the probability of having more than one gamma signal in a single crystal, within the t_{Re} is relatively high. But it is possible to reduce the pile-up probability imposing a software gate t_{sg}, during the sorting of the data, in the first 10 μs, or even less depending on the activity of the source. In Eq. 4.5 the $N\gamma_{det}$ was determined fitting a Gaussian shape to each gamma photo-peak. The $N\gamma_{emit}$ is defined as,

$$N\gamma_{emit}(E_\gamma, t_M) = A(t_0) t_M I_\gamma \tag{4.6}$$

where $A(t_0)$ is the activity of the source at the beginning of the measurement, t_M is the time of the measurement and I_γ is the gamma branching. Now the t_M is determined by the software gate, t_{sg} and the total number of gamma events registered, $N\gamma_{ev}$. In this case it is not necessary to introduce a normalisation due to the life-time/dead-time of acquisition, because we have already chosen a t_{sg} in which we can neglect the probability

of having more than one gamma event in the same crystal within the tiny t_{sg} gate. Then the gamma efficiency stays as,

$$\epsilon_\gamma(E_\gamma) = \frac{N\gamma_{det}(E_\gamma)}{A(t_0)t_{sg}N\gamma_{ev}I_\gamma} \tag{4.7}$$

Results

The measured sources were ^{152}Eu, ^{133}Ba, ^{60}Co,^{137}Cs, ^{226}Ra and ^{56}Co. The only source which was not measured just after the experiment was ^{56}Co which was available one year later and measured by the RISING group on July 2008 (12 months after the experiment) in identical conditions. This ^{56}Co is very important for the determination of the efficiency at high energy because it emits a γ-ray line at 3545 keV.
The results for the RISING Ge array used in this thesis were analysed using two different methods: Single Crystal and Add-back mode (see Fig. 4.28 -p.69-). The single crystal mode consists of the addition of the spectra from the 105 individual crystals. The add-back mode is constructed with an event-by-event software routine which allowed the reconstruction of a gamma ray event which deposited its energy in two or more adjacent crystals of the same cluster, within a time window of 100 ns. In the add-back mode the total statistics is given by the sum of the 15 clusters. For further details of the reconstruction algorithm and the add-back code created for the analysis of this experiment, see Appendix C -p.217-.

An efficiency curve was fitted to the experimental points according to the expression given by the work of Z.Hu et al. on the CLUSTER CUBE Ge array [Hu98], which also used the Euroball detectors for decay studies. The efficiency energy dependence was defined as,

$$\epsilon(E_\gamma) = \prod_{k=0}^{5} \exp(p_k \ln^k(E_\gamma)) \tag{4.8}$$

The results of fitting the experimental points with the expression given in Eq. 4.8 -p.68-, are shown in Fig. 4.28 -p.69-. The detailed efficiency values are given in an extensive table in Appendix D -p.223-.
Since the measured points reach only 3.5 MeV, a simulation was used to extrapolate the efficiency curve beyond this value as explained in the subsection entitled *Simulated Efficiency Results*.

Montecarlo Simulation

A Montecarlo simulation was required in order to extrapolate the gamma efficiency energy dependence to higher energies in the interval 3.5 to 6 MeV. The RISING array simulated geometry was obtained from a Geant4 simulation performed by Pavel Detistov [Det07] which was used in the previous Fast Beam RISING campaign. The array geometry had changes but the construction of each cluster and each individual crystal was the same. We used this previous work and adapted the code to the geometry of the Active Stopper Campaign geometry. The six DSSSD detectors were included in the simulation as well as the pertinax box where the DSSSD were placed (see Fig. 4.30

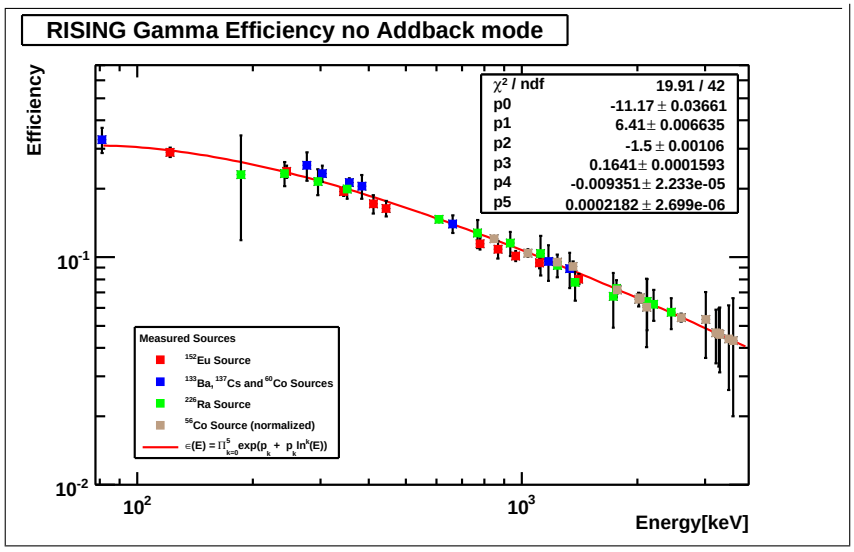

(a) Experimental efficiency measurements using ^{152}Eu, ^{133}Ba, ^{60}Co,^{137}Cs, ^{226}Ra and ^{56}Co gamma sources for the RISING Ge array in single crystal mode.

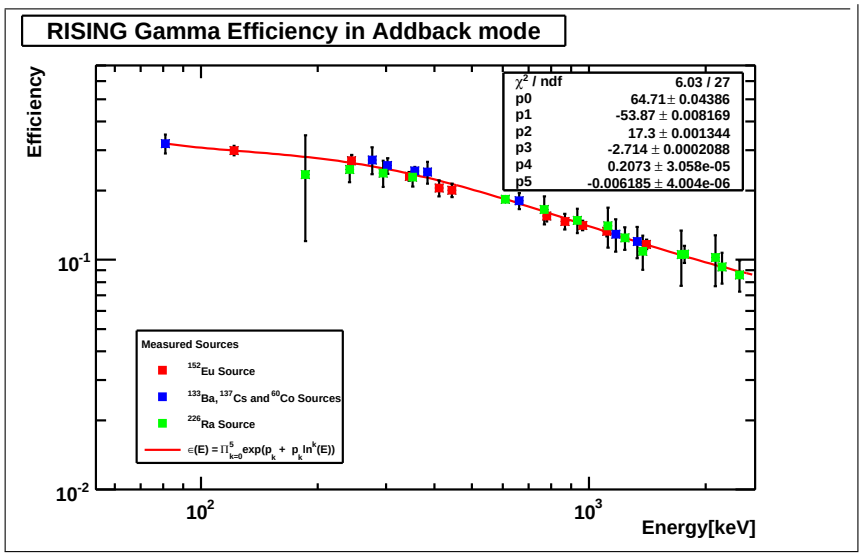

(b) Experimental efficiency measurements using ^{152}Eu, ^{133}Ba, ^{60}Co,^{137}Cs and ^{226}Ra gamma sources for the RISING Ge array in add-back mode.

Figure 4.28: RISING experimental efficiency curve in single crystal and add-back mode.

-p.71-). We simulated 44 spot-like sources of mono-energetic gamma rays originating in the middle of the M2 DSSSD which was at the geometric centre of the Ge array.

We have seen that the real sources were spatially distributed all over the detector during the experiment (i.e. implanted nuclei of interest in the DSSSD) illuminating several pixels. To check the possible influence of an extend source in the γ-efficiency the following comparison was done; a) simulation of an extended source illuminating the complete detector with a Gaussian implantation profile, b) simulation of a point-like source. As it can be seen in Fig. 4.29 -p.70- the difference was not significative.

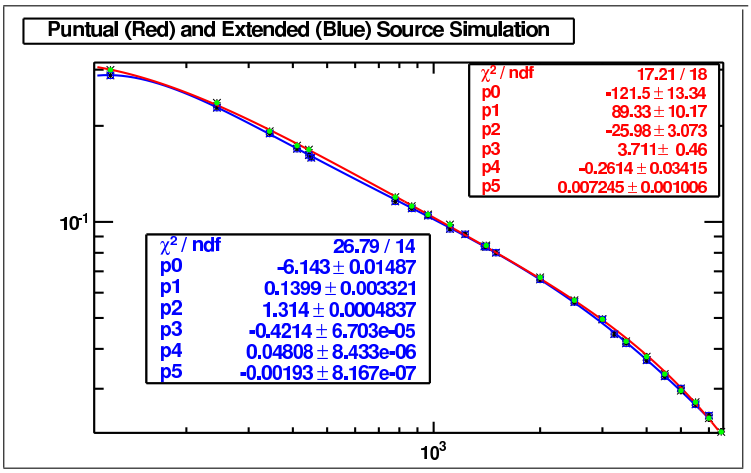

Figure 4.29: Comparison of the simulated efficiency for a point-like source and an extended source (see text).

As the efficiency is geometry dependent, a second important test was performed in order to understand how much small changes in the germanium sphere radius affects the efficiency curve (see Fig. 4.31 -p.72-). We can conclude that changes in the array radius are equivalent to efficiency curve displacements in general without significant changes in the shape of the curve itself. From these results one can estimate that 1 cm displacement in radius is equivalent to 7-8% relative displacement in efficiency. More details can be found in Appendix D -p.223-.

Simulated Efficiency Results

The aim of simulating the RISING geometry is to obtain the efficiency curve for high γ-ray energies. Then, only if the simulation can reliably represent the experimental efficiencies up to 3.5 MeV, can we be confident in the simulation results at higher energies. Fortunately in the experimental region (i.e. energies less than 3.5 MeV) the simulation and the experimental measurements agree (see Fig. 4.32 -p.73-).
As can be seen in Fig. 4.32 -p.73-, the simulation points represented by black squares in the figure agree nicely with the experimental points. This validates the Montecarlo simulations for energies higher than 3.5 MeV, which are included in Fig. 4.32 -p.73-.

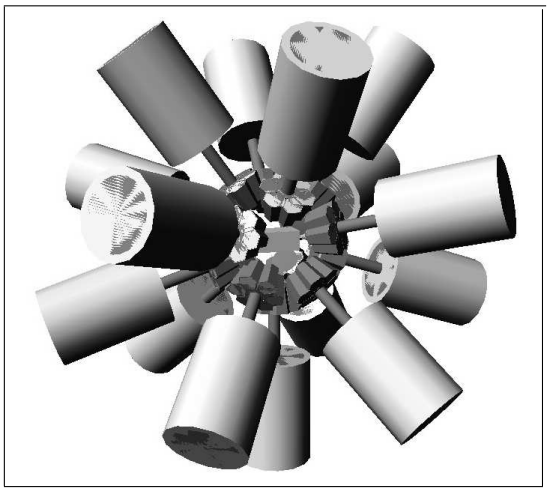

Figure 4.30: Geometry of the RISING Ge array for the Active Stopper Campaign implemented in the Montecarlo simulation. The pertinax box with the 6 DSSSD configuration was included in the simulation.

These two curves have been used in the present analysis. Our efficieny analysis provides the following numbers for the generaly quoted ^{60}Co points; ϵ(1332 keV; add-back)= 0.123 and ϵ(1332 keV; no add-back)= 0.089.

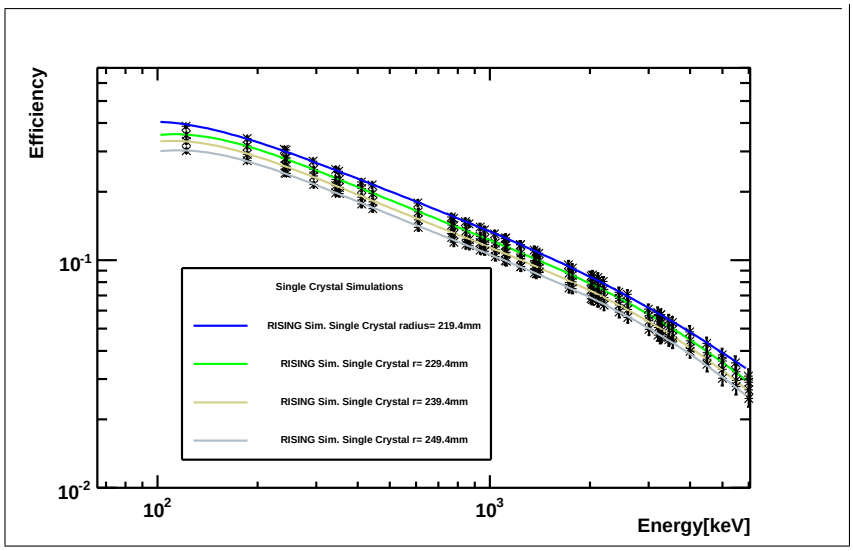

(a) Efficiency results from a Geant 4 simulation in single crystal mode for different geometrical radii of the RISING Ge array.

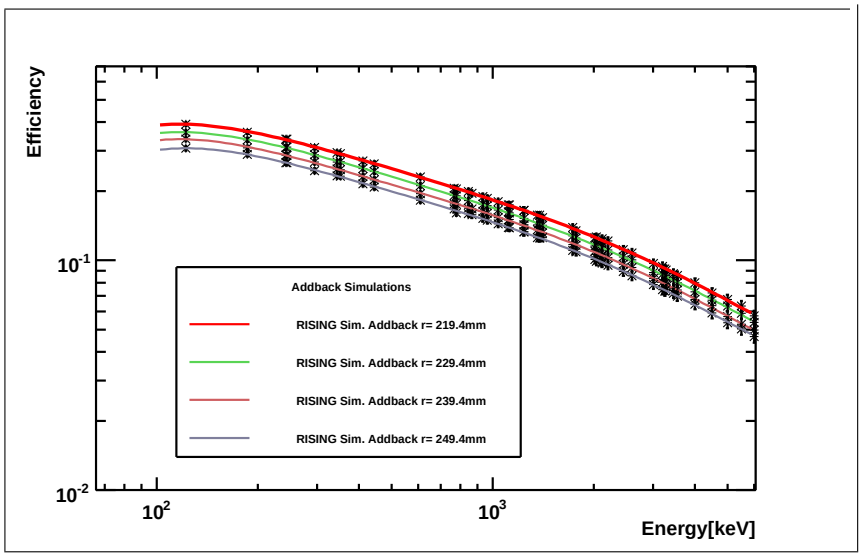

(b) Efficiency results from a Geant4 simulation using addback mode for different geometrical radii of the RISING Ge array.

Figure 4.31: Geant4 simulated efficiency in addback and single crystal modes varying the geometrical radius of the Ge array.

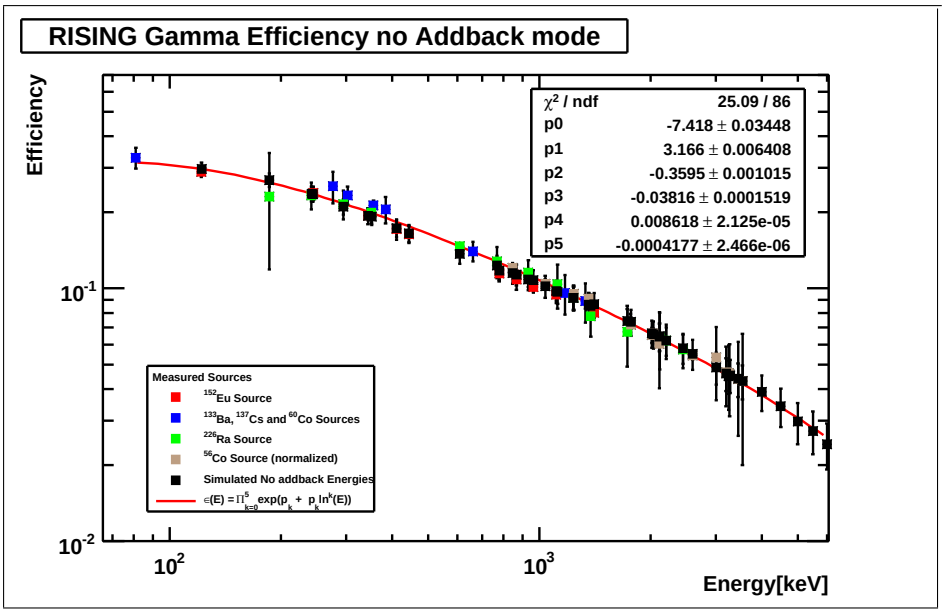

(a) Efficiency curve using the sum of single crystals.ϵ(1332 keV)= 0.089 from the evaluation of the fitted function.

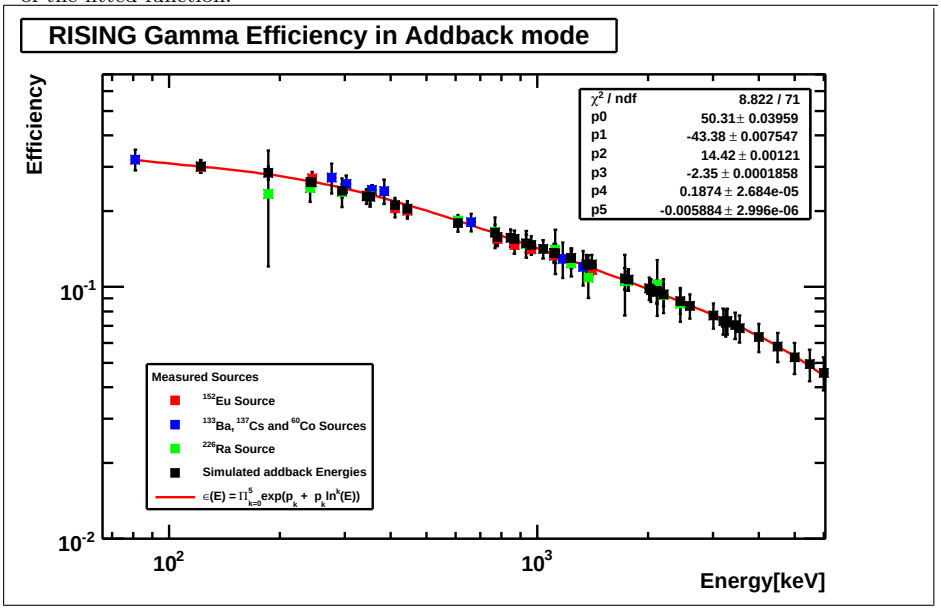

(b) Efficiency curve using the Addback routine. ϵ(1332 keV)= 0.123 from the evaluation of the fitted function.

Figure 4.32: Experimental and simulated γ-efficiencies using addback and single efficiency. The experimental values for: 1) ^{152}Eu source are shown in red squares, 2) ^{133}Ba-^{137}Cs-^{60}Co mixed source are shown in blue squares, 3) ^{226}Ra source are shown in green squares, and 4) ^{56}Co source are shown in brown squares. The simulated points are shown in black squares. The efficiency curve from Eq. 4.8 -p.68- is shown in red. The evaluation of the efficiency curves for Single Crystal and Addback are detailed in Appendix D -p.223-.

CHAPTER 5

RESULTS OF GSI EXPERIMENT ANALYSIS

In this chapter the results of the analysis of our sata on the β-decay of each nucleus is presented.
The chapter is divided into four sections according to the main output expected from the analysis. The first of these four sections is the gamma-ray the analysis. The contaminants are identified and the gamma intensities are obtained.
The second section presents the half-life analysis and how the need for a precise value with a small error lead us to use and improve the "All Betas/All Implants" time correlation method.
In the third section we describe a method for obtaining the ground state feeding, based on time correlations between a β-delayed γ-event and an implantation, where a clean gamma spectrum of the implanted nuclei is obtained as well as the β-decay half-life from the β-delayed γ decays of the first excited state for the four nuclei under study.
In the fourth section the β branching ratios and the ground state feeding extracted from our experimental results are presented.

5.1 Gamma Analysis

The RISING Ge array electronics was triggered either by a β-event or an implantation-event. When a β-event triggers the acquisition, a coincidence gate of 100 μs is opened in all DGF-4C modules and a γ-event detected by any crystal in this interval is registered (see Section 4.1.5 -p.54- for details). Of course all background γ-ray lines, for example ^{40}K, and long-lived decays from previously implanted nuclei can also be registered in that coincidence gate. In order to reduce the unwanted γ-lines, a shorter gate of 250 ns was set in the off-line analysis (see Fig. 5.1 -p.76-).

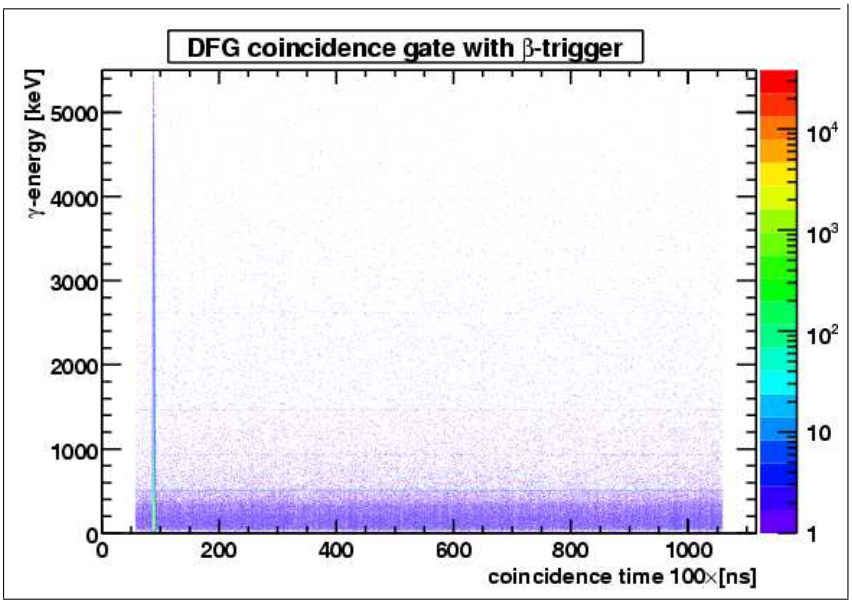

Figure 5.1: ^{54}Ni β-delayed γ-events in the coincidence gate of 100 μs. In the analysis software the β-γ coincidence gate of 250 ns was set in the 86.5-89.0 [100ns] time interval.

The γ-spectra for the four settings were obtained in coincidence with any decay event in the M2 detector. As a consequence the γ lines presented in these spectra correspond to all those fragments produced in the run which gave a decay-trigger in detector M2. This decay-trigger could be a *beta* or proton signal from the decay of the fragment. Unfortunately we were not able to distinguish between these two types of radiation.

5.1.1 ^{54}Ni run, γ-analysis

In the analysis of mass 54 with the clean condition of a decay trigger in M2, we have observed the gamma lines shown in Table 5.1 -p.80- (single crystal mode) and Table 5.2 -p.81- (addback mode). The addback spectrum is shown in Figs 5.2-5.7 -pp.78-79-.

The analysis has two aims namely (i) We need the γ-energies and intensities in the decay of ^{54}Ni in order to extract the $B(GT)$ values for the different states populated in ^{54}Co and (ii) it can be used for the identification of possible contaminants.

Amongst the observed gammas, 936.7 keV, 2424.6 keV, 3376.1 keV, 3889.6 keV, and 4543.8 keV (♣) belong to ^{54}Ni β-decay. This identification is based on (i) the literature: I.Reusen et al [Reu99b] have already observed the 936.7 keV gamma-line and (ii) agreement in energy with the results obtained from the ^{54}Co(^{3}He,t)^{54}Ni CE reaction [Ada07c] (see Tables in Appendix B -p.213-).
In the following we will first discuss the possible contaminants in the ^{54}Ni γ-spectrum:

- ⊕ The 782.7 keV , 1097.8 keV and 1442.3 keV gammas probably come from the β-decay of the 1.75 minute isomeric state in ^{50}Mn [Ram72]. This half-life is considerably longer than the ^{54}Ni β-decay half-life.

ℵ The 849.0 keV and 1535.1 keV gamma rays correspond to the 2+ → 0+ and 4+ → 2+ transitions in ^{52}Fe respectively. They are probably not produced in the ^{52}Co (115(23) ms) β-decay due to the absence of the 1941 keV gamma ray reported by [Hag97] where the possible existence of another isomer is also discussed. Another possibility is the proton decay of ^{53m}Co (247 ms) [Hon89].

∇ The 1327.5 keV gamma line probably originates from the ^{54}Ni (152 ns) proton decaying isomer into ^{53}Co (240 ms) [Rud08b] which β-decays, populating the 1328 keV state in ^{52}Fe which, instantaneously, gamma decays to the ground state emitting a 1328 keV γ-ray.

□ The 1433.8 keV gamma line probably belongs to the ^{52}Cr $2^+ \rightarrow 4^+$ transition. This could be produced through ^{52}Mn^m (2^+ isomer, 21.1 m) β^+ decay or through the ^{52}V β-decay (3+ to g.s., 3.75 m) [Yaf77]. In the first case a gamma of 377.7 keV energy exists, it is the E4 $2^+ \rightarrow 6^+$ transition. A gamma-ray of similar energy appears in our spectra (377.0 keV), however the intensity of this gamma line is too large (62% of the 1433.8 keV gamma intensity instead of ∼2% as the literature would suggest). Moreover this transition would in principle not be in our data because it would give no trigger.
Another possible explanation for the presence of the 377.0 keV gamma line in our spectrum is the ^{53}Fe β-decay (8.51 m) [Bla75] which populates the 377.9 keV state in ^{53}Mn (3.7×10^6 y) 41% of the time, being practically the only gamma-ray produced. But the energy differs by 0.9 keV from our result, which is a bit too large.
Finally in ^{54}Co a 3^+ level exists at 1821 keV which gamma decays to the 1445.7 keV 2^+ state emitting a 375.8 keV gamma ray, but this energy is again 1 keV different from ours. In summary we do not have a convincing explanation of the origin for the 377.0 keV gamma line.

♣ The 4323.0 keV gamma line has the same intensity in addback and in single crystal mode, it is not present in other runs and does not belong to any known contaminant. In the C.E. reaction a peak at 4301 keV is detected. The same situation appears regarding the 4822.8 keV (4828.0 keV in the C.E. reaction) and 5202.4 keV (5225.0 keV). We therefore conclude that they probably belong to the ^{54}Ni β-decay and that the C.E. reaction calibration deviates from the real values at high energy.

It is very important to note that this is the first time that it has been possible to see more than one excited state in ^{54}Co in a β-decay experiment. This was possible due to the overwhelming production of the parent nucleus by the fragmentation reaction at GSI, the good transmission of the separator and the excellent efficiency of the Ge array. The level scheme using the γ-spectrometry results from this experiment is shown in Fig. 6.1 -p.134-.

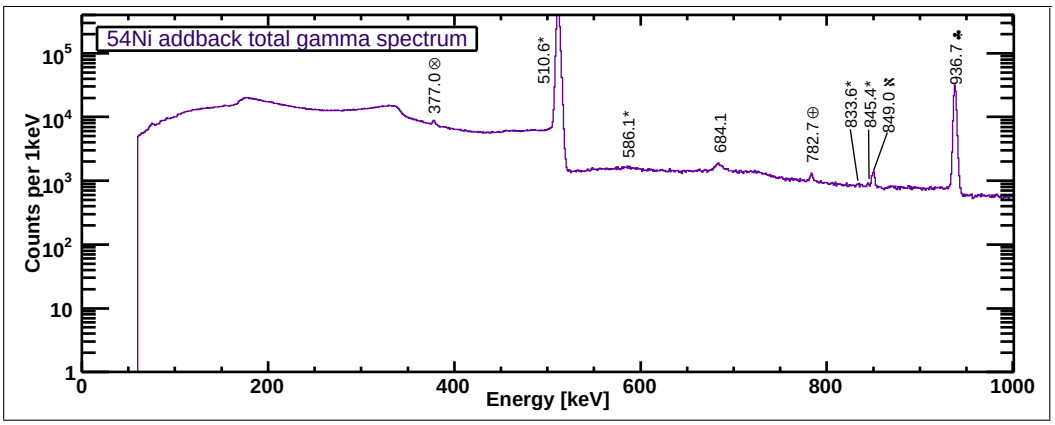

Figure 5.2: ^{54}Ni addback β-delayed γ-spectrum Part 1. Energy range: 0-1000 keV.

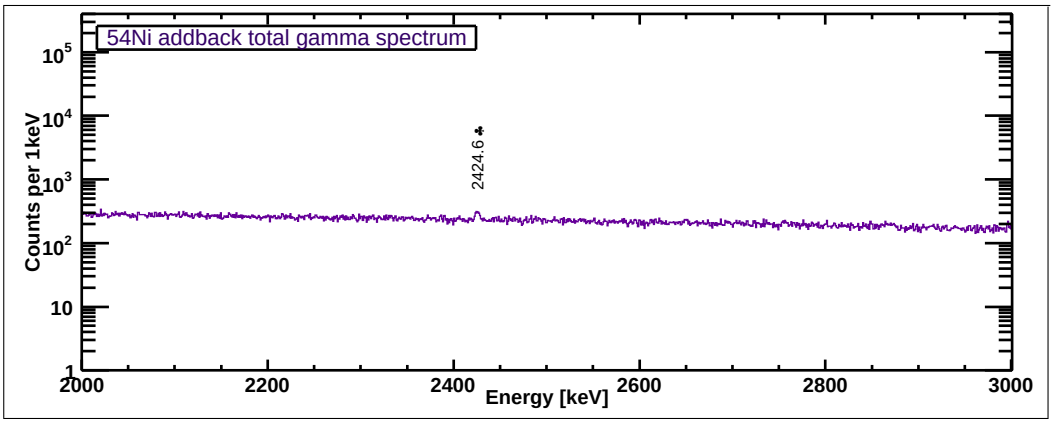

Figure 5.3: ^{54}Ni addback β-delayed γ-spectrum Part 3. Energy range: 2000-3000 keV.

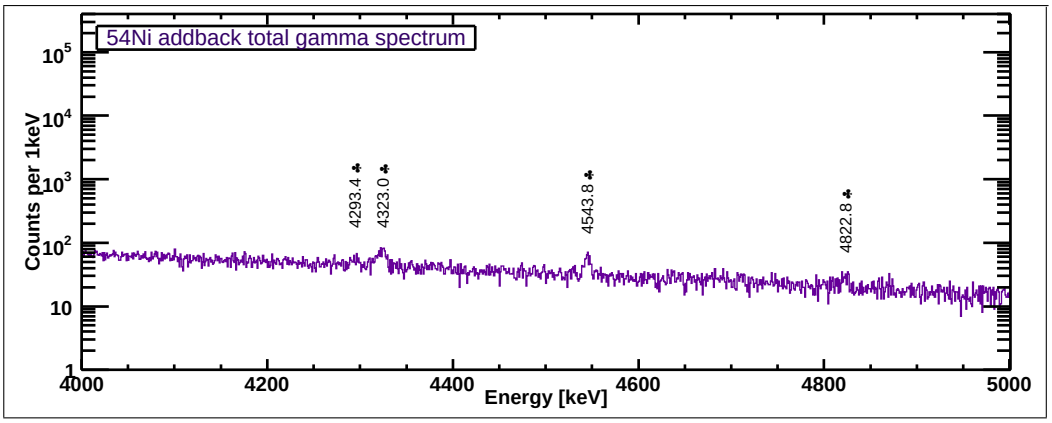

Figure 5.4: ^{54}Ni addback β-delayed γ-spectrum Part 5. Energy range: 4000-5000 keV.

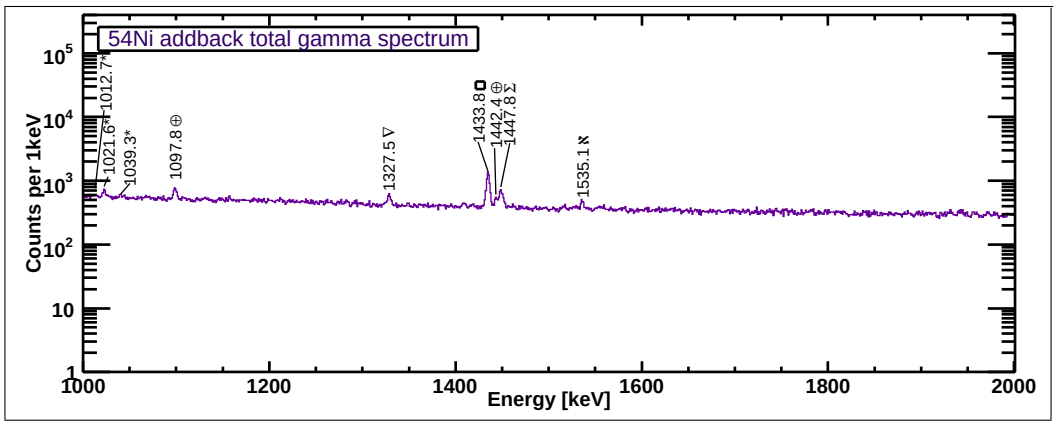

Figure 5.5: ^{54}Ni addback β-delayed γ-spectrum Part 2. Energy range: 1000-2000 keV.

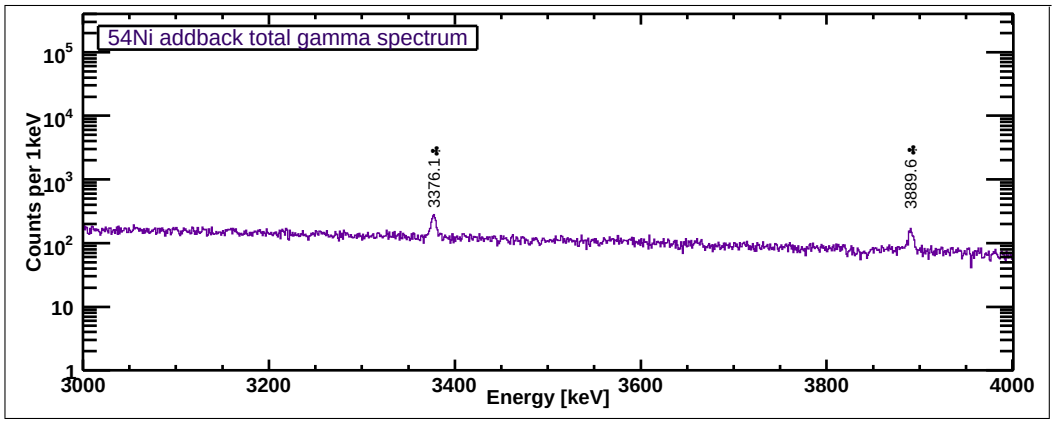

Figure 5.6: ^{54}Ni addback β-delayed γ-spectrum Part 4. Energy range: 3000-4000 keV.

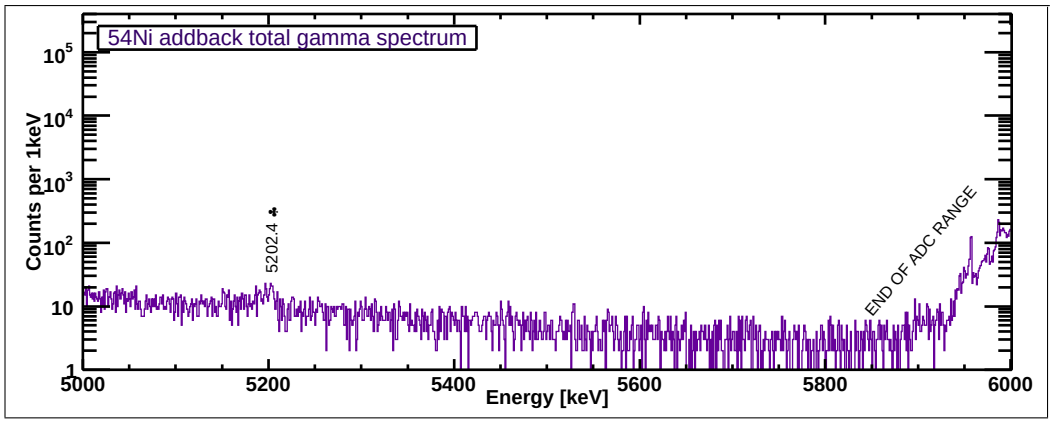

Figure 5.7: ^{54}Ni addback β-delayed γ-spectrum Part 6. Energy range: 5000-6000 keV.

Table 5.1: List of γ-ray energies for the ^{54}Ni setup at RISING in Single Crystal mode (sum of all crystals).

Energy[keV]	FWHM[keV]	Counts	I(γ)	Comments (*)
377.0 (0.1)	2.8 (0.3)	3793.3 (305.4)	27.73 (2.43)	$\otimes^{53}$Mn (^{53}Fe β^+)
510.5 (0.0)	3.5 (0.0)	1898977.8 (1405.3)	16378.88 (573.39)	$m_e c^2$ (e^+e^-)
594.5 (0.6)	9.6 (4.4)	1752.2 (153.5)	16.51 (1.56)	$*^{74}$Ge (n-capture)
681.3 (0.9)	7.0 (3.0)	908.8 (441.8)	9.30 (4.53)	
782.6 (0.2)	3.3 (0.4)	997.6 (114.7)	11.12 (1.34)	$\oplus^{50}$Cr (^{50}Mn β^+)
833.3 (0.6)	5.7 (2.2)	482.1 (172.4)	5.59 (2.01)	$*^{72}$Ge (n-capture)
843.3 (0.3)	2.5 (0.8)	274.5 (83.1)	3.21 (0.98)	$*^{27}$Al (n-capture)
848.9 (0.1)	3.0 (0.2)	1697.2 (102.7)	19.91 (1.39)	$\aleph^{52}$Fe ([1])
936.6 (0.0)	3.0 (0.0)	80016.0 (297.4)	**1000.00 (35.20)**	**$\clubsuit^{54}$Co (^{54}Ni β^+)**
1012.3 (1.1)	4.3 (2.4)	302.4 (182.9)	3.98 (2.41)	$*^{27}$Al (n-capture)
1039.0 (0.7)	7.2 (2.6)	502.5 (201.3)	6.72 (2.70)	$*^{70}$Ge (n-capture)
1097.6 (0.2)	3.3 (0.4)	677.6 (80.8)	9.40 (1.17)	$\oplus^{50}$Cr (^{50}Mn β^+)
1327.6 (0.2)	4.1 (0.7)	689.7 (95.3)	10.89 (1.55)	∇^{53}Fe (^{53}Co β^+)
1433.7 (0.1)	3.2 (0.1)	2684.6 (85.0)	44.69 (2.11)	$\square^{52}$Cr (^{52m}Mn β^+)
1442.4 (0.2)	1.6 (0.5)	210.9 (48.5)	3.53 (0.82)	$\oplus^{50}$Cr (^{50}Mn β^+)
1534.9 (0.2)	2.9 (0.5)	366.4 (60.5)	6.40 (1.08)	$\aleph^{52}$Fe ([1])
2424.0 (0.6)	7.1 (2.6)	420.4 (161.2)	**10.30 (3.97)**	**$\clubsuit^{54}$Co (^{54}Ni β^+)**
3376.2 (0.2)	5.3 (0.5)	631.0 (61.2)	**20.23 (2.08)**	**$\clubsuit^{54}$Co (^{54}Ni β^+)**
3890.2 (0.3)	5.6 (0.8)	336.2 (49.8)	**12.19 (1.85)**	**$\clubsuit^{54}$Co (^{54}Ni β^+)**
4291.6 (1.5)	9.0 (3.7)	128.9 (94.3)	**5.10 (3.74)**	**$\clubsuit^{54}$Co (^{54}Ni β^+)**
4323.2 (0.4)	5.8 (1.1)	185.8 (37.4)	**7.41 (1.51)**	**$\clubsuit^{54}$Co (^{54}Ni β^+)**
4544.0 (0.5)	6.6 (1.0)	173.3 (32.7)	**7.23 (1.39)**	**$\clubsuit^{54}$Co (^{54}Ni β^+)**
4824.3 (1.4)	6.5 (2.8)	37.7 (17.0)	**1.66 (0.75)**	**$\clubsuit^{54}$Co (^{54}Ni β^+)**
5201.5 (0.9)	4.2 (2.3)	30.5 (14.8)	**1.45 (0.70)**	**$\clubsuit^{54}$Co (^{54}Ni β^+)**

(*) See Section 5.1.1 -p.76- for explanation.
([1]) ^{52}Co β^+/^{53}Co p-decay

Table 5.2: List of γ-ray energies for the ^{54}Ni setup at RISING in Add-back mode. (^{1}) ^{52}Co $\beta^+/^{53}$Co p-decay

Energy[keV]	FWHM[keV]	Counts	I(γ)	Comments(*)
377.0 (0.1)	2.8 (0.2)	4228.7 (271.9)	26.60 (1.95)	$\otimes^{53}$Mn(^{53}Fe β^+)
510.6 (0.0)	3.8 (0.0)	2254027.0 (1537.0)	16104.89 (563.78)	$m_ec^2(e^+e^-)$
586.1 (1.1)	16.6 (4.3)	2028.0 (669.6)	15.43 (5.12)	$*^{74}$Ge(n-capture)
684.1 (0.2)	9.9 (0.6)	4202.6 (256.7)	34.39 (2.42)	
782.7 (0.1)	3.2 (0.4)	1059.5 (113.9)	9.26 (1.05)	$\oplus^{50}$Cr(^{50}Mn β^+)
833.6 (0.9)	5.2 (8.6)	306.2 (146.8)	2.76 (1.33)	$*^{72}$Ge(n-capture)
845.4 (0.2)	2.0 (0.5)	280.8 (85.0)	2.55 (0.78)	$*^{27}$Al(n-capture)
849.0 (0.1)	3.0 (0.2)	1986.6 (99.8)	18.09 (1.11)	$\aleph^{52}$Fe(^{1})
936.7 (0.0)	3.3 (0.0)	104470.7 (341.0)	**1000.00 (35.15)**	**$\clubsuit^{54}$Co(^{54}Ni β^+)**
1012.7 (1.1)	5.8 (2.7)	250.9 (191.7)	2.50 (1.91)	$*^{27}$Al(n-capture)
1021.6 (0.2)	3.5 (0.7)	625.2 (112.0)	6.26 (1.14)	$2m_ec^2(e^+e^-)$
1039.3 (0.9)	7.0 (3.5)	371.3 (187.1)	3.75 (1.90)	$*^{70}$Ge(n-capture)
1097.8 (0.1)	3.4 (0.3)	956.2 (83.0)	9.94 (0.93)	$\oplus^{50}$Cr(^{50}Mn β^+)
1327.5 (0.2)	4.3 (0.6)	857.5 (97.3)	9.87 (1.17)	∇^{53}Fe(^{53}Co β^+)
1433.8 (0.0)	3.4 (0.1)	3437.5 (93.1)	41.29 (1.83)	$\square^{52}$Cr(^{52m}Mn β^+)
1442.4 (0.2)	1.9 (0.4)	293.7 (61.6)	3.54 (0.75)	$\oplus^{50}$Cr(^{50}Mn β^+)
1447.8 (0.1)	5.1 (0.4)	1619.6 (142.1)	19.56 (1.85)	Σ(510.6+936.7)
1535.1 (0.2)	2.9 (0.4)	413.7 (60.0)	5.16 (0.77)	$\aleph^{52}$Fe(^{1})
2424.6 (0.3)	5.2 (0.8)	491.9 (75.5)	**8.00 (1.26)**	**$\clubsuit^{54}$Co(^{54}Ni β^+)**
3376.1 (0.2)	5.9 (0.5)	939.7 (73.5)	**18.85 (1.61)**	**$\clubsuit^{54}$Co(^{54}Ni β^+)**
3889.6 (0.2)	5.7 (0.6)	480.5 (53.0)	**10.60 (1.23)**	**$\clubsuit^{54}$Co(^{54}Ni β^+)**
4293.4 (1.0)	12.9 (7.1)	234.5 (213.3)	**5.55 (5.05)**	**$\clubsuit^{54}$Co(^{54}Ni β^+)**
4323.0 (0.7)	9.4 (2.2)	312.1 (96.2)	**7.42 (2.30)**	**$\clubsuit^{54}$Co(^{54}Ni β^+)**
4543.8 (0.4)	6.9 (1.0)	245.1 (40.4)	**6.04 (1.02)**	**$\clubsuit^{54}$Co(^{54}Ni β^+)**
4822.8 (0.7)	7.7 (1.5)	87.7 (17.1)	**2.26 (0.45)**	**$\clubsuit^{54}$Co(^{54}Ni β^+)**
5202.4 (0.5)	3.7 (1.3)	43.4 (14.0)	**1.18 (0.38)**	**$\clubsuit^{54}$Co(^{54}Ni β^+)**

(*) See Section 5.1.1 -p.76- for explanation.
(^{1}) ^{52}Co $\beta^+/^{53}$Co p-decay

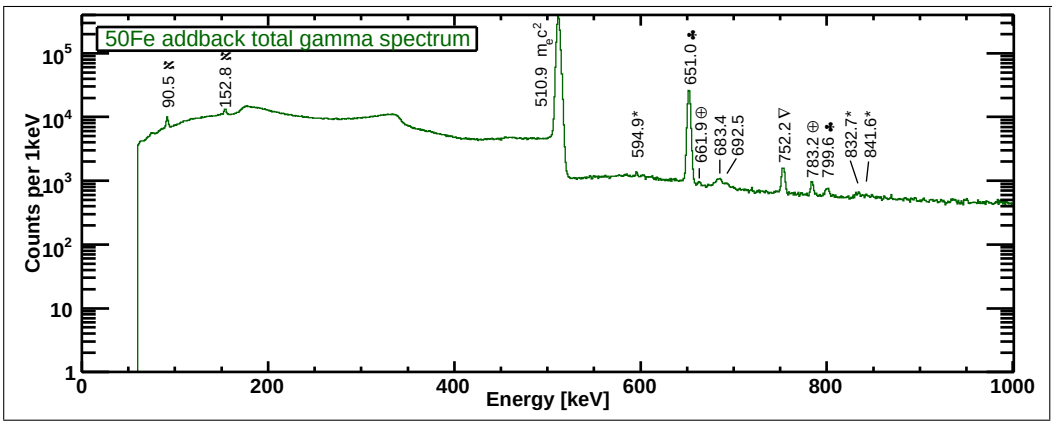

Figure 5.8: ^{50}Fe addback β-delayed γ-spectrum Part 1. Energy range: 0-1000 keV.

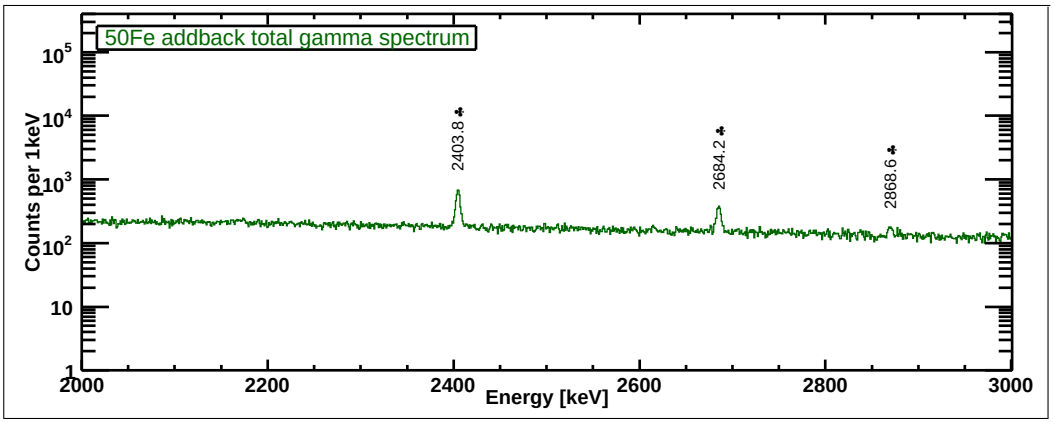

Figure 5.9: ^{50}Fe addback β-delayed γ-spectrum Part 3. Energy range: 2000-3000 keV.

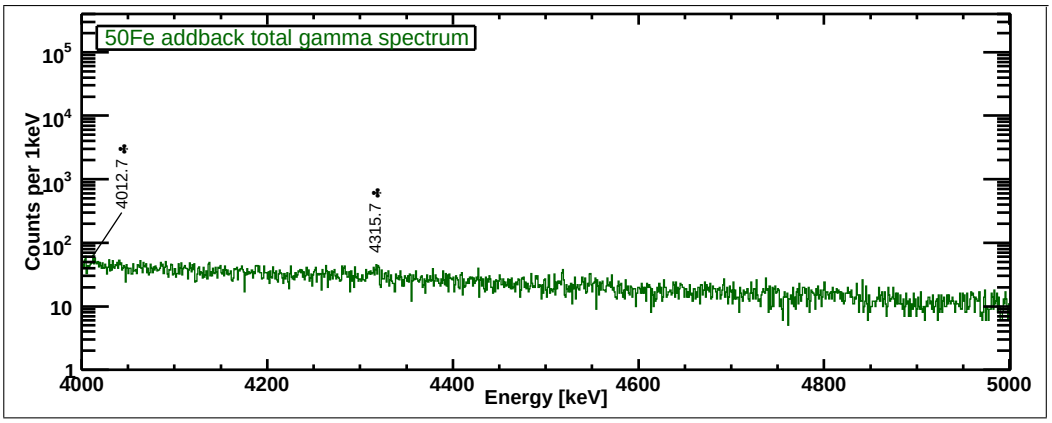

Figure 5.10: ^{50}Fe addback β-delayed γ-spectrum Part 5. Energy range: 4000-5000 keV.

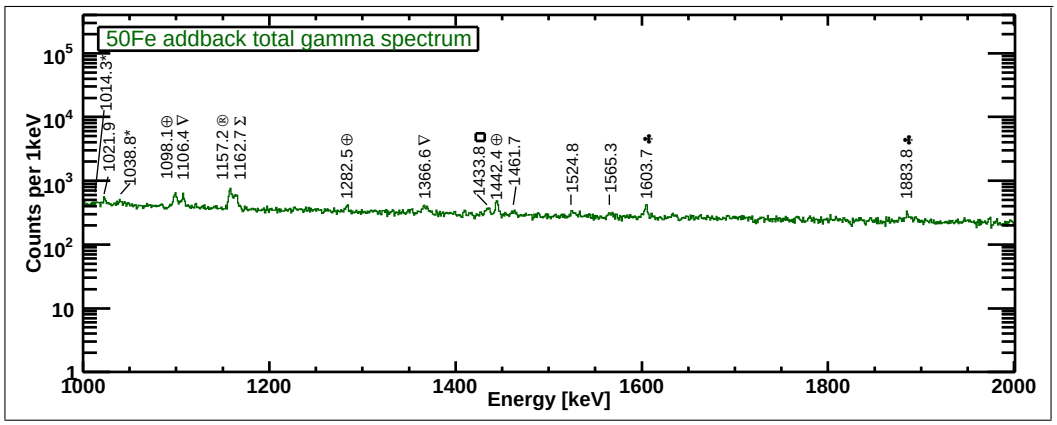

Figure 5.11: ^{50}Fe addback β-delayed γ-spectrum Part 2. Energy range: 1000-2000 keV.

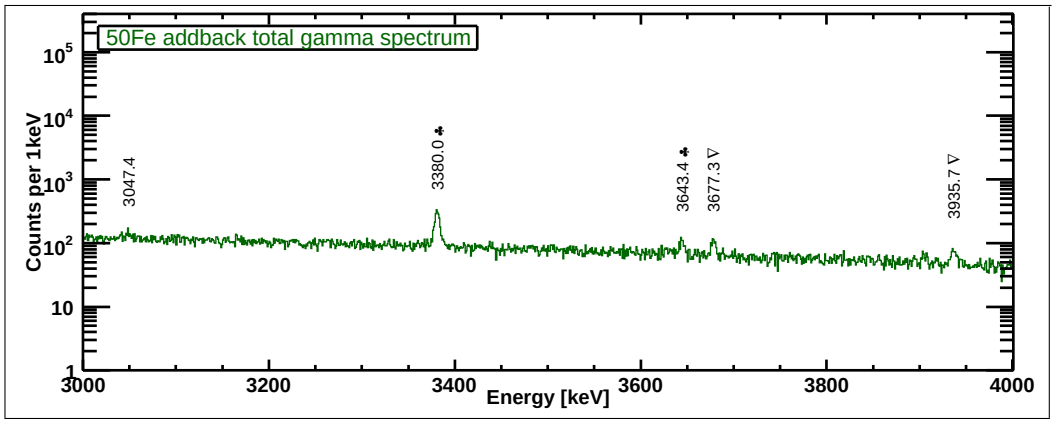

Figure 5.12: ^{50}Fe addback β-delayed γ-spectrum Part 4. Energy range: 3000-4000 keV.

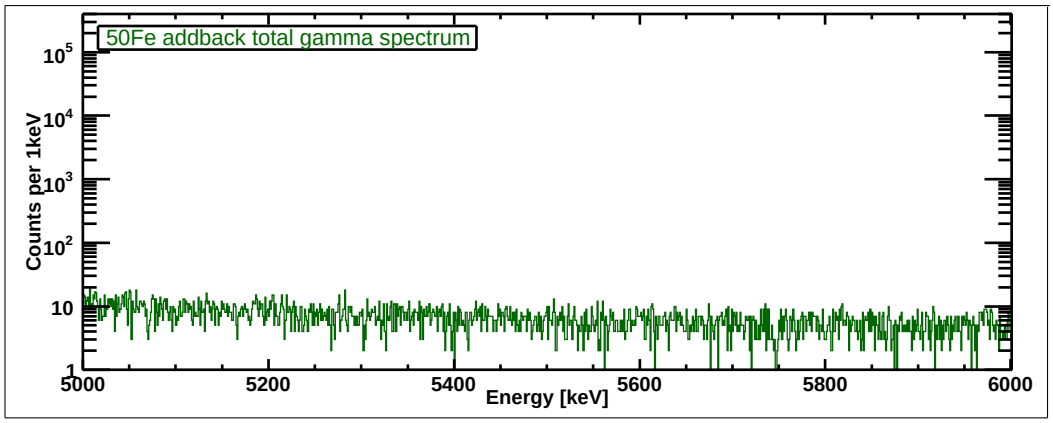

Figure 5.13: ^{50}Fe addback β-delayed γ-spectrum Part 6. Energy range: 5000-6000 keV.

Table 5.3: List of γ-ray energies for the ^{50}Fe setup at RISING in Single Crystal mode (sum of all crystals).

Energy[keV]	FWHM[keV]	Counts	I(γ)	Comments(*)
90.5 (0.0)	2.5 (0.1)	8996.8 (318.5)	53.06 (2.64)	$\aleph^{49}$V(^{49}Cr β^+)
152.8 (0.1)	2.8 (0.2)	8220.0 (431.0)	53.98 (3.40)	$\aleph^{49}$V(^{49}Cr β^+)
510.7 (0.0)	3.8 (0.0)	1366003.1 (1193.8)	15434.17 (540.36)	m_ec^2(e^+e^-)
594.8 (0.2)	2.9 (0.5)	833.2 (120.6)	10.28 (1.53)	$*^{74}$Ge(n-capture)
650.9 (0.0)	3.0 (0.0)	76773.5 (296.5)	**1000.00 (35.21)**	**$\clubsuit^{50}$Mn(^{50}Fe β^+)**
661.7 (0.4)	3.4 (1.2)	323.2 (112.2)	4.25 (1.48)	$\oplus^{50}$Cr (^{50m}Mnβ^+)
752.1 (0.1)	3.0 (0.1)	2822.5 (96.2)	40.17 (1.96)	∇^{48}Cr (^{48}Mnβ^+)
783.1 (0.1)	3.0 (0.2)	1114.9 (84.3)	16.27 (1.36)	$\oplus^{50}$Cr (^{50m}Mnβ^+)
799.2 (0.2)	4.0 (0.5)	691.9 (93.5)	**10.23 (1.43)**	**$\dagger\clubsuit^{50}$Mn($2^+ \rightarrow 0^+$)**
832.5 (0.3)	5.6 (1.1)	804.5 (187.8)	12.20 (2.88)	$*^{72}$Ge(n-capture)
843.3 (0.7)	7.5 (1.7)	600.9 (140.2)	9.19 (2.17)	$*^{27}$Al(n-capture)
1012.1 (1.3)	11.0 (3.2)	1436.1 (504.8)	24.71 (8.73)	$*^{27}$Al(n-capture)
1038.3 (0.6)	6.0 (2.6)	503.0 (198.4)	8.80 (3.49)	$*^{70}$Ge(n-capture)
1098.1 (0.1)	3.5 (0.3)	849.1 (73.8)	15.42 (1.45)	$\oplus^{50}$Cr(^{50m}Mn β^+)
1106.3 (0.2)	4.6 (0.6)	765.5 (89.4)	13.98 (1.70)	∇^{48}Cr(^{48}Mn β^+)
1156.8 (0.1)	3.2 (0.3)	1232.6 (127.0)	23.19 (2.52)	$®^{44}$Ca(^{44}Sc β^+)
1163.3 (0.4)	3.5 (2.8)	607.0 (145.2)	11.46 (2.77)	Σ(510.9+651.0)
1282.4 (0.4)	4.1 (0.9)	314.5 (70.9)	6.35 (1.45)	$\oplus^{50}$Cr(^{50m}Mn β^+)
1366.0 (0.5)	5.3 (1.2)	384.3 (92.7)	8.10 (1.97)	∇^{48}Cr(^{48}Mn β^+)
1433.5 (0.4)	4.2 (1.5)	305.0 (100.3)	6.65 (2.20)	$\square^{52}$Cr(^{52m}Mn β^+)
1443.4 (0.2)	3.2 (0.6)	458.2 (84.4)	10.04 (1.88)	$\oplus^{50}$Cr(^{50m}Mn β^+)
1460.8 (0.9)	4.7 (1.9)	151.7 (71.1)	3.35 (1.57)	
1524.0 (0.3)	1.1 (2.8)	89.0 (57.8)	2.02 (1.32)	
1603.4 (0.2)	3.3 (0.4)	506.9 (61.3)	**11.96 (1.51)**	**$\ddagger\clubsuit^{50}$Mn($1^+ \rightarrow 2^+$)**
1883.8 (0.3)	2.1 (1.4)	152.9 (62.8)	**4.06 (1.67)**	**$\ddagger\clubsuit^{50}$Mn($1^+ \rightarrow 2^+$)**
2403.6 (0.1)	4.4 (0.2)	1768.3 (72.2)	**56.40 (3.03)**	**$\clubsuit^{50}$Mn(^{50}Fe β^+)**
2684.1 (0.1)	4.7 (0.3)	902.2 (61.4)	**31.39 (2.40)**	**$\clubsuit^{50}$Mn(^{50}Fe β^+)**
2868.1 (0.3)	3.7 (0.7)	228.3 (42.4)	8.38 (1.58)	
3047.5 (0.2)	1.5 (0.8)	79.3 (26.1)	3.06 (1.01)	
3379.6 (0.1)	5.4 (0.3)	984.1 (57.1)	**41.36 (2.80)**	**$\clubsuit^{50}$Mn(^{50}Fe β^+)**
3642.4 (0.4)	4.1 (0.7)	152.1 (30.4)	**6.82 (1.38)**	**$\clubsuit^{50}$Mn(^{50}Fe β^+)**
3677.0 (0.3)	4.6 (0.8)	202.6 (36.0)	9.15 (1.66)	∇^{48}Cr (^{48}Mnβ^+)
3935.8 (0.4)	4.8 (0.9)	162.0 (32.5)	7.77 (1.58)	∇^{48}Cr (^{48}Mnβ^+)
4013.0 (0.7)	3.7 (3.7)	52.6 (21.9)	**2.57 (1.07)**	**$\clubsuit^{50}$Mn(^{50}Fe β^+)**
4316.1 (0.8)	6.0 (2.0)	87.3 (25.2)	**4.55 (1.32)**	**$\clubsuit^{50}$Mn(^{50}Fe β^+)**

(*) See Section 5.1.2 -p.92- for explanation.

Table 5.4: List of γ-ray energies for the ^{50}Fe setup at RISING in Add-back mode.

Energy[keV]	FWHM[keV]	Counts	I(γ)	Comments(*)
90.5 (0.0)	2.5 (0.1)	8499.1 (254.4)	51.42 (2.37)	$\aleph^{49}$V(^{49}Crβ^+)
152.8 (0.1)	2.7 (0.1)	7365.5 (321.6)	46.66 (2.61)	$\aleph^{49}$V(^{49}Crβ^+)
510.9 (0.0)	4.1 (0.0)	1626151.0 (1309.6)	15247.16 (533.79)	m_ec^2(e$^+$e$^-$)
594.9 (0.2)	1.7 (0.6)	443.4 (101.9)	4.46 (1.04)	$*^{74}$Ge(n-capture)
651.0 (0.0)	3.4 (0.0)	95382.0 (332.6)	**1000.00 (35.17)**	**$\clubsuit^{50}$Mn(^{50}Fe β^+)**
661.9 (0.3)	2.6 (0.7)	329.6 (93.9)	3.48 (1.00)	$\oplus^{50}$Cr(^{50m}Mnβ^+)
683.4 (0.3)	7.6 (1.0)	2060.0 (358.9)	22.11 (3.93)	
692.5 (0.5)	3.7 (1.2)	447.2 (207.2)	4.83 (2.24)	
752.2 (0.0)	3.4 (0.1)	3723.8 (107.7)	41.87 (1.90)	∇^{48}Cr(^{48}Mnβ^+)
783.2 (0.1)	3.1 (0.2)	1281.0 (86.4)	14.69 (1.12)	$\oplus^{50}$Cr(^{50m}Mnβ^+)
799.6 (0.2)	4.2 (0.5)	848.6 (99.8)	**9.84 (1.21)**	**$\dagger\clubsuit^{50}$Mn($2^+ \rightarrow 0^+$)**
832.7 (0.5)	6.5 (1.4)	599.1 (148.0)	7.09 (1.77)	$*^{72}$Ge(n-capture)
841.6 (0.4)	1.7 (0.8)	105.1 (58.0)	1.25 (0.69)	$*^{27}$Al(n-capture)
1014.3 (0.8)	2.9 (1.3)	99.9 (58.5)	1.31 (0.77)	$*^{27}$Al(n-capture)
1021.9 (0.2)	1.8 (0.8)	247.1 (65.7)	3.25 (0.87)	$2m_ec^2$(e$^+$e$^-$)
1038.8 (0.4)	2.5 (1.6)	183.4 (73.1)	2.43 (0.97)	$*^{70}$Ge(n-capture)
1098.1 (0.1)	4.2 (0.6)	1010.1 (126.2)	13.78 (1.79)	$\oplus^{50}$Cr(^{50m}Mn β^+)
1106.4 (0.2)	3.6 (1.0)	701.7 (125.5)	9.61 (1.75)	∇^{48}Cr(^{48}Mn β^+)
1157.2 (0.1)	3.3 (0.3)	1278.1 (116.3)	17.93 (1.75)	®^{44}Ca(^{44}Sc β^+)
1162.7 (0.2)	4.8 (0.7)	1174.2 (147.4)	16.52 (2.15)	Σ(510.9+651.0)
1282.5 (0.3)	3.4 (1.1)	300.7 (76.2)	4.46 (1.14)	$\oplus^{50}$Cr(^{50m}Mn β^+)
1366.6 (0.6)	9.8 (2.1)	1010.7 (299.8)	15.51 (4.63)	∇^{48}Cr(^{48}Mn β^+)
1433.8 (0.3)	4.5 (0.8)	383.5 (81.8)	6.04 (1.31)	$\square^{52}$Cr(^{52m}Mn β^+)
1442.4 (0.1)	2.9 (0.5)	612.9 (76.0)	9.69 (1.25)	$\oplus^{50}$Cr(^{50m}Mn β^+)
1461.7 (0.7)	4.8 (1.3)	219.5 (70.4)	3.50 (1.13)	
1524.8 (0.6)	4.0 (1.7)	218.7 (76.6)	3.57 (1.26)	
1565.3 (0.9)	5.7 (1.9)	250.6 (91.2)	4.15 (1.52)	
1603.7 (0.2)	3.3 (0.5)	531.4 (65.6)	**8.91 (1.14)**	**$\ddagger\clubsuit^{50}$Mn($1^+ \rightarrow 2^+$)**
1883.8 (0.2)	1.5 (0.7)	153.0 (43.8)	**2.81 (0.81)**	**$\ddagger\clubsuit^{50}$Mn $1^+ \rightarrow 2^+$)**
2403.8 (0.1)	4.9 (0.2)	2607.2 (83.3)	**55.37 (2.62)**	**$\clubsuit^{50}$Mn(^{50}Fe β^+)**
2684.2 (0.1)	5.1 (0.3)	1226.1 (70.7)	**27.86 (1.88)**	**$\clubsuit^{50}$Mn(^{50}Fe β^+)**
2868.6 (0.4)	4.3 (0.7)	222.8 (44.5)	5.28 (1.07)	
3047.4 (0.4)	0.8 (1.4)	58.5 (21.6)	1.44 (0.53)	
3380.0 (0.1)	5.9 (0.3)	1421.9 (68.6)	**37.45 (2.23)**	**$\clubsuit^{50}$Mn(^{50}Fe β^+)**
3643.4 (0.3)	4.9 (0.8)	239.2 (41.0)	**6.62 (1.16)**	**$\clubsuit^{50}$Mn(^{50}Fe β^+)**
3677.3 (0.3)	4.8 (0.6)	257.7 (37.7)	7.18 (1.08)	∇^{48}Cr(^{48}Mnβ^+)
3935.7 (0.5)	6.9 (1.5)	222.4 (49.9)	6.49 (1.47)	∇^{48}Cr(^{48}Mnβ^+)
4012.7 (1.2)	5.6 (3.0)	65.8 (30.2)	**1.95 (0.90)**	**$\clubsuit^{50}$Mn(^{50}Fe β^+)**
4315.7 (1.4)	10.7 (4.5)	114.2 (45.5)	**3.56 (1.42)**	**$\clubsuit^{50}$Mn(^{50}Fe β^+)**

(*) See Section 5.1.2 -p.92- for explanation.

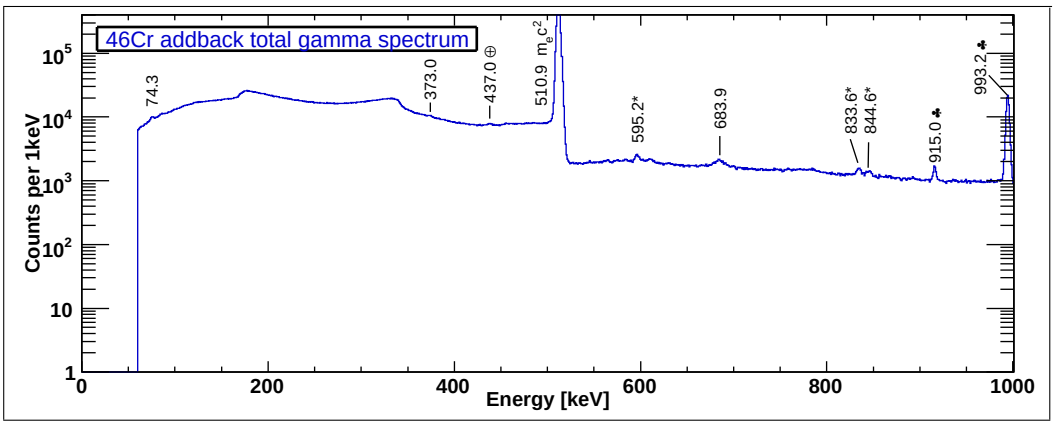

Figure 5.14: ^{46}Cr addback β-delayed γ-spectrum Part 1. Energy range: 0-1000 keV.

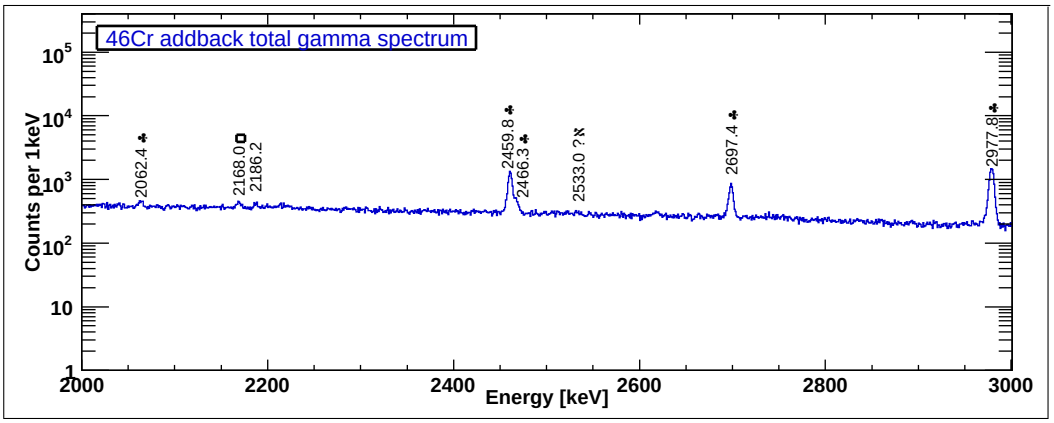

Figure 5.15: ^{46}Cr addback β-delayed γ-spectrum Part 3. Energy range: 2000-3000 keV.

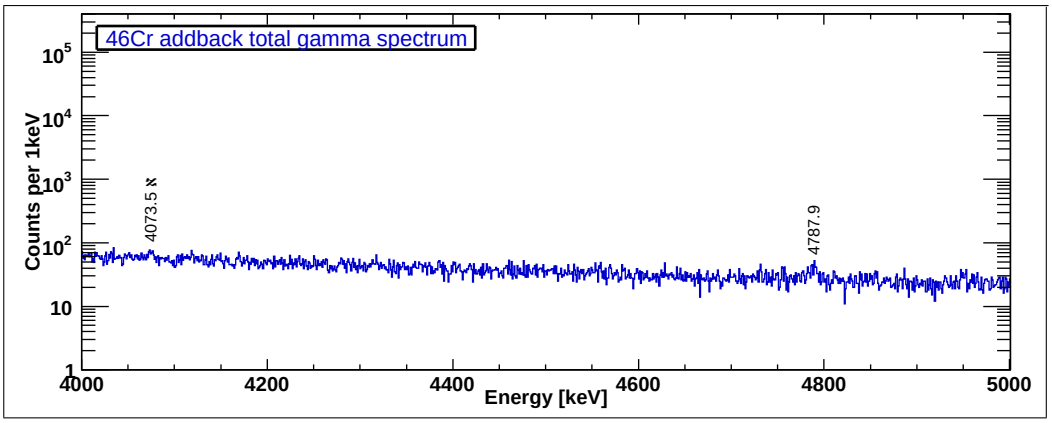

Figure 5.16: ^{46}Cr addback β-delayed γ-spectrum Part 5. Energy range: 4000-5000 keV.

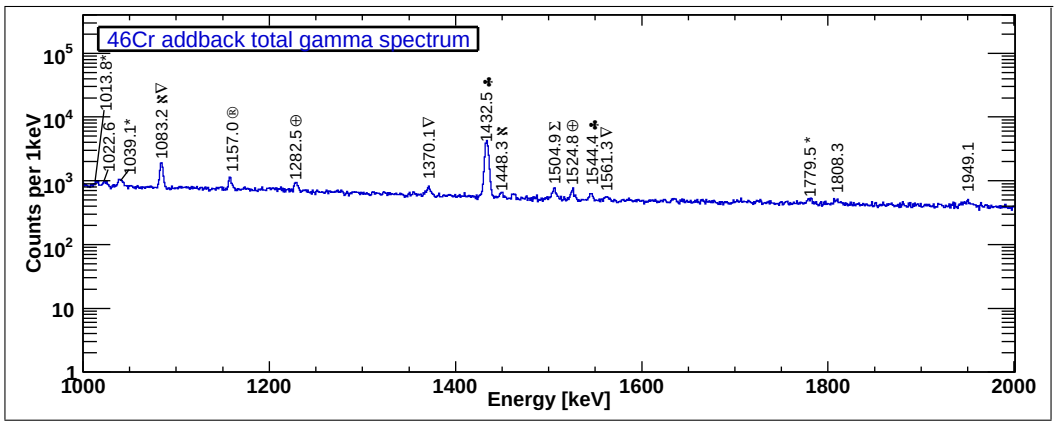

Figure 5.17: ^{46}Cr addback β-delayed γ-spectrum Part 2. Energy range: 1000-2000 keV.

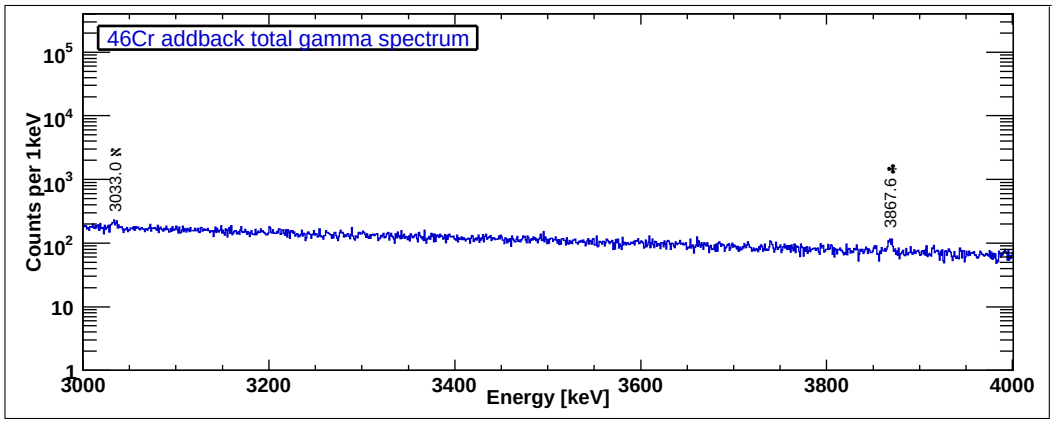

Figure 5.18: ^{46}Cr addback β-delayed γ-spectrum Part 4. Energy range: 3000-4000 keV.

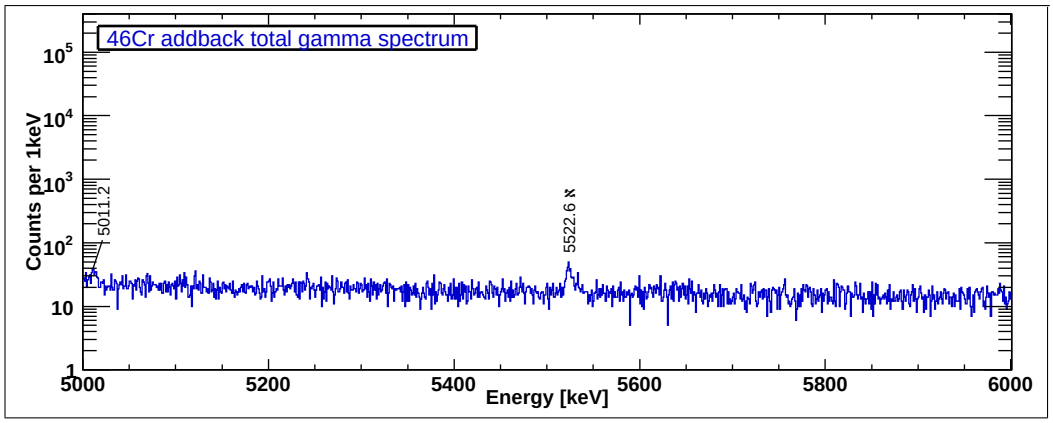

Figure 5.19: ^{46}Cr addback β-delayed γ-spectrum Part 6. Energy range: 5000-6000 keV.

Table 5.5: List of γ-ray energies for the ^{46}Cr setup at RISING in Single Crystal mode (sum of all crystals).

Energy[keV]	FWHM[keV]	Counts	I(γ)	Comments(*)
74.1 (0.1)	3.7 (0.4)	4509.7 (485.4)	25.13 (2.84)	
437.1 (0.3)	4.1 (0.9)	2077.9 (426.1)	20.31 (4.23)	$\oplus^{42}$Ca(^{42}Sc^{m} β^+)
510.7 (0.0)	3.8 (0.0)	2437038.2 (1595.7)	25987.70 (909.73)	m_ec^2 (e^+e^-)
595.1 (0.1)	3.9 (0.3)	3675.4 (416.4)	42.83 (5.08)	$*^{74}$Ge(n-capture)
833.1 (0.1)	4.9 (0.3)	3043.9 (201.2)	43.62 (3.26)	$*^{72}$Ge(n-capture)
843.3 (0.3)	7.7 (0.9)	2396.9 (286.7)	34.61 (4.31)	$*^{27}$Al(n-capture)
914.9 (0.1)	3.5 (0.2)	2100.8 (127.8)	**31.96 (2.24)**	**$\dagger\clubsuit^{46}$V($2^+ \rightarrow 0^+$)**
993.1 (0.0)	3.2 (0.0)	62311.6 (274.2)	**1000.00 (35.28)**	**$\clubsuit^{46}$V(^{46}Cr β^+)**
1013.8 (0.3)	5.7 (1.5)	1004.5 (220.9)	16.34 (3.64)	$*^{27}$Al(n-capture)
1038.8 (0.2)	5.0 (0.4)	1997.5 (161.3)	33.02 (2.91)	$*^{70}$Ge(n-capture)
1083.1 (0.1)	3.4 (0.1)	3651.1 (117.4)	62.05 (2.95)	$\aleph\nabla^{44}$Ti(^{44g,m}V β^+)
1156.9 (0.1)	3.1 (0.4)	1120.4 (108.3)	19.90 (2.05)	$®^{44}$Ca(^{44}Sc β^+)
1227.6 (0.2)	3.3 (0.4)	764.3 (90.6)	14.13 (1.75)	$\oplus^{42}$Ca(^{42}Sc^{m} β^+)
1369.4 (0.3)	5.7 (0.7)	920.7 (128.9)	18.35 (2.65)	∇^{44}Ti(^{44m}V β^+)
1432.4 (0.0)	3.8 (0.1)	11972.1 (147.2)	**246.20 (9.13)**	**$\clubsuit^{46}$V(^{46}Cr β^+)**
1448.2 (0.3)	3.0 (0.7)	319.2 (74.1)	6.61 (1.55)	$\aleph^{44}$Ti(^{44g}V β^+)
1524.6 (0.2)	4.3 (0.6)	860.9 (106.0)	18.50 (2.37)	$\oplus^{42}$Ca (^{42}Sc^{m} β^+)
1544.7 (0.3)	3.8 (0.9)	439.8 (90.9)	**9.54 (2.00)**	**$\ddagger\clubsuit^{46}$V ($1^+ \rightarrow 2^+$)**
1560.9 (0.4)	3.0 (1.2)	209.1 (93.2)	4.57 (2.04)	∇^{44}Ti(^{44m}V β^+)
1779.3 (0.4)	3.9 (0.9)	340.0 (78.6)	8.16 (1.91)	$*^{28}$Si(n-capture)
1808.0 (0.9)	7.7 (2.4)	462.9 (176.9)	11.24 (4.31)	
1949.0 (0.3)	3.3 (1.2)	332.7 (91.7)	8.54 (2.37)	
1955.0 (0.3)	4.3 (0.9)	490.6 (97.2)	12.62 (2.54)	
2062.0 (0.4)	4.1 (1.2)	313.1 (84.7)	**8.38 (2.29)**	**$\ddagger\clubsuit^{46}$V($1^+ \rightarrow 2^+$)**
2168.1 (0.4)	4.5 (0.9)	380.3 (79.5)	10.57 (2.24)	$\square^{38}$Ar(^{38m}K β^+)
2185.6 (0.3)	4.2 (0.7)	386.3 (73.4)	10.80 (2.09)	
2459.6 (0.1)	4.5 (0.2)	3684.3 (108.4)	**112.87 (5.16)**	**$\clubsuit^{46}$V(^{46}Cr β^+)**
2466.3 (0.2)	4.0 (0.4)	931.2 (81.4)	**28.59 (2.69)**	**$\clubsuit^{46}$V(^{46}Cr β^+)**
2697.1 (0.1)	4.9 (0.2)	2174.7 (92.0)	**71.65 (3.93)**	**$\clubsuit^{46}$V(^{46}Cr β^+)**
2977.6 (0.0)	5.0 (0.1)	5180.6 (99.7)	**184.89 (7.38)**	**$\clubsuit^{46}$V(^{46}Cr β^+)**
3032.9 (1.1)	9.4 (3.8)	376.7 (236.7)	13.65 (8.59)	$\aleph^{44}$Ti(^{44g}Vβ^+)
3866.4 (1.0)	8.7 (3.3)	228.6 (127.2)	**10.19 (5.68)**	**$\clubsuit^{46}$V(^{46}Cr β^+)**
4073.1 (0.6)	3.7 (1.3)	74.7 (26.5)	3.49 (1.24)	$\aleph^{44}$Ti(^{44g}V β^+)
4786.1 (0.6)	5.6 (1.2)	100.3 (25.7)	5.43 (1.41)	
5011.3 (0.5)	3.7 (1.1)	72.8 (20.2)	4.12 (1.15)	
5523.1 (0.5)	6.3 (1.0)	138.6 (26.1)	8.64 (1.65)	$\aleph^{44}$Ti(^{44g}V β^+)

(*) See Section 5.1.3 -p.94- for explanation.

Table 5.6: List of γ-ray energies for the ^{46}Cr setup at RISING in Add-back mode.

Energy[keV]	FWHM[keV]	Counts	I(γ)	Comments(*)
74.3 (0.1)	3.3 (0.3)	3479.3 (317.5)	19.95 (1.95)	
373.0 (0.3)	3.0 (0.7)	1302.6 (313.1)	10.07 (2.45)	
437.0 (0.3)	4.6 (1.0)	2269.6 (473.6)	18.71 (3.96)	$\oplus^{42}$Ca(^{42}Sc^{m} β^{+})
510.9 (0.0)	4.1 (0.0)	2920452.8 (1756.2)	25761.12 (901.77)	$m_e c^2$ (e^+e^-)
595.2 (0.2)	5.0 (0.5)	3240.6 (338.3)	30.64 (3.37)	$*^{74}$Ge(n-capture)
683.9 (0.3)	13.2 (0.8)	5995.3 (367.7)	60.54 (4.28)	
833.6 (0.2)	5.2 (0.7)	2156.2 (223.5)	24.01 (2.63)	$*^{72}$Ge(n-capture)
844.3 (0.3)	7.9 (1.7)	2527.1 (315.8)	28.32 (3.67)	$*^{27}$Al(n-capture)
915.0 (0.1)	3.3 (0.2)	2437.0 (120.7)	**28.45 (1.72)**	**†♣^{46}V($2^+ \rightarrow 0^+$)**
993.2 (0.0)	3.6 (0.0)	82116.2 (313.2)	**1000.00 (35.21)**	**♣^{46}V(^{46}Cr β^+)**
1013.8 (0.3)	4.9 (0.9)	828.2 (164.5)	10.19 (2.06)	$*^{27}$Al(n-capture)
1022.6 (0.3)	5.5 (0.7)	998.8 (171.1)	12.35 (2.16)	$2m_e c^2$(e^+e^-)
1039.1 (0.2)	5.6 (0.6)	1431.4 (159.9)	17.85 (2.09)	$*^{70}$Ge(n-capture)
1083.2 (0.0)	3.7 (0.1)	4739.5 (124.8)	60.40 (2.65)	ℵ∇^{44}Ti(^{44g,m}V β^+)
1157.0 (0.1)	3.0 (0.2)	1362.8 (97.4)	17.98 (1.43)	®^{44}Ca(^{44}Sc β^+)
1227.8 (0.2)	3.7 (0.3)	1043.1 (97.0)	14.21 (1.41)	$\oplus^{42}$Ca(^{42}Sc^{m} β^+)
1370.1 (0.2)	4.9 (0.7)	1035.9 (130.9)	14.98 (1.96)	∇^{44}Ti(^{44m}V β^+)
1432.5 (0.0)	4.2 (0.0)	16331.8 (165.4)	**242.03 (8.82)**	**♣^{46}V (^{46}Cr β^+)**
1448.3 (0.0)	3.4 (0.9)	436.1 (102.4)	6.50 (1.54)	ℵ^{44}Ti(^{44g}V β^+)
1504.9 (0.2)	4.1 (0.4)	1025.9 (102.7)	15.62 (1.66)	Σ(510.9+993.2)
1524.8 (0.2)	4.2 (0.5)	972.7 (99.9)	14.92 (1.62)	$\oplus^{42}$Ca(^{42}Sc^{m} β^+)
1544.4 (0.2)	4.1 (0.6)	626.0 (89.2)	**9.67 (1.42)**	**‡♣^{46}V ($1^+ \rightarrow 2^+$)**
1561.3 (0.3)	5.2 (1.5)	410.5 (121.6)	6.38 (1.90)	∇^{44}Ti(^{44m}V β^+)
1779.5 (0.5)	5.8 (1.2)	521.7 (118.8)	8.73 (2.01)	$*^{28}$Si(n-capture)
1808.3 (0.7)	6.5 (1.7)	422.0 (127.9)	7.13 (2.18)	
1949.1 (0.1)	5.0 (0.1)	5392.8 (132.8)	95.14 (4.07)	
2062.4 (0.4)	5.2 (0.9)	484.3 (94.0)	**8.83 (1.74)**	**‡♣^{46}V($1^+ \rightarrow 2^+$)**
2168.0 (0.4)	5.2 (1.1)	471.3 (96.5)	8.85 (1.84)	□^{38}Ar(^{38}K β^+)
2186.2 (0.5)	4.2 (0.9)	287.3 (70.3)	5.42 (1.34)	
2459.8 (0.1)	5.0 (0.1)	5392.8 (132.8)	**109.26 (4.68)**	**♣^{46}V(^{46}Cr β^+)**
2466.3 (0.2)	4.3 (0.6)	870.3 (107.2)	**17.66 (2.26)**	**♣^{46}V(^{46}Cr β^+)**
2533.0 (1.1)	7.3 (4.7)	241.4 (250.6)	4.98 (5.17)	?ℵ^{44}Ti(^{44g}Vβ^+)
2697.4 (0.1)	5.2 (0.2)	3166.3 (100.9)	**67.90 (3.21)**	**♣^{46}V(^{46}Cr β^+)**
2977.8 (0.0)	5.5 (0.1)	7482.6 (120.7)	**170.77 (6.58)**	**♣^{46}V(^{46}Cr β^+)**
3033.0 (0.7)	8.9 (2.9)	472.8 (199.3)	10.92 (4.62)	ℵ^{44}Ti(^{44g}Vβ^+)
3867.6 (0.4)	5.4 (1.0)	235.4 (45.7)	**6.39 (1.26)**	**♣^{46}V(^{46}Cr β^+)**
4073.5 (0.8)	5.4 (2.0)	98.8 (38.4)	2.78 (1.08)	ℵ^{44}Ti(^{44g}Vβ^+)
4787.9 (0.9)	7.3 (3.0)	116.5 (54.0)	3.68 (1.71)	
5011.2 (0.8)	5.9 (1.9)	81.5 (27.9)	2.67 (0.92)	
5522.6 (0.4)	5.2 (1.0)	134.1 (25.3)	4.73 (0.91)	ℵ^{44}Ti(^{44g}Vβ^+)

(*) See Section 5.1.3 -p.94- for explanation.

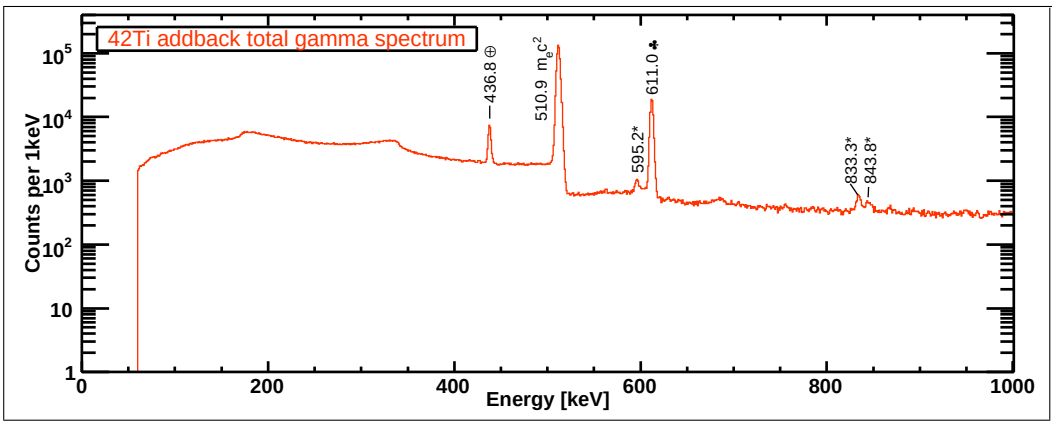

Figure 5.20: ^{42}Ti addback β-delayed γ-spectrum Part 1. Energy range: 0-1000 keV.

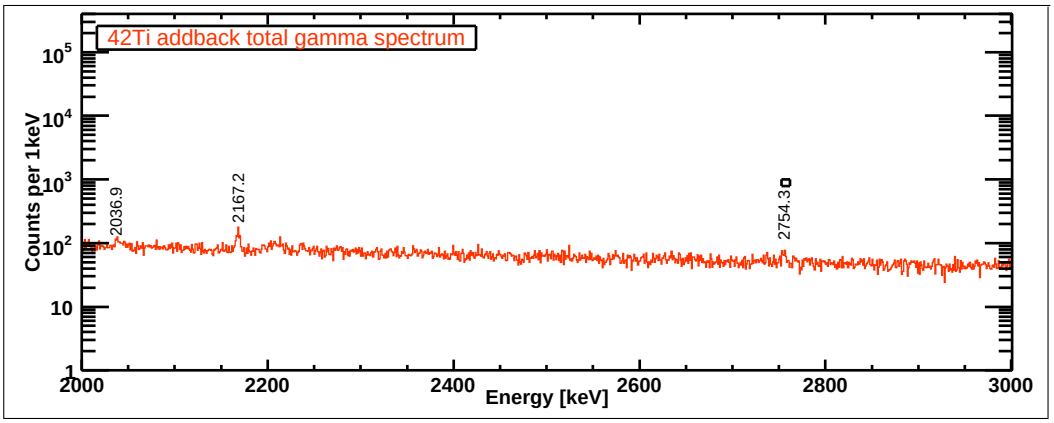

Figure 5.21: ^{42}Ti addback β-delayed γ-spectrum Part 3. Energy range: 2000-3000 keV.

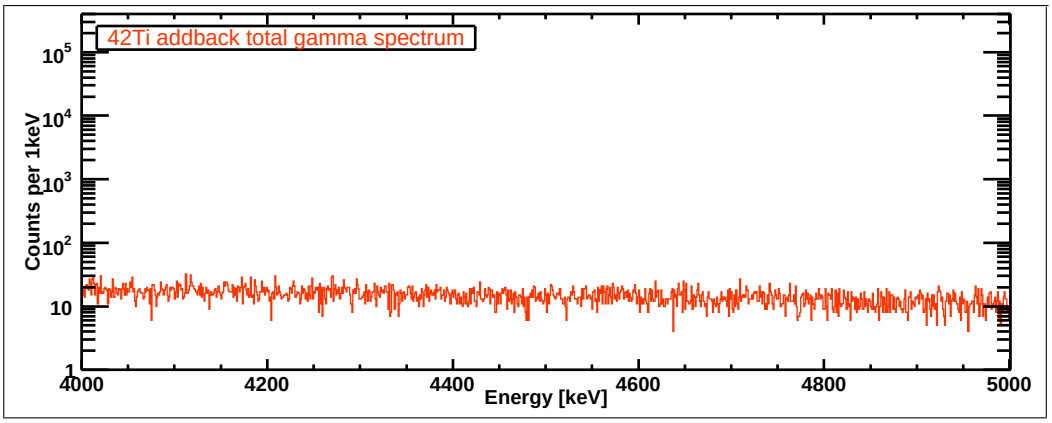

Figure 5.22: ^{42}Ti addback β-delayed γ-spectrum Part 5. Energy range: 4000-5000 keV.

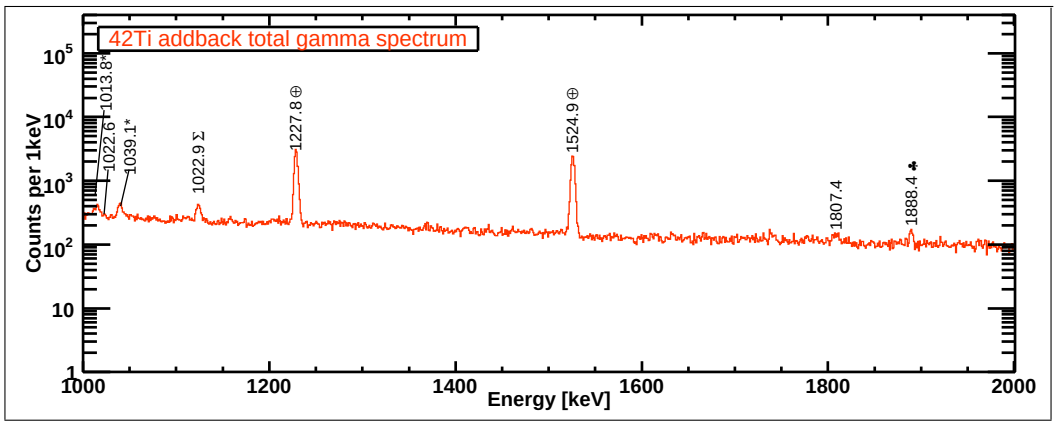

Figure 5.23: ^{42}Ti addback β-delayed γ-spectrum Part 2. Energy range: 1000-2000 keV.

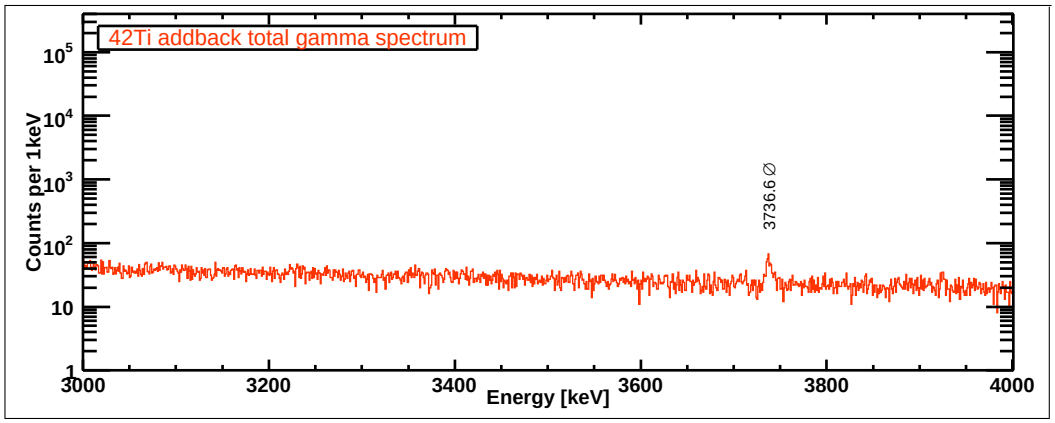

Figure 5.24: ^{42}Ti addback β-delayed γ-spectrum Part 4. Energy range: 3000-4000 keV.

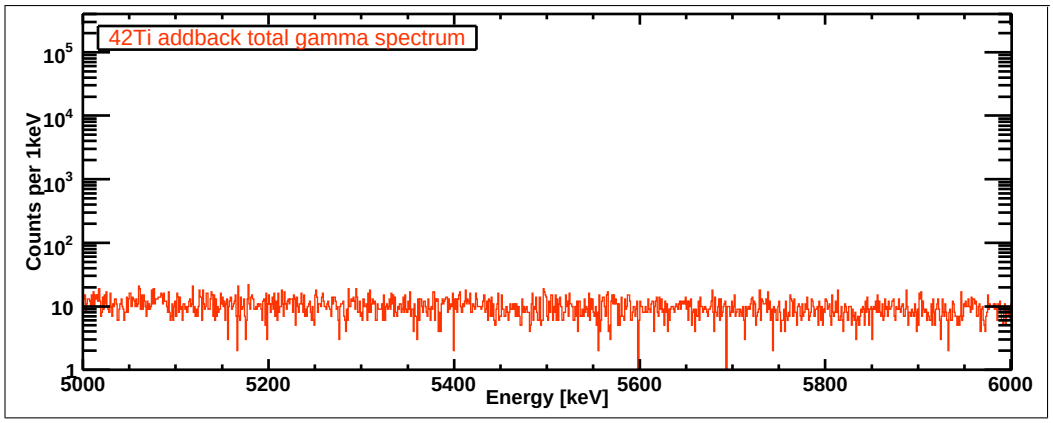

Figure 5.25: ^{42}Ti addback β-delayed γ-spectrum Part 6. Energy range: 5000-6000 keV.

Table 5.7: List of γ-ray energies for the ^{42}Ti setup at RISING in Single Crystal mode (sum of all crystals).

Energy[keV]	FWHM[keV]	Counts	I(γ)	Comments(*)
436.7 (0.0)	2.9 (0.0)	16840.6 (197.2)	253.39 (9.35)	$\oplus^{42}$Ca (^{42m}Sc β^+)
510.7 (0.0)	3.8 (0.0)	473394.8 (708.1)	7770.51 (272.22)	m_ec^2 (e^+e^-)
595.3 (0.9)	4.2 (0.3)	2692.3 (141.5)	48.30 (3.05)	$*^{74}$Ge (n-capture)
610.8 (0.0)	3.0 (0.0)	54894.5 (254.6)	**1000.00 (35.31)**	**$\clubsuit^{42}$Sc (^{42}Ti β^+)**
833.2 (0.1)	5.1 (0.3)	1975.8 (110.3)	43.56 (2.87)	$*^{72}$Ge (n-capture)
843.5 (0.3)	8.2 (1.0)	1293.7 (137.6)	28.75 (3.22)	$*^{27}$Al (n-capture)
1010.5 (0.3)	2.3 (0.6)	243.9 (60.7)	6.09 (1.53)	
1014.4 (0.2)	2.7 (0.4)	505.7 (68.6)	12.66 (1.77)	$*^{27}$Al (n-capture)
1038.5 (0.1)	4.5 (0.4)	1112.9 (91.4)	28.30 (2.53)	$*^{70}$Ge (n-capture)
1227.6 (0.0)	3.3 (0.0)	8907.8 (111.2)	253.43 (9.42)	$\oplus^{42}$Ca (^{42m}Sc β^+)
1524.8 (0.0)	3.6 (0.1)	7723.8 (101.5)	255.46 (9.55)	$\oplus^{42}$Ca (^{42m}Sc β^+)
1806.3 (0.6)	7.7 (1.3)	389.1 (85.0)	14.54 (3.22)	
1887.9 (0.2)	3.0 (0.5)	209.4 (36.0)	**8.08 (1.42)**	**$\clubsuit^{42}$Sc (^{42}Ti β^+)**
2167.3 (0.3)	4.6 (0.8)	315.5 (49.6)	13.50 (2.17)	$\square^{38}$Ar (^{38m}K β^+)
3736.2 (0.3)	4.8 (0.9)	147.2 (26.1)	9.80 (1.77)	$\oslash^{40}$Ca (^{40}Sc β^+)

(*) See Section 5.1.4 -p.95- for explanation.

5.1.2 ^{50}Fe run, γ-analysis

In the analysis of the data on mass 50 with the condition of a clean decay trigger in M2, we have observed the gamma lines shown in Tables 5.3 -p.84- (single crystal mode) and 5.4 -p.85- (addback mode). The addback spectrum is shown in Figs 5.8-5.13 -pp.82 to 83-.
The analysis, as in the mass 54 case, has two aims (i) First we need the gamma energies and intensities to extract the $B(GT)$ values to the different states populated in ^{50}Mn and (ii) it can be used for the identification of possible contaminants.
From the list of γ-ray lines, the 651.0 keV, 2403.1 keV and 2684.2 keV ($\clubsuit$) belong clearly to ^{50}Fe β-decay. This identification is based on (i) the literature: Koslowsky et al. [Kos97] have already observed the 651.0 keV gamma-peak and (ii) coincidence with the energies of levels observed in the ^{50}Mn(^{3}He,t)^{50}Fe CE reaction, by Y.Fujita et al. [Fuj05a].

In the following cases we identified the origin of possible γ-ray contaminants in the ^{50}Fe set-up β-decay γ-spectrum, and consider if these contaminations affect the analysis of the $T_{1/2}$ based on the implantation-beta correlations or not:

- ℵ The 90.5 keV and 152.8 keV γ-ray lines are the most intense γ-ray lines in the ^{49}Cr β-decay [Jac75]. The half-life of ^{49}Cr β-decay is 42.0 min.

Table 5.8: List of γ-energies for the ^{42}Ti setup at RISING in Add-back mode.

Energy[keV]	FWHM[keV]	Counts	I(γ)	Comments(*)
436.8 (0.0)	3.1 (0.0)	18637.6 (200.9)	239.21 (8.76)	$\oplus^{42}$Ca (^{42m}Sc β^+)
510.9 (0.0)	4.1 (0.0)	568233.4 (777.8)	7813.21 (273.67)	m_ec^2 (e^+e^-)
595.2 (0.1)	4.0 (0.4)	1496.9 (145.4)	22.11 (2.28)	$*^{74}$Ge (n-capture)
611.0 (0.0)	3.3 (0.0)	66866.5 (271.6)	**1000.00 (35.23)**	**$\clubsuit^{42}$Sc (^{42}Ti β^+)**
833.3 (0.1)	5.0 (0.4)	1380.7 (86.8)	24.12 (1.74)	$*^{72}$Ge (n-capture)
843.8 (0.3)	7.5 (0.9)	1060.2 (111.5)	18.64 (2.07)	$*^{27}$Al (n-capture)
1010.8 (0.4)	2.4 (1.2)	176.1 (68.6)	3.40 (1.33)	
1014.6 (0.2)	2.7 (0.8)	333.1 (80.7)	6.45 (1.58)	$*^{27}$Al (n-capture)
1038.7 (0.2)	4.8 (0.5)	814.2 (82.5)	15.96 (1.71)	$*^{70}$Ge (n-capture)
1122.9 (0.2)	5.0 (0.4)	968.2 (70.3)	19.78 (1.59)	Σ(510.9 + 611.0)
1227.8 (0.0)	3.8 (0.0)	11635.3 (134.6)	249.21 (9.19)	$\oplus^{42}$Ca (^{42m}Sc β^+)
1524.9 (0.0)	4.1 (0.0)	10255.5 (114.8)	246.72 (9.07)	$\oplus^{42}$Ca (^{42m}Sc β^+)
1807.4 (0.7)	6.8 (1.4)	231.8 (61.9)	6.12 (1.65)	
1888.4 (0.2)	3.5 (0.4)	271.6 (37.1)	**7.34 (1.03)**	**$\clubsuit^{42}$Sc (^{42}Ti β^+)**
2036.9 (0.5)	3.2 (1.5)	97.3 (64.3)	2.74 (1.81)	
2167.2 (0.2)	4.4 (0.5)	368.4 (41.5)	10.75 (1.27)	$\square^{38}$Ar (^{38m}K β^+)
2754.3 (0.5)	6.0 (2.1)	147.6 (51.6)	4.95 (1.74)	
3736.6 (0.3)	6.0 (1.0)	218.5 (36.5)	8.94 (1.52)	$\oslash^{40}$Ca (^{40}Sc β+)

(*) See Section 5.1.4 -p.95- for explanation.

$\oplus$ The 661.9 keV, 783.2 keV, 1098.1 keV, 1282.5 keV and 1442.4 keV γ-ray lines belong to ^{50}Cr produced in the β-decay of ^{50m}Mn. The half-life of this isomeric state is 1.75(3) min [Ram72]. It is also important to note that this contamination was also present in the ^{54}Ni β-decay spectra although the weakest γ-ray lines of 661.9 keV and 1282.5 keV energy were not seen.

∇ The 752.2 keV, 1106.4 keV, 1366.6 keV, 3677.3 keV, 3935.7 keV γ-ray lines were identified as belonging to ^{48}Cr, produced in the decay of ^{48}Mn [Sek87]. In this case the half-life of the ^{48}Mn β-decay is 150(10)ms. It is important to note the good agreement with the energies quoted in the literature up to 4 MeV [Sek87]. Our values and the literature values agree within 1 keV.

® The 1157 keV line was identified as an E2 $2^+ \rightarrow 0^+$ transition in ^{44}Ca most probably coming from the β-decay of the 3.92 h, 2^+ isomeric-state in ^{44}Sc [CM76]. This nucleus, ^{44}Sc, also has a long-lived 2.4 day 6^+ isomer which decays to the 2^+ state by an internal E4 transition and β-decays to the 2283.1 keV (4^+) and 3301.3 keV (2^+) states in ^{44}Ca, both of which decay to the 1157.0 keV (2^+) level. None of the gamma peaks associated with the decay of the 2.4 day isomer were found in our spectra.

$\square$ The 1433.8 keV γ-ray may be the $2^+ \rightarrow 0^+$ transition in ^{52}Cr, which can be populated either by the 21.3 min β-decay of the ^{52m}Mn isomer or by the 5.59 day β-decay of the ^{52g}Mn [Yaf77]. The presence of ^{52g}Mn decay cannot be the reason

because, if so, we should also see the 935.5 keV line with 94% of the intensity of the 1433.8 keV line.

‡♣ The 1603.7 keV and 1883.8 keV γ-rays probably belong to the ^{50}Fe β-decay studied here. They are internal transitions from the states at 2403.8 keV (1^+) and 2684.2 keV (1^+) respectively, to the 799.6 keV (2^+) state which compete with γ-decays to the ground state. The main argument for this assignment is the energy matching.

♣ The 3380.0 keV, 3643.4 keV, 4012.7 keV and 4315.7 keV γ-ray lines do not correspond to any possible contaminant. In Fujita's CE reaction studies, peaks at 3390 keV, 3654 keV, 4028 keV and 4332 keV were identified as states in ^{50}Mn populated in the (^{3}He,t) reaction with angular momentum transfer L=0. Assuming that the differences in energy are due to a possible systematic error in the CE energy calibrations, we can assume that our observed γ-ray transitions belong to the decay of ^{50}Fe and correspond to de-excitations of levels of the same energy as the ground state.

• We could not identify the origins of the lines with the following γ-ray energies: 683.4 keV, 692.5 keV, 1461.7 keV, 1524.8 keV, 1565.3 keV, 2868.6 keV and 3047.4 keV.

As in the case of ^{54}Ni β-decay, it is very important to notice that this is the first time that it has been possible to see more than one excited state in ^{50}Mn in a β-decay experiment. Again this is possible thanks to the overwhelming production of the parent nuclei in the fragmentation reaction at GSI and the excellent efficiency of the RISING array. The β-decay level scheme using the results from this experiment is shown in Fig. 6.2 -p.135-.

5.1.3 ^{46}Cr run, γ-analysis

In the analysis of the data on mass 46 with the condition of a clean decay trigger in M2, we have observed the gamma lines shown in Table 5.5-p.88- (single crystal mode) and Table 5.6 -p.89- (addback mode). The addback spectrum is shown in Figs 5.14-5.19 -pp.86-87-.
As for the previous masses the aim of the analysis, is two fold (i) Firstly we need it to extract the $B(GT)$ values to the different states populated in ^{46}V and (ii) to identify possible contaminants.
Amongst the observed gamma lines , the 993.2 keV, 1432.5 keV, 1544.4 keV, 2062 keV, 2697.4 keV, 2977.8 keV and 3867.6 keV γ-rays (♣) belong to ^{46}Cr β-decay. This identification is based on (i) the literature: T.K.Onishi et al. [Oni05] have already observed the 993 keV gamma-peak and (ii) coincidence with the energies of levels obtained from the ^{46}Ti(^{3}He,t)^{46}V CE reaction results of T.Adachi et al. [Ada06].
In the following we identified possible contaminants in the ^{50}Fe β-decay γ-spectrum:

⊕ The 437.0 keV, 1227.8 keV and 1524.8 keV γ-rays belong to the ^{42}Ca nucleus produced in the ^{42m}Sc β-decay [Uzu94]. The half-life of ^{42m}Sc is 61.5 s.

⊕ The 1157.0 keV γ-line also belongs to ^{42}Ca but it is populated in the β-decay of ^{42g}Sc [Gal69].

$\aleph\nabla$ The 1083.2 keV, 1370.1 keV, 1448.3 keV, 1561.3 keV, 3033.0 keV, 4073.5 keV and 5522.6 keV belong to ^{44}Ti, they were populated either in the β-decay of ^{44g}V or ^{44m}V [Hag97]. For the decay of ^{44g}V we can see γ-rays up to 5.5 MeV. Our values and the literature values coincide within 2 keV, which gives us confidence in our γ-ray calibration extrapolation.
The β-decay half-lives of ^{44g}V or ^{44m}V are 111 ms and 150 ms respectively.

?$\aleph$ The 2533.0 keV line probably belongs to the decay of ^{44g}V into ^{44}Ti (2530.9 keV in literature), but it was only seen in the add-back spectrum.

$\square$ The 2168.0 keV γ-line belongs to ^{38}Ar populated in the β-decay of ^{38}K [Man76]. The half-life of this contaminant is 7.64 min, so it is not relevant as a half-life contaminant.

$\clubsuit$ We assign the 2459.8 keV and 2466.3 keV γ-rays to the decay of ^{46}Cr in ^{46}V. In the CE reaction experiment a 2461 keV peak was observed with L=0, as reported in [Ada06]. Since the Grand Raiden spectrometer has a resolution around 30 keV it is impossible to separate these two energies.

$\ddagger\clubsuit$ The 1544.4 keV and 2062 keV γ-ray lines belong to the $1^+ \rightarrow 2^+$ internal transitions in ^{46}V, from the 2459.8 keV and 2977.8 keV 1^+ states to the 915.0 keV 2^+ state which decays in turn to the 0^+ ground state.

It is important to note that this is the first time that more than one 1^+ state in the daughter nucleus is seen in β-decay experiments on ^{46}Cr. The β-decay level scheme derived from the results of this experiment is shown in Fig. 6.3 -p.136-.

5.1.4 ^{42}Ti run γ-analysis

In the analysis of mass 42 with the condition of a clean decay trigger in M2, we have observed the gamma lines shown in Table 5.7 -p.92- (single crystal mode) and Table 5.8 -p.93- (addback mode).
The aim of the analysis as for the previous masses, is two fold (i) Firstly we need it to extract the $B(GT)$ values to the different states populated in ^{42}Ti and (ii) it can be used for the identification of possible contaminants.
The observed 611.0 keV and 1888.4 keV γ-rays ($\clubsuit$) belong to ^{42}Ti β-decay. This identification is based on (i) the literature: T. Kurtukian-Nieto et al. [Kur09] have already observed the first excited state at 611 keV and (ii) coincidence with the level energies obtained from the ^{42}Ca(^{3}He,t)^{42}Sc CE reaction results from T.Adachi et al. [Ada07c].
In the following cases we identified the origins of possible γ-ray contaminants in the ^{42}Ti β-decay γ-spectrum:

$\oplus$ The 436.8 keV, 1227.8 keV and 1524.9 keV γ-rays belong to the ^{42}Ca nucleus produced in the ^{42m}Sc β-decay[Uzu94], as well as in the mass 46 case. The half-life of the ^{42m}Sc is 61.5 s.

$\square$ The 2167.2 keV γ-line belongs to ^{38}Ar populated in the β-decay of ^{38m}K [Man76]. The half-life of this contaminant is 7.64 min.

⊘ The 3736.6 keV γ-ray belongs to ^{40}Ca populated in the β-decay of ^{40}Sc. The half-life of the ^{40}Sc is 182.3 ms.

It is important to note that this is the first time that more than one 1^+ state in the daughter nucleus is seen in β-decay experiments on ^{42}Ti. The β-decay level scheme using the results of this experiment is shown in Fig. 6.4 -p.137-.

With the γ-analysis results presented here, we constructed β-decay level schemes of Figs. 6.1-6.4 -pp.134 to 137-. They include level energies, gamma de-excitations including intensities and energies with errors and J^π assignments. The γ-intensities were also used to calculate the direct β-feeding to each excited state together with the ground state feeding which will be discussed in Section 5.4 -p.126-.

5.2 β-decay half-life analysis

A precise β-decay half-life value is one of our main aims in this experiment. In the following we will describe the analysis of implant-beta correlations carried out in order to obtain a half-life value for the ground states of the four cases of interest.

An ion was produced in the fragmentation reaction, selected in the FRS, and implanted in the DSSSD in a period of time negligible in comparison with its half-life. After some time a beta-decay is expected. If we are able to correlate the implantation time in a specific pixel with the decay time in the same pixel, we can calculate statistically the β-decay half-life using the Bateman equations,

$$A(t) = N_o \lambda \exp(-\lambda t) \tag{5.1}$$

where $A(t)$ is the beta-activity at time t, N_o is the initial number nuclei and $\lambda = \ln(2)/T_{1/2}$ is the decay constant. The activity can be obtained experimentally from the correlations between the implants and the associated decay. The question is how to obtain the true correlations if random correlations are expected, as in the present case. In other words, how does one correlate in a precise and correct way an implantation with its corresponding decay.

To approach the right answer, we established some general criteria. Thus

- An implantation event is defined by the implantation event trigger (see Section 4.3.1 -p.56-) and its energy must be in the implantation energy range in the DSSSD strip (see Section 4.3.2 -p.57-).
- A decay is defined by the decay event trigger (see Section 4.3.1 -p.56-) and its energy must be in the decay energy range in the DSSSD strip (see Section 4.3.2 -p.57-).
- Implantation-decay time correlations are defined as time differences between implantation and decay events occurring in the same DSSSD pixel (formed by an X-strip and a Y-strip) and requiring the presence of the energy signal

First of all let us examine the statistics presented in Table 5.9 -p.97-.

Run	Total Measurement Time	Total Number of Implantations	Counting rates in M2 [ions/sec]	Counting Rates per Pixel[ions/sec]	Peak to background in $T_{1/2}$ analysis in $1T_{1/2}$ interval
^{54}Ni	2151 min	6.38 10^6	Imp. 50.4 Decay 62.9	$\sim$ 0.47 $\sim$ 0.59	29.6 %
^{50}Fe	1402 min	2.80 10^6	Imp. 33.8 Decay 40.4	$\sim$ 0.23 $\sim$ 0.38	26.3 %
^{46}Cr	1140 min	3.3 10^6	Imp. 45.3 Decay 74.2	$\sim$ 0.40 $\sim$ 0.66	52.5 %
^{42}Ti	531 min	6.46 10^5	Imp. 20.7 Decay 32.8	$\sim$ 0.17 $\sim$ 0.26	28.0 %

Table 5.9: Statistics for the different runs in DSSSD M2. The counting rate per pixel was calculated for the 64 beam-centred pixels in M2.

As we see the counting rate for implants and decays per pixel (an average for the 64 beam-centred pixels) is of the order of 0.5 counts/sec. This is relatively high if we aim to precise (less than 1%) value of the $T_{1/2}$.

In the following we describe the analysis of implant-beta correlations carried out in order to obtain a half-life value for the ground states of the four cases of interest.

5.2.1 Immediate time correlations

At the beginning of the analysis we used the RISING on-line program, CRACOW [Gre07]. This program presents many advantages for sorting large numbers of list-mode files with the corresponding calibration files and produces the required spectra, but it was not written to correlate implantations and beta events, because the main aim of the program was to provide an on-line analysis tool. In principle the immediate time correlation method may work if the randoms can be neglected, which is not the present case, or if they can be taken into account analytically. In the present analysis we decided to correlate all decays with all implants as we will explain in the next section.

5.2.2 All Betas/All Implantations (ABAI) time correlations

The "All Betas/All Implantation" time correlation method ABAI is a statistical method which consists in correlating each beta with all past and future implantations in a given time window. This method is used for example in Dossat et al.'s work on the decay of proton-rich nuclei [Dos07]. In order to understand it, we could imagine a constant radioactive ion rate, which decays in one step to the line of stability, implanted in a pixel of the DSSSD. Beta-decays could occur between two implantations, between two decays or between an implantation and a decay (or vice-versa). If we measure the time difference between one of these decays and all the previous N implantations, one will be the correct correlation. In addition to the one good correlation, we will have $(N-1)$ wrong correlations. Thus measuring the time differences between all the decays and all

the implants detected during the experiment per pixel of the DSSSD, we will finally obtain the typical exponential decay curve on top of a large constant flat background (See Fig. 5.26 -p.98-). How large the background is will clearly depend on the counting rates.

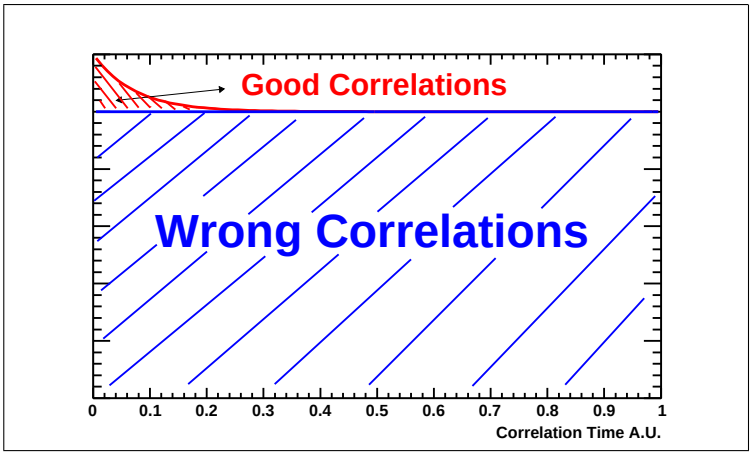

Figure 5.26: Good and wrong correlations using the All Betas/All Implantation method. The red area corresponds to the good correlations. The blue area contains the wrong correlation events which correspond to correlations with random events.

In our case the situation is slightly more complicated because (i) the implantation rate is not constant, and depends on the primary beam spill period from the synchrotron, (ii) the implanted ion has two decays until the line of stability is reached (iii) the dead-time of the acquisition system may affect the correlations.

Correlation Procedure

The correlations were done for all 256 pixels of DSSSD detector M2 situated at the centre of the Si detector array. We chose only this detector because the settings were optimised in such a way that the majority of the ions for the four nuclei of interest were implanted in the middle of this detector [the beam illuminates only the middle detectors (M1, M2 and L2)].
Implantation identification conditions were set in order to correlate betas only with the desired ion. On the other hand, betas cannot be identified. Thus all betas were correlated with all correctly identified implanted ions. If the correlation is done for the betas and implantations in the same pixel (i, j), where i is the i-th X-strip and j is the j-th Y-strip, then good and wrong time correlations will be included as shown in Fig. 5.26 -p.98-.

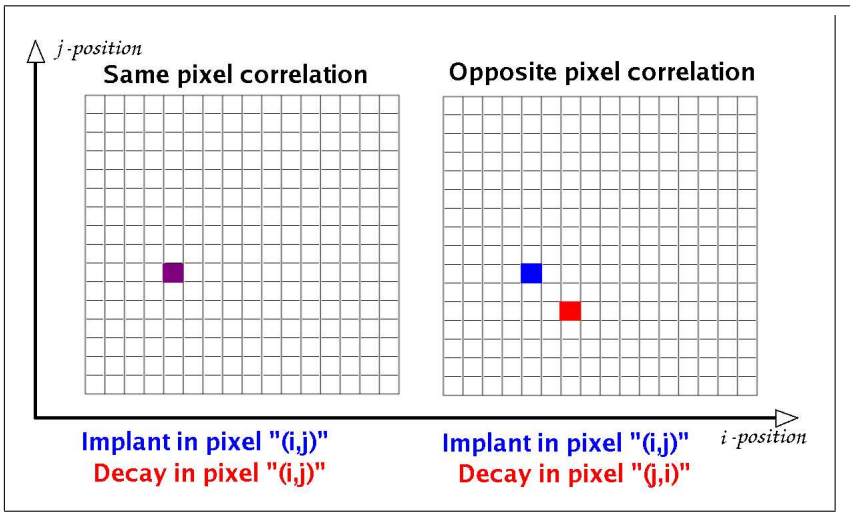

Figure 5.27: Schematic picture of the "Same" (good and wrong correlations can be found) and "Opposite" (wrong correlations only can be found) pixel correlations.

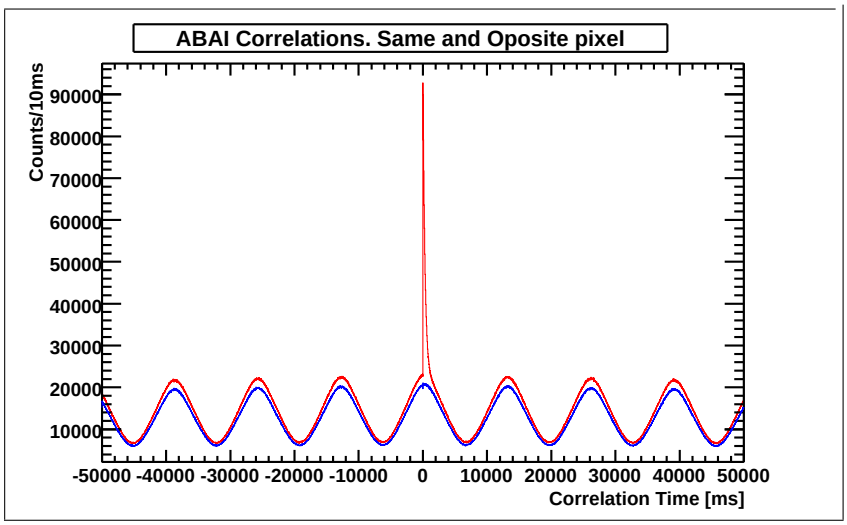

Figure 5.28: Same (red) and opposite (blue) pixel time correlations corresponding to the full statistics for ^{54}Ni in a $\pm$50 s time correlation window

As mentioned before, in our case we could not assume a constant background produced by the randoms because the ions were implanted with a time structure, the beam spill of the SIS synchrotron (see for instance Fig. 5.32 -p.103-). Consequently a method has to be defined in order to reproduce the background. In our case it was done in the following way. It is possible to create wrong correlations (i.e. random background), by correlating a beta decay with an implantation which belongs to a different pixel. In our analysis we correlate a beta decay in pixel (j, i) with an implantation in pixel

(i, j), except when i=j (see Fig. 5.27 -p.99-) . For all the four nuclei studied, the main source of wrong correlations is β-decay events from our own selected nuclei, due to its high production rate in comparison with other contaminants implanted (see Table 4.4 -p.59-). The opposite pixel correlations will give us good information on the shape of the wrong correlation background.
As an example of the method, the "same" and "opposite" pixel correlations for the ^{54}Ni analysis are shown in Fig. 5.28 -p.99-. As expected we see in this figure that the background is not flat as in Fig. 5.26 -p.98-. For all four cases the background produced by wrong correlations due to differences in the implantation rate followed the period of the spill, namely 13 sec (10 sec of primary beam on target and 3 sec of primary beam off target). Further details are given in Appendix E -p.235-.

In all four cases the background of wrong correlations has a similar shape, which means that the origin of the wrong correlations is the same. We can normalise the opposite-pixel correlations to the same-pixel correlations by the ratio between the integrals of both spectra in the region from 10s to 50s. As we can see in Fig. 5.29 -p.100- the shape of the oscillating background is perfectly reproduced.

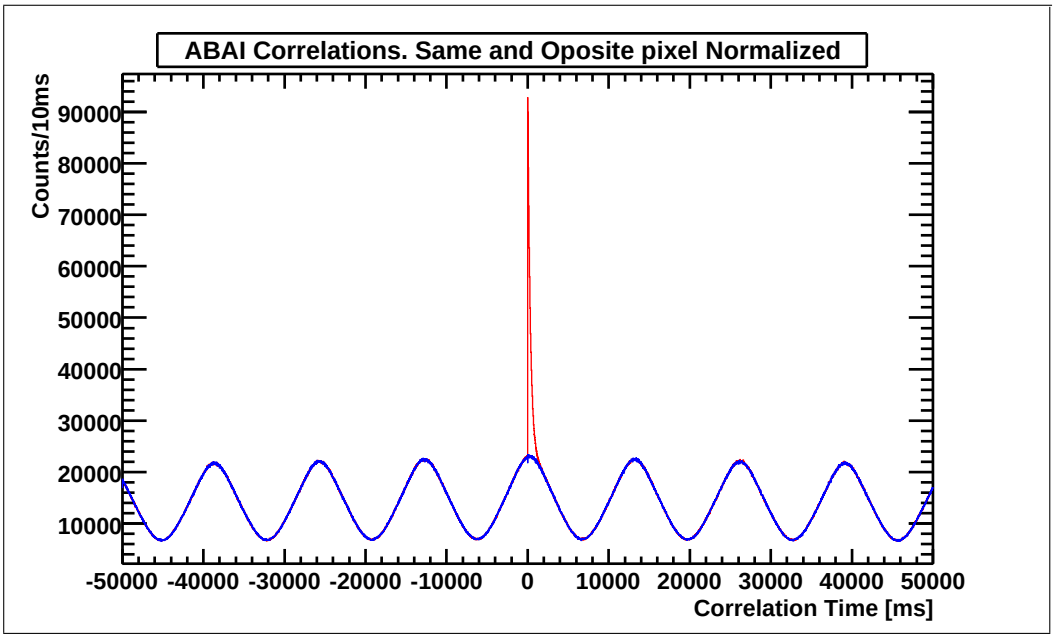

Figure 5.29: Same (red) and opposite (blue) pixel time correlations corresponding to the full statistics for ^{54}Ni in a $\pm$50 s time correlation window. Opposite pixel correlations are normalised by a factor of 1.11206. The same (red) and opposite (blue) correlation curves are indistinguishable except for the interval associated with the activity under study.

The background was subtracted using 10 ms bins. The result is presented in Fig. 5.30 -p.101-. Error bars associated with this subtraction are also included. As expected the resulting 'true' correlations are now sitting on a flat background close to zero counts. After the subtraction we will have all the betas in the time window correlated with an

identified ^{54}Ni implantation (true correlations). However the beta could belong to the β-decay of ^{54}Ni $\rightarrow$ ^{54}Co or to the β-decay of ^{54}Co $\rightarrow$ ^{54}Fe. A decay function, from the decay of the mother nucleus, and the growth and decay of the daughter nucleus (Eq. 5.2 -p.101-) is fitted to the "true correlations" according to the Bateman equations.

$$\begin{aligned} A(t) &= N_0\lambda_m\left(\exp(-\lambda_m t)\right) \\ &\quad + N_0\lambda_m\left(\frac{\lambda_d}{\lambda_d-\lambda_m}\left(\exp(-\lambda_m t)-\exp(-\lambda_d t)\right)\right)+C \end{aligned} \tag{5.2}$$

where if $t > 0$, $A(t)$ is the activity at time t, N_0 is the initial number of mother nuclei, λ_m and λ_d are the corresponding decay constants of the mother and daughter nuclei and C is the constant background. If $t < 0$ only the constant background C is adjusted.

For all four cases of interest, the daughter nuclei decay by a well known, super-allowed transitions, and the associated half-lifes $T^d_{1/2}$ are known precisely. Then from Eq. 5.2 -p.101- we can find the mother half-life $T^m_{1/2}$ and the number of initial, good correlated implantations N_0. The fit for ^{54}Ni beta-decay is shown in Fig. 5.31 -p.102-.

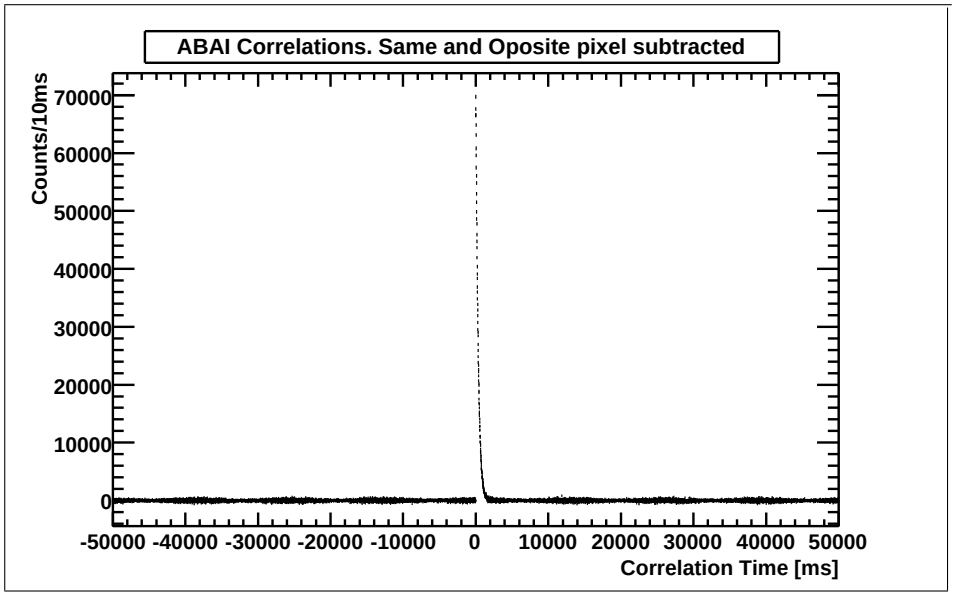

Figure 5.30: Same (red) and opposite (blue) pixel time correlations corresponding to the full statistics for ^{54}Ni in a $\pm$50 s time correlation window. The normalised opposite-pixel spectrum is subtracted from the same-pixel spectrum bin by bin. Each 10ms bin includes the error bar associated with the subtraction

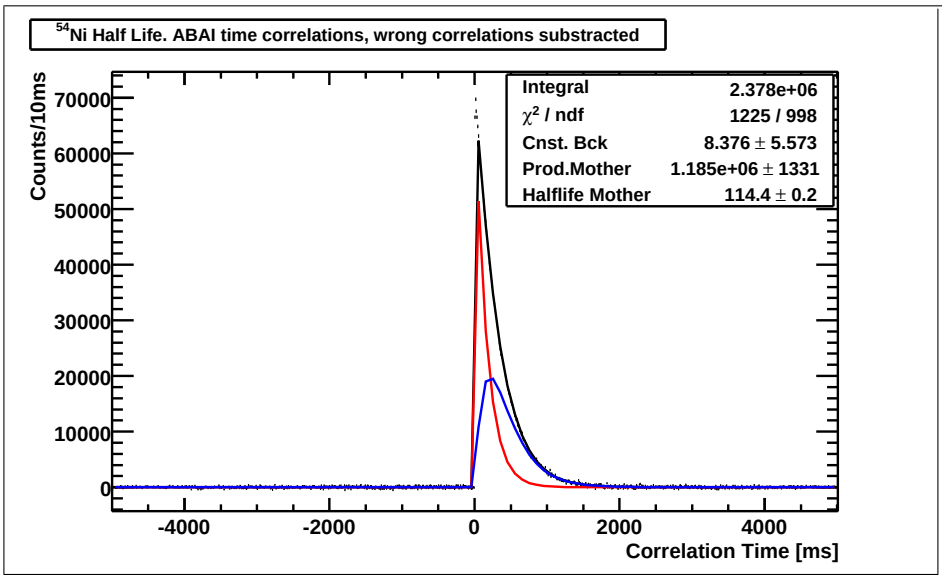

Figure 5.31: True correlations fitted by Eq. 5.2 -p.101- in black. Mother beta-decay curve in red, daughter beta growth and decay curve in blue. In this case the minimisation of the function was done using the least squares method

The fitted function was minimised using the ROOT minimisation package MINOS by two standard methods; the Maximum Likelihood (ML) and the Least Squares (LS) methods, but this will be discussed later. In the inset to the figure we show the integral in the range shown, the χ^2 over the number of degrees-of-freedom (ndf), and the three fitted parameters: The constant background, the production of mother nuclei (the same as the total numbers of mother beta-decays when $t \rightarrow \infty$) and the mother half-life $T^m_{1/2}$. We expect the integral number of counts to be approximately twice the total decays of the mother nuclei. The reason is that for each implantation two β-particles are emitted and the probability of detecting one or the other must be very similar since the mother and the daughter Q_β-values are very similar. As we see in Fig. 5.31 -p.102- this expectation is fulfilled. The $T_{1/2}$ obtained is 114.4(2) where the error only reflects the fitting error.

5.2.3 Possible sources of systematic error in the half-life determination

In order to determine the systematic error we studied two possible sources : 1) Possible changes in the acquisition dead-time and 2) the β-decaying implanted nuclei (contaminants) with half-lives close to those of the nuclei we observe.

Dead-time corrections

The dead-time is the time that the electronic acquisition system needs to process an incoming event. All acquisition systems working with trigger signals to process a buffer of data suffer from dead-time, but the real problem of concern here is not the

dead-time itself, but fluctuations in dead-time, which could lead to a time dependence in the correlations between an implantation and the subsequent decay. To avoid this possibility, we restricted our analysis to the implantation-events occurring during the spill period, selecting the time region where we consider that these events do not suffer significant fluctuations (see Figs. 5.32- 5.35 -pp.103 to 105-). Then the acquisition dead-time should be constant on average.
Sorting the data with the implantation in this part of the spill and making the correlations using the ABAI method with a least squares (LS) minimisation we obtain a half-life.
In Table 5.10 -p.105- we compare the values of the half-life using the complete spill and the "plateau" range. Here we can observe that the half-life values differ by ∼0.2 ms but the statistical error from the fit increases by the same amount due to the fact that there are fewer β-implantations and hence poorer statistics. Although the $T_{1/2}$ values are not very much affected we decided to use the range inside the spill.

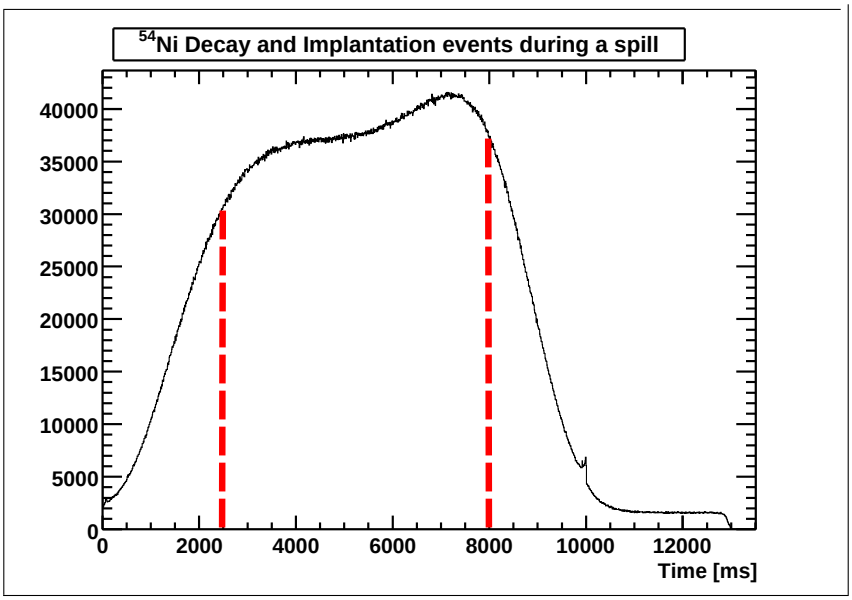

Figure 5.32: Time difference between the beginning of the spill and the time-stamp of a decay trigger or implantation trigger during the measurement of the ^{54}Ni. The time-region selected was 2500-8000 [ms]

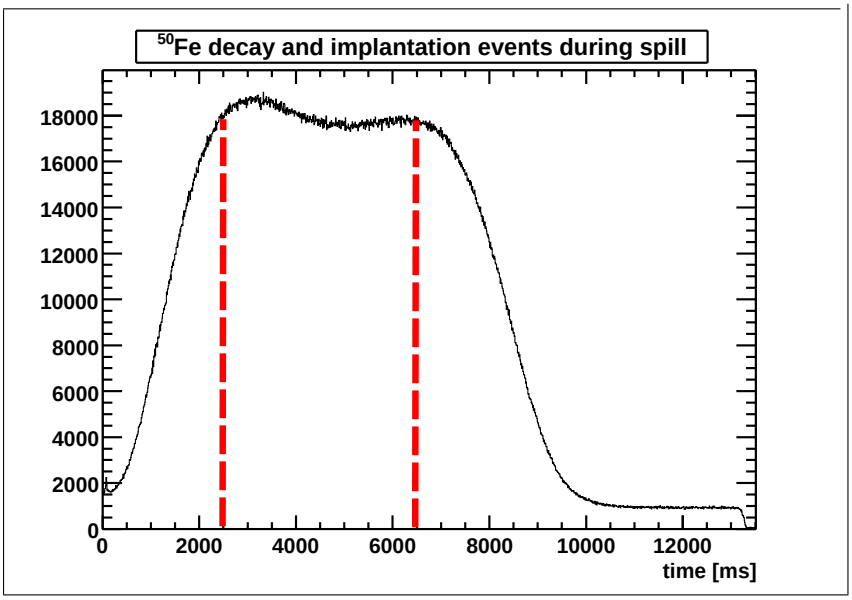

Figure 5.33: Time difference between the beginning of the spill and the time-stamp of a decay or implantation trigger during the measurement of the ^{50}Fe setup. The time-region selected was 2500-6500 [ms]

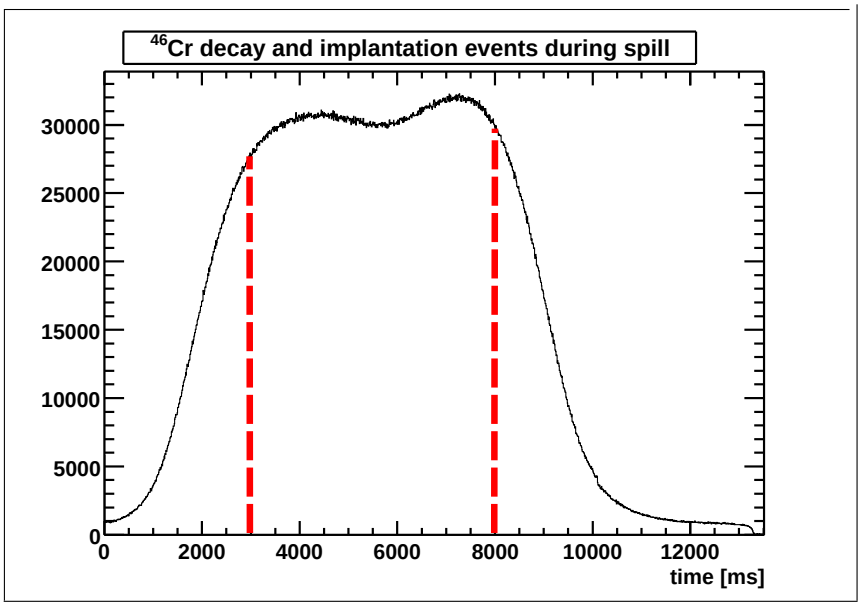

Figure 5.34: Time difference between the beginning of the spill and the time-stamp of a decay or implantation trigger during the measurement of the ^{46}Cr setup. The time-region selected was 3000-8000 [ms]

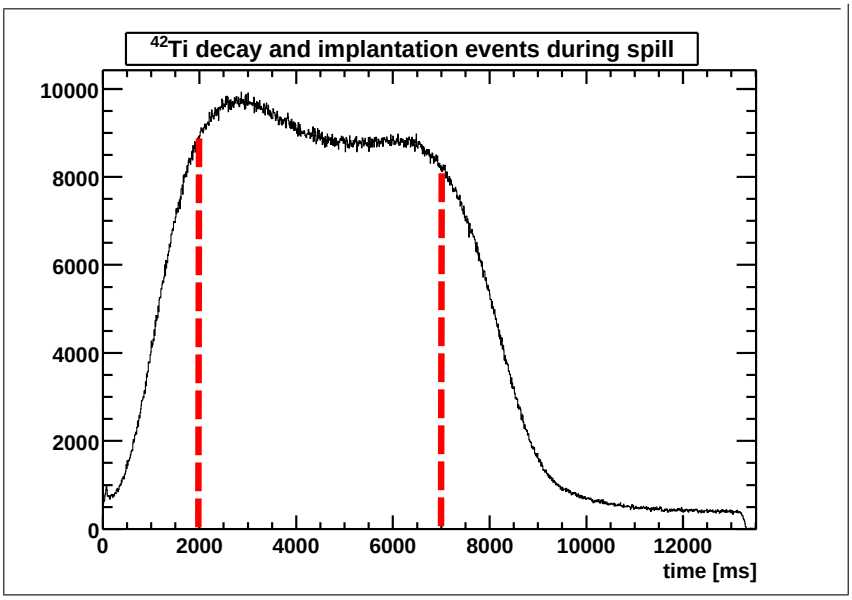

Figure 5.35: Time difference between the beginning of the spill and the time-stamp of a decay or implantation trigger during the measurement of the ^{42}Ti setup. The time-region selected was 2000-7000 [ms]

	Full range $T^{\beta}_{1/2}$ ms	Selected range $T^{\beta}_{1/2}$ ms
^{54}Ni	114.4(2)	114.2(3)
^{50}Fe	152.5(5)	152.1(6)
^{46}Cr	225.9(10)	224.2(13)
^{42}Ti	211.5(15)	211.7(19)

Table 5.10: Half-life measurements with ABAI correlations in M2, with the complete statistics and using a selected range within the spill period.

The effect of β-contaminations in the time spectra

Another possible source of systematic error is the presence of contaminant nuclei with a $T_{1/2}$ similar to the one we want to determine. These possible contaminant nuclei were identified by the associated γ-ray. See Section 5.1.
However, since all of them belong to nuclei with different values of either Z or A/Q, they will lie in different regions of the identification plot and will be excluded from the analysis. Of course, the β-decay will contribute to the random background but will be subtracted as already explained.

5.2.4 β half-life results

The β-decay half-life was obtained by correlating a β-decay event in a pixel of DSSSD M2 for all the identified implants, in the selected range within the spill period (see Section 5.2.3 -p.102-). For the nuclei of interest, i.e. selecting the nucleus as described in Section

4.3.2 -p.57- Figs. 4.20- 4.23 -pp.60 to 61-, the random background of correlations, as explained in Section 5.2.2 -p.98-, was subtracted for each pixel, and the decay curve was fitted according to the Bateman equations for a parent nucleus decaying into a daughter nucleus which also decays (Eq. 5.2 -p.101-). As the daughter nuclei (^{54}Co, ^{50}Mn, ^{46}V and ^{42}Sc) undergo superallowed β-decay, the daughter half-life $T^d_{1/2}$ is well known. The values used in the fit were taken from a recent re-evaluation of the available experimental half-life results done by J.C. Hardy and I.S. Towner [HT09].
Three parameters are minimised in the fit: 1) The half-life value for the mother nuclei $T^m_{1/2}$, 2) the initial number of well correlated mother nuclei with a β-particle detected in the same DSSSD pixel (called "production of mother"' in the fit) and 3) the constant value of the flat background.
Another important issue is the minimisation method for Eq. 5.2 -p.101- . We used two different minimisation methods: the Least Squares method (LS) and the Maximum Likelihood method (ML).

In Table 5.11 -p.106- we summarise the results for the pf-shell, T_z=-1 β-decay half-lives measured at GSI in the present experiment, and compare them with experimental values in the literature. There is a perfect agreement between our values and the literature values, but the present values are more precise, with the exception of ^{42}Ti. In the following we discuss each individual case separately.

	$T^{LS}_{1/2}$ [ms]	$T^{ML}_{1/2}$ [ms]	$T^{Av}_{1/2}$ [ms]	Lit. $T_{1/2}$ [ms]
^{54}Ni	114.2(3)	114.1(2)	114.2(3)	106(12) [Reu99b]
^{50}Fe	152.1(6)	152.2(6)	152.2(6)	155(11) [Kos97]
^{46}Cr	224.3(13)	223.9(11)	224.1(12)	240(140) [Oni05]
^{42}Ti	211.7(19)	211.2(39)	211.5(29)	208.14(45) [Kur09]

Table 5.11: β-decay half-life results and comparison with values in the literature. $T^{LS}_{1/2}$ is the half-life obtained using a least square minimisation, $T^{ML}_{1/2}$ is the half-life obtained using a maximum likelihood minimisation and $T^{Av}_{1/2}$ is the average of $T^{LS}_{1/2}$ and $T^{ML}_{1/2}$. The error in $T^{Av}_{1/2}$ is the simple average of the $T^{LS}_{1/2}$ and $T^{ML}_{1/2}$ errors.

^{54}Ni β-decay half-life

The ^{54}Ni β-decay half-life was measured by I. Reusen et al. [Reu99b] in the ^{54}Fe(^{3}He,3n)^{54}Ni fusion-evaporation reaction at the LISOL facility in Louvain-la-Neuve, Belgium. Studying the decay curve of the 937 keV γ-ray peak, they obtained a half-life value of $T_{1/2}$= 106(12) ms.
We also studied it in a previous experiment at the same facility (see Chapter 3 -p.25-), obtaining a half-life value of $T_{1/2}$=114.0(79) ms. The ^{54}Ni β-decay results from this experiment are shown in Fig. 5.36 -p.108- (least squares minimisation) and Fig 5.37 -p.109- (maximum likelihood minimisation), and presented in Table 5.11 -p.106-.

^{50}Fe β-decay half-life

The ^{50}Fe β-decay half-life was measured by Koslowsky et al. [Kos97] in a fusion-evaporation reaction [Ca^{nat}(^{12}C,3n)^{50}Fe], at the Chalk River TASCC facility, Ontario,

Canada. Studying the decay curve of the 651 keV γ-ray peak, they obtained a half-life value of $T_{1/2}$= 155(11) ms.
The ^{50}Fe β-decay results from this experiment are shown in Fig. 5.38 -p.110- (using a least squares minimisation) and Fig. 5.39 -p.111- (using a maximum likelihood minimisation), and presented in Table 5.11 -p.106- .

^{46}Cr β-decay half-life

The ^{46}Cr β-decay half-life was measured by T.K. Onishi et al. [Oni05] in a fragmentation reaction involving a ^{50}Cr beam on a ^{9}Be target, at RIKEN, Japan. Studying the decay curve for the 993 keV γ-ray peak, they obtained a half-life value of $T_{1/2}$= 240(140) ms.
The ^{46}Cr β-decay results from this experiment are shown in Fig. 5.40 -p.112- (using a least squares minimisation) and Fig. 5.41 -p.113- (using a maximum likelihood minimisation), and presented in Table 5.11 -p.106-.

^{42}Ti β-decay half-life

The ^{42}Ti β-decay half-life was recently measured by T. Kurtukian et al. [Kur09] in a fusion-evaporation reaction [^{nat}Ca(^{3}He,1n)^{42}Ti], at IGISOL, Jyväskylä, Finland. Studying the β-decay of the ^{42}Ti parent -and the daughter ^{42}Sc activity- separated in a Penning trap, they obtained a half-life value of $T_{1/2}$= 208.14(45) ms.
The ^{42}Ti β-decay results from this experiment are shown in Fig. 5.42 -p.114- (using a least square minimisation) and Fig. 5.43 -p.115- (using a maximum likelihood minimisation), and presented in Table 5.11 -p.106-.

In general we have improved the precision of the $T_{1/2}$ value by at least two orders-of-magnitude, except in the case of ^{42}Ti as mentioned above.

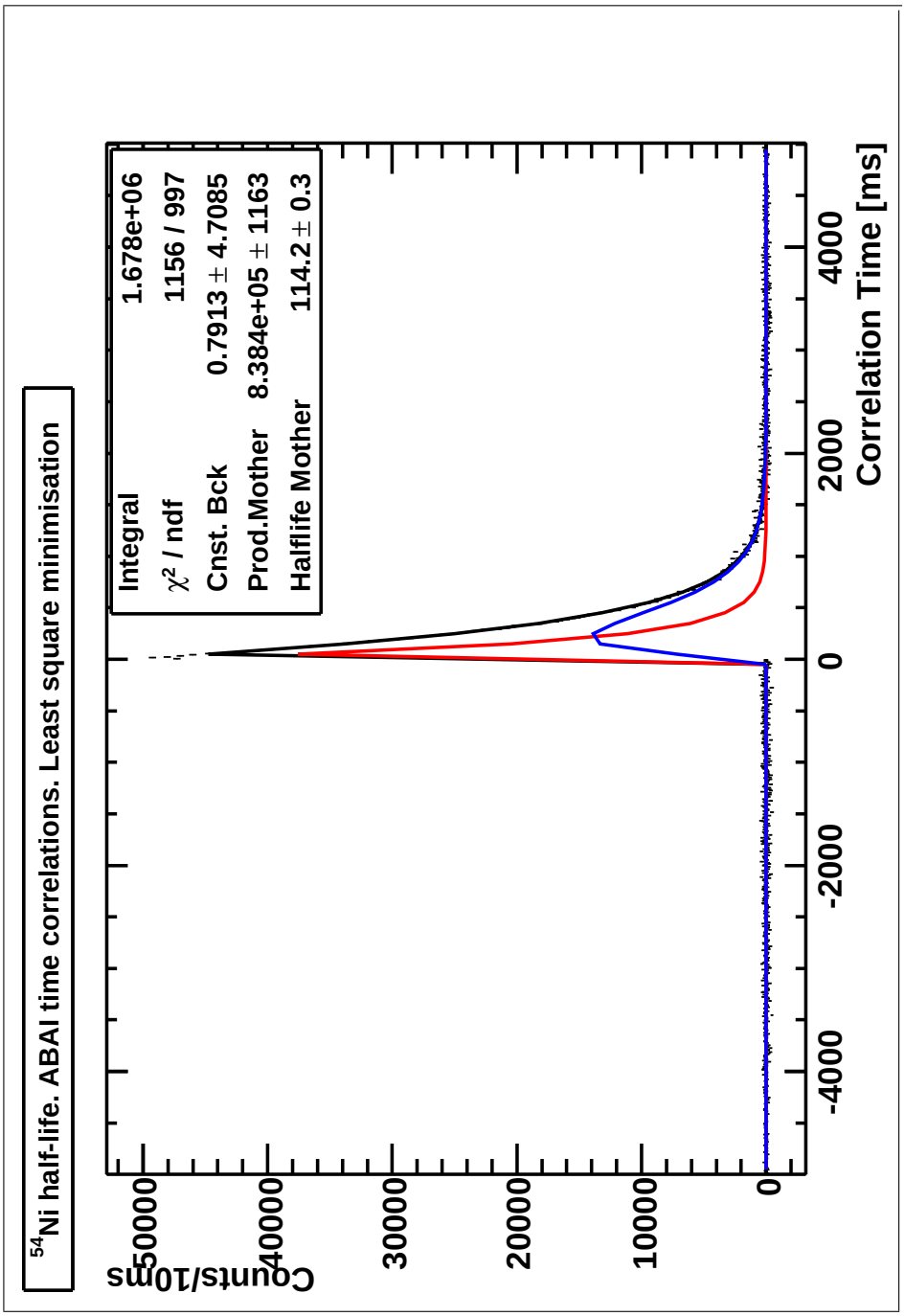

Figure 5.36: ^{54}Ni β-decay half-life for implant-beta correlations using a least squares minimisation. The red curve represents the decay of the mother nucleus ^{54}Ni and the blue curve represents the growth and decay curve of the ^{54}Co superallowed β emitting daughter nucleus. The daughter half-life is $T^d_{1/2}$= 193.271(63) ms [HT09], and is a fixed parameter in the fit.

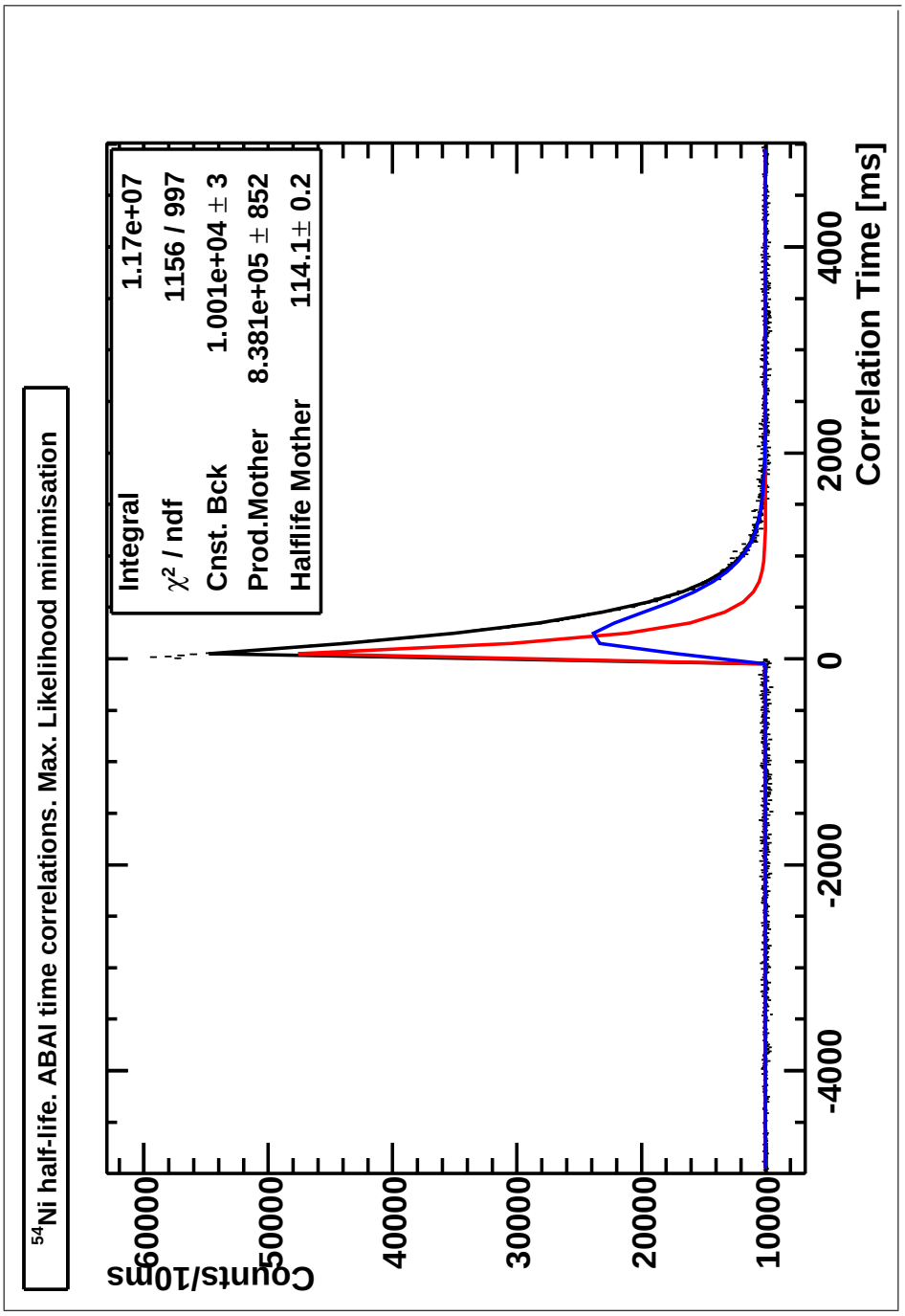

Figure 5.37: ^{54}Ni β-decay half-life for implant-beta correlations using a maximum likelihood minimisation. The red curve represents the decay of the mother nucleus ^{54}Ni and the blue curve represents the growth and decay curve of the ^{54}Co superallowed β emitting daughter nucleus. The daughter half-life is $T^d_{1/2}$= 193.271(63) ms [HT09], and is a fixed parameter in the fit.

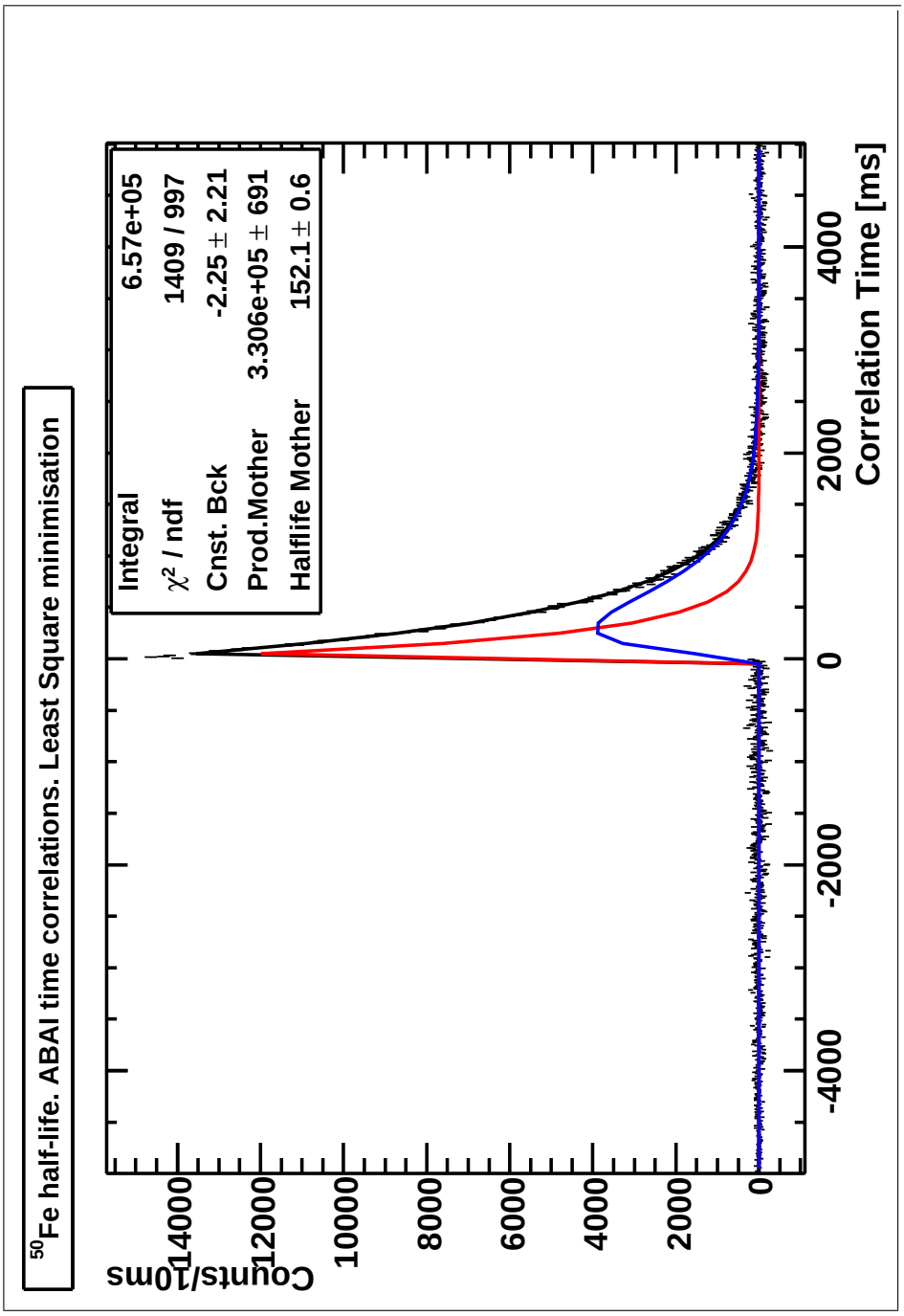

Figure 5.38: ^{50}Fe β-decay half-life for implant-beta correlations using a least squares minimisation. The red curve represents the decay of the mother nucleus ^{50}Fe and the blue curve represents the growth and decay curve of the ^{50}Mn daughter superallowed β emitting nucleus. The daughter half-life is $T^d_{1/2}$= 283.21(11) ms [HT09], and is a fixed parameter in the fit.

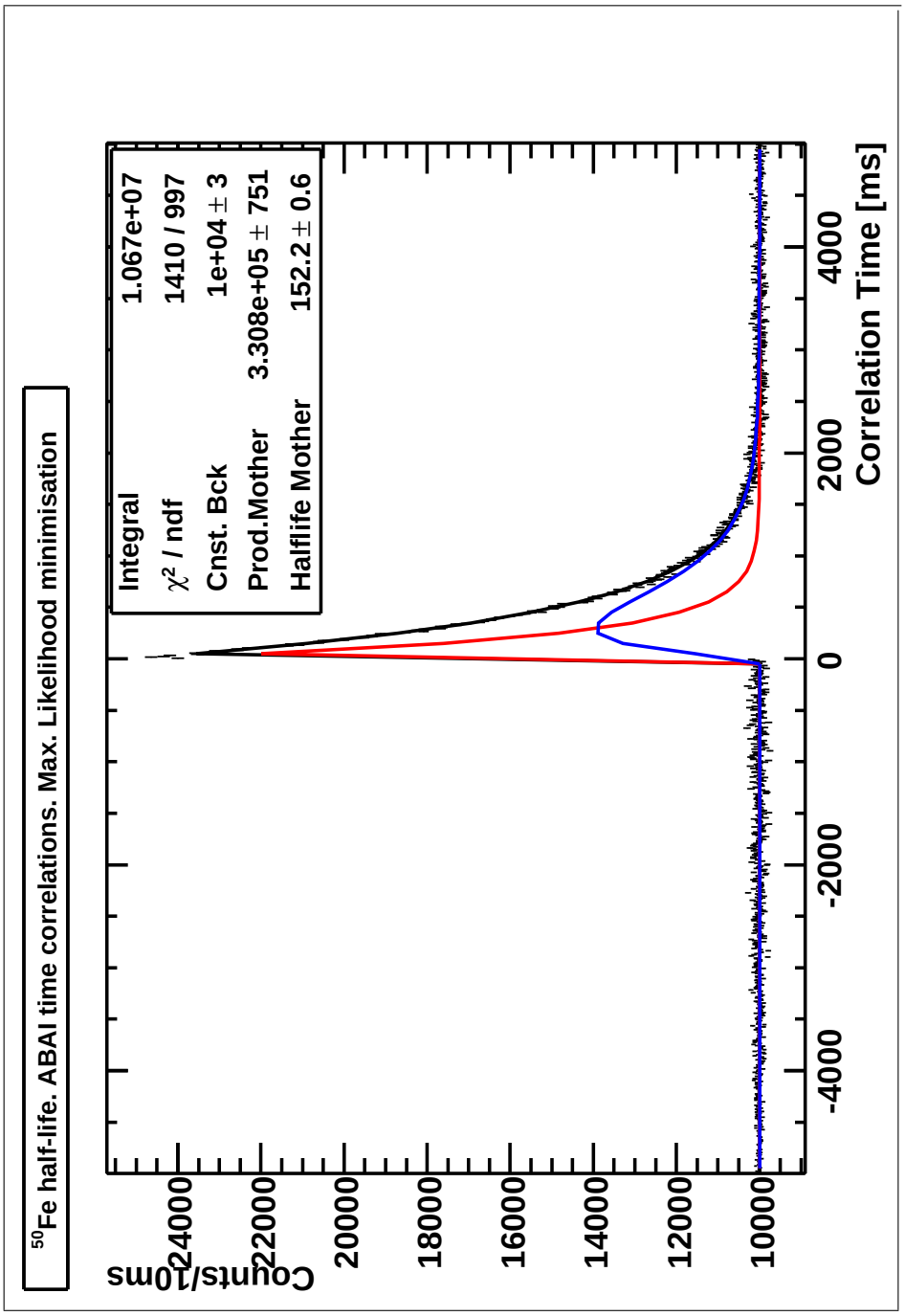

Figure 5.39: ^{50}Fe β-decay half-life for implant-beta correlations using a maximum likelihood minimisation. The red curve represents the decay of the mother nucleus ^{50}Fe and the blue curve represents the growth and decay curve of the ^{50}Mn superallowed β emitting daughter nucleus. The daughter half-life is $T^d_{1/2}$= 283.21(11) ms [HT09], and is a fixed parameter in the fit.

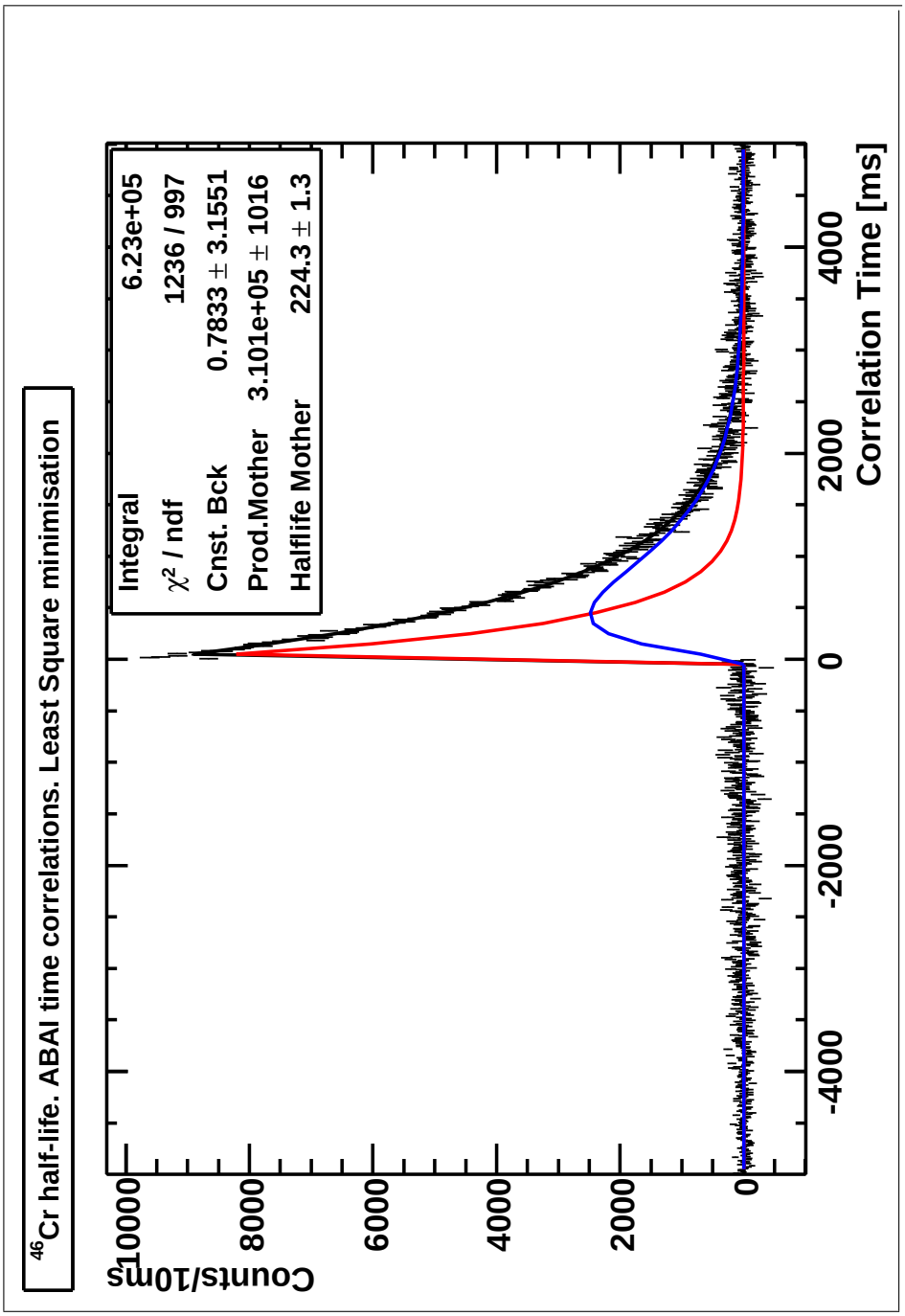

Figure 5.40: ^{46}Cr β-decay half-life for implant-beta correlations using a least squares minimisation. The red curve represents the decay of the mother nucleus ^{46}Cr and the blue curve represents the growth and decay curve of the ^{46}V superallowed β emitting daughter nucleus. The daughter half-life is $T^d_{1/2}$= 422.50(11) ms [HT09], and is a fixed parameter in the fit.

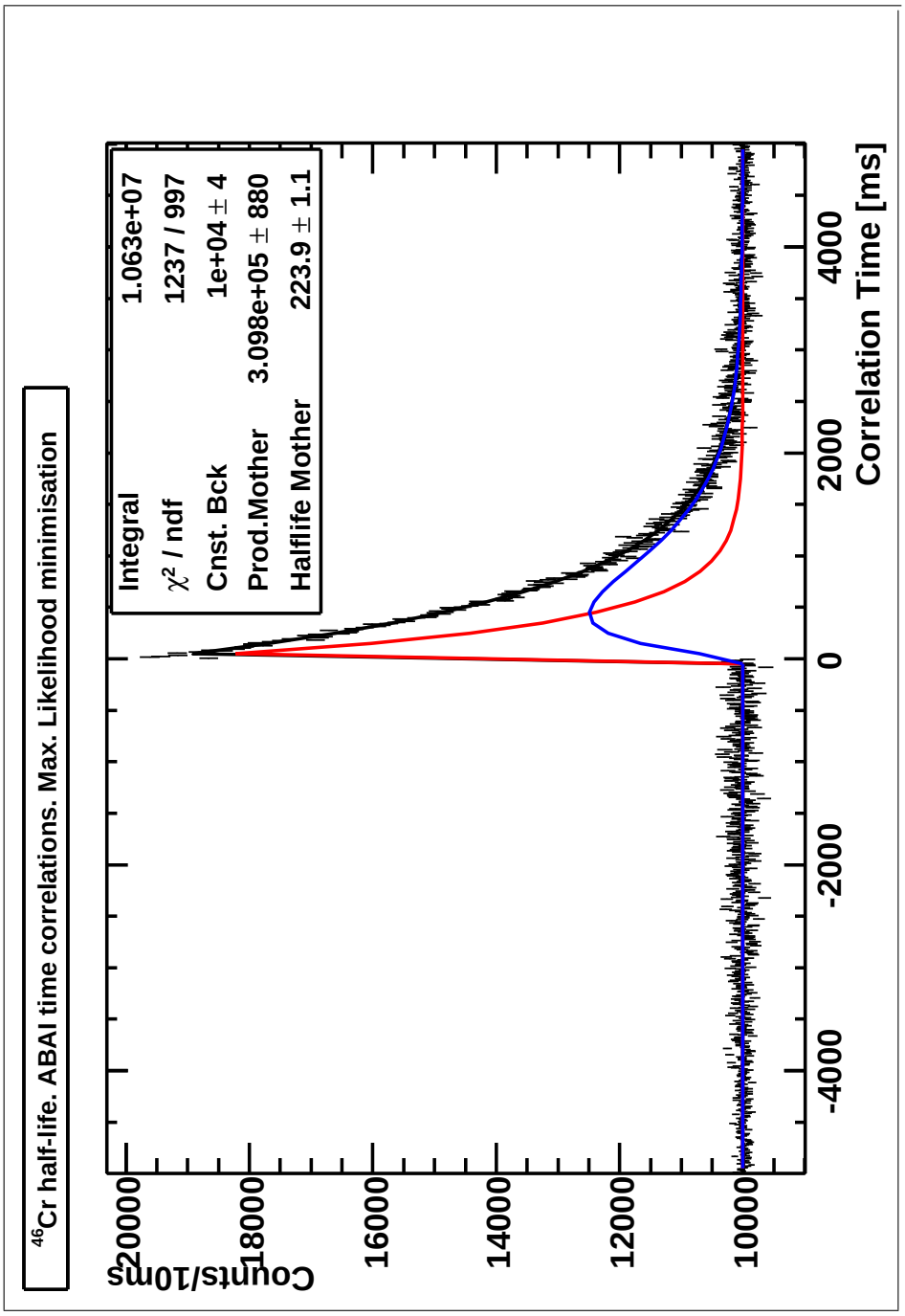

Figure 5.41: ^{46}Cr β-decay half-life for implant-beta correlations using a maximum likelihood minimisation. The red curve represents the decay of the mother nucleus ^{46}Cr and the blue curve represents the growth and decay curve of the ^{46}V superallowed β emitting daughter nucleus. The daughter half-life is $T^d_{1/2}$= 422.50(11) ms [HT09], and is a fixed parameter in the fit.

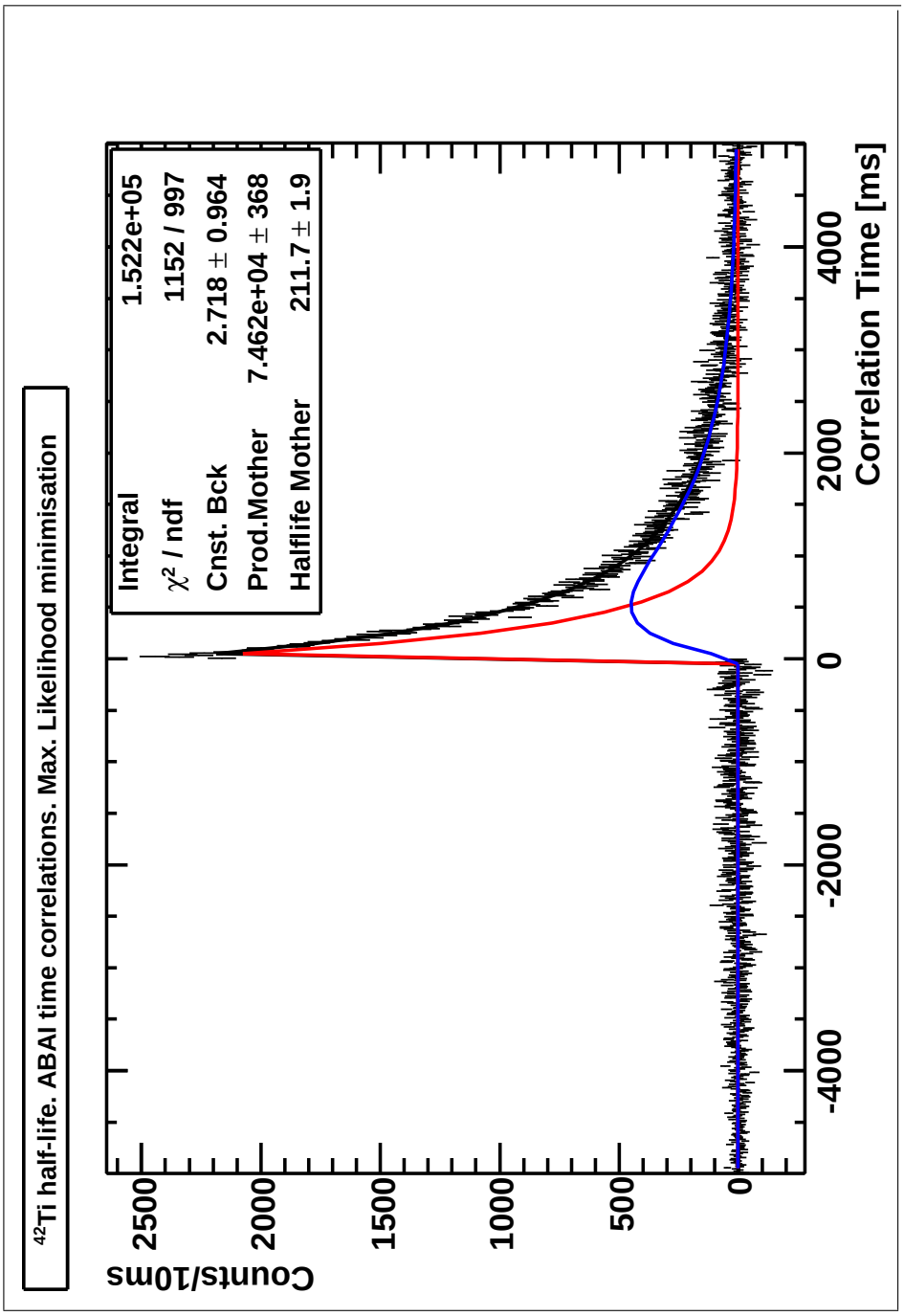

Figure 5.42: ^{42}Ti β-decay half-life for implant-beta correlations using a least squares minimisation. The red curve represents the decay of the mother nucleus ^{42}Ti and the blue curve represents the growth and decay curve of the ^{42}Sc superallowed β emitting daughter nucleus. The daughter half-life is $T^d_{1/2}$= 680.72(26) ms [HT09], and is a fixed parameter in the fit.

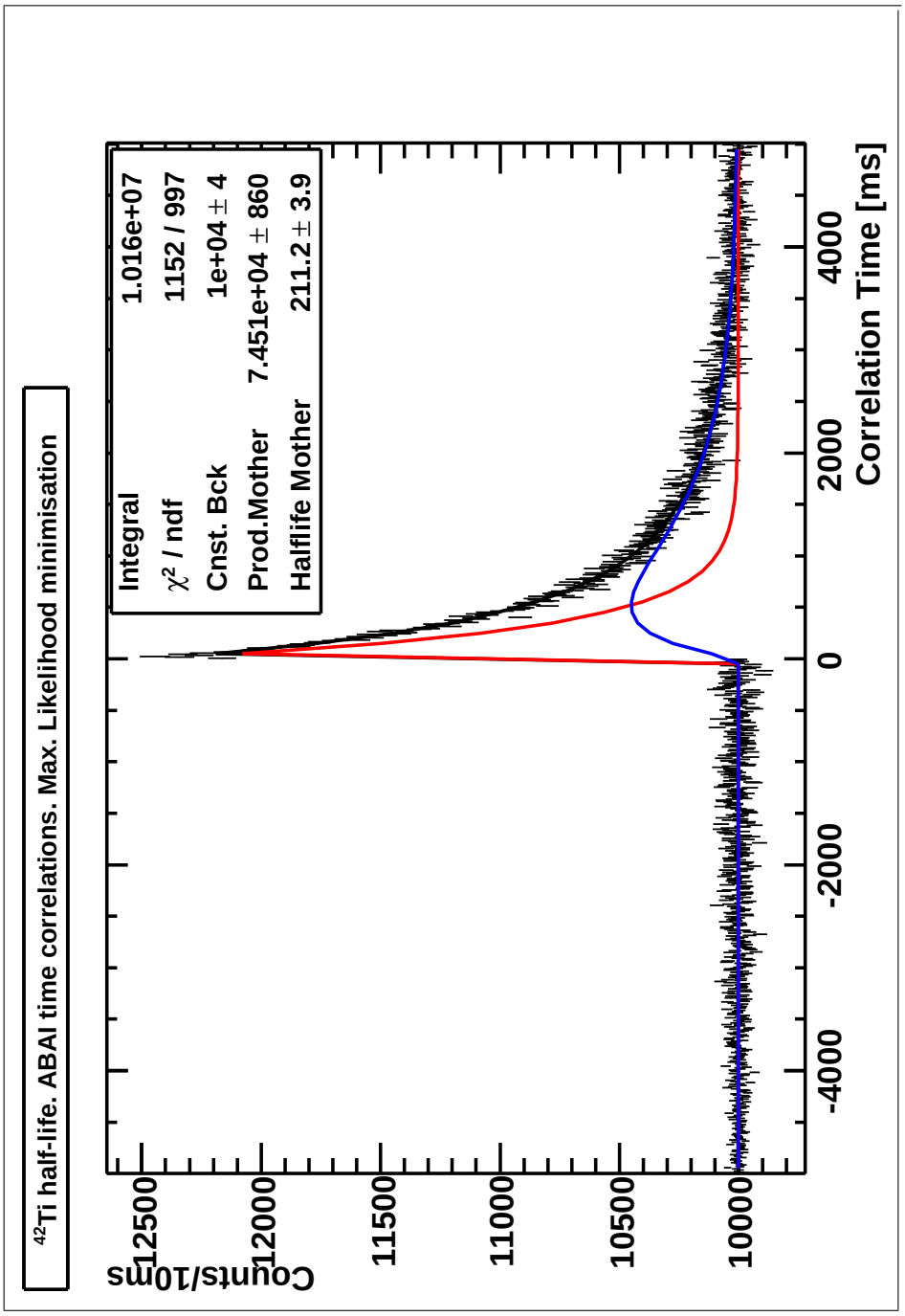

Figure 5.43: ^{42}Ti β-decay half-life for implant-beta correlations using a maximum likelihood minimisation. The red curve represents the decay of the mother nucleus ^{42}Ti and the blue curve represents the growth and decay curve of the ^{42}Sc superallowed β emitting daughter nucleus. The daughter half-life is $T^d_{1/2}$= 680.72(26) ms [HT09], and is a fixed parameter in the fit.

In a recent publication by J.C. Hardy et al. [HT09], they present a compilation of the T_z=0 superallowed β emitters with the half-life values published in the literature and providing an average value of the β half-life, rejecting those half-lifes which were not analysed using the Maximum-Likelihood method. It is known that the Maximum-Likelihood method is the appropriate method to analyse cases with low statistics, instead of the Least Squares minimisation method. For our case, the statistics is good enough to rely on both minimisation methods as it was shown in Table 5.11 -pp.106-, but following the Hardy et al. philosophy we will use the half-lives obtained with the Maximum-Likelihood method for the $B(GT)$ calculation.

5.3 β half-life by γ-implantations time correlations

In the previous measurements for these T_z=-1 nuclei ([Reu99b], [Kos97] and [Oni05]), except in the case of ^{42}Ti [Kur09], the half-life was determined by observing the γ-ray corresponding to the decay of the first excited state in the daughter nucleus. Whereas the ground-state-feeding (g.s.feed) was determined by comparing the total number of β-decays with the total number of decays going through the first excited state, assuming that this state is the only level fed in the decay.
In this experiment it is also possible to see the time behaviour of γ-events by correlating β-delayed gamma events with implantations. This analysis is presented in the following section.

5.3.1 Implant-β-delay γ correlation

As we saw in Section 4.1.5 -p.54- the RISING Ge array electronics was triggered either by a β-event or by an implantation-event. When a β-event triggers the acquisition, a coincidence gate of 100 μs is opened in all DGF-4C modules and the γ-event detected by any crystal is registered. Of course all background γ-ray lines, for example ^{40}K, and long-lived isomers in the implanted nuclei are also registered in such a coincidence window. As explained before, an off-line software gate of 250 ns was set in the region where the β-γ coincidence is expected (see Fig. 5.44 -p.118-).

Once the coincidence gate is fixed, time correlations between an implantation and a β-delayed γ-event are constructed in a time window of $\pm$ 20 s in the same way as it was explained in Section 5.2.2 -p.97- , but including now the γ-energy information for each correlation. Therefore a correlation time vs. γ-energy scatter plot for same-pixel-correlations Fig. 5.45 -p.118- and opposite-pixel-correlations Fig. 5.46 -p.119- , can be constructed.

Using projections on the time axes of the scatter plots, it is possible to obtain the γ-Implantation time correlations in the same pixel (see Fig. 5.47 -p.119- , red colour) and γ-Implantation time correlations in the opposite pixel (see Fig. 5.47 -p.119- , blue colour). In Fig. 5.47 -p.119- we present the same data, now with the normalised background.
Now a γ-ray spectrum can be produced by the projection of Fig. 5.45 -p.118- on to the

energy axis (see Fig. 5.49 -p.120- , red colour) and the projection of Fig. 5.46 -p.119- (see Fig. 5.49 -p.120- , blue colour) on the energy axis.

Applying the same normalisation factor used in Fig. 5.48 -p.120- , it is possible to obtain a "clean" γ-spectrum following ^{54}Ni β-decay into ^{54}Co (see Fig. 5.49 -p.120-).

In Fig. 5.51 -p.122- the clean γ-spectra are constructed for all the four nuclei, following the same procedure as in the ^{54}Ni β-delayed γ-spectrum. It is important to note that the 511 keV annihilation peak and the γ-rays corresponding to the decay of the first excited states are the only gammas visible in the spectra, except in the case of ^{46}Cr, where it is possible to distinguish another two γ-rays in ^{46}V at 1432.5 keV and the 2459.8 keV. No trace of any of the contaminants discussed in Section 5.1 is observed.

5.3.2 β half-life from β-delayed γ-implantation correlation

From Figs. 5.45 -p.118- and 5.46 -p.119- it is possible to obtain the β half-life by gating on the first excited state energy and projecting the spectrum on to the time axis. In fact we made three gates in each case: (i) gate on the desired gamma ray: gamma peak centroid - 4 keV, gamma peak centroid + 5 keV range, and gate on the background: (ii) gamma peak centroid - 8 keV, gamma peak centroid -4 keV and (iii) gamma peak centroid + 5 keV, gamma peak centroid + 10 keV. Then a time spectrum corresponding to implantation-β-γ correlations, free of γ contamination is obtained (see Fig. 5.52 -p.123- , red colour for correlations in same pixel red, and blue colour for correlations in opposite pixels). Then a normalisation factor is applied to the opposite pixel correlations integrating both spectra in the range from 6 to 20 sec. The result is presented in Fig. 5.53 -p.123- .
Fitting the subtracted spectra (see Fig. 5.54 -p.124-) using the single decay Bateman equation (Eq. 5.1 -p.96-) where we now have only one half-life involved, we obtain the half-life and the total number of β-decays of the parent nuclei which populate the first excited state in the daughter nuclei. The half-life fits for the four nuclei are shown in Fig. 5.55 -p.125-.

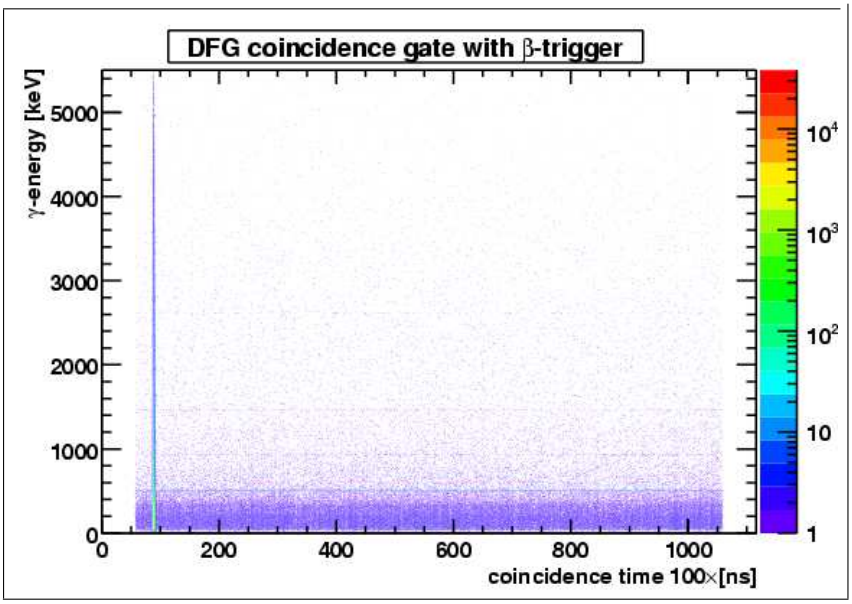

Figure 5.44: ^{54}Ni β-delayed γ-events in the coincidence gate of 100 μs. The software coincidence gate of 250 ns was set in the 86.5-89.0 [100ns] time range.

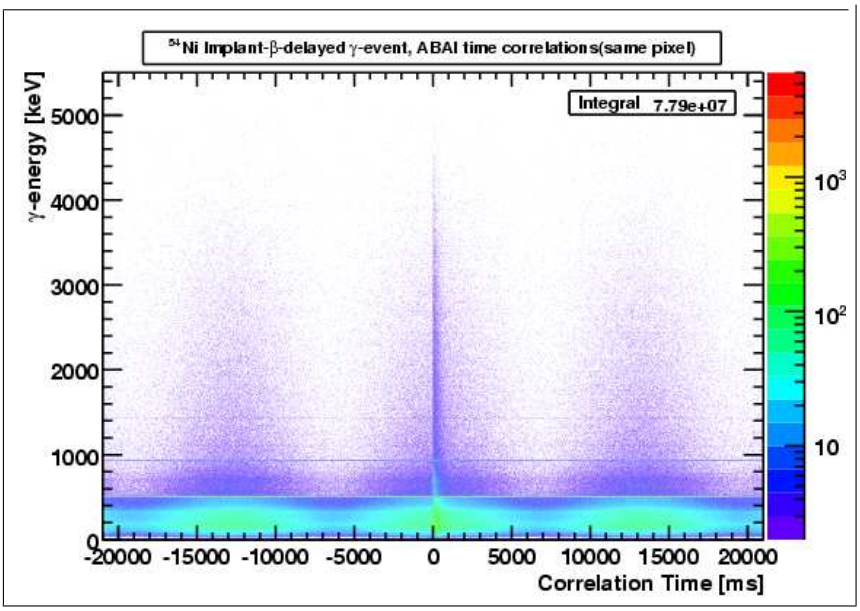

Figure 5.45: Correlation time vs. γ-energy for correlations in the same pixel in the ^{54}Ni experiment.

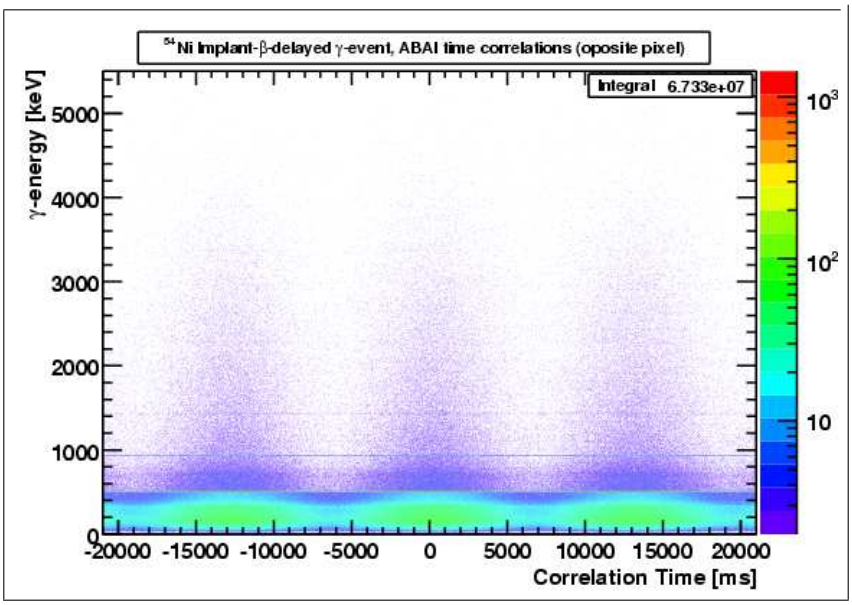

Figure 5.46: Correlation time vs. γ-energy for correlations in the opposite pixel in the^{54}Ni experiment.

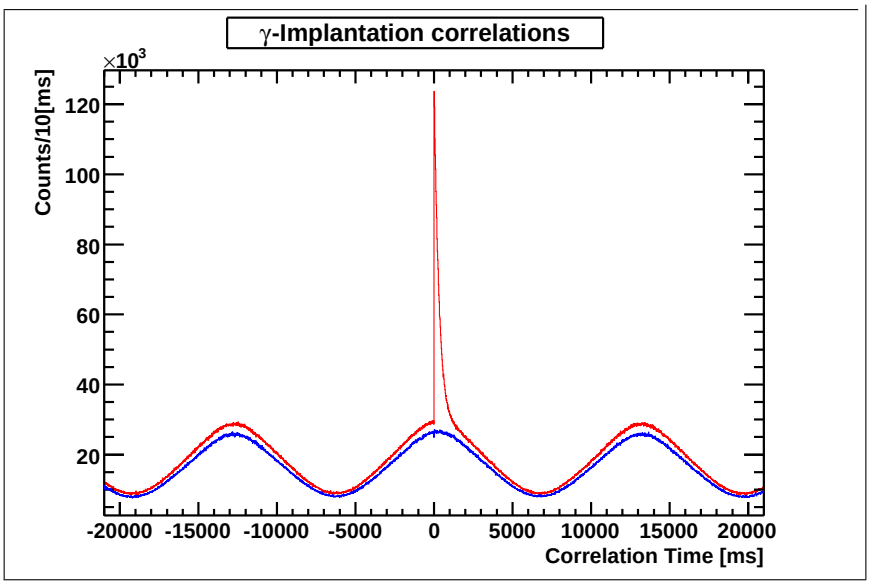

Figure 5.47: All γ-implantation time correlations for the ^{54}Ni setup. In red the same-pixel correlations. In blue the wrong correlations. Normalisation Factor 1.11152. Integration from 6 sec to 20 sec

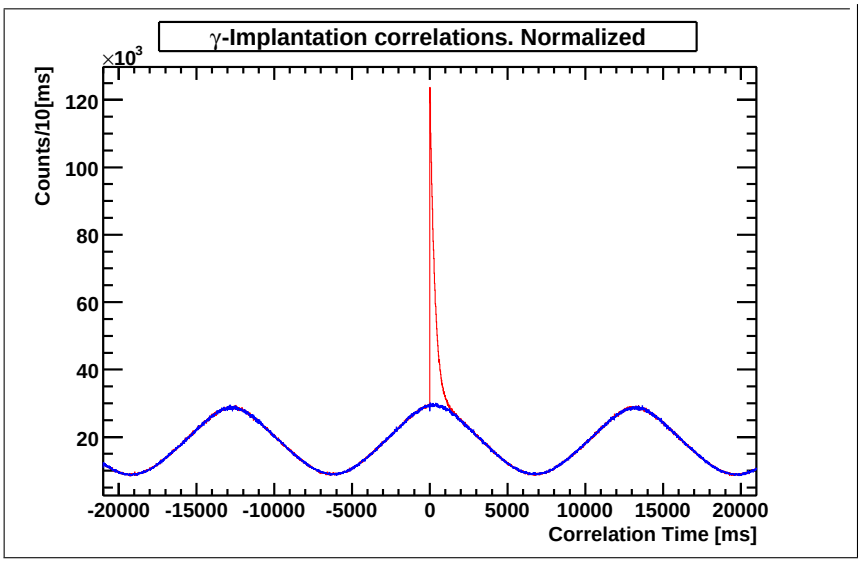

Figure 5.48: Same-pixel γ-implant correlations and wrong correlations normalised.

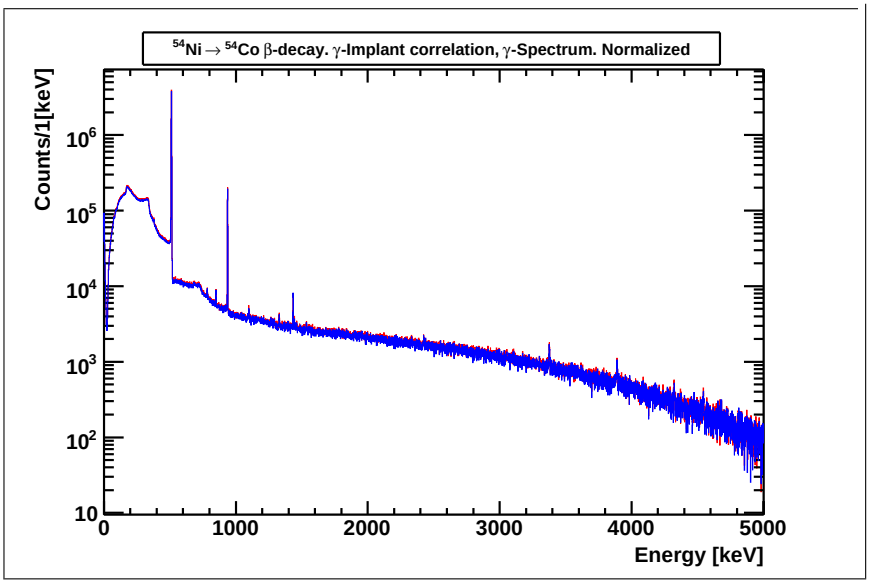

Figure 5.49: ^{54}Ni γ-ray energy spectrum with Same-pixel (red) and wrong correlations (Blue) normalised using the same factor as in Fig. 5.48 -p.120-

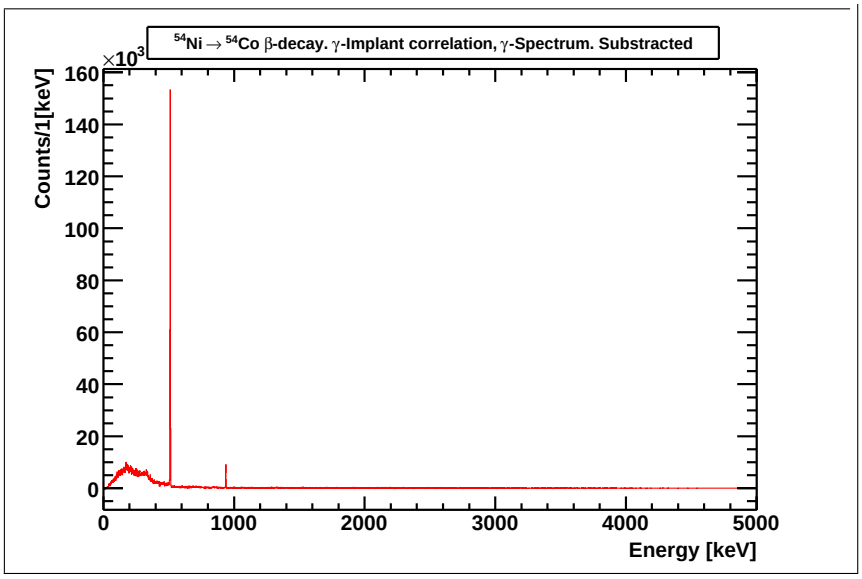

Figure 5.50: A clean ^{54}Ni γ-ray energy spectrum, i.e. without contaminants or randoms for correlations in the same pixel.

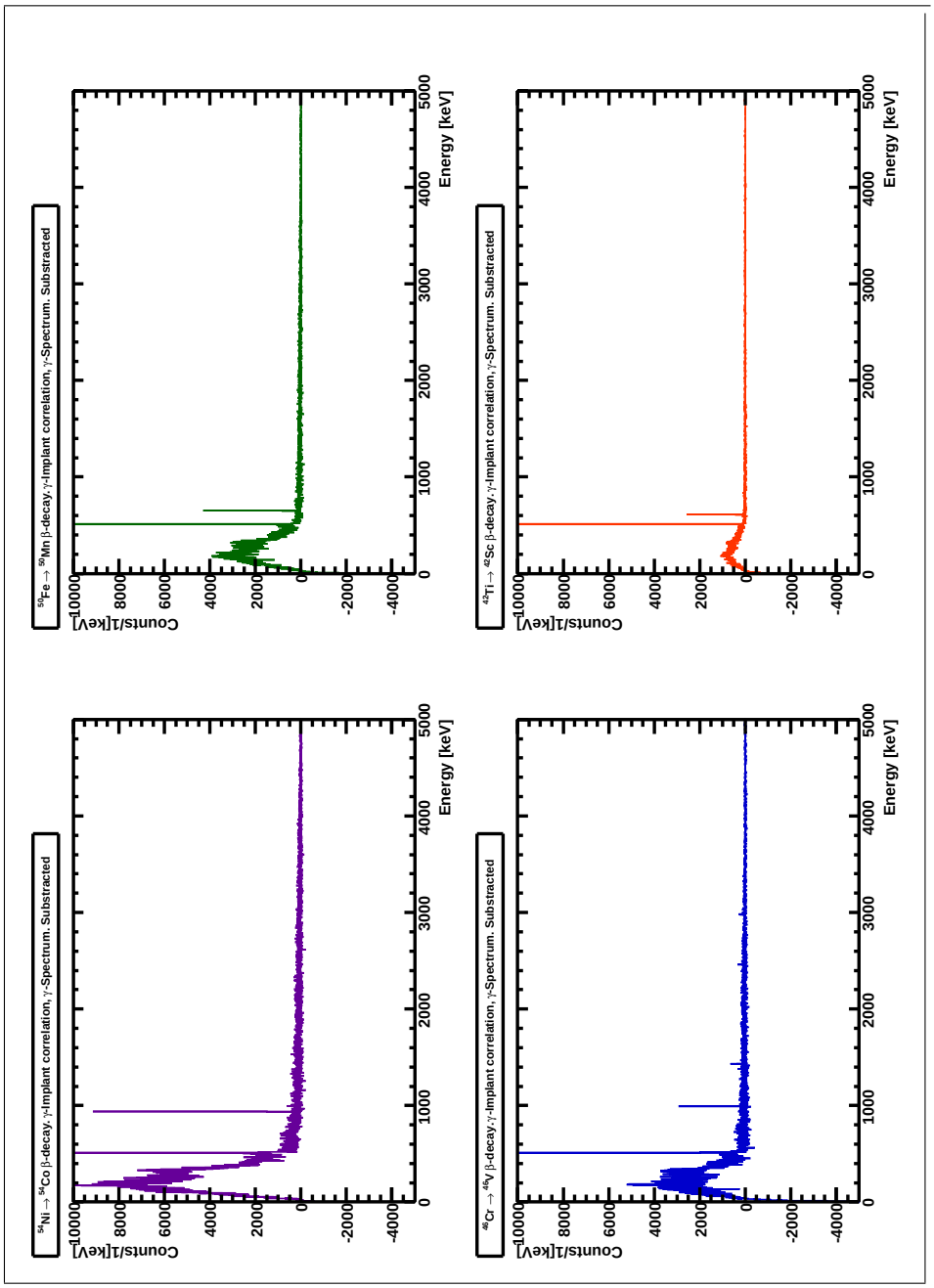

Figure 5.51: ^{54}Ni, ^{50}Fe, ^{46}Cr and ^{42}Ti clean γ-energy spectra, i.e. without contaminants or randoms for correlations in the same pixel.

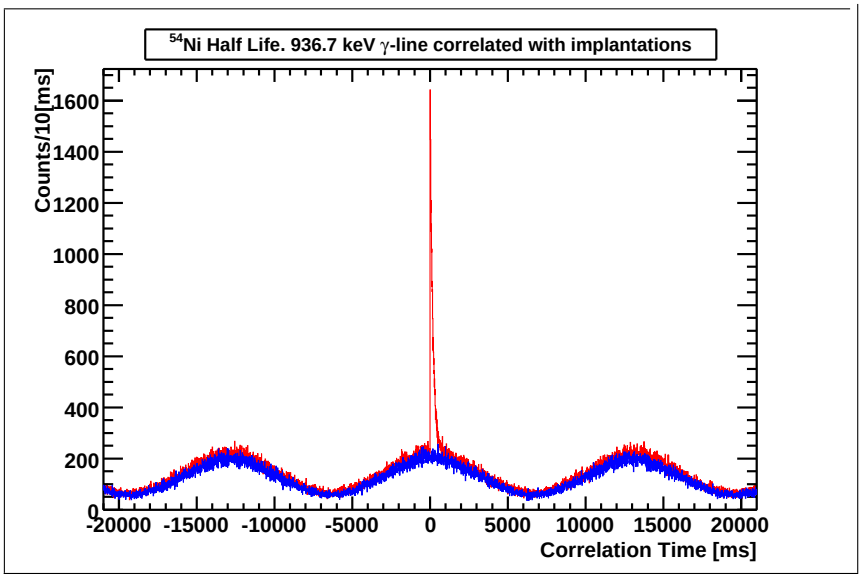

Figure 5.52: ^{54}Ni γ-ray energy spectrum with Same-pixel (red) and wrong correlations (Blue).

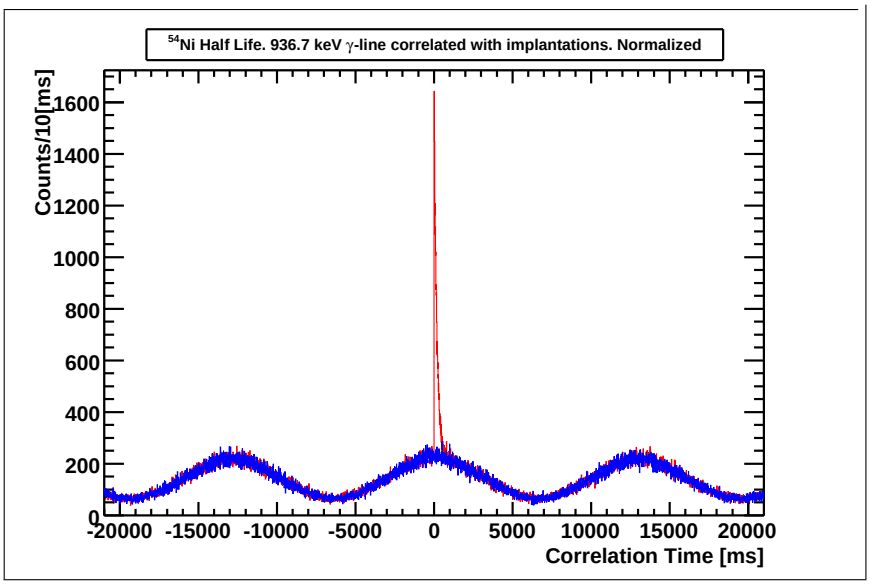

Figure 5.53: ^{54}Ni γ-ray energy spectrum with same-pixel (red) and wrong correlations (Blue) normalised.

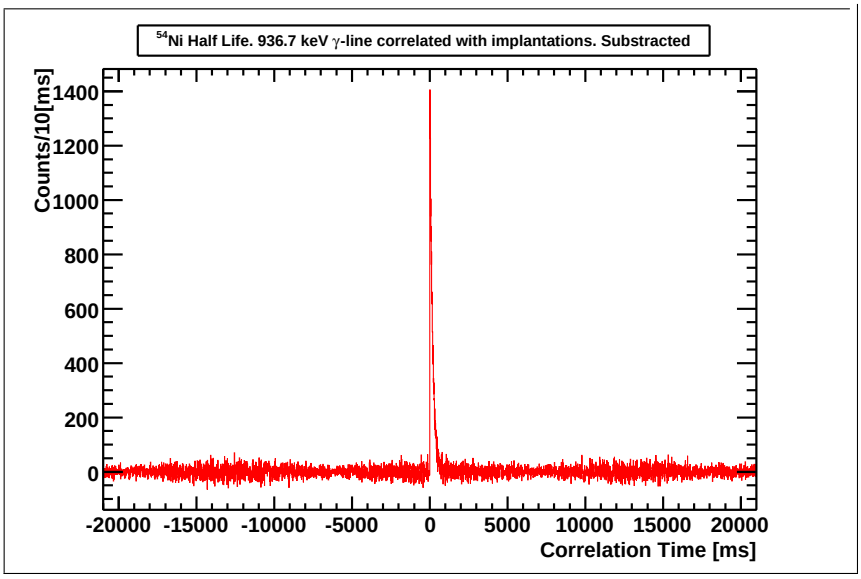

Figure 5.54: ^{54}Ni γ-ray energy spectrum with same-pixel (red) and wrong correlations (Blue) subtracted. This spectrum shows the real ^{54}Ni gamma spectrum without contaminants and randoms, but the implantation and the beta in coincidence with the gammas are correlated in the same pixel.

In Table 7.1 -p.164- we summarised the experimental half-life values obtained from (1) β-implantations time correlations ($T^{\beta}_{1/2}$) and (2) β-delayed first-excited-state-γ-implantation time correlations ($T^{\beta-\gamma}_{1/2}$), in comparison with the literature values. As expected, the half-life obtained by β-delayed first-excited-state-γ-implantation time correlations have a larger statistical error than the results using β-implantation correlations, but they are in perfect agreement as well as in agreement with the literature values.
In the following calculations including $B(GT)$ calculations, we will use the $T^{\beta}_{1/2}$ half-life values because they have smaller uncertainty.

	$T^{\beta}_{1/2}$ [ms]	$T^{\beta-\gamma}_{1/2}$ [ms]	Lit. $T_{1/2}$ [ms]
^{54}Ni	114.1(2)	114.3(18)	106(12) [Reu99b]
^{50}Fe	152.2(6)	150.1(29)	155(11) [Kos97]
^{46}Cr	223.9(11)	223.9(99)	240(140) [Oni05]
^{42}Ti	211.2(39)	209.5(52)	208.14(45) [Kur09]

Table 5.12: β-decay ($T^{\beta}_{1/2}$) and β-delayed first-excited-state-γ ($T^{\beta-\gamma}_{1/2}$) half-life results and comparison with half-life values from the literature (Lit. $T_{1/2}$).

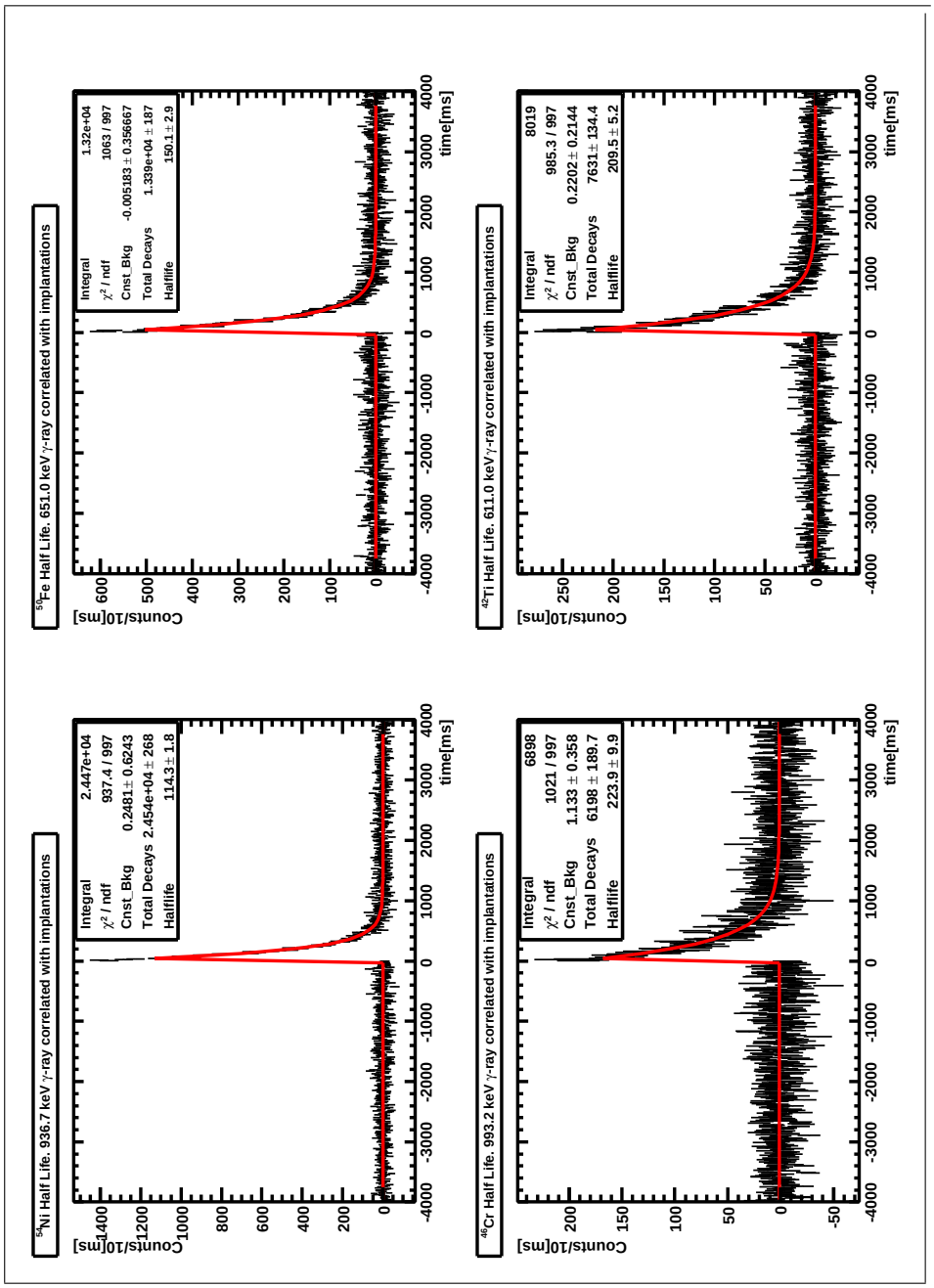

Figure 5.55: Fits to the β-delayed first-excited-state-γ for the ^{54}Ni, ^{50}Fe, ^{46}Cr and ^{42}Ti.

The respective β-decay half-lifes $T^{\beta}_{1/2}$, are included in the β-decay level scheme in Figs. 6.1 - 6.4 -pp.134 to 137- .

5.4 β branching and ground state feeding

To measure the ground-state-to-ground-state feeding in β-decay is in general difficult. The reason is that one has to know the number of β-decaying nuclei and all the decays which proceed through β-delayed gammas. Then the ground-state-to-ground-state feeding is obtained by subtraction.

The total number of decaying nuclei in the sample is normally estimated by detecting the β-particles in a β-detector. This has two inherent difficulties. a) The decay can be produced by the nucleus of interest, or by the daughter activity (or any other contamination). b) One has to know the efficiency of the β-detector which may depend on the β-decay energy.

A typical way to avoid the second difficulty is to measure the total number of βs and the β-γ coincidences, then the β efficiency cancels, but this is only correct if the β efficiency for the ground-state-to-ground-state β-decay is the same as for the ground-state-to-excited-states β-decay.

In the present experiment we have the following advantages:

- We know exactly the number of parent nuclei which have been produced, implanted and surviving as a parent, which have given a ΔE signal in the DSSSD. This is obtained in the following way.

In the implantation plot we select the desired nucleus. Then we look at our correlation plot after random background subtraction (see Section 5.2.4 -p.105-) and from the half-life fit, we obtain the exact number of total selected nuclei which β-decay, (N_0 according to Eq. 5.2 -p.101-). In this way we are sure we do not have any contaminants or randoms; they have been subtracted.
A very nice check to conclude that we have the right activity is the fact that in the half-life fit (See Figs. 5.36-5.43 -pp.108- 115), the total number of counts ("Integral" value in the fit) and the parent N_0-value (called "Prod.Mother" value in the fit) are very close, within a factor of 2.

- We measure the β-delayed gammas under exactly the same conditions.

This was done in the following way. We look at the correlations between the implantations and the β-gamma coincidences. The spectra resulting from this exercise are shown in Fig. 5.51 -p.122- (see Section 5.3.2 -p.117-).

As can be seen from Fig. 5.51 -p.122- , the statistics is much reduced compared with the spectra without implantation condition shown in Figs. 5.2-5.25 -pp.78 to 91-. The consequence is that we can compare only with the feeding to the first excited state. This is good enough since we have the relative intensities for the rest of the gammas (See Tables 5.1-5.8 -pp.80 to 93-).
To be sure that we get the right number of counts we fit the Bateman equations for this gamma activity and obtain the $N_0^{\mathrm{1st.exct.state}}$ from Eq.5.1 -p.96- . A good cross check of this method is given by the fact that we obtain the same half-life using the fit of

the Bateman equations for the implantation-β correlations as with the implantation-β-$\gamma^{\text{1st.exct.state}}$ correlations.

Another important ingredient in this calculation is the γ-efficiency for this excited state which is obtained from Fig. 4.32(b) -p.73- as explained in Section 4.3.3 -p.67- . We note that for this range of gamma energies the efficiency is well known (based on calibration sources).

With all this information, we can calculate the β-decay branching ratio to the first excited state in the daughter nuclei $Br(\gamma_1)$, as following

$$Br(\gamma_1) = \frac{N_0^{\text{1st.exct.state}}/(\epsilon_{\gamma_1}\epsilon_\beta\epsilon_{\text{surv}})}{N_0^\beta/(\epsilon_\beta\epsilon_{\text{surv}})} = \frac{N_0^{\text{1st.exct.state}}}{N_0^\beta\epsilon_{\gamma_1}} \tag{5.3}$$

where ϵ_{γ_1} is the RISING γ-efficiency for the first excited state; ϵ_β is the β-efficiency of a pixel of the DSSSD and ϵ_{surv} is the survival efficiency of the identified ion (in FRS) and implanted in a pixel of the DSSSD. In general, and as we have the γ intensities $\mathrm{I}_\gamma^{\text{Rel}}$, relative to the first excited state (see Tables 5.2-5.8 -pp.81 to 93-), the branching ratio to the excited state k is given by

$$Br(\gamma_k) = \frac{N_0^{\text{1st.exct.state}}}{N_0^\beta\epsilon_{\gamma_1}} I_{\gamma_k}^{\text{Rel}} \tag{5.4}$$

So, the ground-state-to-ground-state feeding is,

$$Br(\text{g.s.}) = 1 - \frac{N_0^{\text{1st.exct.state}}}{N_0^\beta\epsilon_{\gamma_1}} \sum_k I_{\gamma_k}^{\text{Rel}} \tag{5.5}$$

In Tables 5.13-5.16 -pp.128 to 129- the branching ratio values to the excited state in the daughter nuclei are shown, for the four cases under study.

Energy [keV]	Rel.Intensity	Branching %
936.7	1000.0(35.2)	19.75(122)
2424.6	8.0(1.3)	0.16(3)
3376.1	18.9(1.6)	0.37(4)
3889.6	10.6(1.2)	0.21(3)
4293.4	5.6(5.1)	0.11(10)
4323.0	7.4(2.3)	0.15(5)
4543.8	6.0(1.0)	0.12(2)
4822.8	2.3(0.5)	0.04(1)
5202.4	1.2(0.4)	0.02(1)
g.s feed		79.07(123)

Table 5.13: ^{54}Ni β branching ratio. The total number of ^{54}Ni nuclei which were produced and β-decay giving a signal in the M2 DSSSD, N_0^{β}, was taken from the fit to the β-decay half-life (see Figs. 5.36 and 5.37 -pp.108 and 109-, N_0^{β}= 838204.8(686.3)). The number of ^{54}Ni nuclei produced and β-decays populating the first excited state in ^{54}Co and the γ detected in the RISING array, $N_0^{\text{1st.exct.state}}$, was taken from the fit of the β-delayed γ half-life (see Fig. 5.55 -p.125-, $N_0^{\text{1st.exct.state}}$ = 24535.1(268.5)). The Branching Ratio was obtained using Eq. 5.4 and 5.5 -p.127-.

Energy [keV]	Rel.Intensity	Branching %
651.0	1000.0(35.2)	22.80(142)
2403.8	55.4(2.6)	1.47(10)
2684.2	27.9(1.9)	0.70(6)
3380.0	37.5(2.2)	0.85(7)
3643.4	6.6(1.2)	0.15(3)
4012.7	1.9(0.9)	0.04(2)
4315.7	3.6(1.4)	0.08(3)
g.s feed		73.90(143)

Table 5.14: ^{50}Fe β branching ratio. The total number of ^{50}Fe nuclei which were produced and β-decay giving a signal in the M2 DSSSD, N_0^{β}, was taken from the fit to the β-decay half-life (see Figs. 5.38 and 5.39 -pp.110 and 111- , N_0^{β}= 330691.7(508.5)). The number of ^{50}Fe nuclei which were produced and β-decay giving a signal in the M2 DSSSD populating the first excited state in ^{50}Mn and the γ detected in the RISING array, $N_0^{\text{1st.exct.state}}$, was taken from the fit of the β-delayed γ half-life (see Fig. 5.55 -p.125-, $N_0^{\text{1st.exct.state}}$ = 13391.5(187.0)). The Branching Ratio was obtained using Eq. 5.4 and 5.5 -p.127-.

Energy [keV]	Rel.Intensity	Branching %
993.2	1000.0(35.21)	13.90(95)
1432.5	242.0(8.82)	3.36(23)
2459.8	109.3(4.68)	1.52(11)
2466.3	17.7(2.26)	0.38(4)
2697.4	67.9(3.21)	0.94(7)
2977.8	170.8(6.58)	2.50(17)
3867.6	6.4(1.26)	0.09(2)
g.s feed		77.17(100)

Table 5.15: ^{46}Cr β branching ratio. The total number of ^{46}Cr nuclei which were produced and β-decay giving a signal in the M2 DSSSD, N_0^{β}, was taken from the fit to the β-decay half-life (see Figs. 5.40 and 5.41 -pp.112 and 113-, N_0^{β}= 310096.1(1009.3)). The number of ^{46}Cr nuclei which were produced and β-decay giving a signal in the M2 DSSSD populating the first excited state in ^{46}V and the γ detected in the RISING array, $N_0^{\text{1st.exct.state}}$, was taken from the fit of the β-delayed γ half-life (see Fig. 5.55 -p.125-, $N_0^{\text{1st.exct.state}}$ = 6198.0(190.0)). The Branching Ratio was obtained using Eq. 5.4 and 5.5 -p.127-.

Energy [keV]	Rel.Intensity	Branching %
611.0	1000.0(35.3)	55.92(355)
1888.4	7.3(1.0)	0.41(6)
g.s feed		43.66(355)

Table 5.16: ^{42}Ti β branching ratio. The total number of ^{42}Ti nuclei which were produced and β-decay giving a signal in the M2 DSSSD, N_0^{β}, was taken from the fit to the β-decay half-life (see Figs. 5.42 and 5.43 -pp.115 and 115-, N_0^{β}= 74565.7(250.9)). The number of ^{42}Ti nuclei which were produced and β-decay giving a signal in the M2 DSSSD populating the first excited state in ^{42}Sc and the γ detected in the RISING array, $N_0^{\text{1st.exct.state}}$, was taken from the fit of the β-delayed γ half-life (see Fig. 5.55 -p.125-, $N_0^{\text{1st.exct.state}}$ = 7631.3(134.3)). The Branching Ratio was obtained using Eq. 5.4 and 5.5 -p.127-.

	$T_{1/2}^{\beta exp}$ [ms]	T_F [ms]	Q-Value [keV]	g.s.feed(Experiment)	g.s.feed(Expected)
^{54}Ni	114.1(1)	139.7(42)	8800(50)	0.791(12)	0.817(25)
^{50}Fe	152.2(2)	204.1(81)	8150(60)	0.739(14)	0.746(30)
^{46}Cr	224.1(7)	288.1(41)	7599(20)	0.772(10)	0.778(11)
^{42}Ti$_K$	211.7(36)	429.9(1)	7016.83(25)	0.437(36)	0.492(8)
^{42}Ti$_A$	211.7(36)	435.6(17)	7000(5)	0.437(36)	0.486(9)

Table 5.17: Experimental results: Beta half-life ($T_{1/2}^{\beta exp}$), estimated T_F, with the corresponding Q-value from Audi et al. [Aud03]. In the case of ^{42}Ti we also used a recently measured Q-value from T.Kurtukian-Nieto et al. [Kur09]. In the fifth column we give the experimental g.s. to g.s. feeding and in the sixth column the expected g.s. feed = $T_{1/2}^{\beta exp}/T_F$

We can now test if the experimental g.s. feeding values are in agreement with expectations since all the transitions to the ground state are "superallowed" (log $ft \sim 3.5$) Fermi transitions and the Fermi half-life is known from:

$$T_F = \frac{K}{2(1-\delta_c)f_F} \tag{5.6}$$

The Fermi half-life values T_F for the four cases of interest are shown in Table 5.17 -p.130-. The value of K=6143.6(16) was taken from [HT09] and the δ_c Coulomb correction factor was taken from [TH02].
The ratio of the total half-life $T_{1/2}^{\beta exp}$ and the Fermi half-life gives us the expected ground-state-feeding shown in Table 5.17 -p.130- last column. If we compare the g.s. feeding (Experiment) coming from our measurement with the g.s. feeding (Expected) obtained from Eq. 5.6, we see that the agreement is perfect (except in the case of ^{42}Ti).
Moreover, since we use the Q$_\beta$-values from [Aud03] in the estimation of the Fermi function f we conclude that these values are also correct.

The β-decay branching ratios and ground state feedings obtained in this work, are included in the β-decay level scheme in Figs. 6.1 to 6.4 -pp.134 to 137 -.

5.5 Gamow-Teller transition Strength

In the analysis of the β-decay experiments we have obtained the following results for the four cases studied: (i) The β-decay half-life $T_{1/2}^{\beta}$ (see Section 5.2 -p.96-), (ii) the β branching ratio to the excited states in the daughter nuclei (see Section 5.4 -p.126-) and (iii) the ground state feeding in the daughter nuclei.

With all this information, extracted exclusively from our experiment and the Q_β-values from Audi [Aud03] and Kurtukian-Nieto [Kur09], we can calculate now the B(GT$^+$)$_j$ value, using the following formula,

$$B(GT+)_j = \frac{K}{\lambda^2}\frac{Br(\gamma_j)}{f_j T_{1/2}^{\beta}} \tag{5.7}$$

where K=6143.6 ± 1.6 [HT09], $\lambda = g_A/g_V$=-1.270 ± 0.003 [HT06] and f_j is the Fermi-factor (phase space factor) which depends on the Q_β-value and the excitation energy of the state j[WB74].
In Tables 5.18-5.22 -p.131 to 132- the $B(GT^+)_j$ results are presented.

Energy state (β) [keV]	$B(GT^+)_j^\beta$
936.7	0.542(38)
2424.6	0.014(2)
3376.1	0.079(9)
3889.6	0.079(11)
4293.4	0.068(62)
4323.0	0.095(30)
4543.8	0.103(20)
4822.8	0.059(13)
5202.4	0.056(20)

Table 5.18: Gamow-Teller transition strength to the excited states in ^{54}Co in the β^+-decay of ^{54}Ni, using the Q_β-value from [Aud03].

Energy state (β) [keV]	$B(GT^+)_j^\beta$
651.0	0.588(45)
2403.8	0.164(15)
2684.2	0.104(11)
3380.0	0.276(30)
3643.4	0.068(14)
4012.7	0.033(16)
4315.7	0.096(40)

Table 5.19: Gamow-Teller transition strength to the excited states in ^{50}Mn in the β^+-decay of ^{50}Fe, using the Q_β-value from [Aud03].

Energy state (β) [keV]	$B(GT^+)_j^\beta$
993.2	0.472(33)
1432.5	0.167(12)
2459.8	0.210(16)
2466.3	0.053(6)
2697.4	0.172(14)
2977.8	0.639(47)
3867.6	0.082(17)

Table 5.20: Gamow-Teller transition strength to the excited states in ^{46}V in the β^+-decay of ^{46}Cr, using the Q_β-value from [Aud03].

Energy state (β) [keV]	$B(GT^+)^{\beta}_j$
611.0	2.30(15)
1888.4	0.06(1)

Table 5.21: Gamow-Teller transition strength to the excited state in ^{42}Sc in the β^+-decay of ^{42}Ti, using the Q_β-value from [Kur09].

Energy state [keV]	$B(GT^+)_\beta$
611.0	2.33(15)
1888.4	0.06(1)

Table 5.22: Gamow-Teller transition strength to the excited state in ^{42}Sc in the β^+-decay of ^{42}Ti, using the Q_β-value from [Aud03].

The $B(GT^+)^{\beta}_j$ values obtained in this work are included in the β-decay level scheme in Figs. 6.1 - 6.4 -pp.134 to 137-.

CHAPTER 6

DISCUSSIONS AND CONCLUSIONS

In this work we have used the γ-ray spectra shown in Fig. 5.2 to Fig. 5.25 -pp.78 to 91- and the intensities and energies tabulated in Table 5.1 to Table 5.7 -pp.80 to 92- to construct the level schemes shown in Figs. 6.1-6.4 -pp.134 to 137- . As can be seen in the identification plots (see Figs. 4.20-4.23 -pp.60 to 61-) the identification of the implanted ion was very clean and most of the observed activity corresponds to the nucleus of interest. From the γ-analysis in Section 5.1 -p.75-, we have identified gamma peaks that correspond to, (i) the γ-rays already known in the daughter nucleus. In general this corresponded to transitions from the first 1^+ excited state or the yrast 2^+ to the ground state, (ii) possible decays to the ground state of levels observed in the (^{3}He,t) charge exchange reaction experiments, (iii) possible contaminants known in the literature as described previously. (iv) summing peaks (no single escape or double escape peaks were seen), which were clearly identified by comparison of the gamma spectra using single crystal or add-back mode.
We have also looked for possible gamma transitions from the highly excited levels to the first 1^+ or 2^+ state. We have observed a few such stopover transitions, but they all connect 1^+ states at high energy with the 2^+ state, never with the first 1^+ excited state. We will come back to this intriguing observation later.
There are a few gammas which were neither identified as contaminants, nor as transitions between the established states.
Also in the level schemes we put the adopted value for the parent half-life and the ground state feeding (see Table 5.17 -p.130-) obtained from our measurements.
We also include the β-feedings to the different levels populated using the intensity balance for the incoming and outgoing gamma intensity for each level and the ground state feeding information.

In summary, with this information we have constructed the level schemes, shown in Figs. 6.1 - 6.4 -pp.134 to 137- where all the information presented, except the Q_β-values and the daughter half-life, come from the present work.

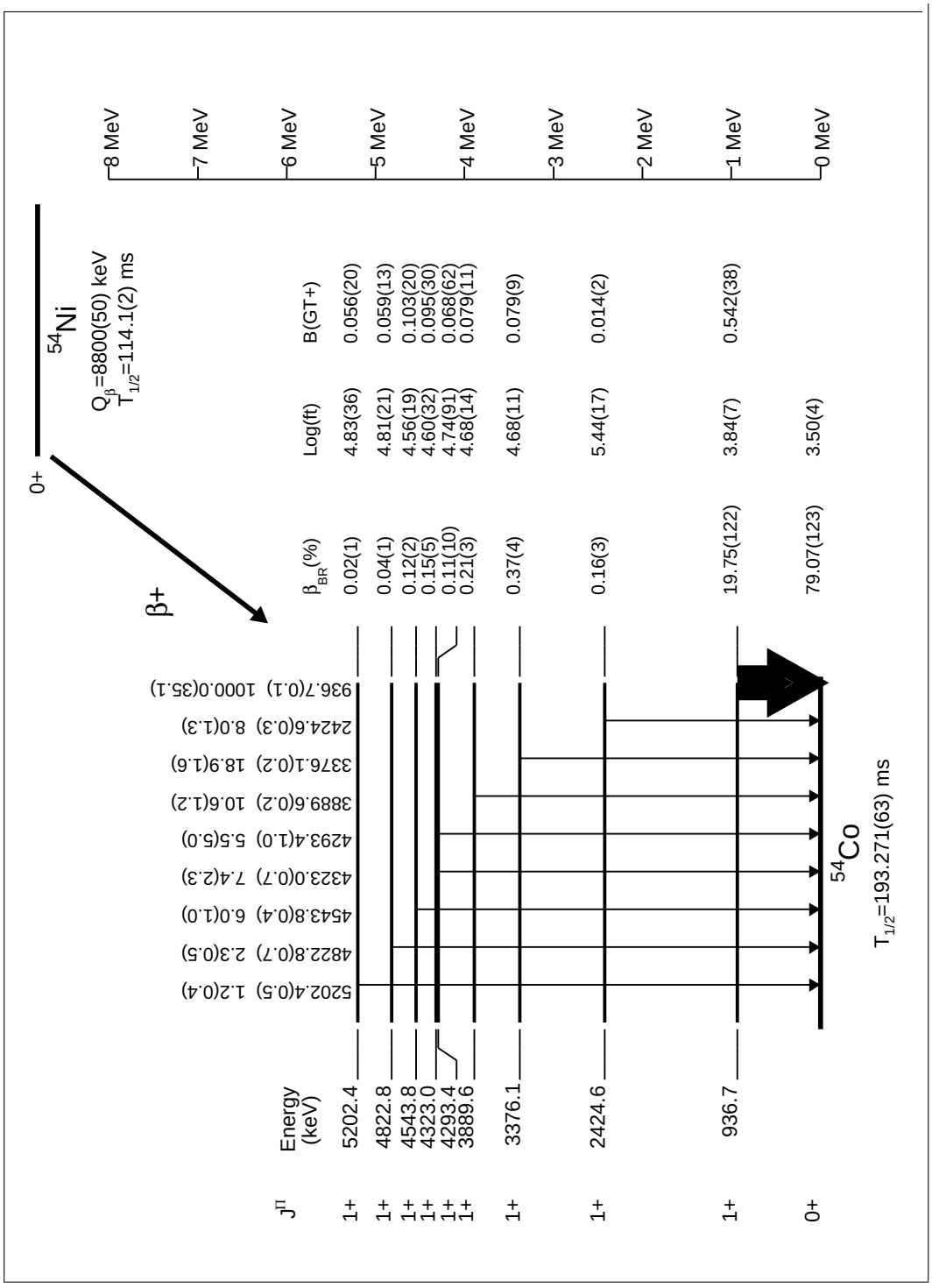

Figure 6.1: ^{54}Ni β-decay scheme. All the values given in this figure originate from the present work except for the Q_β-value which is taken from [Aud03] and the daughter half-life, taken from [HT09].

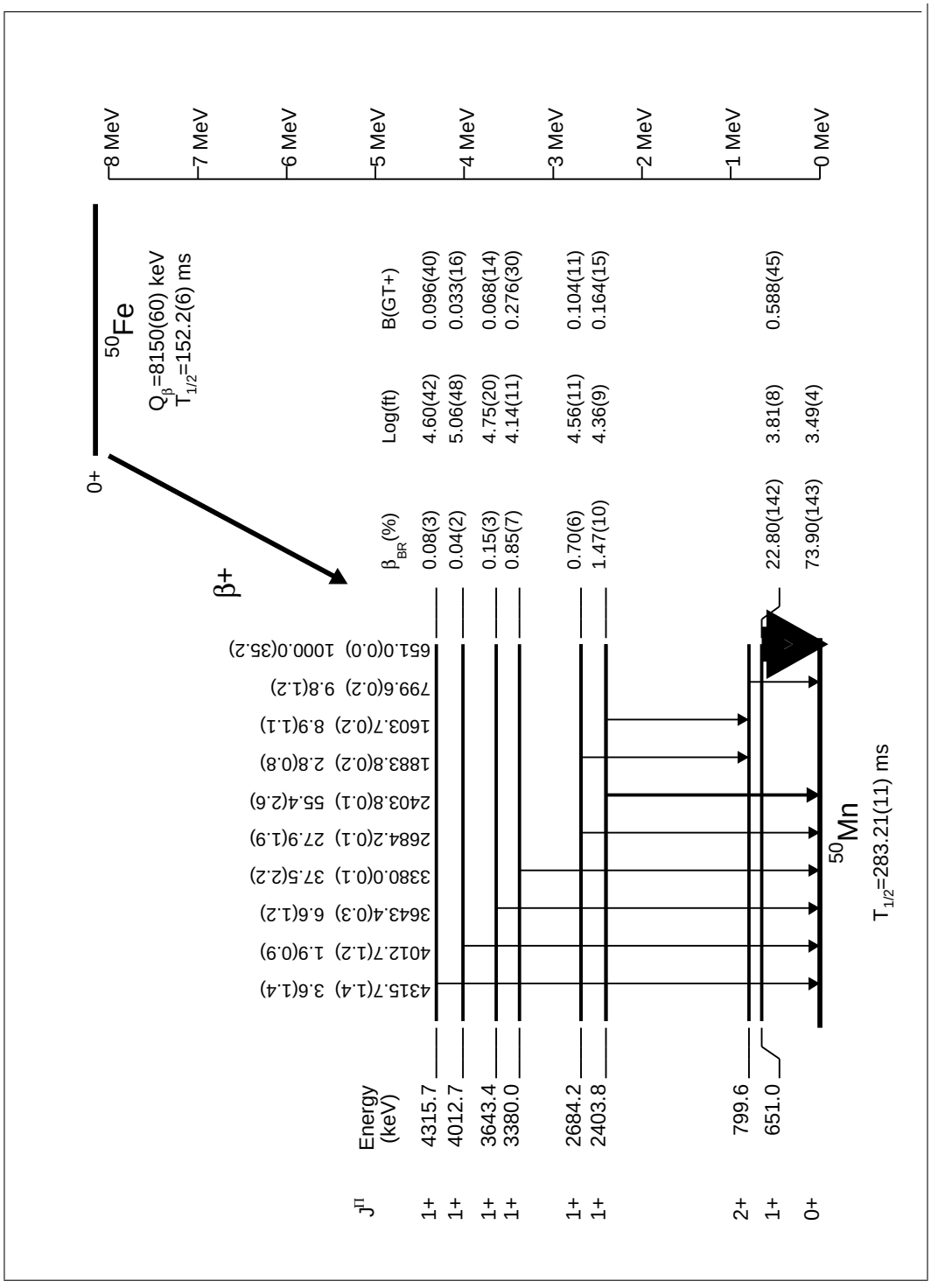

Figure 6.2: ^{50}Fe β-decay scheme. All the values given in this figure originate from the present work except for the Q_β-value which is taken from [Aud03] and the daughter half-life, taken from [HT09].

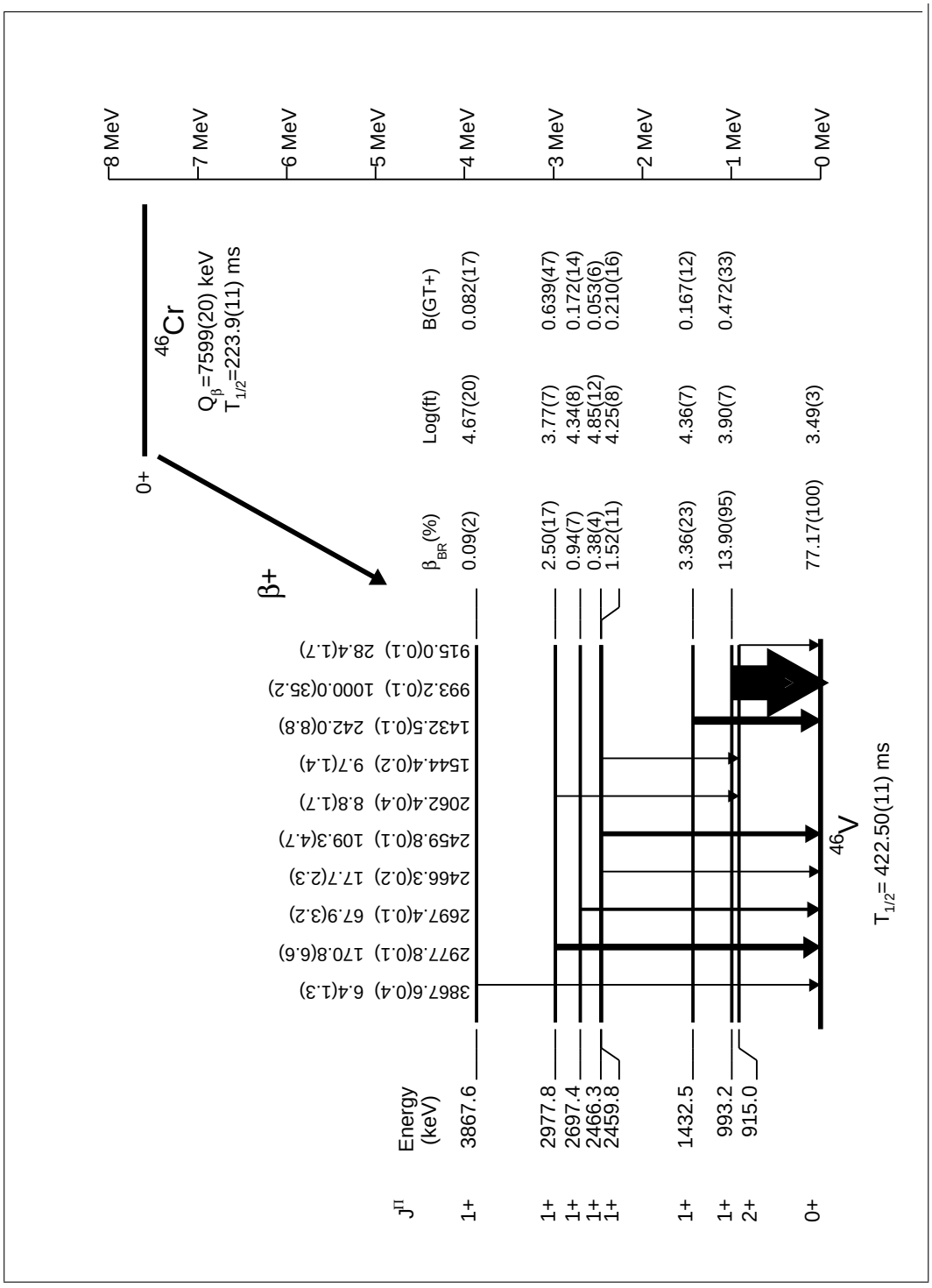

Figure 6.3: ^{46}Cr β-decay scheme. All the values given in this figure originate from the present work except for the Q_β-value which is taken from [Aud03] and the daughter half-life, taken from [HT09].

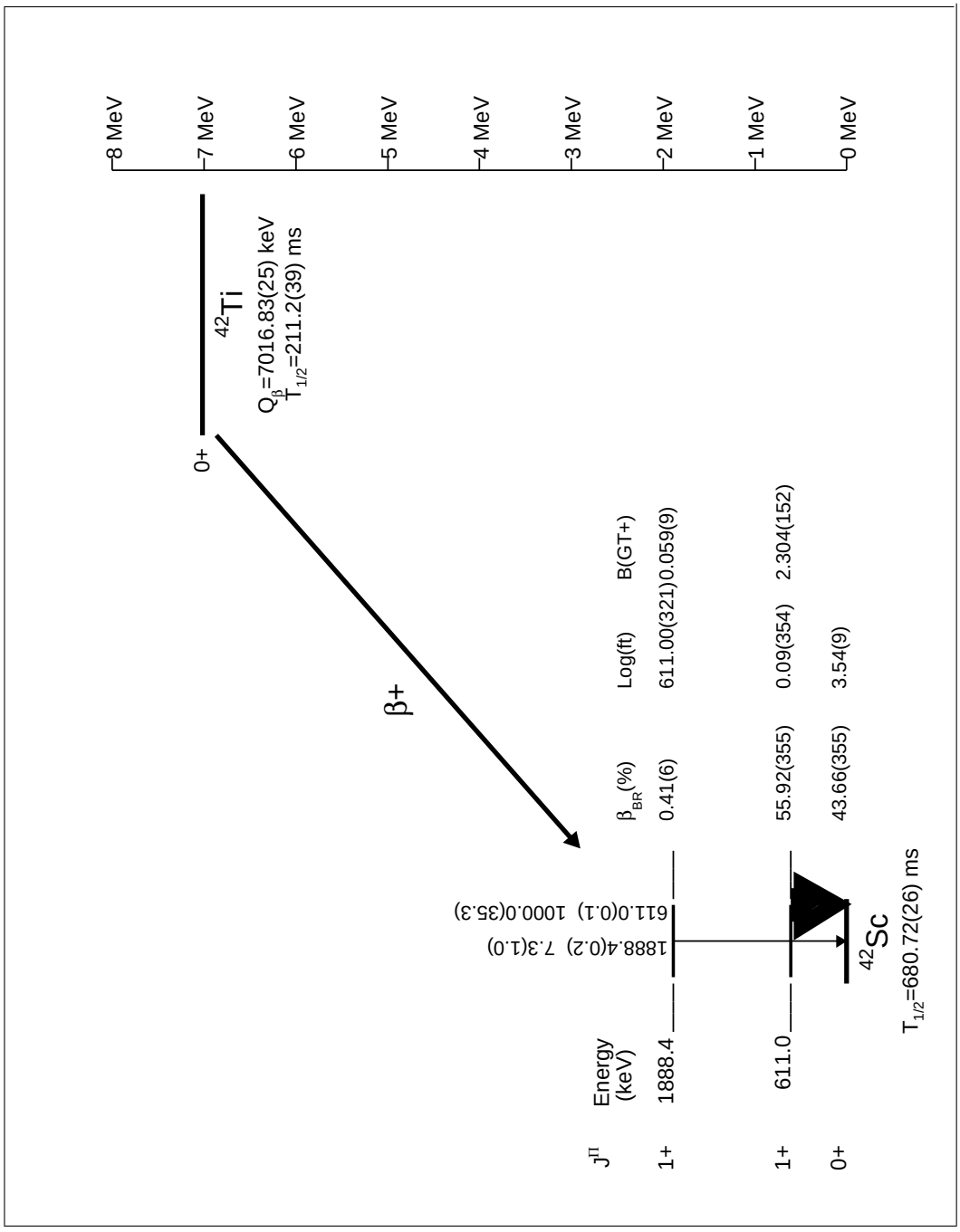

Figure 6.4: ^{42}Ti β-decay scheme using the Q-value reported by T.Kurtukian-Nieto et al [Kur09]. All the values given in this figure originate from the present work except for the Q_β-values which are taken from [Kur09] and the daughter half-life, taken from [HT09].

6.1 B(GT) compared with the Extreme Single Particle Model

A Gamow-Teller transition can be viewed as a one-body process in which a proton is changed into a neutron by the $\sigma\tau_+$ operator. The measured Gamow-Teller strengths are usually compared with the results of a calculation in an extreme single particle model [GFN82], in which the nuclear ground state is described by non-interacting nucleons occupying the lowest possible shell-model orbitals outside an inner core. The Gamow-Teller strength is then estimated from,

$$B(GT+) = \sum_{i,j} n_i^p \frac{n_f^h}{(2j_f+1)} |\langle i|\sigma\tau_+|f\rangle|^2 \tag{6.1}$$

where n_i^p is the number of particles in orbit i, $|\langle i|\sigma\tau_+|f\rangle|^2$ is the single-particle matrix element connecting particle state i and hole state f, n_f^h is the number of holes in orbit f and $2j_f+1$ is the degeneracy of the final orbit, thus $\frac{n_f^h}{(2j_f+1)}$ is the fractional number of holes available in the daughter nucleus.
The $|\langle i|\sigma\tau_+|f\rangle|^2$ for $j_i = l \pm 1/2$ and $j_f = l \pm 1/2$ in the extreme independent particle picture is given by,

$$|\langle i|\sigma\tau_+|f\rangle|^2 = 6(2j_f+1) \cdot \begin{Bmatrix} 1/2 & 1/2 & 1 \\ j_i & j_f & l \end{Bmatrix}^2 \tag{6.2}$$

The six-j symbol can be easily evaluated. In general for each particle orbit j_i, there are two possible final hole orbits, corresponding to no-spin-flip (nsf) $j_f = j_i$ and spin-flip (sf), $j_f = j_i \pm 1/2$. The single valence particle orbit case is then given by,

$$B(GT+) = n_p \frac{n_h^{nsf}}{(2j_f^{nsf}+1)} |\langle i|\sigma\tau_+|f\rangle|^2_{nsf} + n_p \frac{n_h^{sf}}{(2j_f^{sf}+1)} |\langle i|\sigma\tau_+|f\rangle|^2_{sf} \tag{6.3}$$

In β+-decay, each term in Eq. 6.3 -p.138- is the number of protons in the valence orbit times the fractional number of holes in the neutron orbit, times the characteristic single particle matrix element (See Table 6.1).

	j_f	
j_i	$l+1/2$	$l-1/2$
$l+1/2$	$\frac{2l+3}{2l+1}$	$\frac{4l}{2l+1}$
$l-1/2$	$\frac{4l+4}{2l+1}$	$\frac{2l-1}{2l+1}$

Table 6.1: Single Particle Gamow-Teller matrix element $|\langle i|\sigma\tau_+|f\rangle|^2$, where l is the angular momentum (s=0,d=1,f=2,g=3,h=4).

In the following section we will present the extreme single particle model calculation for the cases studied in the f-shell.

6.1.1 Extreme Single Particle Calculations

The four cases studied are in the f-shell with a core of $^{40}_{20}Ca_{20}$: 20 protons in the proton shells (closing the $d_{3/2}$ π-shell) and 20 neutrons in the neutron shells (closing the $d_{3/2}$ ν-shell). In order to determine the ν and π single particle states, we took as reference the experimental level schemes for ^{41}Ca [Uoz94] and ^{41}Sc [You70].

$^{54}_{26}$Ni$_{28}$ $B(GT+)$ calculation

For the ^{54}Ni β-decay we have eight protons in the $f_{7/2}$ proton sub-shell $(\pi f_{7/2})^{8p}$, two holes in the $f_{7/2}$ neutron sub-shell $(\nu f_{7/2})^{2h}$ and six holes in the $f_{5/2}$ neutron sub-shell $(\nu f_{5/2})^{6h}$, as shown in Fig. 6.5 -p.139-. Then the $B(GT+)$ according to Eq. 6.3 -p.138- is

$$B(GT+) = 8 \cdot \frac{2}{2 \cdot \frac{7}{2} + 1} \frac{2l+3}{2l+1} + 8 \cdot \frac{6}{2 \cdot \frac{5}{2} + 1} \frac{4l}{2l+1} = 8 \left(\frac{18}{56} + \frac{12}{7} \right) = 16.29 \qquad (6.4)$$

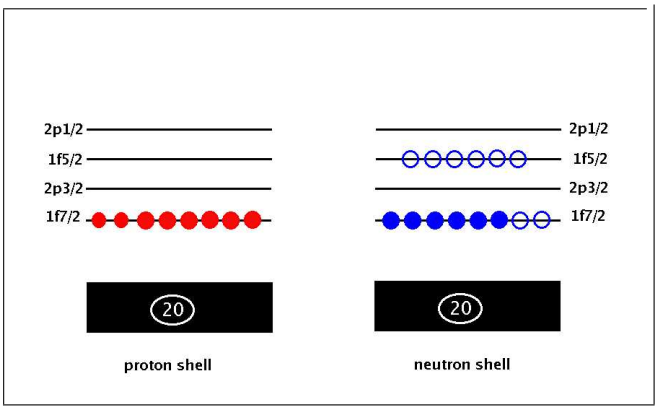

Figure 6.5: ^{54}Ni β-decay in the single particle scheme

$^{50}_{24}$Fe$_{26}$ $B(GT+)$ calculation

For the ^{50}Fe β-decay we have six protons in the $f_{7/2}$ proton sub-shell $(\pi f_{7/2})^{6p}$, four holes in the $f_{7/2}$ neutron sub-shell $(\nu f_{7/2})^{4h}$ and six holes in the $f_{5/2}$ neutron sub-shell $(\nu f_{5/2})^{6h}$, as shown in Fig. 6.6 -p.140- . Then the $B(GT+)$ according to Eq. 6.3 -p.138- is

$$B(GT+) = 6 \cdot \frac{4}{2 \cdot \frac{7}{2} + 1} \frac{2l+3}{2l+1} + 6 \cdot \frac{6}{2 \cdot \frac{5}{2} + 1} \frac{4l}{2l+1} = 6 \left(\frac{9}{14} + \frac{12}{7} \right) = 14.14 \qquad (6.5)$$

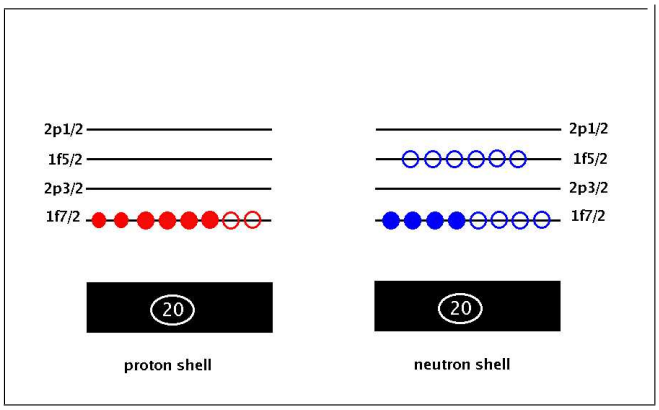

Figure 6.6: ^{50}Fe β-decay in the single particle scheme

$^{46}_{22}\mathbf{Cr}_{24}$ $B(GT+)$ calculation

For the ^{46}Cr β-decay we have four protons in the $f_{7/2}$ proton sub-shell $(\pi f_{7/2})^{4p}$, six holes in the $f_{7/2}$ neutron sub-shell $(\nu f_{7/2})^{6h}$ and six holes in the $f_{5/2}$ neutron sub-shell $(\nu f_{5/2})^{6h}$, as shown in Fig. 6.7 -p.140- . Then the $B(GT+)$ according to Eq. 6.3 -p.138- is

$$B(GT+) = 4 \cdot \frac{6}{2 \cdot \frac{7}{2} + 1} \frac{2l+3}{2l+1} + 4 \cdot \frac{6}{2 \cdot \frac{5}{2} + 1} \frac{4l}{2l+1} = 4 \left(\frac{54}{56} + \frac{12}{7} \right) = 10.70 \qquad (6.6)$$

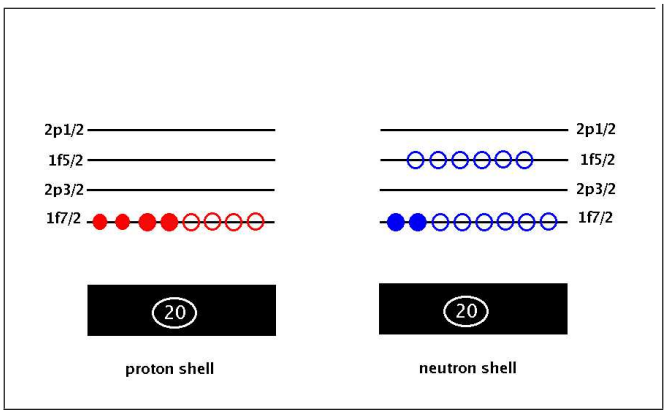

Figure 6.7: ^{46}Cr β-decay in the single particle scheme

$^{42}_{20}\mathbf{Ti}_{22}$ $B(GT+)$ calculation

For the case of the ^{42}Ti β-decay we have two protons in the $f_{7/2}$ proton sub-shell $(\pi f_{7/2})^{2p}$, eight holes in the $f_{7/2}$ neutron sub-shell $(\nu f_{7/2})^{8h}$ and six holes in the $f_{5/2}$

neutron sub-shell $(\nu f_{5/2})^{6h}$, as shown in Fig. 6.8 -p.141- . Then the $B(GT+)$ according to Eq. 6.3 -p.138- is.

$$B(GT+) = 2 \cdot \frac{8}{2 \cdot \frac{7}{2} + 1} \frac{2l+3}{2l+1} + 2 \cdot \frac{6}{2 \cdot \frac{5}{2} + 1} \frac{4l}{2l+1} = \frac{18}{7} + \frac{24}{7} = \frac{42}{7} = 6 \qquad (6.7)$$

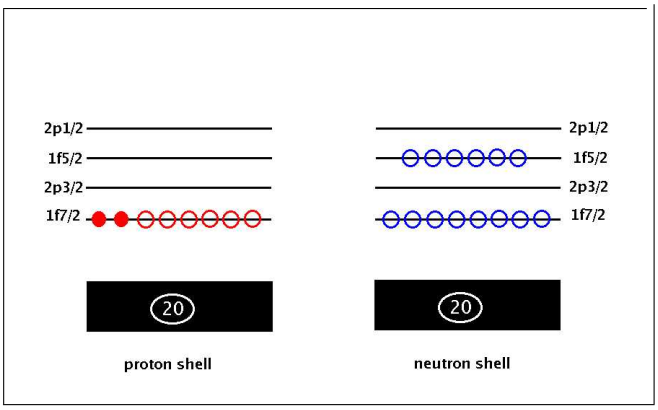

Figure 6.8: ^{42}Ti β-decay single particle scheme.

It is well known that the observed $B(GT+)$ is *quenched*; i.e., it is significantly smaller than the single particle estimate, and this quenching varies significantly from one nucleus to another. Moreover the present estimate is far away from a realistic shell model calculation. It is still interesting to calculate the quenching factor for the Gamow-Teller transitions seen in the β-decay experiment in comparison with this very extreme picture.

	(Z,N)	$B(GT+)_{\text{exp}}$	$B(GT+)_{\text{ESPM}}$	q
^{54}Ni	$(28,26)$	1.095(86)	16.29	14.88(117)
^{50}Fe	$(26,24)$	1.329(73)	14.14	10.64(58)
^{46}Cr	$(24,22)$	1.795(65)	10.70	5.96(22)
$^{42}\text{Ti}_K$	$(22,20)$	2.363(152)	6.00	2.54(16)

Table 6.2: Comparison of measured Gamow-Teller strength in β-decay experiments $B(GT+)_{\text{exp}}$ with the prediction of the extreme single particle method $B(GT+)_{\text{ESPM}}$. The quenching factor q is the ratio of these two quantities. In the ^{42}Ti case the two different results for the experimental B(GT) value, using the Q-values from Kurtukian-Nieto [Kur09] and Audi [Aud03], are shown.

It is interesting to note that the observed $B(GT+)$ strength shows a behaviour opposite to expectation as a function of mass. This might indicate that the strength is shifted to higher energies (towards the GT resonance) as A increased.

6.2 Comparison with Charge Exchange reaction results

One of the main motives to perform this work was the possibility to compare our β-decay results with those obtained in the (^{3}He,t) charge exchange reaction analysis, presented in Figs. 1.5-1.8 -pp. 13-16- and explained in Section 1.6. As mention before one can use the knowledge of the charge exchange reactions to obtain absolute $B(GT)$ values. In order to do that it is essential to have a precise value of the parent half-life in the mirror β-decay and the corresponding Q_β value. In this work we have substantially improved the $T_{1/2}$ value for the ^{54}Ni, ^{50}Fe, ^{46}Cr cases and obtained an independent value for the ^{42}Ti, although it is not as precise as the one given by T. Kurtukian-Nieto [Kur09] but in agreement with it. This can now be used to normalise the relative $B(GT)$ values obtained for the charge exchange reactions on ^{54}Fe, ^{50}Cr, ^{46}Ti and ^{42}Ca target nuclei.
Still missing is a precise value for the Q_β value in the ^{54}Ni, ^{50}Fe and ^{46}Cr cases. This measurement, however, lies outside of the scope of the present work. Discussions with experimental groups specialising in precise mass measurements are going on.
However, our experiments gave not only a precise $T_{1/2}$ value, which is a global value, but also absolute $B(GT)$ values for individual levels which can now be compared with the charge exchange results. This comparison is presented in Figs. 6.9-6.12 -pp.6.9 to 6.12- and Tables 6.3-6.6 -pp.148 to 151-.
First thing we note is that all the states which were observed in the CE reactions on the mirror target nucleus and lie both inside the Q_β window and in the sensitivity limit of our experiments, were also observed in our β-decay experiments. This means that the assumption of mirror symmetry for the two processes is to some extent correct. We should mention here that such studies were not done before in fp-shell nuclei. However a closer inspection of the individual states observed in the two processes shows some differences in terms of the $B(GT)$ values. This can be seen in the Figs. 6.9-6.12 -pp.6.9 to 6.12- where we have normalised the charge exchange reaction Gamow-Teller strength $B(GT-)$ to the strength of the first excited state in the β-decay.
Looking at the different states and their $B(GT)$ values, we see that the differences scatter from one state to another. In other words, one cannot say that the $B(GT)$ provided by one process is systematically lower or higher than the other. Since we want to look at the proportionality between the CE Gamow-Teller strength $B(GT-)$ values and the β-decay Gamow-Teller strength $B(GT+)$ values, we have included in the $B(GT-)$ values only the statistical errors.

There are three reasons which could explain these differences:

a) We know that reactions using hadronic probes are mainly peripherical. One could even imagine that (^{3}He,t) probes a more external part of the nucleus wave function than (p,n) for instance. On the other hand β decay can happen in first approximation in any part of the nucleus. However if we think that most of the decays we are discussing are due to the $f_{7/2}$ protons, outside the ^{40}Ca core, into $f_{7/2}$ or $f_{5/2}$ neutron orbitals, we have to think how these "valence" protons are spatially distributed in the nucleus. An $f_{7/2}$ wave function will be mainly localised in the external part of the nucleus; in this sense the situation is similar to the CE reac-

tion. However similar this situation does not need to be identical, and the small difference could explain the differences we observe.

b) It is well known that tensor components can contribute to the (^{3}He,t) process (and not to the β-decay). These contributions are small in comparison with the $\sigma\tau$ contributions. However if two different components contribute to the $\sigma\tau$ probability in a destructive way, then the tensor contributions could become dominant.
This has been observed, for instance, by Y. Fujita et al. [Fuj07c] in the case of ^{34}S, where the $d_{5/2} \rightarrow d_{3/2}$ and the $d_{3/2} \rightarrow d_{3/2}$ contribute destructively. This phenomenon is also discussed in a recent publication by Y. Fujita, B. Rubio and W. Gelletly [YFG11]. Something similar could very well happen in our case, with the $f_{7/2} \rightarrow f_{7/2}$ and the $f_{7/2} \rightarrow f_{5/2}$ contributions (see Section 6.1 -p.138-).

c) Finally, it could be that the two initial ground states, T_z=-1 and T_z=+1, are not really symmetric. In other words that the wave function of the T_z=-1 nucleus is not completely identical to the wave function of the T_z=+1 nucleus when we exchange protons and neutrons.
If the occupation of proton-levels (neutron-levels) and vacancies of neutron-levels (proton-levels) are different in T_z=-1 and T_z=+1 nuclei, one might naturally expect differences between the $\pi \rightarrow \nu(\beta+)$ process and the $\nu \rightarrow \pi$(CE) process.

We come back now to the normalisation of the relative $B(GT-)$ values obtained from the CE reactions. It happens often that only one state is known experimentally, i.e, the first excited state, and the $B(GT+)^{\text{1st.State}}$ β-decay value is naturally used for normalisation. This is what we have used in Figs. 6.9-6.12 -pp.6.9 to 6.12-, and in the 4th. column of the Tables 6.3-6.6 -pp.148 to 151-. Using this normalisation one could calculate the "expected $T_{1/2}$" and this is shown in Table 6.7 -p.151-.

Another alternative if one sees several levels in β-decay is to normalise to all the $B(GT)$ observed. The result of this normalisation is presented in the 5th. column of Tables 6.3-6.6 -pp.148 to 151-. We see that systematically the first normalisation method gives a shorter $T_{1/2}$ than the second method. And if we now compare with the measured $T_{1/2}$, we see that both measured $T_{1/2}$ values lie between these two values. This is an inderect indication that the *merged analysis* (see Section 1.5.2 -p.8-), where the experimental $T_{1/2}$ is used for normalisation, is probably the most appropriate method of normalisation of the $B(GT-)^{CE}$. The B(GT) values obtained in the merged analysis are also presented in 6th column of Tables 6.3-6.6 -pp.148 to 151-.

As we have seen, the Gamow-Teller transition strengths extracted in the analysis of charge exchange reactions measurements, have to be normalised to: (i) a $B(GT+)^{\beta}$ value from the β-decay measurements, or (ii) to the R^2-value (see Eq.1.5.2 -p.9-) in the so-called *merged analysis* (see Section 1.5.2 -p.8-).

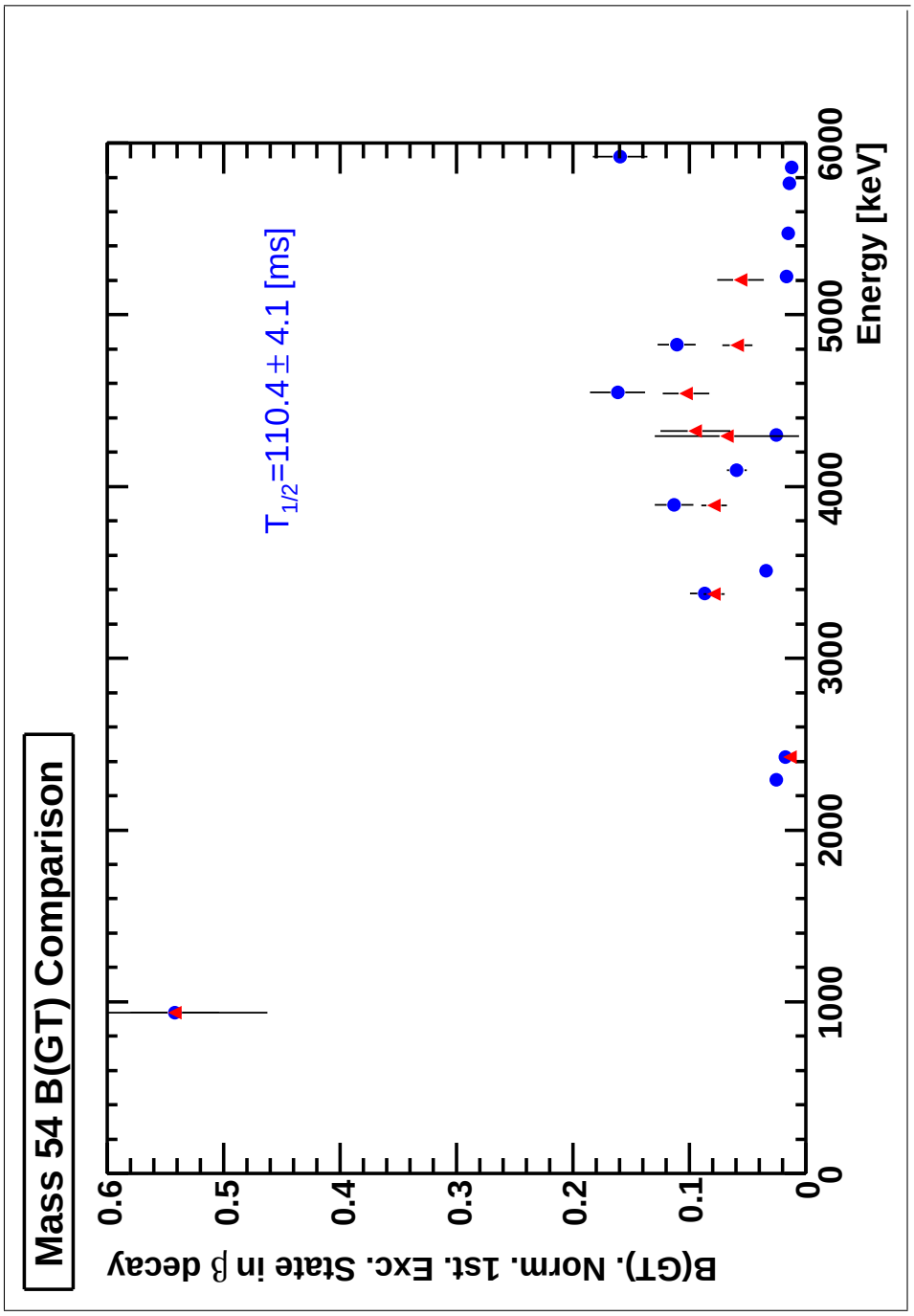

Figure 6.9: Comparison between the absolute Gamow-Teller Strength from β-decay $B(GT+)$, shown in red triangles, and the normalised Gamow-Teller strength from charge exchange reactions $B(GT-)$, for the mass 54 with total isospin T=1. The half-life value shown in blue was obtained from the normalised $B(GT-)$ using Eq. 1.22 -p.9-.

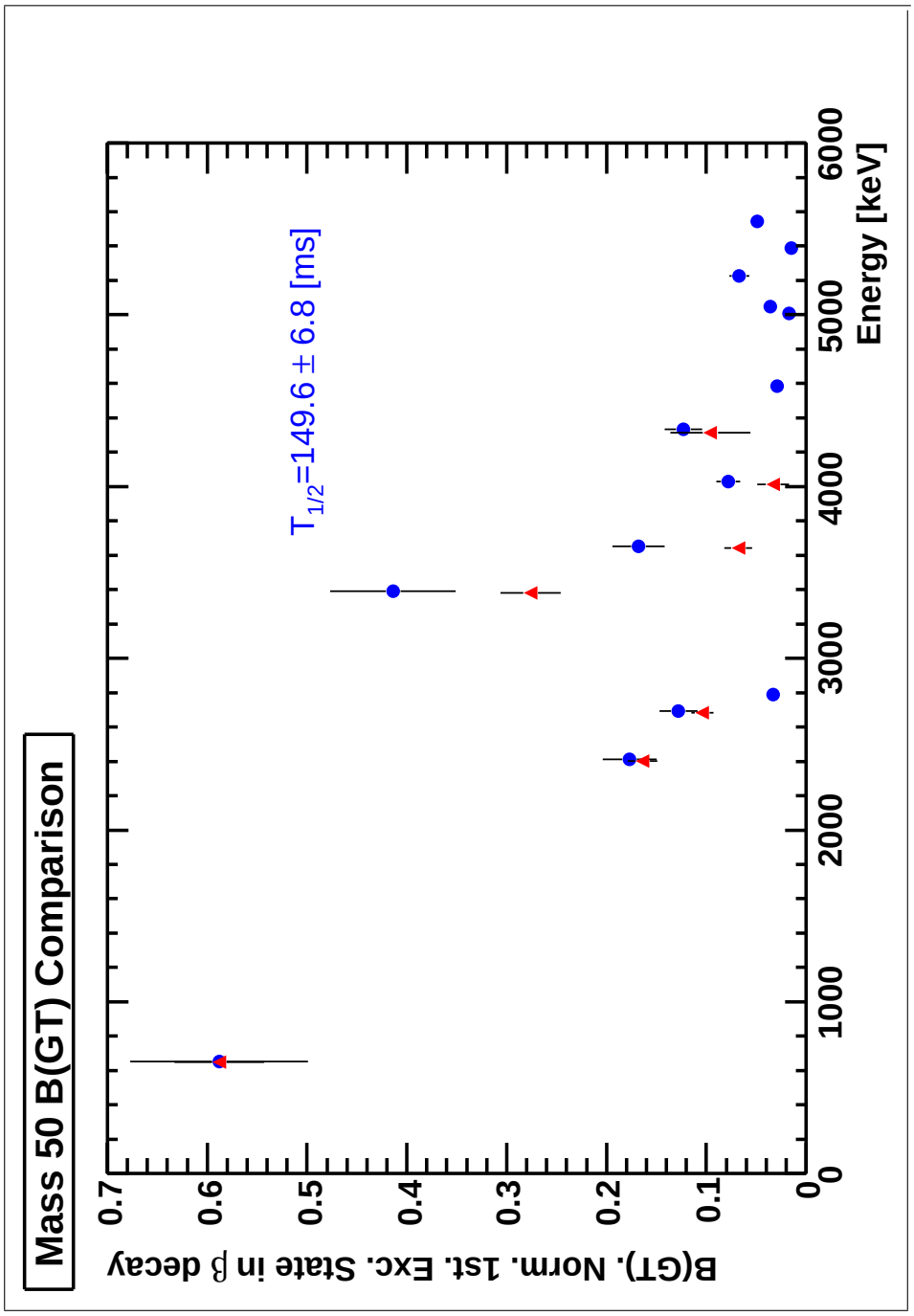

Figure 6.10: Comparison between the absolute Gamow-Teller Strength from β-decay $B(GT+)$, shown in red triangles, and the normalised Gamow-Teller strength from charge exchange reactions $B(GT-)$, for the mass 50 with total isospin T=1. The half-life value shown in blue was obtained from the normalised $B(GT-)$ using Eq. 1.22 -p.9-.

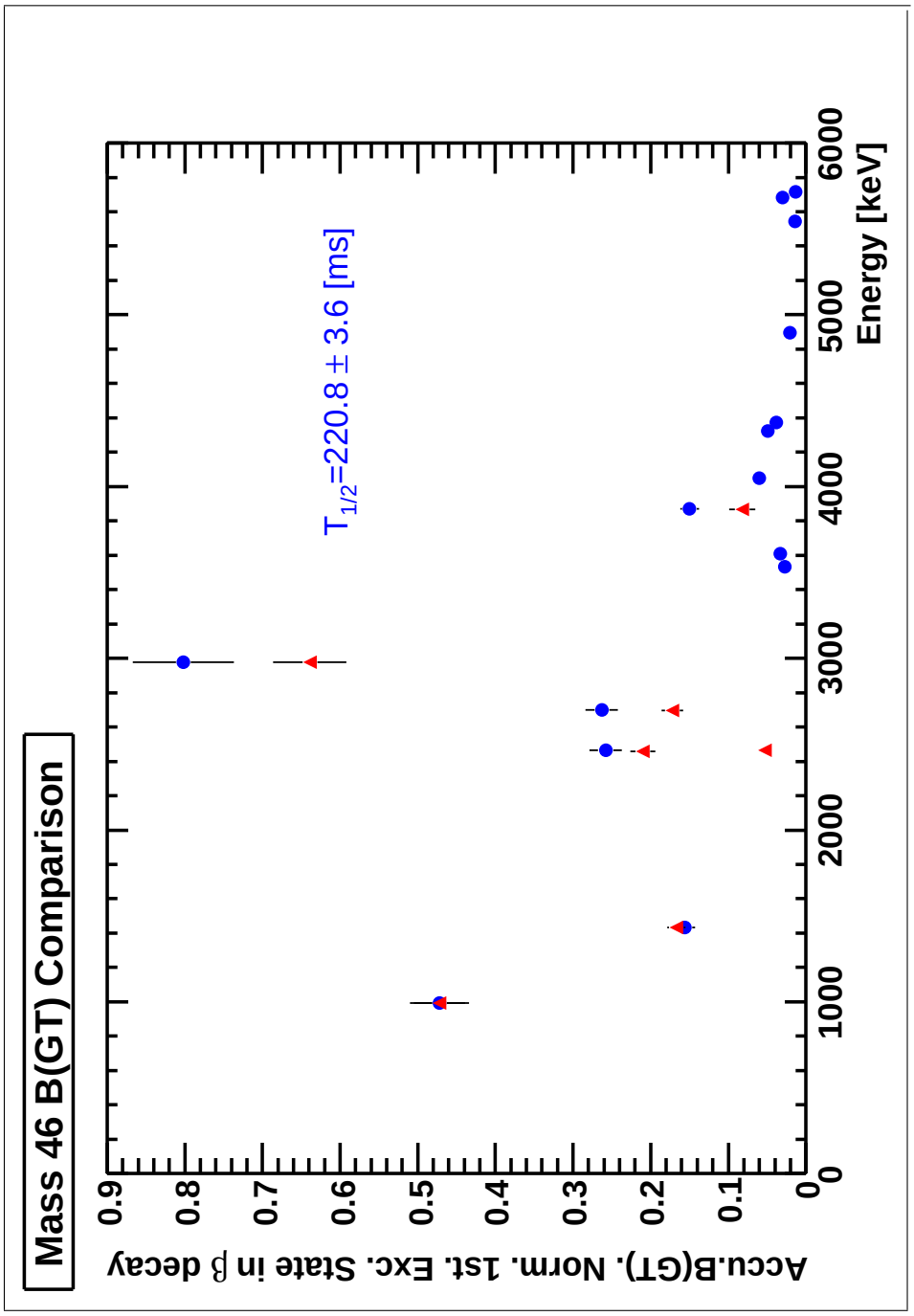

Figure 6.11: Comparison between the absolute Gamow-Teller Strength from β-decay $B(GT+)$, shown in red triangles, and the normalised Gamow-Teller strength from charge exchange reactions $B(GT-)$, for the mass 46 with total isospin T=1. The half-life value shown in blue was obtained from the normalised $B(GT-)$ using Eq. 1.22 -p.9-.

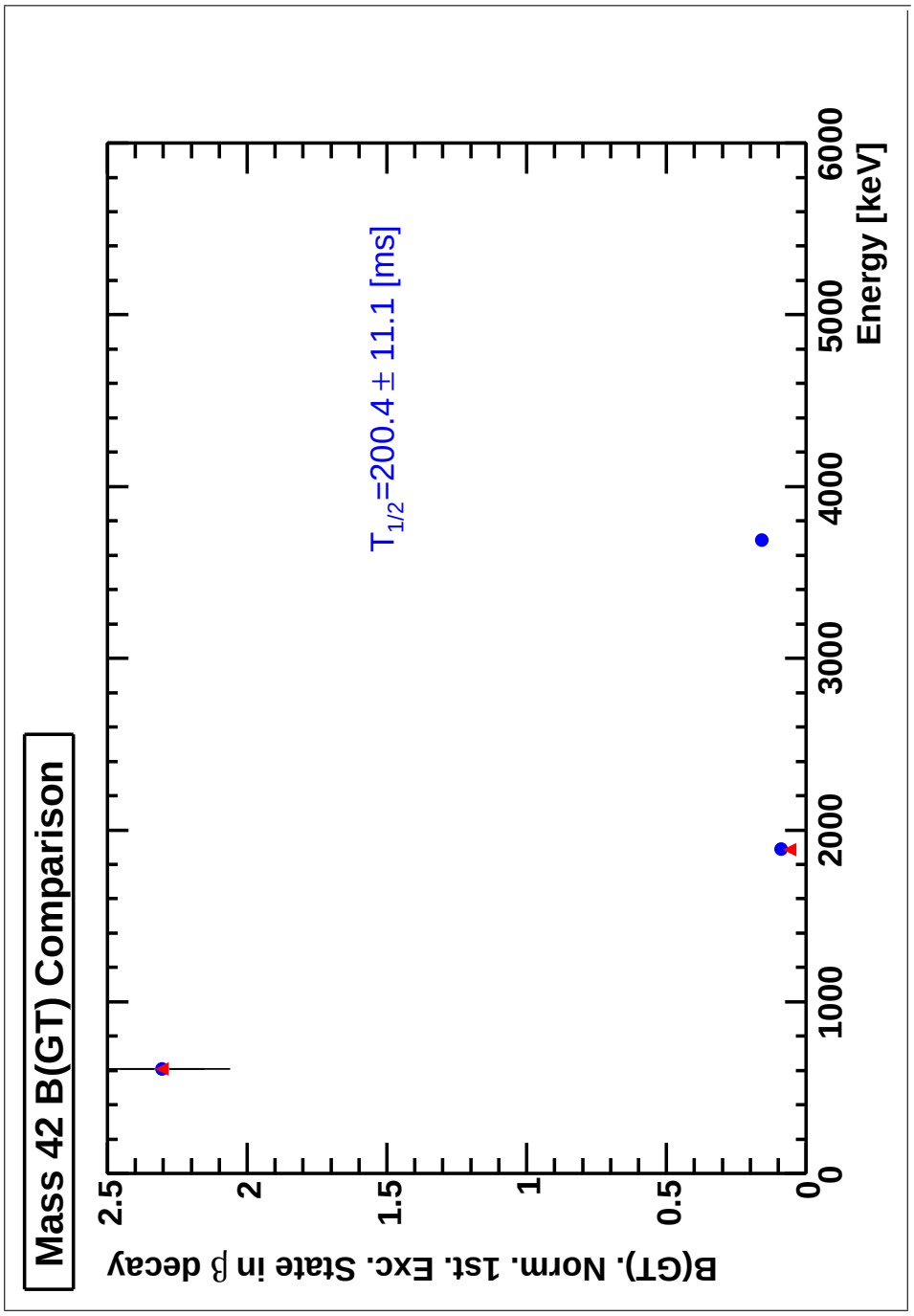

Figure 6.12: Comparison between the absolute Gamow-Teller Strength from β-decay $B(GT+)$, shown in red triangles, and the normalised Gamow-Teller strength from charge exchange reactions $B(GT-)$, for the mass 42 with total isospin T=1. The half-life value shown in blue was obtained from the normalised $B(GT-)$ using Eq. 1.22 -p.9-.

6.2.1 T=1, mass 54

Energy state [keV]	B(GT+)$_\beta$	Ex [keV]	B(GT-)$_{CE1}$	B(GT-)$_{CE2}$	B(GT-)$_{CE3}$
936.7	0.542(38)	938	0.542(80)	0.301(28)*	0.493(63)
2424.6	0.014(2)	2426	0.018(3)	0.010(1)	0.016(2)
3376.1	0.079(9)	3375	0.087(13)	0.048(5)	0.079(10)
		3506	0.034(5)	0.019(2)	0.031(4)
3889.6	0.079(11)	3891	0.113(17)	0.063(6)	0.103(13)
		4092	0.059(9)	0.033(3)	0.054(7)
4293.4	0.068(62)	4296	0.025(4)	0.014(1)	0.023(3)
4323.0	0.095(30)				
4543.8	0.103(20)	4544	0.162(24)*	0.090(8)	0.147(19)
4822.8	0.059(13)	4822	0.111(16)*	0.062(6)	0.101(13)*
5202.4	0.056(20)	5217	0.016(2)*	0.009(1)*	0.015(2)*
		5464	0.015(2)	0.009(1)	0.014(2)
		5755	0.014(2)	0.008(1)	0.013(2)
		5849	0.012(2)	0.007(1)	0.011(1)
		5909	0.159(23)	0.088(8)	0.145(18)
		6083	0.053(8)	0.029(3)	0.048(6)
		6118	0.027(4)	0.015(1)	0.025(3)
		6362	0.027(4)	0.015(1)	0.025(3)
		6466	0.020(3)	0.011(1)	0.018(2)
		6530	0.086(13)	0.048(5)	0.078(10)
		6792	0.045(7)	0.025(2)	0.041(5)
		6859	0.042(6)	0.023(2)	0.038(5)
		7135	0.063(9)	0.035(3)	0.057(7)
		7388	0.038(6)	0.021(2)	0.035(4)
		7449	0.052(8)	0.029(3)	0.047(6)
		7469	0.019(3)	0.010(1)	0.017(2)
		7542	0.027(4)	0.015(1)	0.025(3)
		7642	0.024(4)	0.013(1)	0.022(3)
		7711	0.056(8)	0.031(3)	0.051(6)

Table 6.3: Comparison of the Gamow-Teller strength values from Charge Exchange reactions (B(GT-)$_{CE}$) and β-decay experiments B(GT+)$_\beta$ for mass 54. The B(GT-)$_{CE1}$ are the B(GT) from CE reactions normalised to the first excited state B(GT+). The B(GT-)$_{CE2}$ are the B(GT) from CE reactions normalised to the total strength in the Q$_\beta$ window. The B(GT-)$_{CE3}$ are the B(GT) from CE reactions normalised using the *merged analysis*. The R^2-value was taken from the systematic dependence of R^2 and A. In this case R^2=8.9(9).

6.2.2 T=1, mass 50

Energy state [keV]	B(GT+)$_\beta$	Ex [keV]	B(GT-)$_{CE1}$	B(GT-)$_{CE2}$	B(GT-)$_{CE3}$
651.0	0.588(45)	652	0.588(89)	0.406(33)	0.548(70)
2403.8	0.164(15)	2411	0.177(27)	0.122(10)	0.165(21)
2684.2	0.104(11)	2694	0.128(19)	0.088(7)	0.119(15)
		2790	0.033(5)	0.023(2)	0.031(4)
3380.0	0.276(30)	3392	0.414(63)	0.286(23)	0.386(49)
3643.4	0.068(14)	3654	0.168(26)	0.116(9)	0.157(20)
4012.7	0.033(16)	4028	0.078(12)	0.054(4)	0.073(9)
4315.7	0.096(40)	4333	0.123(19)	0.085(7)	0.115(15)
		4584	0.029(4)	0.020(2)	0.027(4)
		5009	0.017(3)	0.012(1)	0.016(2)
		5047	0.036(6)	0.025(2)	0.034(5)
		5226	0.067(10)	0.046(4)	0.062(8)
		5389	0.015(2)	0.010(1)	0.014(2)
		5545	0.049(7)	0.034(3)	0.046(6)

Table 6.4: Comparison of the Gamow-Teller strength values from Charge Exchange reactions (B(GT-)$_{CE}$) and β-decay experiments B(GT+)$_\beta$ for mass 50. The B(GT-)$_{CE1}$ are the B(GT) from CE reactions normalised to the first excited state B(GT+). The B(GT-)$_{CE2}$ are the B(GT) from CE reactions normalised to the total strength in the Q$_\beta$ window. The B(GT-)$_{CE3}$ are the B(GT) from CE reactions normalised using the *merged analysis*. The R^2-value was calculated using the half-life value obtained from the analysis of the present experiment.

6.2.3 T=1, mass 46

Energy state [keV]	B(GT+)$_\beta$	Ex [keV]	B(GT-)$_{CE1}$	B(GT-)$_{CE2}$	B(GT-)$_{CE3}$
993.2	0.472(33)	994	0.472(38)	0.332(16)	0.368(47)
1432.5	0.167(12)	1433	0.156(13)	0.110(5)	0.122(16)
2459.8	0.210(16)	2465	0.258(21)	0.182(9)	0.201(26)
2466.3	0.053(6)				
2697.4	0.172(14)	2699	0.263(21)	0.185(9)	0.205(26)
2977.8	0.639(47)	2978	0.802(65)	0.565(27)	0.625(80)
		3533	0.027(2)	0.019(1)	0.021(3)
		3609	0.033(3)	0.023(1)	0.026(3)
3867.6	0.082(17)	3870	0.150(12)	0.106(5)	0.117(15)
		4049	0.060(5)	0.042(2)	0.047(6)
		4323	0.049(4)	0.034(2)	0.038(5)
		4374	0.038(3)	0.027(1)	0.030(4)
		4895	0.021(2)	0.014(1)	0.016(2)
		5544	0.014(1)	0.010(0)	0.011(1)
		5684	0.030(2)	0.021(1)	0.023(3)
		5717	0.013(1)	0.009(0)	0.010(1)
		6027	0.067(5)	0.047(2)	0.052(7)
		6175	0.022(2)	0.015(1)	0.017(2)
		6361	0.015(1)	0.011(1)	0.012(2)
		6447	0.021(2)	0.014(1)	0.016(2)
		6509	0.038(3)	0.027(1)	0.030(4)

Table 6.5: Comparison of the Gamow-Teller strength values from Charge Exchange reactions (B(GT-)$_{CE}$) and β-decay experiments B(GT+)$_\beta$ for mass 46. The B(GT-)$_{CE1}$ are the B(GT) from CE reactions normalised to the first excited state B(GT+). The B(GT-)$_{CE2}$ are the B(GT) from CE reactions normalised to the total strength in the Q$_\beta$ window. The B(GT-)$_{CE3}$ are the B(GT) from CE reactions normalised using the *merged analysis*. The R^2-value was taken from the systematic dependence of R^2 and A. In this case R^2=7.8(9).

6.2.4 T=1, mass 42

Energy state [keV]	B(GT+)$_\beta$	Ex [keV]	B(GT-)$_{CE1}$	B(GT-)$_{CE2}$	B(GT-)$_{CE3}$
611.0	2.304(152)	611	2,304(243)	2.135(212)	2.340(298)
1888.4	0.059(9)	1889	0,089(9)	0.082(8)	0.090(11)
		3688	0,158(17)	0.146(15)	0.160(20)

Table 6.6: Comparison of the Gamow-Teller strength values from Charge Exchange reactions (B(GT-)$_{CE}$) and β-decay experiments B(GT+)$_\beta$ for mass 42. The B(GT-)$_{CE1}$ are the B(GT) from CE reactions normalised to the first excited state B(GT+). The B(GT-)$_{CE2}$ are the B(GT) from CE reactions normalised to the total strength in the Q$_\beta$ window. The B(GT-)$_{CE3}$ are the B(GT) from CE reactions normalised using the *merged analysis*. The R^2-value was taken from the systematic dependence of R^2 and A. In this case R^2=5.5(3).

	$T^{\beta}_{1/2}$ ms	$T^{\mathrm{CE1}}_{1/2}$ ms	$T^{\mathrm{CE2}}_{1/2}$ ms
^{54}Ni	114.1(2)	110.4(41)	121.8(35)
^{50}Fe	152.2(6)	149.6(68)	163.1(58)
^{46}Cr	223.9(11)	220.8(36)	237.3(31)
^{42}Ti	211.2(39)	200.4(111)	208.6(106)

Table 6.7: Half-life obtained from the CE-reactions normalising by the first excited state $B(GT+)$ ($T^{\mathrm{CE1}}_{1/2}$) and by the total strength in the Q$_\beta$-window ($T^{\mathrm{CE2}}_{1/2}$), using Eq. 1.22 -p.9-, in comparison with the β-decay half-life obtained from this work.

For the four cases studied in charge exchange reactions [Ada07a], the R^2 values used were: $R^2_{^{54}\mathrm{Ni}}$=8.2(9), $R^2_{^{50}\mathrm{Fe}}$=7.6(11), $R^2_{^{46}\mathrm{Cr}}$=7.8(9) and $R^2_{^{42}\mathrm{Ti}}$=5.5(3). They compare well with our values.

In summary from the comparison between the B(GT-)$_{CE}$ from charge exchange reaction measurements and the B(GT+)$_\beta$ from β-decay experiments, we can conclude the following:

(a) The same states are observed in the two analogue processes, β^+-decay and charge exchange, if we restrict ourselves to the Q$_\beta$-window and sensitivity limits of our experiment. This is as we expected.

(b) The Gamow-Teller transition strengths B(GT)$_i$ observed in both processes, in general, agree with each other, especially in those cases where the β population of the state is strong. Nevertheless, there are some cases where the differences are not negligible. These cases are marked with an asterisk (*) in the tables. Possible reasons for these differences are discussed in the text.

6.3 M1 $1^+ \rightarrow 1^+$ transitions in the daughter nuclei

A very interesting observation from the analysis of the present β-decay experiments, is the absence of M1 $1^+ \rightarrow 1^+$ transitions in the daughter nuclei. If we look at the β-decay level schemes (see Figs.6.1-6.4 -pp.134 to 137-), we can see that in none of the four cases under study, M1 transitions from the high energy 1^+ states to the first excited 1^+ state are observed. We predominantly observe the M1 transitions from these 1^+ states to the 0^+ ground state and in some cases the M1 transitions to the first 2^+ excited state. To understand this we have to think in terms of isospin. The 0^+ ground states of the T_z=0 daughter nuclei have isospin T=1, because it is an odd nucleus with N=Z and the wave function has to be anti-symmetric. On the other hand, the 1^+ excited states have isospin T=0. In the M1 transitions of the type 1^+(T=0) $\rightarrow$ 0^+(T=1) the strong isovector term predominates. These are the transitions we see. In the 1^+(T=0) $\rightarrow$ 2^+(T=1) the isovector term is also dominant. In contrast , in the M1 1^+(T=0) $\rightarrow$ 1^+(T=1) transitions only the isoscalar term can contribute, which is around 20 times weaker than the isovector term.

These transitions are consequently only $\sim$5% of the other ones and are, therefore, below the sensitivity limit of our experiments. This corresponds to the so-called *quasi-selection rule* of Warburton and Weneser [Wil69], and it has been observed to be valid for the first time for fp-shell nuclei, in this work.

CHAPTER 7

RESUMEN EN CASTELLANO

Esta tesis comprende un estudio experimental de la desintegración de cuatro núcleos con T_z=-1. El objetivo principal de este trabajo es comparar esas cuatro desintegraciones con el proceso espejo estudiado en reacciones de intercambio de carga del tipo (^{3}He,t) en dependencias del Centro de Investigacion de Física Nuclear (RCNP) en Osaka, Japón.
Los experimentos de desintegración beta fueron realizados en dos laboratorios distintos, en el Separador En Linea por Ionización con Láser LISOL en el Centro de Investigación del Ciclotrón CRC en Louvain-la-Nueve en Bélgica y en el Separador de FRagmentos FRS en GSI Darmstradt, Alemania. Estos dos laboratorios usan técnicas completamente distintas de separación. En LISOL los núcleos producidos en la reacción de fusión y evaporación, se ionizan usando técnicas de ionización por láser y se separan usando un separador de masas "on-line", mientras que en el FRS los iones se separan en vuelo luego de una reacción de fragmentación.

7.1 Introducción

La desintegración β es un proceso que sucede en la mayoría de los núcleos atómicos conocidos, en el cual un protón se transforma en un neutrón o viceversa, más un neutrino y un anti-neutrino respectivamente. Pueden darse de dos modos distintos de desintegración: Fermi o Gamow-Teller. El modo Fermi de desintegración viene mediado por el operador de aumento o disminución de isoespín: $O_F=\tau^{\pm}$. El modo Gamow-Teller tiene además la posibilidad de cambiar el espín nuclear ya que incluye el operador de Pauli: $O_{GT}=\sigma\tau^{\pm}$. Estos operadores también son los mediadores en las reacciones de intercambio de carga (CE) del tipo (n,p) y (p,n). En una reacción de intercambio de carga, un protón del núcleo que constituye el blanco es reemplazado por un neutrón del haz primario incidente (o viceversa). Al ser la reacción de intercambio de carga un proceso análogo a la desintegración β, estarán necesariamente mediadas por los mismos operadores.

En resumen: se puede extraer información de las propiedades de espín-isoespín del núcleo estudiando tanto la desintegración β como las reacciones de intercambio de carga.

A la hora de comparar estos dos procesos, es importante definir una función, llamada fuerza de transición Gamow-Teller $B(GT)$ de la siguiente manera,

$$B(GT) = |\langle\psi_f| \sum_{k=1}^{A} \sigma_k \tau_k^{\pm} |\psi_i\rangle|^2 = \langle\sigma\tau\rangle^2 \tag{7.1}$$

Esta función es simplemente el elemento de matriz al cuadrado del operador O_{GT} entre el estado inicial del núcleo padre, ya sea el estado fundamental o un isómero, ψ_i y los estados finales en el núcleo hijo ψ_f. Por ello la $B(GT)$ debe estar relacionada con la probabilidad de transición β entre estos estados o con la sección eficaz (n,p) o (p,n) según hablemos de desintegración β o reacciones de intercambio de carga, respectivamente.

7.1.1 Estudio de la B(GT$^+$) en desintegraciones β

La información experimental más directa sobre la $B(GT+)$ es obtenida de experimentos de desintegración β, midiendo la vida media de la desintegración β $T_{1/2}$ y las correspondientes razones de ramificación de las transiciones de un estado en el núcleo padre (en general el estado fundamental) a los estados correspondientes en el núcleo hijo. No obstante, las medidas de las $B(GT+)$ a estados excitados en el núcleo hijo, están limitadas a los estados contenidos en la ventana energética definida por la diferencia de masas entre el núcleo padre y el núcleo hijo (valor Q_β).

$$B_j(GT+)\lambda^2 = K/f_j t_j \qquad \text{y} \qquad B(F)(1-\delta_c) = K/f_F t_F \tag{7.2}$$

donde las constantes K=6143.6(16) [HT09], λ=-1.270(3) [HT06] y δ_c [TH02], factor de correccion de Coulomb , son conocidas. f_j es la función de espacio de fase (o también llamada función de Fermi) para el nivel j, que depende del valor Q_β, del número atómico Z' del núcleo hijo [WB74] y de la energía de excitación del estado, t_j es la vida media parcial al nivel j y $B(F)$ es la fuerza de transición Fermi que, por definición, es $B(F) = N - Z$ (excepto en los casos N=Z cuyo estado fundamental tenga isoespín T=1).

7.1.2 Estudio de la B(GT-) en reacciones de intercambio de carga

Sin embargo, el estudio de las $B(GT-)$ mediante reacciones de intercambio de carga, no sufre de esta restricción energética, pudiendo acceder a estados de alta energía de excitación mayores que el valor Q_β. A pesar de que esto es una gran ventaja, en estos estudios sólo es posible obtener medidas de la $B(GT-)_i$ (fuerza de la transición Gamow-Teller al estado i) relativas entre sí y proporcionales a la sección eficaz diferencial de reacción a cero grados [Tad87].

$$\frac{d\sigma^{CE}}{d\Omega}(0^o) \propto K^{CE} N_{\sigma\tau}^{CE} |J_{\sigma\tau}(q=0)|^2 B(GT-)_i = \hat{\sigma}^{GT} B(GT-)_i \tag{7.3}$$

siendo K^{CE} el factor cinemático definido como $K^{CE} = \frac{E_i E_f}{(\hbar c^2 \pi)^2}$, donde $E_{i(f)}$ es la energía reducida en el canal de entrada (salida); $N_{\sigma\tau}^{CE}$ el factor de distorsión definido por la razón entre las secciones eficaces de onda distorcionada y onda plana; $|J_{\sigma\tau}(q=0)|^2$ la integral de volumen del potencial efectivo de intracción central $\sigma\tau$, con mementum transferido $q = 0$. A su vez, $\hat{\sigma}_i^{GT} = K^{CE} N_{\sigma\tau}^{CE} |J_{\sigma\tau}(q=0)|^2$ es definida como la sección eficaz unitaria Gamow-Teller . Para poder transformar estas fuerzas Gamow-Teller relativas en fuerzas absolutas, es necesario determinar el valor de $\hat{\sigma}_{GT}$. Existen dos formas de hacerlo: (1) usando el valor de la $B(GT+)_i$ para un estado en particular, medido en la desintegración β, o (2) usando la simetría de isoespín en núcleos espejo.
Si usamos la simetría de isoespín para obtener $\hat{\sigma}_{GT}$, debemos suponer dos cosas (i) Toda la fuerza de transición Fermi, se concentra en el estado isobarico análogo (IAS) y es igual a $B(F) = N - Z$ y (ii) la razón entre las secciones eficaces unitarias Gamow-Teller y Fermi, es definida como:

$$R^2 = \frac{\hat{\sigma}_{GT}(0^o)}{\hat{\sigma}_F(0^o)} = \frac{\sigma_{GT}^i(0^o) B(F)}{\sigma_F(0^o) B(GT-)_i} \tag{7.4}$$

El valor de R^2 es constante para una masa nuclear A dada.

7.2 Reacciones de intercambio de carga RCNP

Las primeras medidas de la $B(GT-)$ en reacciones de intercambio de carga fueron realizadas en los 80 en lugares como el ciclotrón de la Universidad de Indiana (IUCF) [RS94], utilizando energías de haz incidente entre los 100-200 MeV a 0^o. La resolución en energías era aproximadamente de 400 keV; estados individuales muy próximos en energía eran imposibles de separar.
Desde el año 2000, experimentos de alta resolución del tipo (^{3}He,t) se han llevado a cabo en Centro de Investigación de Física Nuclear (RCNP) en Osaka, Japón, donde se han logrado resoluciones en energía de 35 keV [Fuj07a].

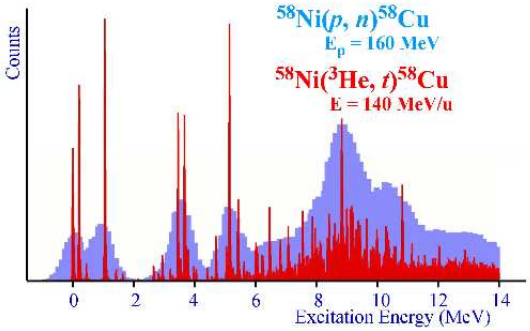

Figure 7.1: Espectros de energía de reacciones de intercambio de carga a 0°. Comparación entre medidas de la reacción ^{58}Ni$(p,n)^{58}$Cu llevadas a cabo en los 80 [RS94] (ΔE $\sim$ 400 keV) y las medidas recientes de la reacción ^{58}Ni$(^3$He$,t)^{58}$Cu [Fuj07a] (ΔE $\sim$ 35 keV).

Con esta mejoría en la resolución en energías, es posible estudiar la fuerza de transición Gamow-Teller $B(GT-)_i$ resultantes de medidas de reacciones de intercambio de carga y compararla con las medidas absolutas de $B(GT+)_i$ a partir de experimentos de desintegración β.

7.3 Simetría de Isoespín en núcleos con la misma masa A

El isoespín se considera un buen número cuántico, suponiendo que la interacción nuclear es independiente de la carga [BM98]. Por lo tanto, se puede esperar una estrucutura análoga en núcleos isóbaros con distintos valores de T_z (tercera componente de isoespín. $T_z = \frac{N-Z}{2}$).

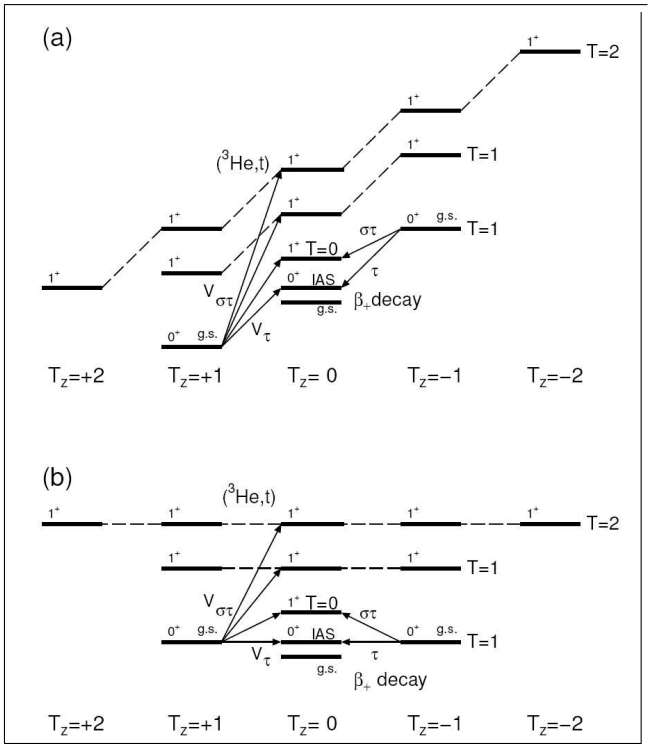

Figure 7.2: Estructura de la simetría de isoespín en núcleos isóbaros con $T_z = 0, \pm 1, \pm 2$. (a) Esquema de niveles en el espacio real de energías. (b) Esquema de niveles sustrayendo la energía Coulombiana de desplazamiento. La estructura simétrica es evidente. Los estados análogos estan conectados mediante líneas discontínuas [Ada07a].

En la Fig. 7.2(a) se muestra el esquema de niveles para núcleos con $T_z = 0, \pm 1, \pm 2$ y una masa A par. Al sustraer la enegía de desplazamiento Coulombiana, se puede apreciar con claridad la estructura de la simetría de isoespín (ver Fig. 7.2(b)). Los estados correspondientes en núcleos con distinto T_z son los llamados *estados análogos*

que en la figura están conectados por líneas discontínuas. Estos estados análogos tienen los mismos valores de espín tota y paridad ,J^{Π}, e isoespín total T. Estados con isoespín total T=0 son posibles únicamente en núcleos con T_z=0, mientras que estados con T=1 son posibles en el triplete de núcleos con T_z= 0 y ±1. Los estados con T=2 son posibles en el quinteto de núcleos con T_z= 0, ±1, ±2.
Las transiciones que conectan los distintos estados análogos, son análogas también. Estas *transiciones análogas*, a su vez, deben tener energías y fuerzas de transición ($B(F)$ y $B(GT)$) correspondientes.
En resumen, si suponemos que existe simetría de isoespín en núcleos espejo, las fuerzas de transición Gamow-Teller $B(GT-)$ observadas tanto en reacciones de intercambio de carga del tipo (^{3}He, t) como en experimentos de desintegración β ($B(GT+)$), deben tener el mismo valor.

7.4 Transiciones Gamow-Teller en la capa fp

7.4.1 Transiciones Gamow-Teller en el colapso del núcleo de una supernova

Las medidas de las transiciones Gamow-Teller son muy importantes en astrofísica. Una estrella masiva, al llegar al final de su evolución, ha acumulado en su núcleo estelar núcleos atómicos correspondientes a la capa nuclear fp. Si la masa del núcleo estelar excede el límite de Chandrasekhar (1.44 $M_\odot$), la "presión de degeneración de electrones"[1] no puede soportar al núcleo, comenzando el colapso de la estrella. Esto es el comienzo de una supernova del tipo II [RR88].
Es así como la captura electrónica, la desintegración β y reacciones inducidas por neutrinos comienzan a tomar un papel importante [LMP02, LMP03]. Debido a la captura electrónica los núcleos atómicos, que constituyen el núcleo estelar, se vuelven ricos en neutrones. Al disminuir el número de electrones, el colapso estelar se acelera. Además neutrinos y anti-neutrinos, que casi no iteractúan con la materia, sacan energía del núcleo estelar. La energía cinética en el núcleo de la estrella disminuye aún más y la velocidad del colapso se acelera.
Las tasas de reacción para estos procesos de interaccón débil son parámetros importantes para la simulación del colapso. Es aquí donde las fuerzas de transición Fermi y Gamow-Teller tienen gran importancia [LMP00]. Las tasas de interacción débil, en especial aquellas que involucran transiciones Gamow-Teller en modelos de formación de una supernova, han sido estudiados por G.M. Fuller, W.A. Fowler y M.J. Newman para núcleos con masas $A \leq$60 [GFN82]. Sin embargo sus cálculos no están basados en datos experimentales. También se ha evaluado la fuerza de transición Gamow-Teller para isotopos de Fe y Ni usando cálculos de modelo de capas [LMP02, LMP03, LMP00]. Es por ello que las medidas experimentales de la $B(GT)$ son importantes para contrastar la simulación que nos permite calcular el colapso de una supernova de tipo II.

[1] Principio de exclusión de Pauli: prohibición de la existencia de dos fermiones con números cuánticos idénticos en el mismo estado de energía.

7.4.2 Medidas de $B(GT)$ en núcleos con T=1 en la capa fp

La comparación de la probabilidad de transiciónes Gamow-Teller $B(GT-)$, por medio de reacciones de intercambio de carga y desintegración β $B(GT+)$ en la capa fp para núcleos con isoespín total T=1, presenta dos grandes ventajas desde el punto de vista experimental:

1.- Los núcleos con T_z=+1 en la capa fp, es decir ^{42}Ca, ^{46}Ti, ^{50}Cr y ^{54}Fe, son estables. Por lo tanto es posible construir blancos para el estudio de reacciones del tipo $(^3\mathrm{He}, t)$ (ver Fig. 7.3).

2.- Los núcleos con T_z=-1 en la capa fp, es decir ^{42}Ti, ^{46}Cr, ^{50}Fe y ^{54}Ni, se desintegran β^+ y tienen un valor Q_β [Aud03, Kur09] entre 7 y 9 MeV. Lo cual nos permite acceder a niveles de alta energía de excitación, siempre menores que su respectivo Q_β, en el núcleo hijo (ver Fig. 7.3).

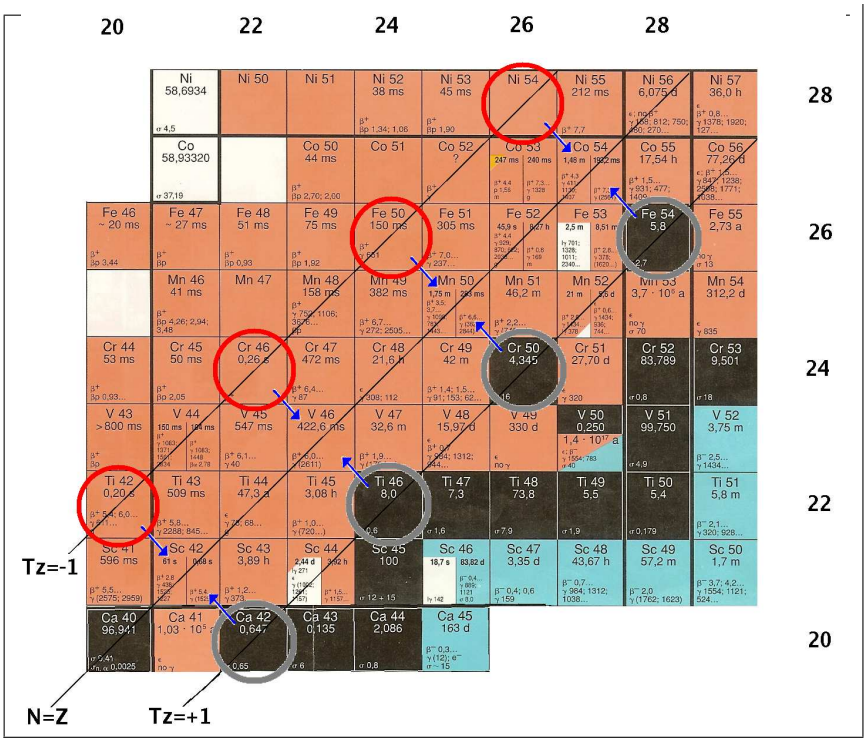

Figure 7.3: Carta de Nucleidos. En la figura se muestran algunos núcleos de la capa fp. Las líneas muestran los núcleos con tercera componente de isoespín $T_z = \frac{N-Z}{2}$ = 0, ±1. El código de colores usual en la carta de nucleidos es: rojo para núcleos que se desintegran β^+, azul para núcleos que se desintegran β-, negro para núcleos radioactivamente estables.

7.4.3 Resultados: Reacciones (^{3}He, t), $\mathbf{T}_z$=+1 → 0

Los experimentos de reacciones de intercambio de carga se realizaron en dependencias del RCNP en Osaka, Japón. Los resultados de estos experimentos formaron parte de la tesis doctoral de Dr. Tatsuya Adachi [Ada07a].

El experimento

Un haz de ^{3}He es acelerado hasta 140 MeV/u desde el Ring Cyclotron (K=400 MeV) hasta el blanco estable. La reacción nuclear sucede en una camara de dispersión (scattering chamber) en donde se encuentra el blanco. El núcleo de ^{3}He incidente intercambia un protón con un neutrón del blanco (^{42}Ca, ^{46}Ti, ^{50}Cr o ^{54}Fe), formando tritio ^{3}H.

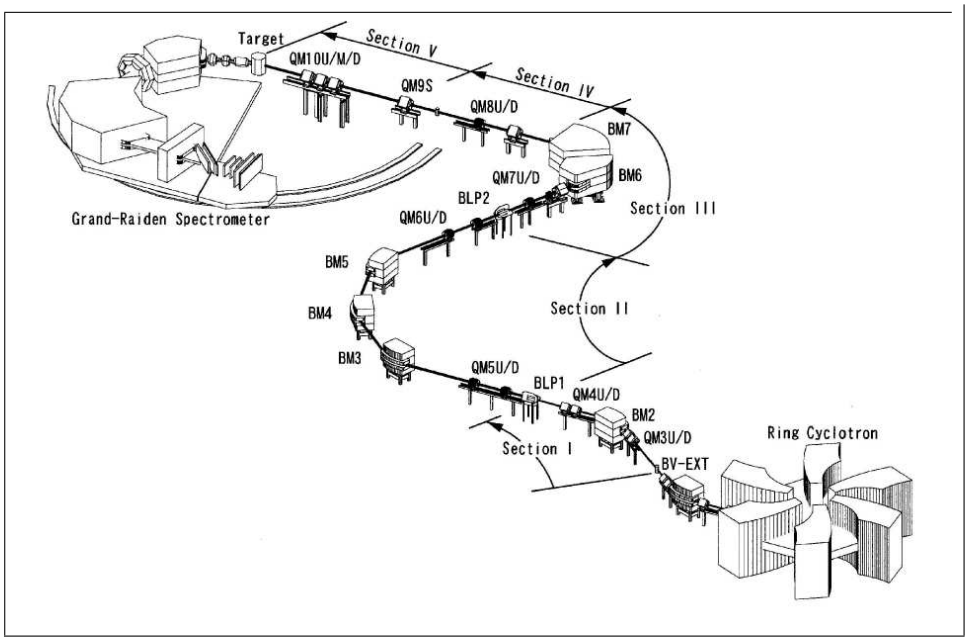

Figure 7.4: Esquema del experimento de reacción de intercambio de carga en RCNP Osaka, Japón.

Luego de la cámara de dispersión se encuentra el espectrómetro 'Grand Raiden' (resolución en momentum $p/\Delta p$ = 37000 y rigidez magnética Bρ= 5.4 Tm) ubicado a 0^o respecto al eje del haz incidente. El tritio seguirá distintas trayectorias dentro del espectrómetro dependiendo del momentum/energía adquirida luego de la reacción.
En el último plano focal existe un conjunto de detectores formado por dos cámaras multihilos y dos detectores plásticos de centelleo. Los detectores plásticos dan dos señales ΔE-ΔE que sirven tanto para la identificación de la partícula, como para el trigger de la cámara multi-hilos que detecta la posición y ángulo de incidencia del tritio en el plano focal.

Resultados

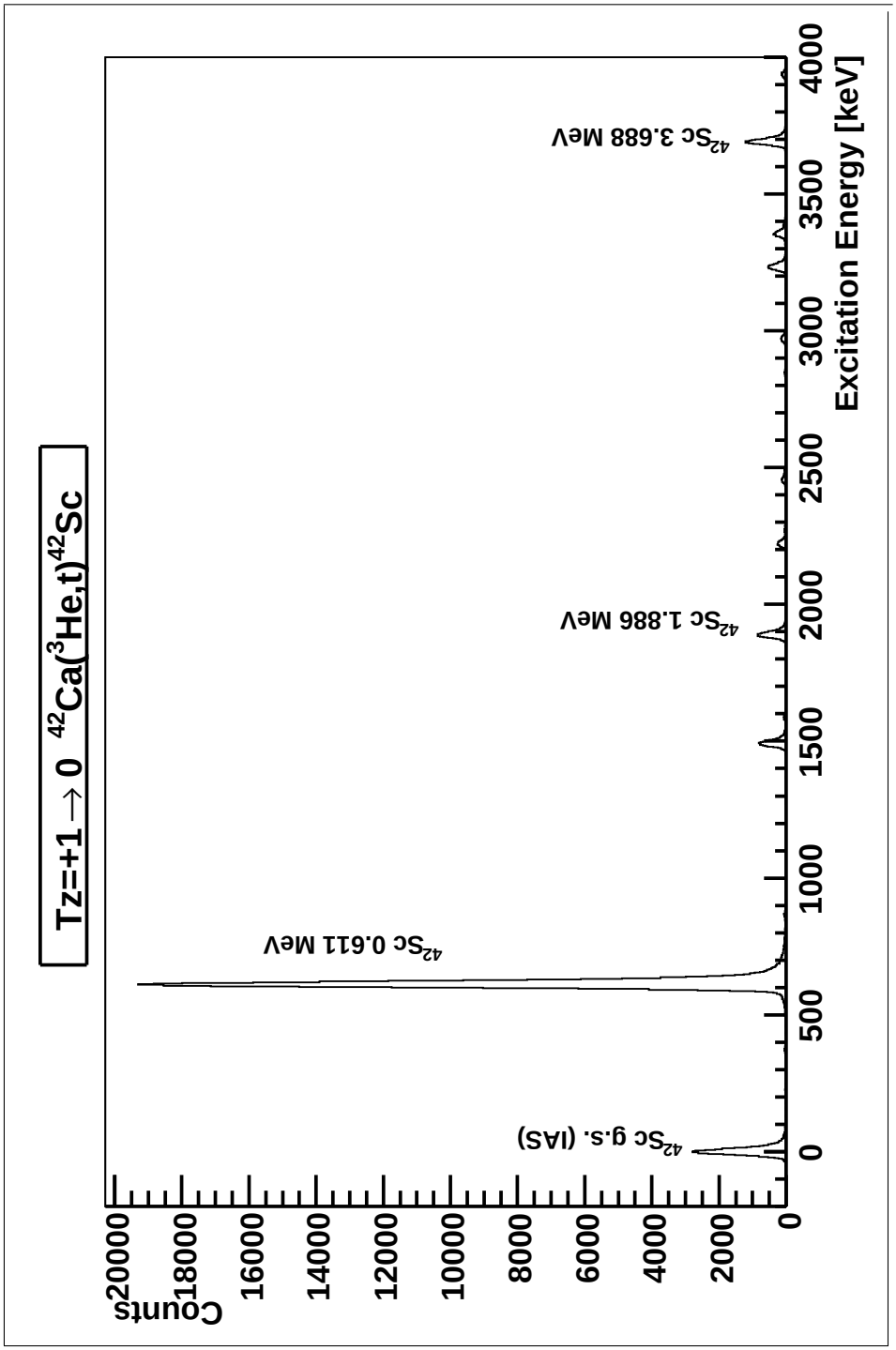

Figure 7.5: Resultados de la reacción ^{42}Ca(^{3}He, t)^{42}Sc de alta resolución [Ada07b]. Las tablas con las energías de excitación y el valor de la fuerza de transición Gamow-Teller medida en esta reacción puede verse en el Apéndice B.

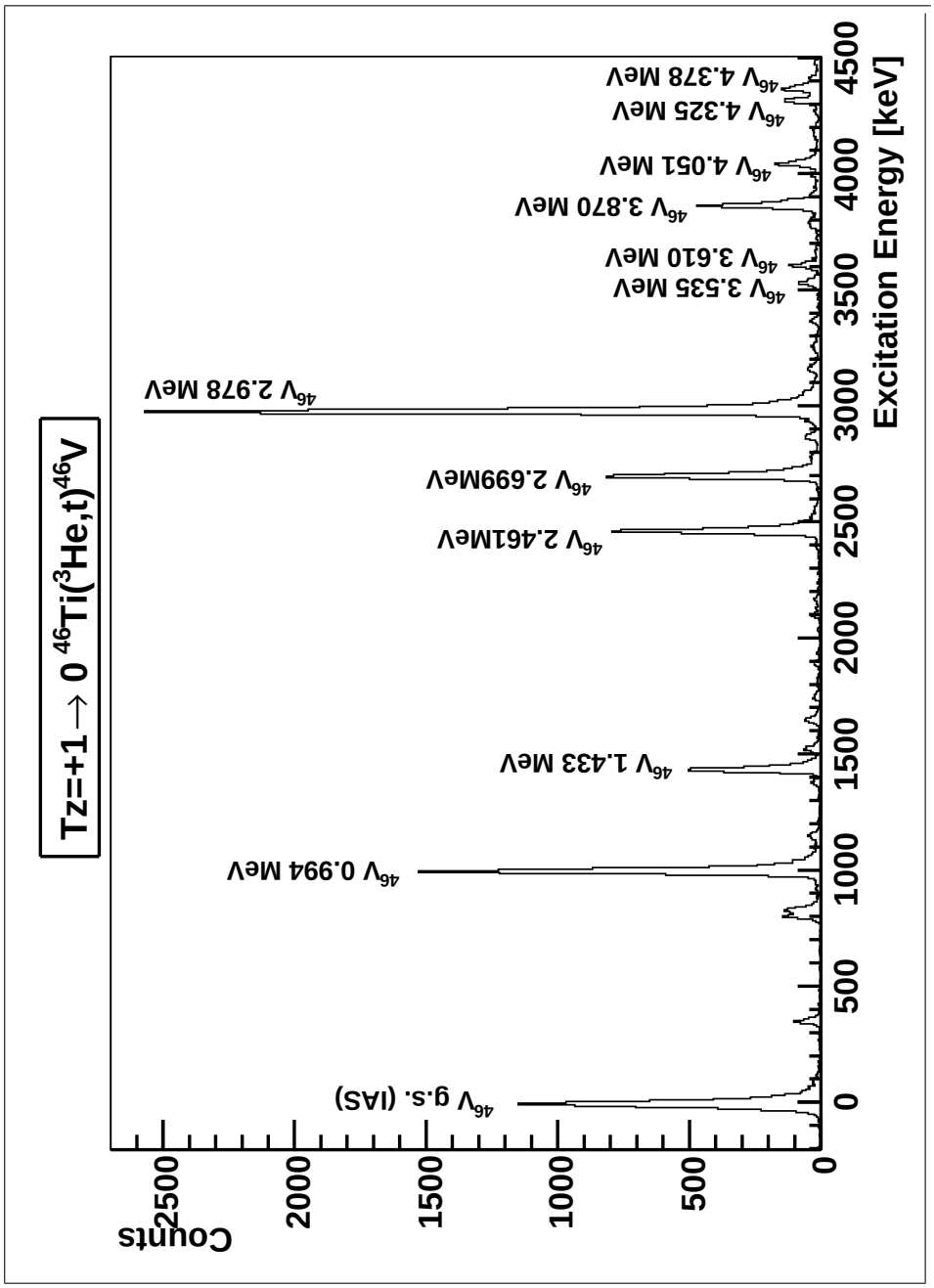

Figure 7.6: Resultados de la reacción ^{46}Ti(^{3}He, t)^{46}V de alta resolución [Ada06]. Las tablas con las energías de excitación y el valor de la fuerza de transición Gamow-Teller medida en esta reacción puede verse en el Apéndice B.

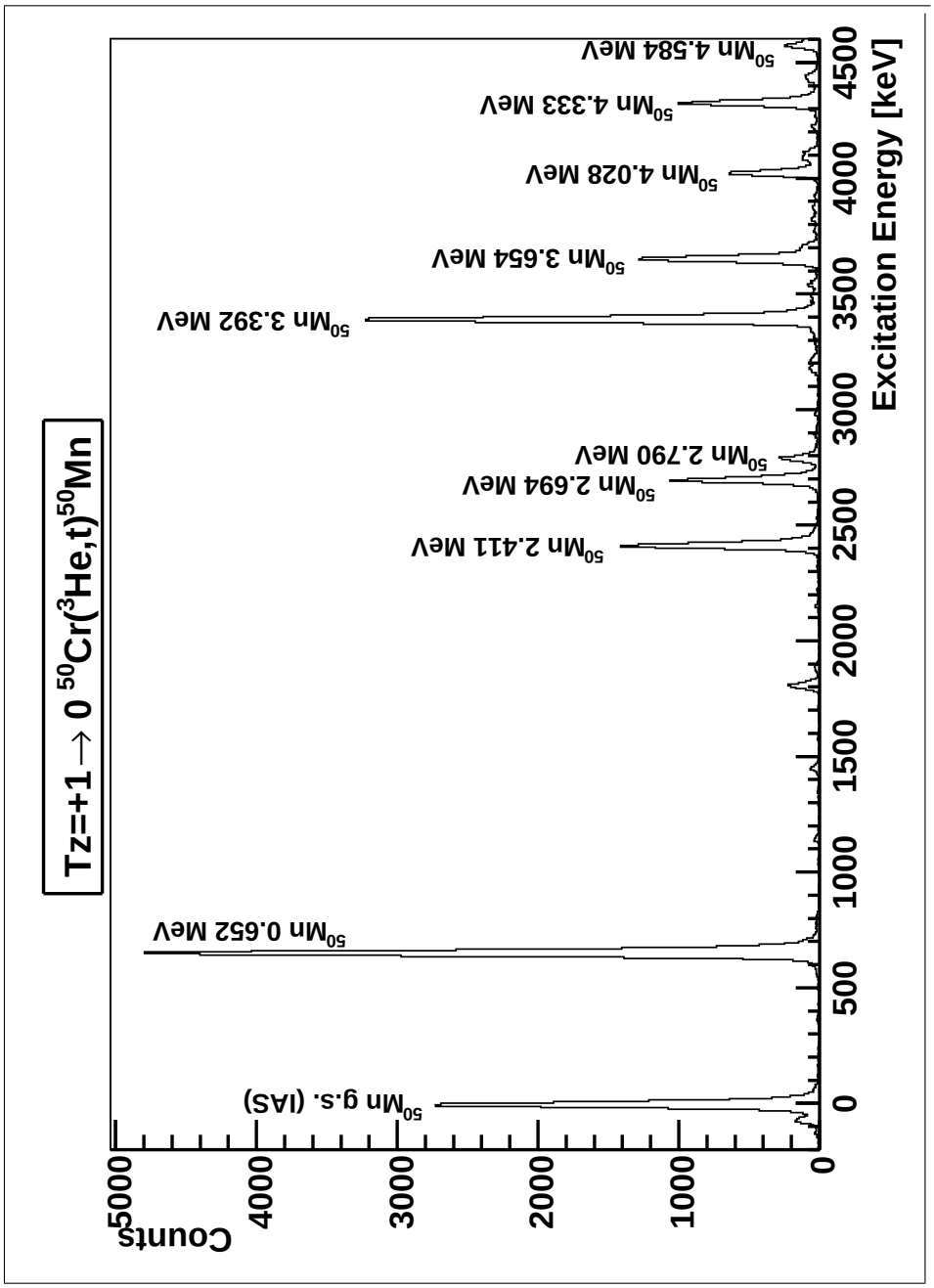

Figure 7.7: Resultados de la reacción ^{50}Cr(^{3}He, t)^{50}Mn de alta resolución [Fuj05a]. Las tablas con las energías de excitación y el valor de la fuerza de transición Gamow-Teller medida en esta reacción puede verse en el Apéndice B.

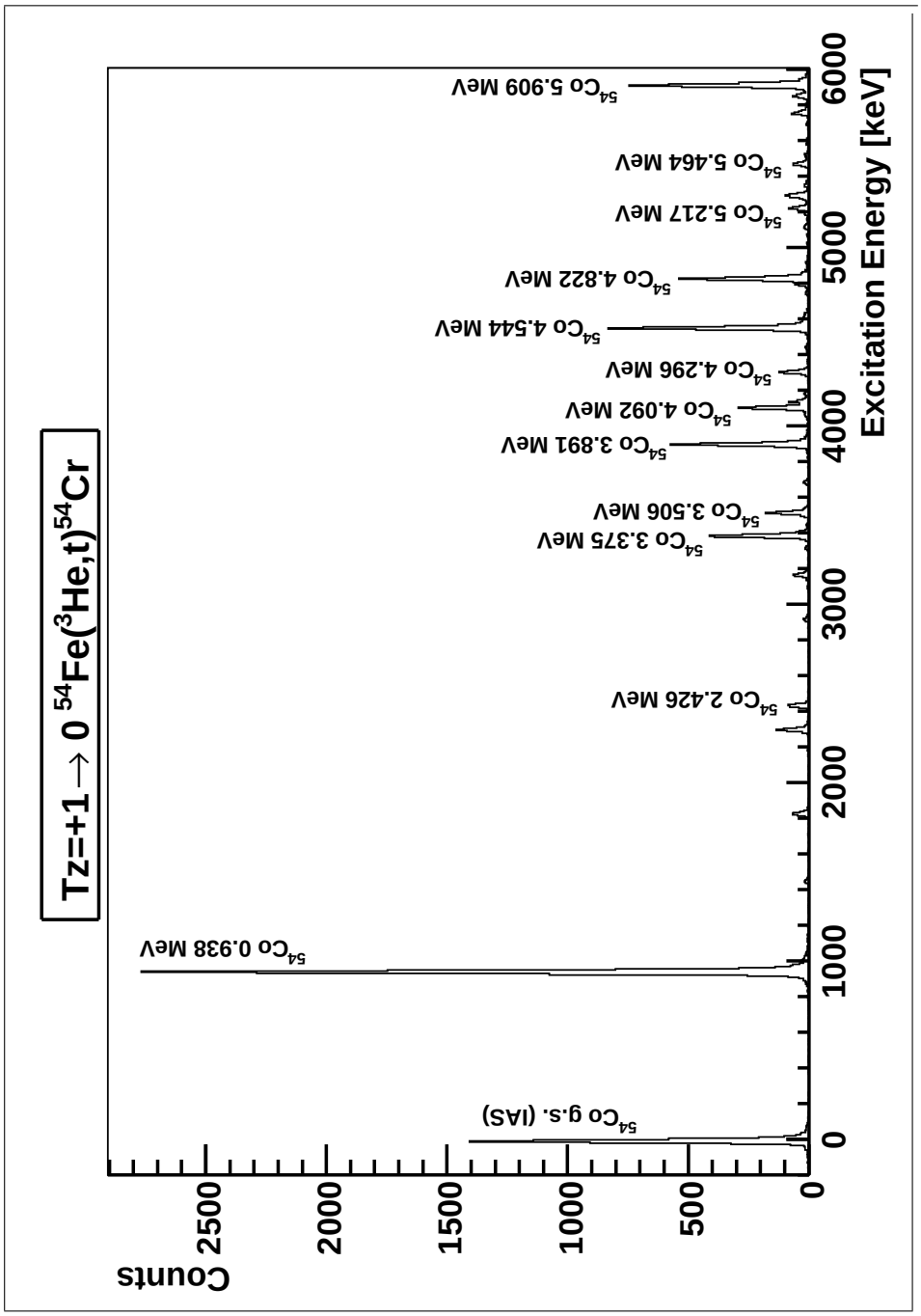

Figure 7.8: Resultados de la reacción ^{54}Fe(^{3}He, t)^{54}Cr de alta resolución [Ada07b]. Las tablas con las energías de excitación y el valor de la fuerza de transición Gamow-Teller medida en esta reacción puede verse en el Apéndice B.

7.4.4 Resultados: Desintegración β^+, T_z=-1 → 0

Medidas anteriores

La desintegración β de los núcleos ^{42}Ti, ^{46}Cr, ^{50}Fe y ^{54}Ni ha sido medida y los resultados pueden verse en la literatura [Kur09, Oni05, Kos97, Reu99b]. En todos estos casos solamente se ha visto el primer estado excitado en el núcleo hijo. Además el error en el valor de la vida media de la desintegración β es ∼10%, excepto en el caso del ^{42}Ti donde se ha realizado una medida de vida media muy precisa (∼ 0.2% $T_{1/2}$) en el 2009 por T. Kurtukian-Nieto et al. [Kur09]. Por lo tanto es necesario obtener experimentalmente (i) la población del estado fundamental y los distintos estados excitados en el núcleo hijo dentro de la ventana de energía Q_β. (ii) medidas de la vida media $T^\beta_{1/2}$ más precisas.

	$T^\beta_{1/2}$ [ms]	Pobl. estado fundamental	Q_β [keV]
^{54}Ni	106(12) [Reu99b]	0.776(44) [Reu99b]	8800(50) [Aud03]
^{50}Fe	155(11) [Kos97]	0.770(60) [Kos97]	8150(60) [Aud03]
^{46}Cr	240(140) [Oni05]	0.784(50) [Oni05]	7599(20) [Aud03]
^{42}Ti	208.14(45) [Kur09]	0.477(12) [Kur09]	7016.83(25) [Kur09]/7000(5) [Aud03]

Table 7.1: Resultados de medidas experimentales en la literatura de los núcleos en la capa fp con T_z=-1.

Los experimentos de desintegración β se realizaron en dos laboratorios distintos: LISOL en Louvain-la-Neuve, Bélgica y RISING-FRS en el GSI Darmstadt, Alemania. El análisis de estos experimentos forman parte integral de esta tesis doctoral.

Experimento en LISOL. Medida de la desintegración del ^{54}Ni

LISOL es un separador de iones en línea por ionización por láser. El núcleo deseado, en nuestro caso ^{54}Ni, es producido en una reacción de fusión-evaporación de un haz primario de ^{3}He, acelerado a 45 MeV/u en el ciclotrón CYCLONE110 que incide sobre un blanco de ^{54}Fe. La selección del núcleo de interés se hace mediante ionización por láser dentro la cámara de gas donde se encuentra el blanco. Existe un flujo constante de Ar gaseoso que arrastra los núcleos ionizados a través de una guía electromagnética (SPIG: SextuPole Ion Guide). Una vez los iones son extraidos, se separan según su valor de masa-sobre-carga y se implantan en una cinta ubicada en el centro de un montaje experimental con dos detectores de germanio (MINIBALL) y tres centelladores plásticos (ver Fig. 7.9). Los iones se implantaban macrociclos de 1 segundo. En los primeros 400 ms se implantaba a intervalos de 50ms, esperando otros 50 ms; en los 600 ms siguientes no se implantaba. La cinta se movía cada 6 macro ciclos.

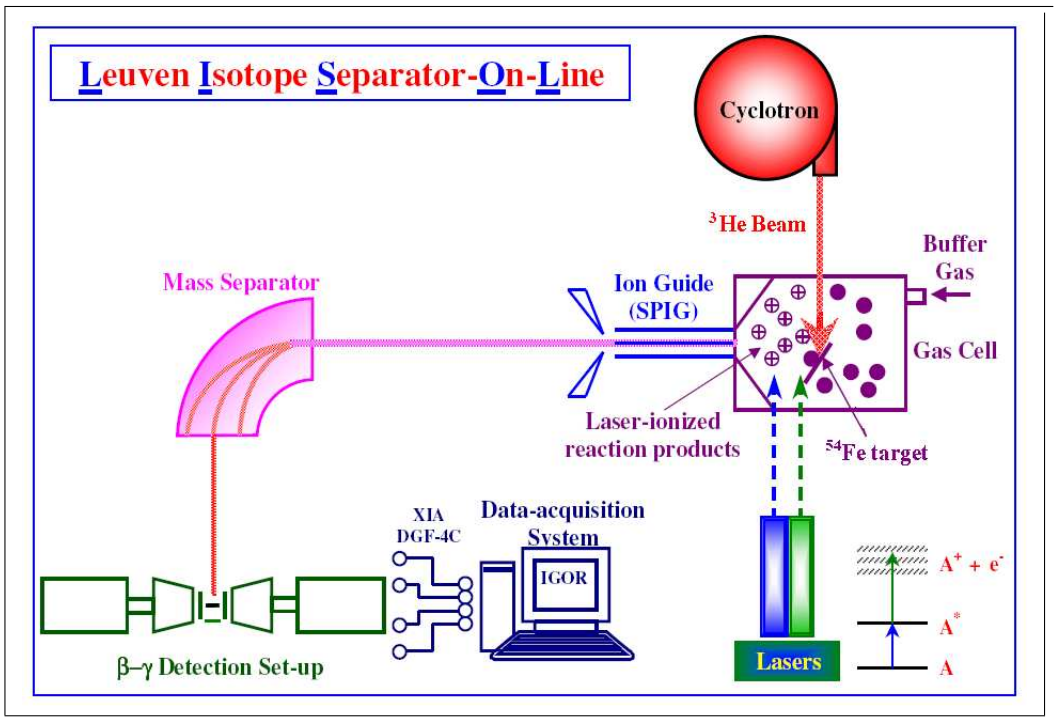

Figure 7.9: Esquema de LISOL.

Resultados en LISOL

Durante los seis días de experimento, se logró ver el primer estado excitado a 937 keV en ^{54}Co poblado por la desintegración β^+ del núcleo padre ^{54}Ni.
La Fig. 7.10, muestra el espectro γ de la desintegración del ^{54}Ni. A pesar de selecciónar mediante ionización por láser el ^{54}Ni, en la reacción se producía abundantemente ^{54}Co tanto en estado fundamental ^{54}Co^g como en su isómero ^{54}Co^m, los cuales son extraidos de la cámara de gas. Debido a su valor de masa sobre carga (A/Q) también son separados e implantados en la cinta. El isómero ^{54}Co^m se desintegra β^+ poblando el estado 6^+ en ^{54}Fe que a su vez se desintegra al estado fundamental a través de una cascada gamma $6^+ \rightarrow 4^+$ (411 keV), $4^+ \rightarrow 2^+$ (1130 keV) y $2^+ \rightarrow 0^+$ (1407 keV). Estos rayos γ son la principal fuente de contaminación del espectro (ver Fig. 7.10).

La vida media del ^{54}Ni se midió observando la evolución del γ a 937 keV durante el macro ciclo de 1 segundo. De los distintos ajustes para sustraer el fondo, se obtuvieron 3 valores de la vida media (i) $T_{1/2}$=114.9(60) ms (ver Fig. 7.10), (ii) $T_{1/2}$=113.8(44) ms(ver Fig. 7.11) y (iii) $T_{1/2}$=113.7(46) ms (ver Fig. 7.12). El valor final pesado por su error es $T_{1/2}$= 114.0(79) ms.
A parte del primer estado excitado en ^{54}Co a 937 keV, no fue visto ningún otro estado correspondiente a la desintegración del ^{54}Ni.

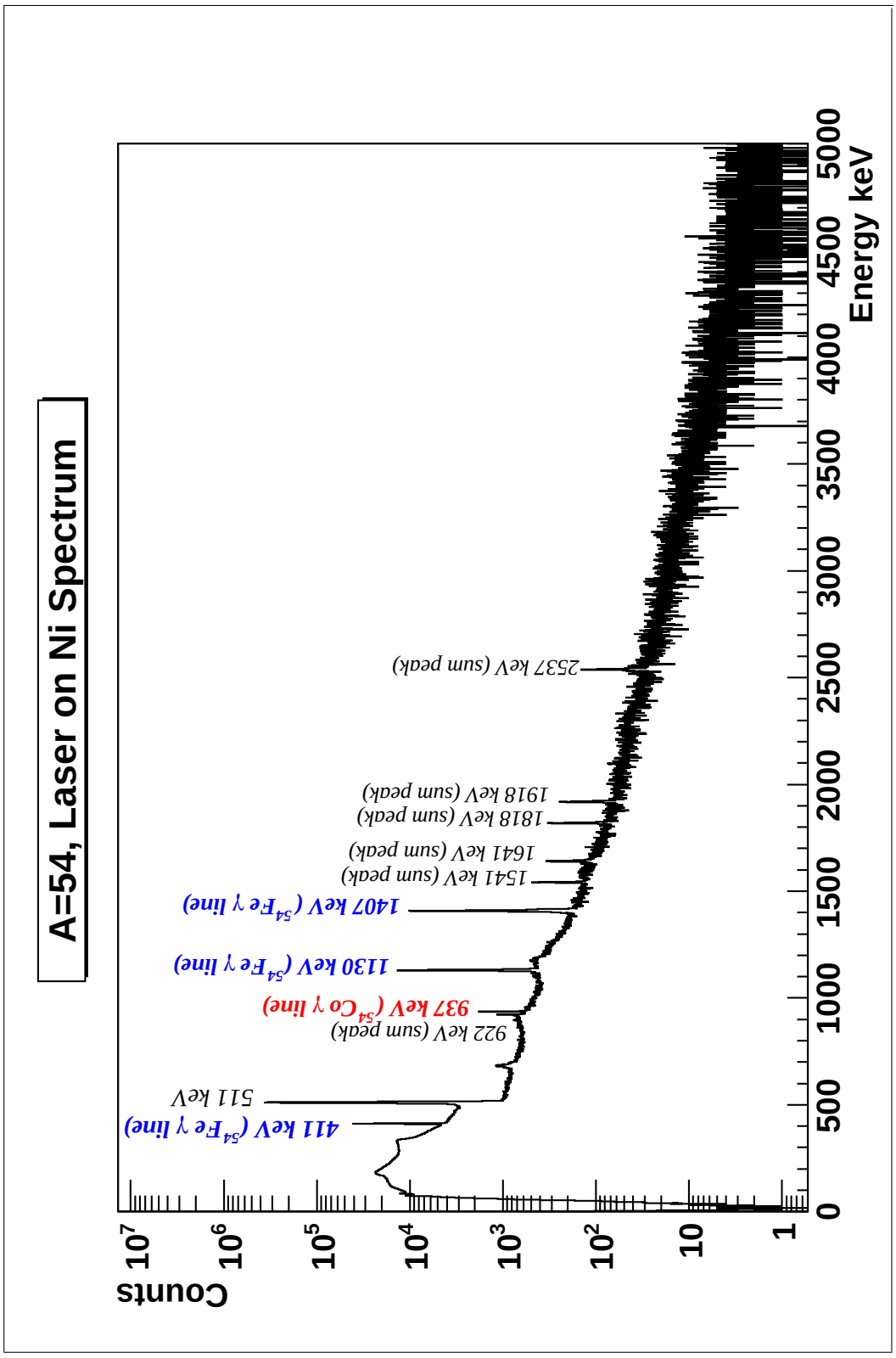

Figure 7.10: Espectro de energía γ del ^{54}Ni

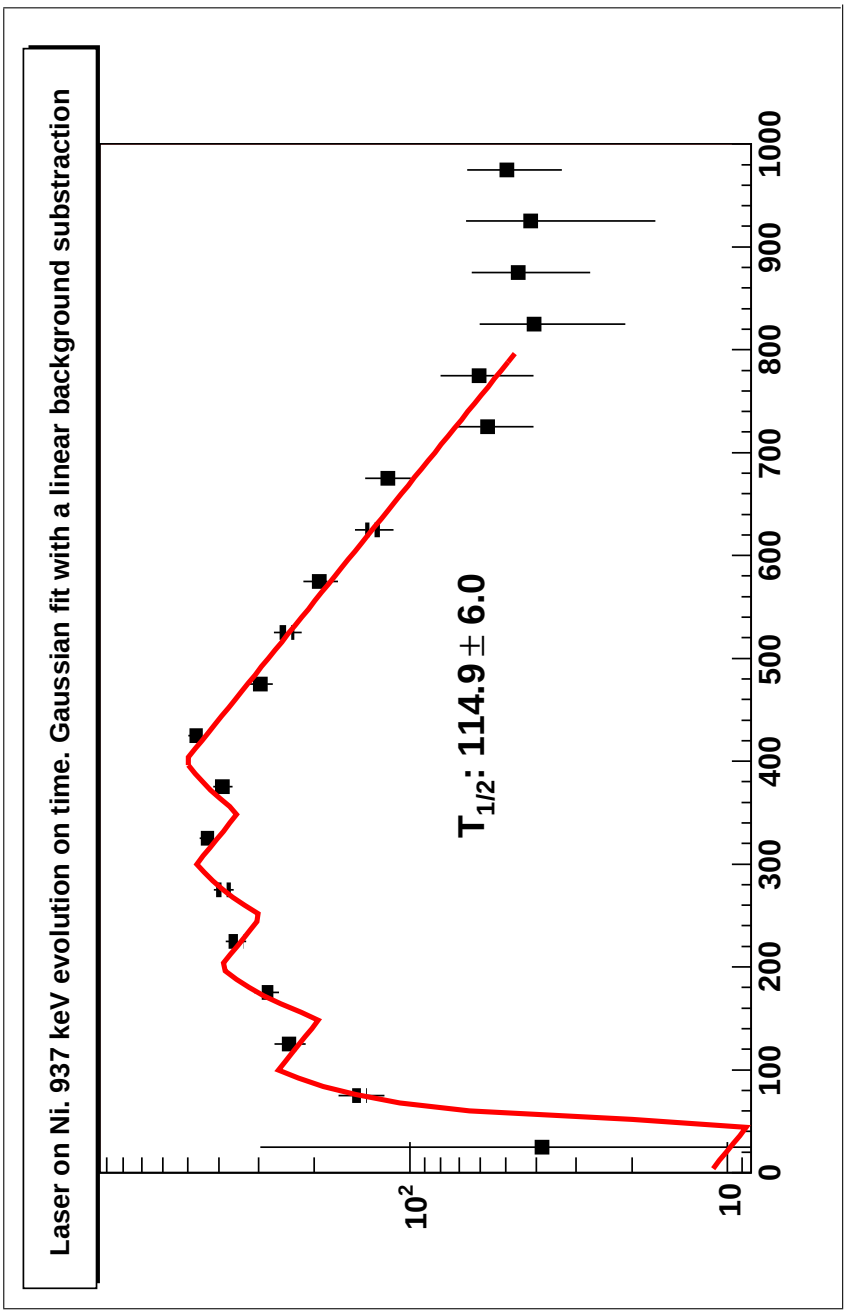

Figure 7.11: Curva de implantación y desintegración del ^{54}Ni. Cada punto representa el area de una función Gaussiana ajustada al γ de 937 keV, sustrayendo un fondo líneal en la región cercana.

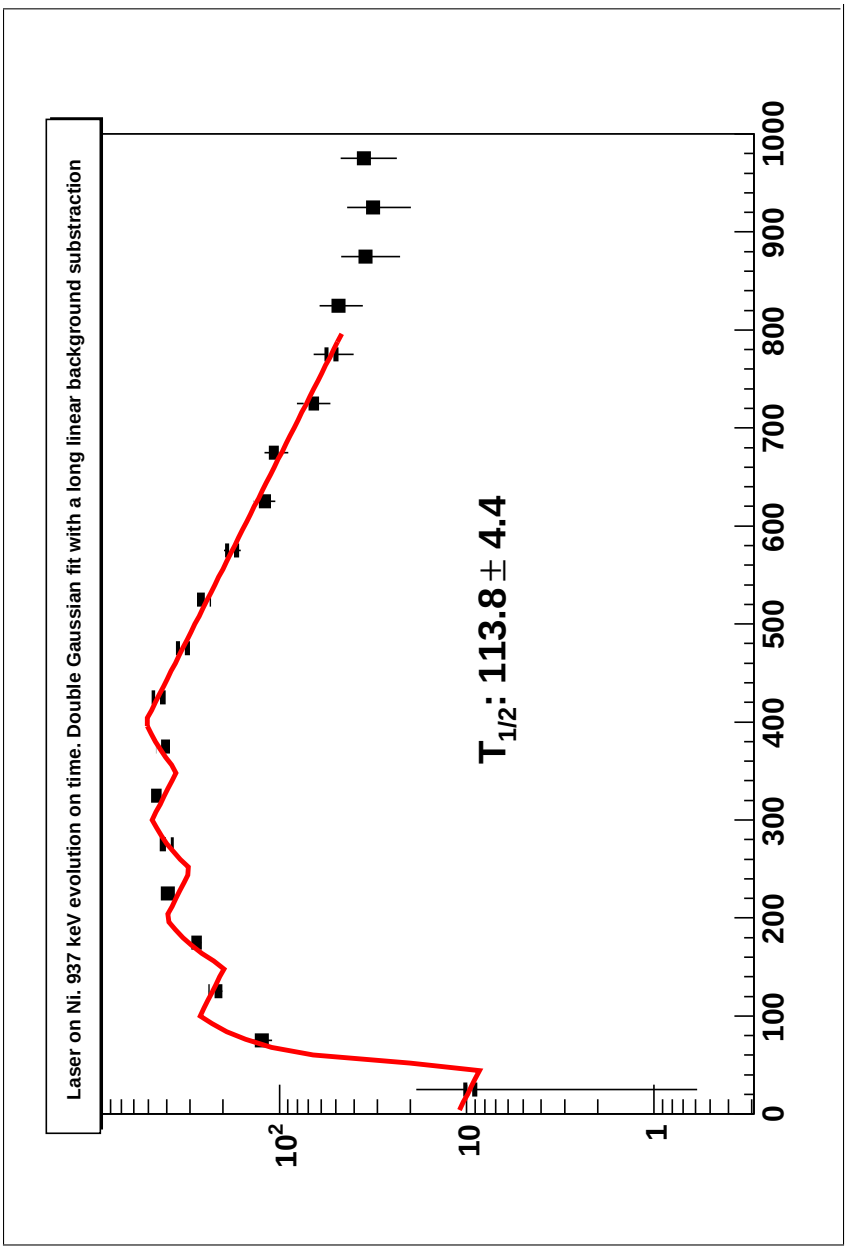

Figure 7.12: Curva de implantación y desintegración del ^{54}Ni. Cada punto representa el area de una función Gaussiana ajustada al γ de 937 keV, sustrayendo un fondo líneal obtenido en la región de sólo fondo 800 keV - 1100 keV.

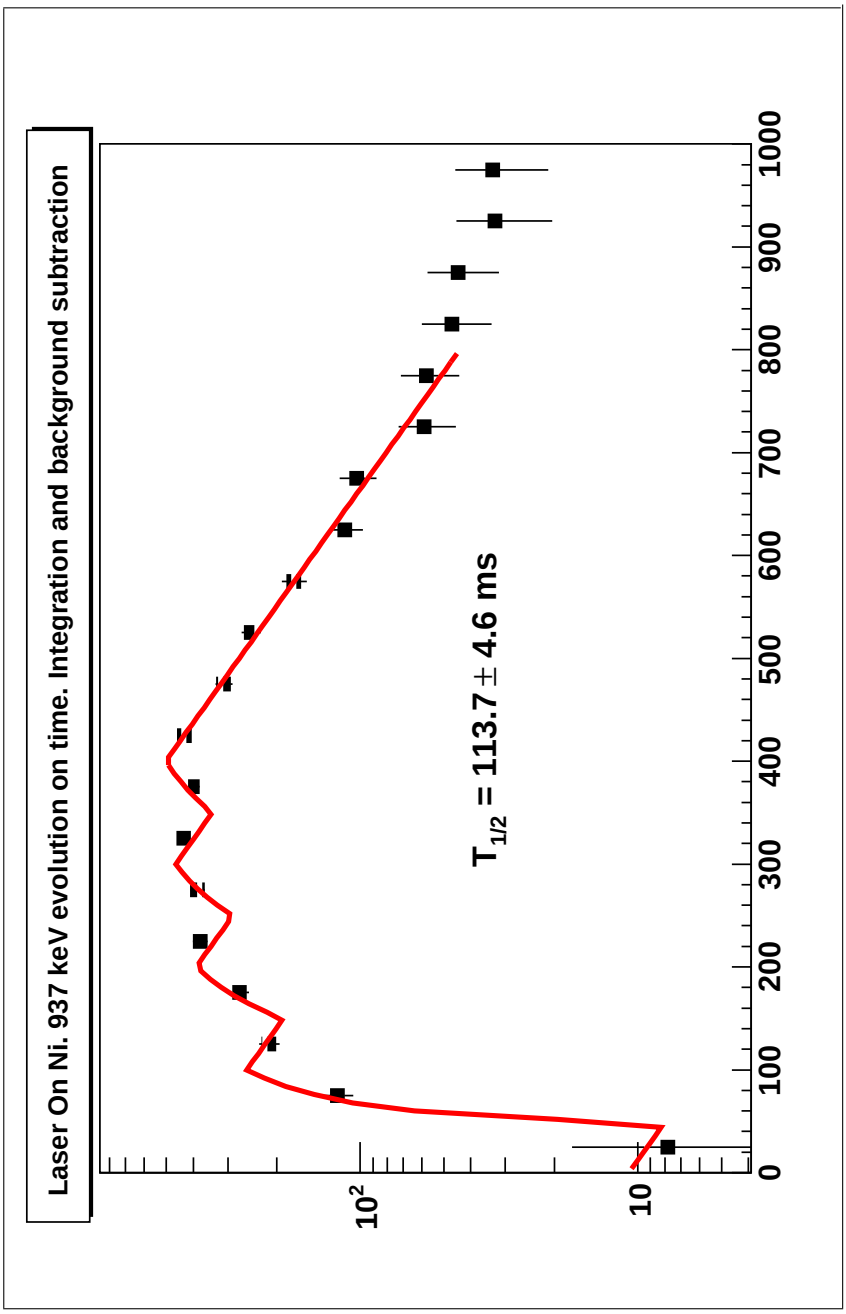

Figure 7.13: Curva de implantación y desintegración del ^{54}Ni. Cada punto representa el area de una función Gaussiana ajustada al γ de 937 keV. El fondo fue sustraido a ajustando una segunda Gaussiana al rayo γ suma a 922 keV más un fondo líneal tomado entre 800 to 1100 keV.

Experimento en GSI (RISING-FRS). Medida de la desintegración β del ^{54}Ni, ^{50}Fe, ^{46}Cr y ^{42}Ti

Los núcleos ^{54}Ni, ^{50}Fe, ^{46}Cr y ^{42}Ti fueron producidos mediante una reacción de fragmentación de un haz de ^{58}Ni (680 MeV/u) sobre un blanco de berilio de 4000 mg/cm^2. Los iones del haz primario son acelerados en el sincrotrón SIS18. Su forma temporal consiste en un periodo de 10 seg ON y 3 seg OFF. Este periodo de 13 seg es llamado "spill" y en él se envían 2×10^9 partículas sobre el blanco. Los fragmentos de la reacción son separados en vuelo en el separador de fragmentos FRS (ver Fig. 7.14). El tiempo de vuelo de un ión es medido mediante dos centelladores plásticos, sc21 y sc41, y la energía perdida por la partícula se mide usando dos cámaras de ionización MUSIC.
Se utilizaron detectores de multi hilos (MW) para medir la posición y posterior corrección angular de la trayectoria de los iones en el FRS.
En la sección final del FRS se ubicaron 6 detectores de bandas de silicio (DSSSD: Double Sided Silicon Strip Detector) cada uno de ellos con 16 bandas en posición X y otras 16 bandas en posición Y. Los iones seleccionados en el FRS (fundamentalmente ^{54}Ni, ^{50}Fe, ^{46}Cr y ^{42}Ti) se implantan en los detectores DSSSD donde se registra la energía depositada del orden de un par de GeV. En este mismo detector, se registra el ΔE producido por el positrón en la desintegración β del núcleo implantado, del orden de unos cientos de keV.
Rodeando el montaje de los DSSSD, se encuentra la bola de detectores de germanio RISING, que consiste en 15 CLUSTER de 7 cristales de Ge, en una geometría esférica. Estos detectores de Ge se utilizaron para medir la energía de la radiación gamma procedente de la desintegración del núcleo implantado.

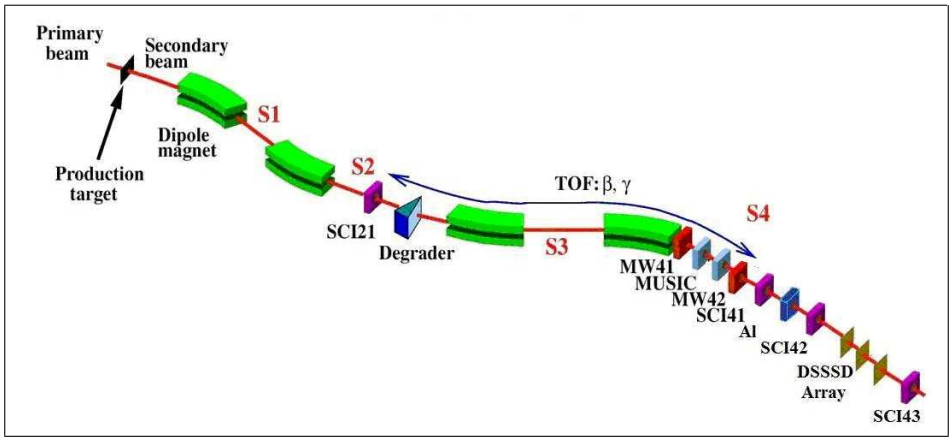

Figure 7.14: Esquema general del separador de fragmentos FRS y los distintos detectores utilizados para la identificación del ión implantado en los detectores de silicio DSSSD.

El "trigger" del experimento lo daba la implantación (señal en el centellador sc41 y senãl OR en las bandas DSSSD) o la desintegración β (senãl OR de las bandas DSSSD).

Resultados en GSI: Espectros γ

El espectro γ de los detectores de RISING se construyó en coincidencia con una señal β proveniente de los detectores DSSSD. La ventana de coincidencia fue fijada en 250 ns a partir de la señal β.

Cada vez que hay una señal β, se registran las energías provenientes de cada uno de los 105 cristales de Germanio que componen a RISING. Estas energías pueden provenir de un mismo evento γ, que deja su energía en distintos cristales (por dispersión Compton). Para poder reconstruir este evento, se creo una rutina computacional, llamada ADDBACK, que suma las energías γ de cristales adyacentes en un mismo cluster de RISING, en una ventana temporal de 100 ns. De esta manera, se mejora la relación entre el área del fotopico γ respecto al fondo (pero a su vez, se aumenta la probabilidad de suma de dos γs distintos en el mismo CLUSTER).

En las Figs.7.15-7.20 se muestra el espectro γ de la desintegración del ^{54}Ni. Los rayos γ correspondientes a estados excitados identificados en el núcleo hijo, ^{54}Co, están etiquetados con el símbolo ♣. Es importante destacar que se han logrado ver por primera vez, en un experimento de desintegración β, los estados excitados 2424.6 keV, 3376.1 keV, 3889.6 keV, 4293.4 keV, 4323.0 keV, 4543.8 keV, 4822.8 keV y 5202.4 keV en ^{54}Co.

En las Figs. 7.21-7.26 se muestra el espectro γ de la desintegración del ^{50}Fe. Los rayos γ correspondientes a estados excitados identificados en el núcleo hijo, ^{50}Mn, están etiquetados con el símbolo ♣. Es importante destacar que se han logrado ver por primera vez, en un experimento de desintegración β, los estados excitados a 2403.8 keV, 2684.2 keV, 3380.0 keV, 3643.4 keV, 4012.7 keV y 4315.7 keV en ^{50}Mn.

En las Figs. 7.27-7.32 se muestra el espectro γ de la desintegración del ^{46}Cr. Los rayos γ correspondientes a estados excitados identificados en el núcleo hijo, ^{46}V, están etiquetados con el símbolo ♣. Es importante destacar que se han logrado ver por primera vez, en un experimento de desintegración β, los estados excitados a 1432.5 keV, 2459.8 keV, 2466.3 keV, 2697.4 keV, 2977.8 keV y 3867.6 keV en ^{46}V.

En las Figs. 7.33-7.38 se muestra el espectro γ de la desintegración del ^{42}Ti. Los rayos γ correspondientes a estados excitados identificados en el núcleo hijo, ^{42}Sc, están etiquetados con el símbolo ♣. Es importante destacar que se ha logrado ver por primera vez, en un experimento de desintegración β, el estado excitado a 1888.4 keV en ^{42}Sc.

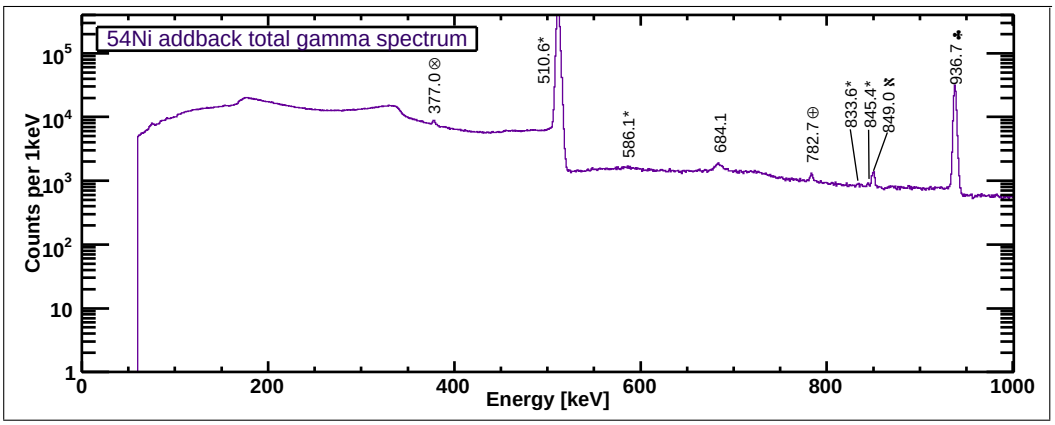

Figure 7.15: Espectro γ del set-up del ^{54}Ni, Parte 1. Rango de Energía: 0-1000 keV.

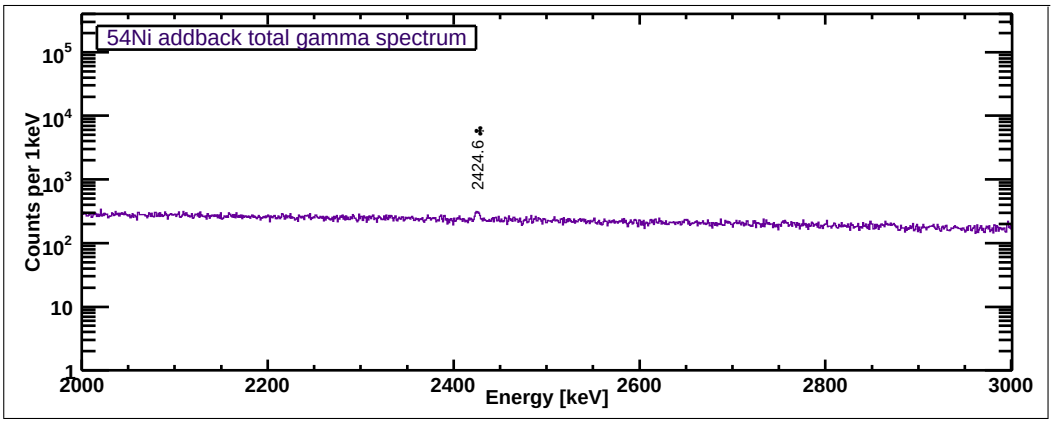

Figure 7.16: Espectro γ del set-up del ^{54}Ni, Parte 3. Rango de Energía: 2000-3000 keV.

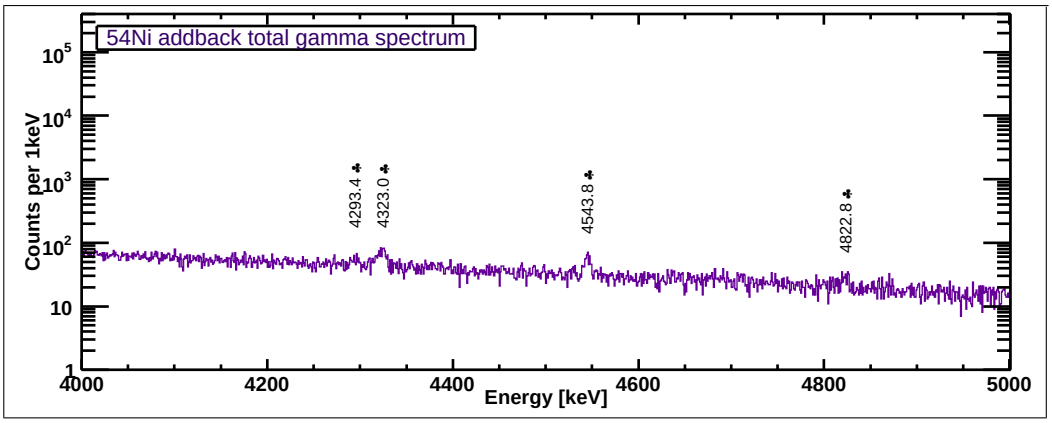

Figure 7.17: Espectro γ del set-up del ^{54}Ni, Parte 5. Rango de Energía: 4000-5000 keV.

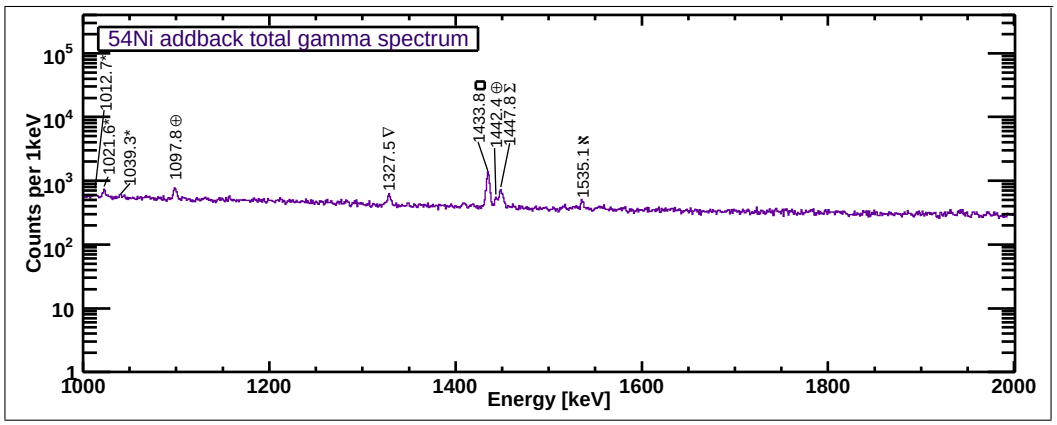

Figure 7.18: Espectro γ del set-up del ^{54}Ni, Parte 2. Rango de Energía: 1000-2000 keV.

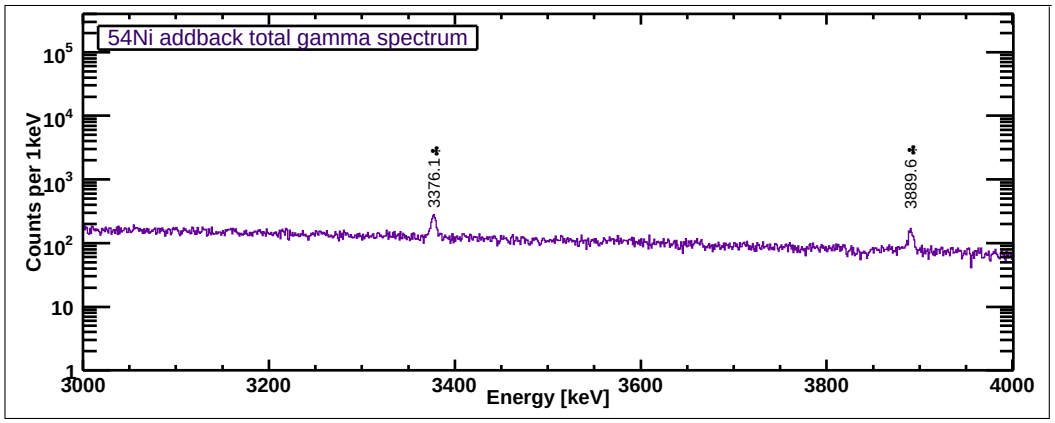

Figure 7.19: Espectro γ del set-up del ^{54}Ni, Parte 4. Rango de Energía: 3000-4000 keV.

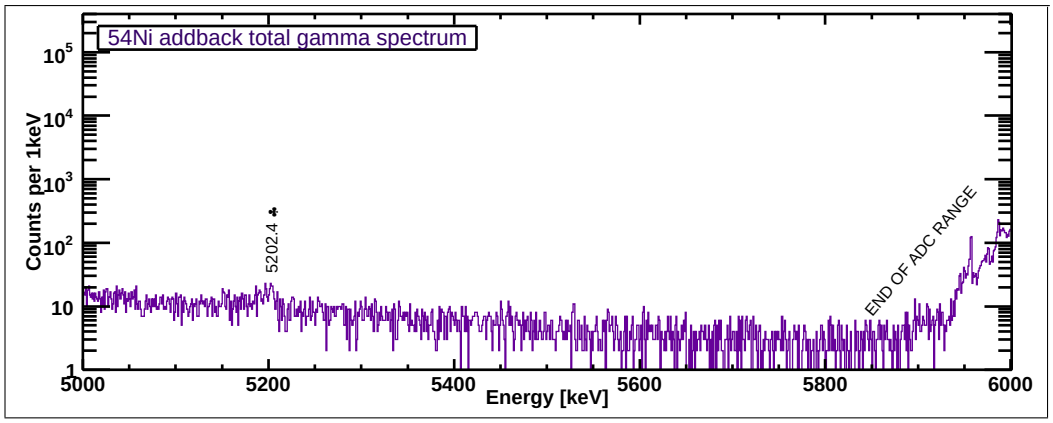

Figure 7.20: Espectro γ del set-up del ^{54}Ni, Parte 6. Rango de Energía: 5000-6000 keV.

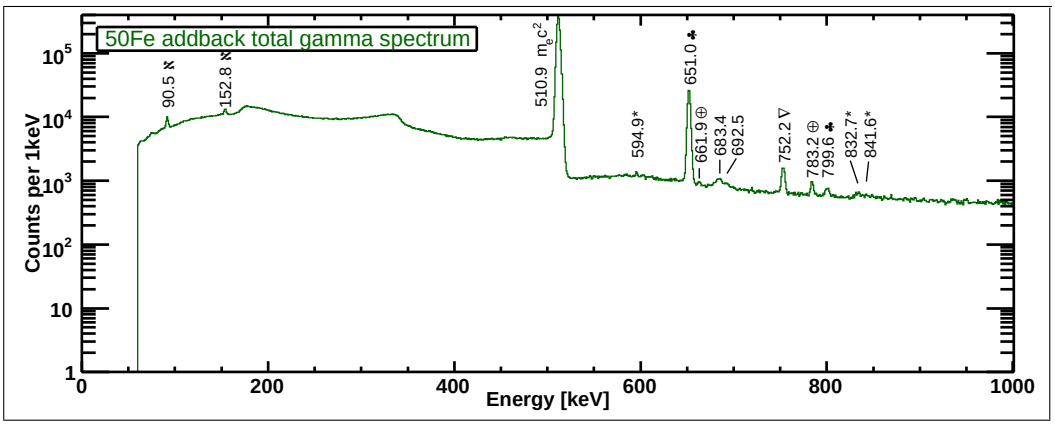

Figure 7.21: Espectro γ del set-up del ^{50}Fe Parte 1. Rango de Energía: 0-1000 keV.

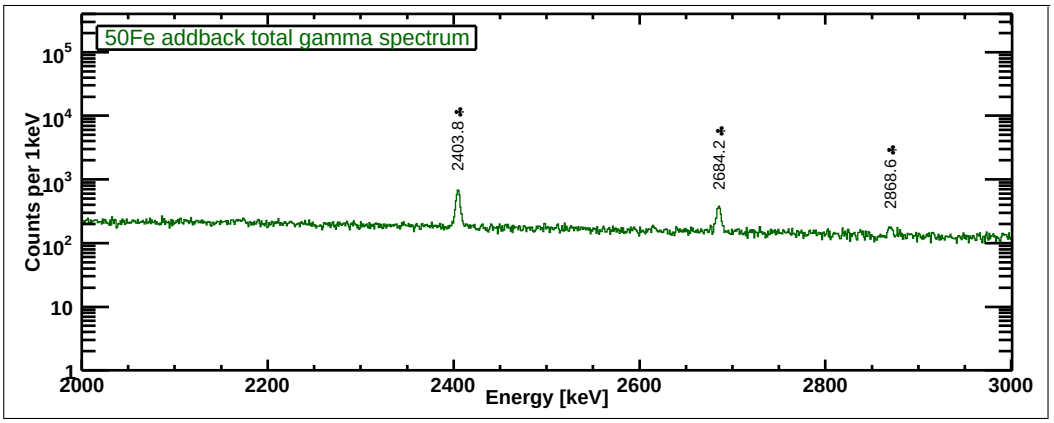

Figure 7.22: Espectro γ del set-up del ^{50}Fe Parte 3. Rango de Energía: 2000-3000 keV.

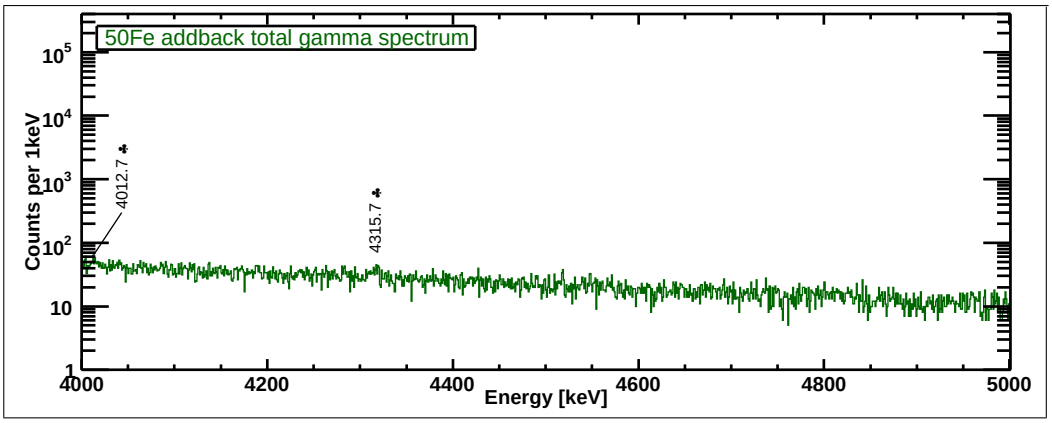

Figure 7.23: Espectro γ del set-up del ^{50}Fe Parte 5. Rango de Energía: 4000-5000 keV.

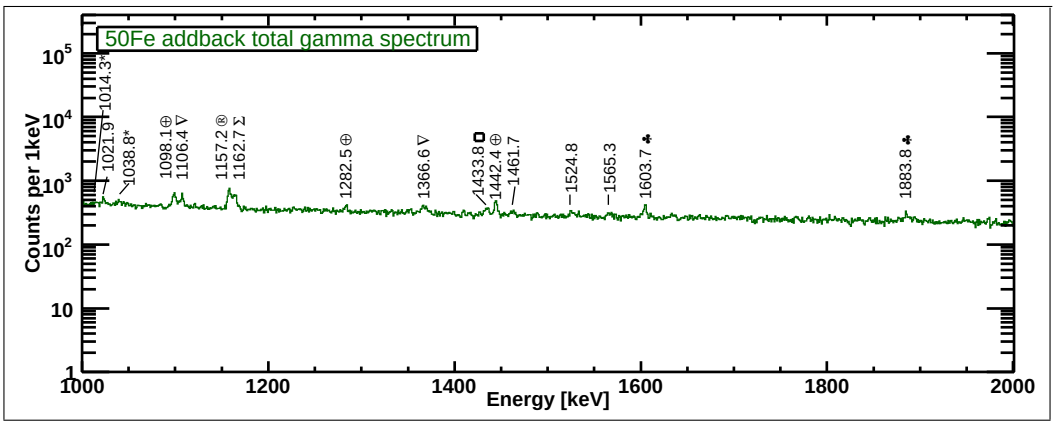

Figure 7.24: Espectro γ del set-up del ^{50}Fe Parte 2. Rango de Energía: 1000-2000 keV.

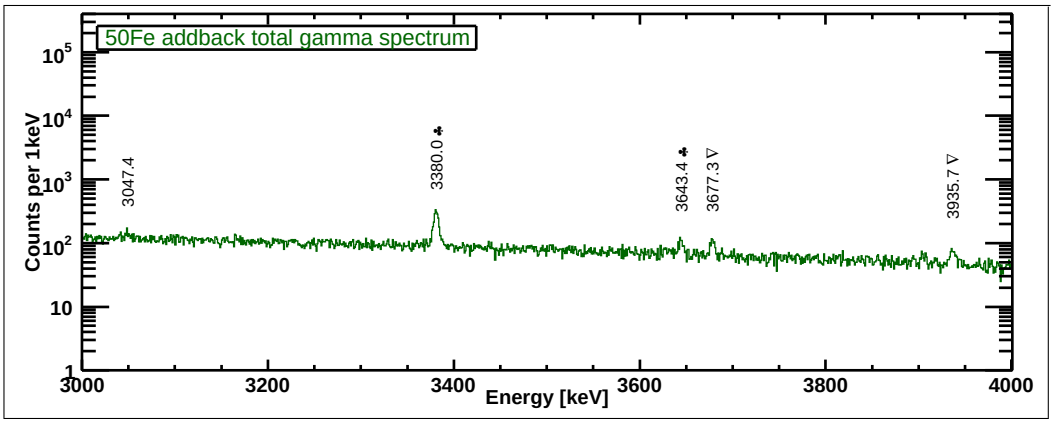

Figure 7.25: Espectro γ del set-up del ^{50}Fe Parte 4. Rango de Energía: 3000-4000 keV.

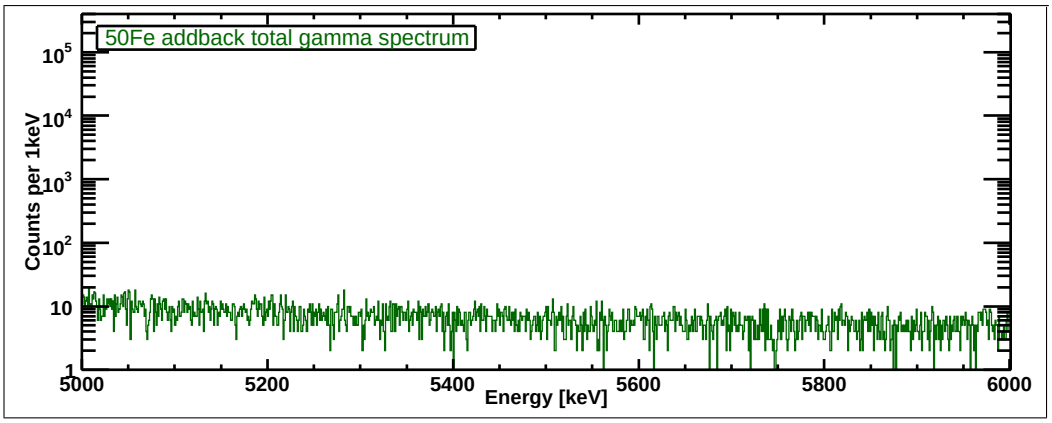

Figure 7.26: Espectro γ del set-up del ^{50}Fe Parte 6. Rango de Energía: 5000-6000 keV.

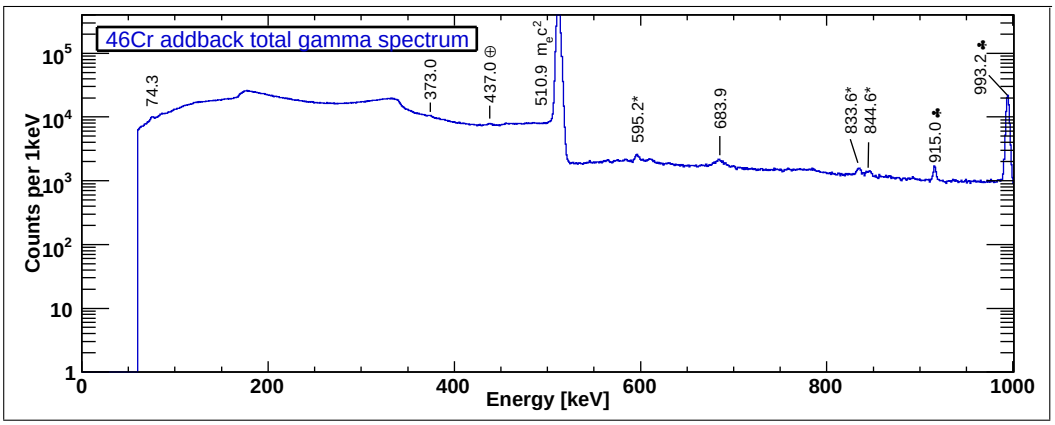

Figure 7.27: Espectro γ del set-up del ^{46}Cr, Parte 1. Rango de Energía: 0-1000 keV.

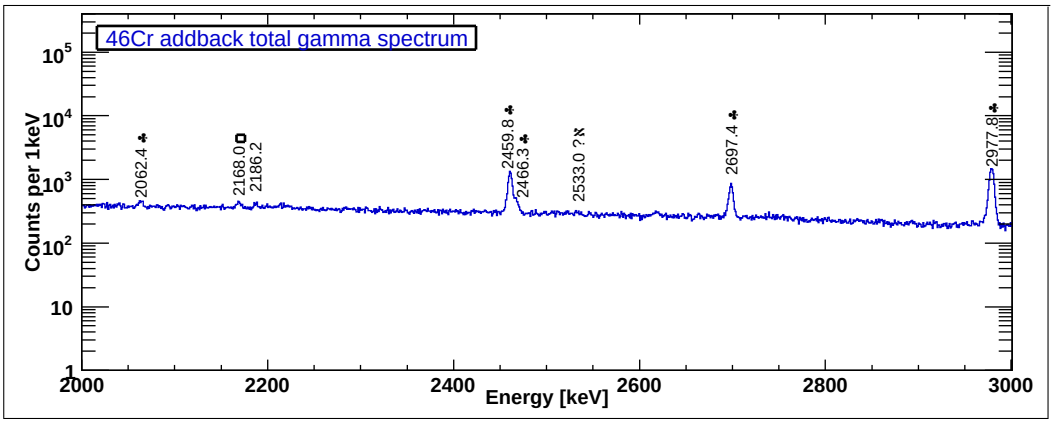

Figure 7.28: Espectro γ del set-up del ^{46}Cr, Parte 3. Rango de Energía: 2000-3000 keV.

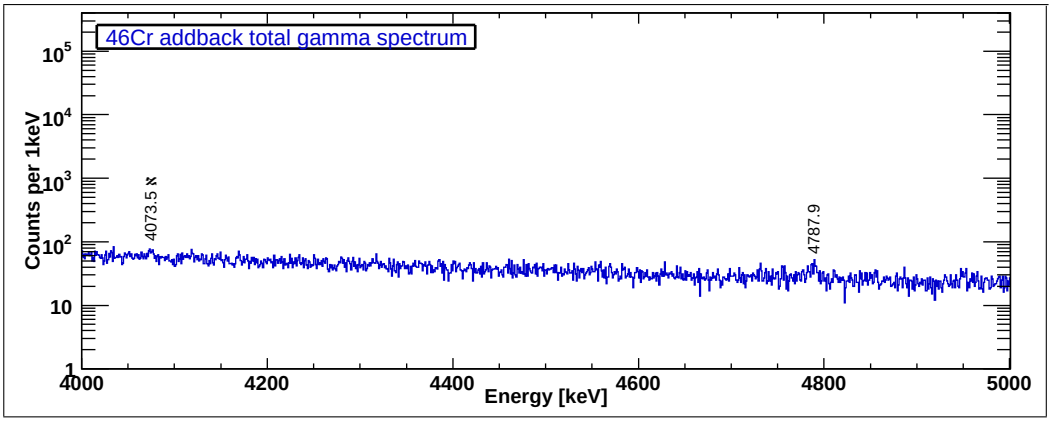

Figure 7.29: Espectro γ del set-up del ^{46}Cr, Parte 5. Rango de Energía: 4000-5000 keV.

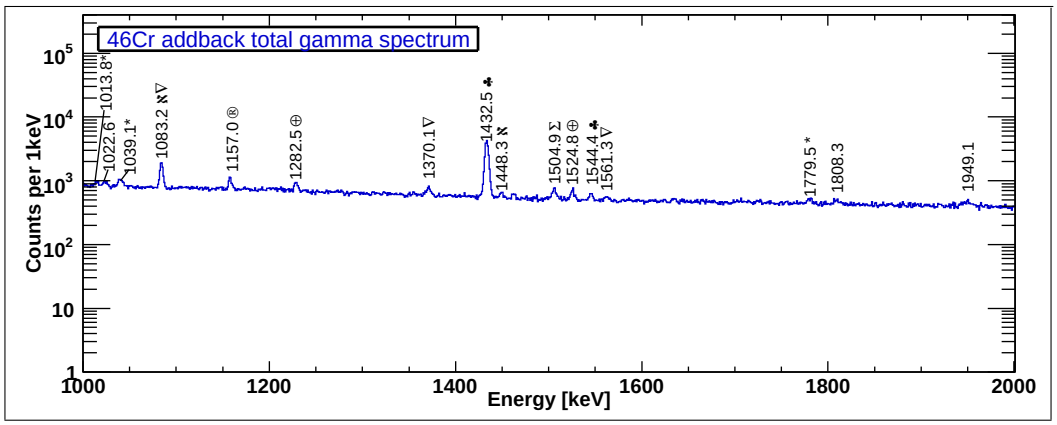

Figure 7.30: Espectro γ del set-up del ^{46}Cr, Parte 2. Rango de Energía: 1000-2000 keV.

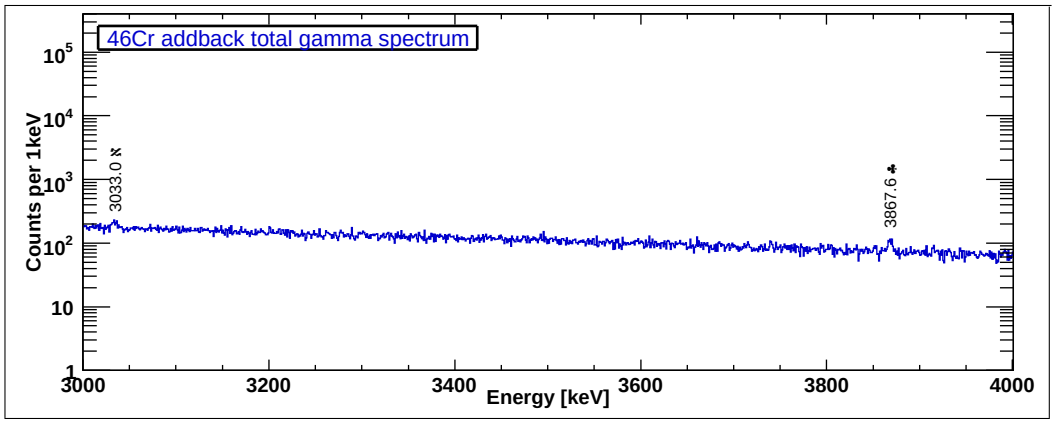

Figure 7.31: Espectro γ del set-up del ^{46}Cr, Parte 4. Rango de Energía: 3000-4000 keV.

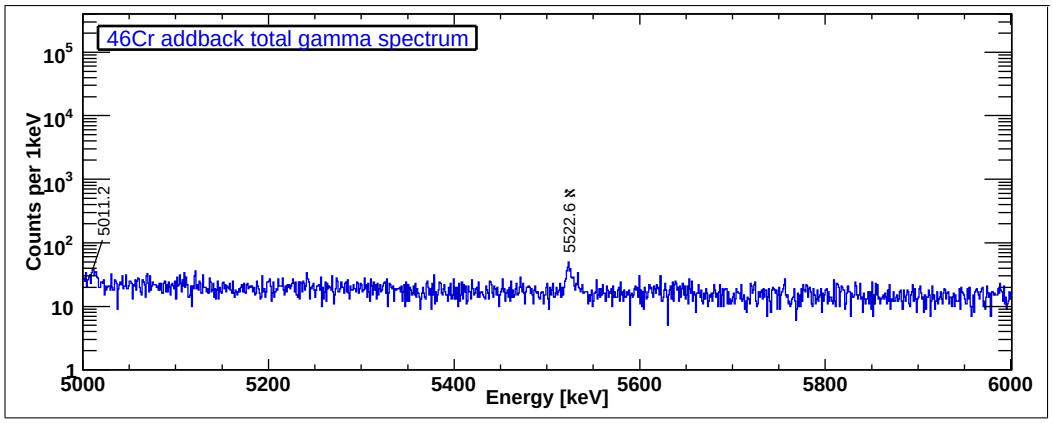

Figure 7.32: Espectro γ del set-up del ^{46}Cr, Parte 6. Rango de Energía: 5000-6000 keV.

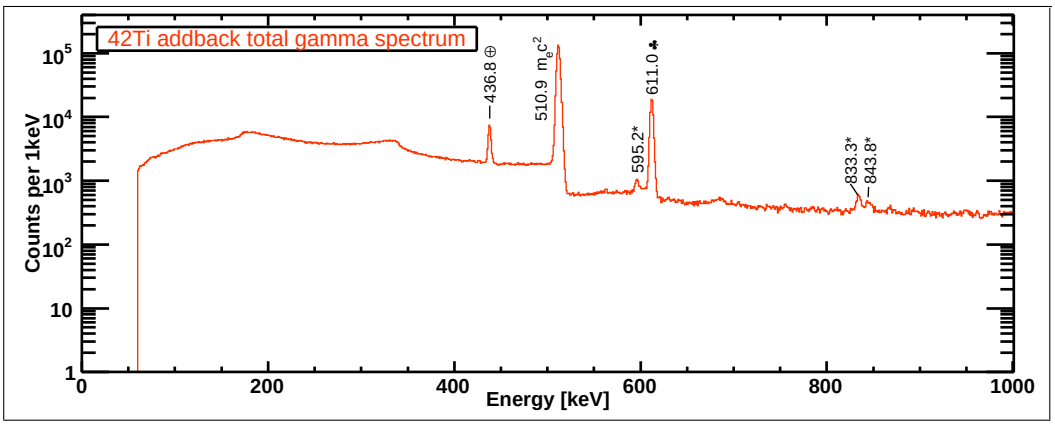

Figure 7.33: Espectro γ del set-up del ^{42}Ti, Parte 1. Rango de Energía: 0-1000 keV.

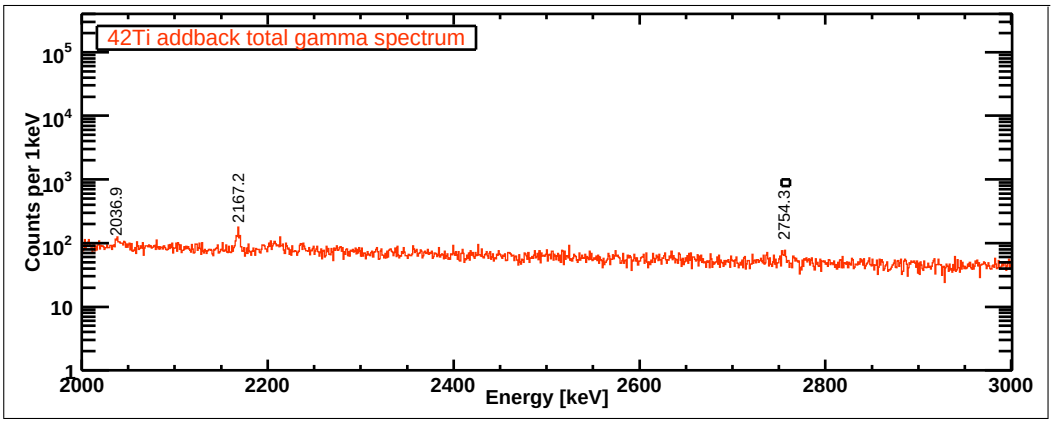

Figure 7.34: Espectro γ del set-up del ^{42}Ti, Parte 3. Rango de Energía: 2000-3000 keV.

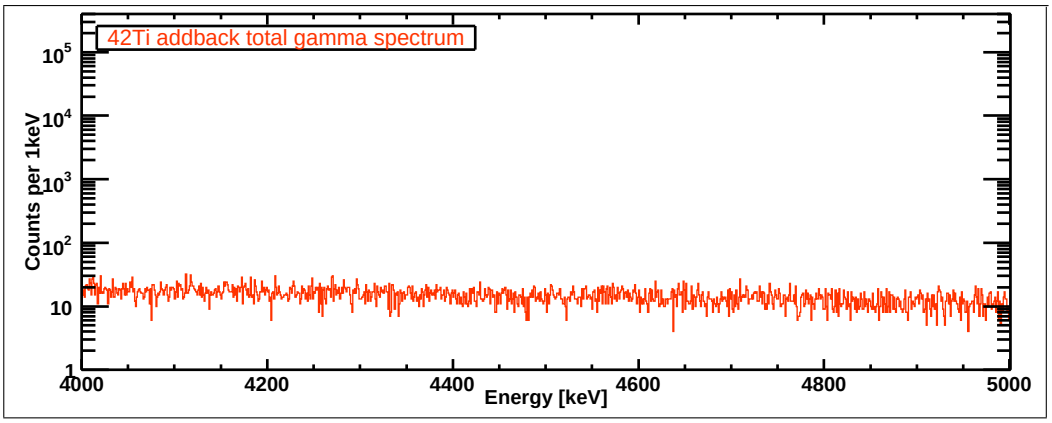

Figure 7.35: Espectro γ del set-up del ^{42}Ti, Parte 5. Rango de Energía: 4000-5000 keV.

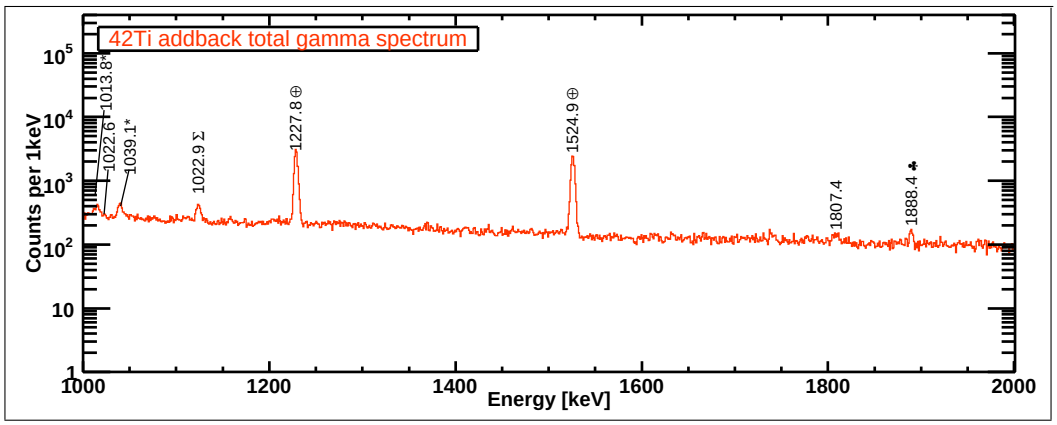

Figure 7.36: Espectro γ del set-up del ^{42}Ti, Parte 2. Rango de Energía: 1000-2000 keV.

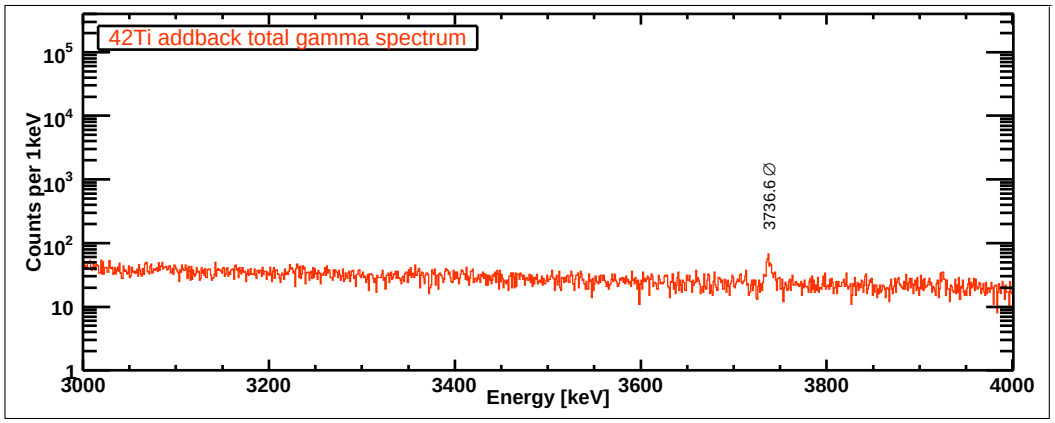

Figure 7.37: Espectro γ del set-up del ^{42}Ti, Parte 4. Rango de Energía: 3000-4000 keV.

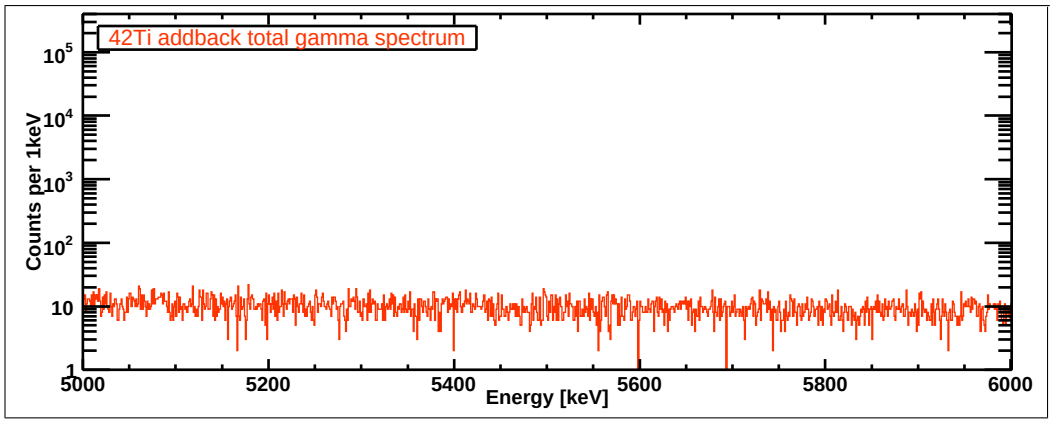

Figure 7.38: Espectro γ del set-up del ^{42}Ti, Parte 6. Rango de Energía: 5000-6000 keV.

Resultados en GSI: Intensidades γ

Para el cálculo de las intensidades γ es necesario medir con presición la eficiencia γ de RISING. Para ello, luego del experimento, se midieron fuentes de calibración conocidas (^{152}Eu, ^{133}Ba, ^{60}Co, ^{226}Ra,^{137}Cs y ^{56}Co). La máxima energía γ de estas fuentes es de 3545 keV. Por lo tanto fue necesario incluir simulaciones Monte Carlo para obtener eficiencias a energías mayores (hasta 6MeV).

Energía[keV]	fwhm[keV]	Cuentas	I(γ)	
377.0 (0.1)	2.8 (0.2)	4228.7 (271.9)	26.60 (1.95)	$\otimes^{53}$Mn (^{53}Fe β^+)
510.6 (0.0)	3.8 (0.0)	2254027.0 (1537.0)	16104.89 (563.78)	m_ec^2 (e^+e^-)
586.1 (1.1)	16.6 (4.3)	2028.0 (669.6)	15.43 (5.12)	$*^{74}$Ge (n-capture)
684.1 (0.2)	9.9 (0.6)	4202.6 (256.7)	34.39 (2.42)	
782.7 (0.1)	3.2 (0.4)	1059.5 (113.9)	9.26 (1.05)	$\oplus^{50}$Cr (^{50}Mn β^+)
833.6 (0.9)	5.2 (8.6)	306.2 (146.8)	2.76 (1.33)	$*^{72}$Ge (n-capture)
845.4 (0.2)	2.0 (0.5)	280.8 (85.0)	2.55 (0.78)	$*^{27}$Al (n-capture)
849.0 (0.1)	3.0 (0.2)	1986.6 (99.8)	18.09 (1.11)	$\aleph^{52}$Fe (^{1})
936.7 (0.0)	3.3 (0.0)	104470.7 (341.0)	**1000.00 (35.15)**	**$\clubsuit^{54}$Co (^{54}Ni β^+)**
1012.7 (1.1)	5.8 (2.7)	250.9 (191.7)	2.50 (1.91)	$*^{27}$Al (n-capture)
1021.6 (0.2)	3.5 (0.7)	625.2 (112.0)	6.26 (1.14)	$2m_ec^2$ (e^+e^-)
1039.3 (0.9)	7.0 (3.5)	371.3 (187.1)	3.75 (1.90)	$*^{70}$Ge (n-capture)
1097.8 (0.1)	3.4 (0.3)	956.2 (83.0)	9.94 (0.93)	$\oplus^{50}$Cr (^{50}Mn β^+)
1327.5 (0.2)	4.3 (0.6)	857.5 (97.3)	9.87 (1.17)	∇^{53}Fe (^{53}Co β^+)
1433.8 (0.0)	3.4 (0.1)	3437.5 (93.1)	41.29 (1.83)	$\square^{52}$Cr (^{52m}Mn β^+)
1442.4 (0.2)	1.9 (0.4)	293.7 (61.6)	3.54 (0.75)	$\oplus^{50}$Cr (^{50}Mn β^+)
1447.8 (0.1)	5.1 (0.4)	1619.6 (142.1)	19.56 (1.85)	Σ(510.6 + 936.7)
1535.1 (0.2)	2.9 (0.4)	413.7 (60.0)	5.16 (0.77)	$\aleph^{52}$Fe (^{1})
2424.6 (0.3)	5.2 (0.8)	491.9 (75.5)	**8.00 (1.26)**	**$\clubsuit^{54}$Co (^{54}Ni β^+)**
3376.1 (0.2)	5.9 (0.5)	939.7 (73.5)	**18.85 (1.61)**	**$\clubsuit^{54}$Co (^{54}Ni β^+)**
3889.6 (0.2)	5.7 (0.6)	480.5 (53.0)	**10.60 (1.23)**	**$\clubsuit^{54}$Co (^{54}Ni β^+)**
4293.4 (1.0)	12.9 (7.1)	234.5 (213.3)	**5.55 (5.05)**	**$\clubsuit^{54}$Co (^{54}Ni β^+)**
4323.0 (0.7)	9.4 (2.2)	312.1 (96.2)	**7.42 (2.30)**	**$\clubsuit^{54}$Co (^{54}Ni β^+)**
4543.8 (0.4)	6.9 (1.0)	245.1 (40.4)	**6.04 (1.02)**	**$\clubsuit^{54}$Co (^{54}Ni β^+)**
4822.8 (0.7)	7.7 (1.5)	87.7 (17.1)	**2.26 (0.45)**	**$\clubsuit^{54}$Co (^{54}Ni β^+)**
5202.4 (0.5)	3.7 (1.3)	43.4 (14.0)	**1.18 (0.38)**	**$\clubsuit^{54}$Co (^{54}Ni β^+)**

Table 7.2: Lista de las energías γ vistas en la desintegración del ^{54}Ni en RISING, usando el modo Add-back. (^{1}) ^{52}Co β^+/^{53}Co p-decay.

Energía[keV]	fwhm[keV]	Cuentas	I(γ)	
90.5 (0.0)	2.5 (0.1)	8499.1 (254.4)	51.42 (2.37)	$\aleph^{49}$V (^{49}Cr β^+)
152.8 (0.1)	2.7 (0.1)	7365.5 (321.6)	46.66 (2.61)	$\aleph^{49}$V (^{49}Cr β^+)
510.9 (0.0)	4.1 (0.0)	1626151.0 (1309.6)	15247.16 (533.79)	m_ec^2 (e^+e^-)
594.9 (0.2)	1.7 (0.6)	443.4 (101.9)	4.46 (1.04)	$*^{74}$Ge (n-capture)
651.0 (0.0)	3.4 (0.0)	95382.0 (332.6)	**1000.00 (35.17)**	**♣^{50}Mn (^{50}Fe β^+)**
661.9 (0.3)	2.6 (0.7)	329.6 (93.9)	3.48 (1.00)	$\oplus^{50}$Cr (^{50m}Mn β^+)
683.4 (0.3)	7.6 (1.0)	2060.0 (358.9)	22.11 (3.93)	
692.5 (0.5)	3.7 (1.2)	447.2 (207.2)	4.83 (2.24)	
752.2 (0.0)	3.4 (0.1)	3723.8 (107.7)	41.87 (1.90)	∇^{48}Cr (^{48}Mn β^+)
783.2 (0.1)	3.1 (0.2)	1281.0 (86.4)	14.69 (1.12)	$\oplus^{50}$Cr (^{50m}Mn β^+)
799.6 (0.2)	4.2 (0.5)	848.6 (99.8)	**9.84 (1.21)**	**†♣^{50}Mn ($2^+ \rightarrow 0^+$)**
832.7 (0.5)	6.5 (1.4)	599.1 (148.0)	7.09 (1.77)	$*^{72}$Ge (n-capture)
841.6 (0.4)	1.7 (0.8)	105.1 (58.0)	1.25 (0.69)	$*^{27}$Al (n-capture)
1014.3 (0.8)	2.9 (1.3)	99.9 (58.5)	1.31 (0.77)	$*^{27}$Al (n-capture)
1021.9 (0.2)	1.8 (0.8)	247.1 (65.7)	3.25 (0.87)	$2m_ec^2$ (e^+e^-)
1038.8 (0.4)	2.5 (1.6)	183.4 (73.1)	2.43 (0.97)	$*^{70}$Ge (n-capture)
1098.1 (0.1)	4.2 (0.6)	1010.1 (126.2)	13.78 (1.79)	$\oplus^{50}$Cr (^{50m}Mn β^+)
1106.4 (0.2)	3.6 (1.0)	701.7 (125.5)	9.61 (1.75)	∇^{48}Cr (^{48}Mn β^+)
1157.2 (0.1)	3.3 (0.3)	1278.1 (116.3)	17.93 (1.75)	®^{44}Ca (^{44}Sc β^+)
1162.7 (0.2)	4.8 (0.7)	1174.2 (147.4)	16.52 (2.15)	Σ(510.9 + 651.0)
1282.5 (0.3)	3.4 (1.1)	300.7 (76.2)	4.46 (1.14)	$\oplus^{50}$Cr (^{50m}Mn β^+)
1366.6 (0.6)	9.8 (2.1)	1010.7 (299.8)	15.51 (4.63)	∇^{48}Cr (^{48}Mn β^+)
1433.8 (0.3)	4.5 (0.8)	383.5 (81.8)	6.04 (1.31)	$\square^{52}$Cr (^{52m}Mn β^+)
1442.4 (0.1)	2.9 (0.5)	612.9 (76.0)	9.69 (1.25)	$\oplus^{50}$Cr (^{50m}Mn β^+)
1461.7 (0.7)	4.8 (1.3)	219.5 (70.4)	3.50 (1.13)	
1524.8 (0.6)	4.0 (1.7)	218.7 (76.6)	3.57 (1.26)	
1565.3 (0.9)	5.7 (1.9)	250.6 (91.2)	4.15 (1.52)	
1603.7 (0.2)	3.3 (0.5)	531.4 (65.6)	**8.91 (1.14)**	**‡♣^{50}Mn ($1^+ \rightarrow 2^+$)**
1883.8 (0.2)	1.5 (0.7)	153.0 (43.8)	**2.81 (0.81)**	**‡♣^{50}Mn ($1^+ \rightarrow 2^+$)**
2403.8 (0.1)	4.9 (0.2)	2607.2 (83.3)	**55.37 (2.62)**	**♣^{50}Mn (^{50}Fe β^+)**
2684.2 (0.1)	5.1 (0.3)	1226.1 (70.7)	**27.86 (1.88)**	**♣^{50}Mn (^{50}Fe β^+)**
2868.6 (0.4)	4.3 (0.7)	222.8 (44.5)	5.28 (1.07)	
3047.4 (0.4)	0.8 (1.4)	58.5 (21.6)	1.44 (0.53)	
3380.0 (0.1)	5.9 (0.3)	1421.9 (68.6)	**37.45 (2.23)**	**♣^{50}Mn (^{50}Fe β^+)**
3643.4 (0.3)	4.9 (0.8)	239.2 (41.0)	**6.62 (1.16)**	**♣^{50}Mn (^{50}Fe β^+)**
3677.3 (0.3)	4.8 (0.6)	257.7 (37.7)	7.18 (1.08)	∇^{48}Cr (^{48}Mn β^+)
3935.7 (0.5)	6.9 (1.5)	222.4 (49.9)	6.49 (1.47)	∇^{48}Cr (^{48}Mn β^+)
4012.7 (1.2)	5.6 (3.0)	65.8 (30.2)	**1.95 (0.90)**	**♣^{50}Mn (^{50}Fe β^+)**
4315.7 (1.4)	10.7 (4.5)	114.2 (45.5)	**3.56 (1.42)**	**♣^{50}Mn (^{50}Fe β^+)**

Table 7.3: Lista de las energías γ vistas en la desintegración del ^{50}Fe en RISING, usando el modo Add-back.

Energía[keV]	fwhm[keV]	Cuentas	I(γ)	
74.3 (0.1)	3.3 (0.3)	3479.3 (317.5)	19.95 (1.95)	
373.0 (0.3)	3.0 (0.7)	1302.6 (313.1)	10.07 (2.45)	
437.0 (0.3)	4.6 (1.0)	2269.6 (473.6)	18.71 (3.96)	$\oplus^{42}$Ca (^{42}Sc^{m} β^+)
510.9 (0.0)	4.1 (0.0)	2920452.8 (1756.2)	25761.12 (901.77)	m_ec^2 (e^+e^-)
595.2 (0.2)	5.0 (0.5)	3240.6 (338.3)	30.64 (3.37)	$*^{74}$Ge (n-capture)
683.9 (0.3)	13.2 (0.8)	5995.3 (367.7)	60.54 (4.28)	
833.6 (0.2)	5.2 (0.7)	2156.2 (223.5)	24.01 (2.63)	$*^{72}$Ge (n-capture)
844.3 (0.3)	7.9 (1.7)	2527.1 (315.8)	28.32 (3.67)	$*^{27}$Al (n-capture)
915.0 (0.1)	3.3 (0.2)	2437.0 (120.7)	**28.45 (1.72)**	**†♣^{46}V ($2^+ \rightarrow 0^+$)**
993.2 (0.0)	3.6 (0.0)	82116.2 (313.2)	**1000.00 (35.21)**	**♣^{46}V (^{46}Cr β^+)**
1013.8 (0.3)	4.9 (0.9)	828.2 (164.5)	10.19 (2.06)	$*^{27}$Al (n-capture)
1022.6 (0.3)	5.5 (0.7)	998.8 (171.1)	12.35 (2.16)	$2m_ec^2$ (e^+e^-)
1039.1 (0.2)	5.6 (0.6)	1431.4 (159.9)	17.85 (2.09)	$*^{70}$Ge (n-capture)
1083.2 (0.0)	3.7 (0.1)	4739.5 (124.8)	60.40 (2.65)	ℵ∇^{44}Ti (^{44g,m}V β^+)
1157.0 (0.1)	3.0 (0.2)	1362.8 (97.4)	17.98 (1.43)	®^{44}Ca (^{44}Sc β^+)
1227.8 (0.2)	3.7 (0.3)	1043.1 (97.0)	14.21 (1.41)	$\oplus^{42}$Ca (^{42}Sc^{m} β^+)
1370.1 (0.2)	4.9 (0.7)	1035.9 (130.9)	14.98 (1.96)	∇^{44}Ti (^{44m}V β^+)
1432.5 (0.0)	4.2 (0.0)	16331.8 (165.4)	**242.03 (8.82)**	**♣^{46}V (^{46}Cr β^+)**
1448.3 (0.0)	3.4 (0.9)	436.1 (102.4)	6.50 (1.54)	ℵ^{44}Ti (^{44g}V β^+)
1504.9 (0.2)	4.1 (0.4)	1025.9 (102.7)	15.62 (1.66)	Σ(510.9 + 993.2)
1524.8 (0.2)	4.2 (0.5)	972.7 (99.9)	14.92 (1.62)	$\oplus^{42}$Ca (^{42}Sc^{m} β^+)
1544.4 (0.2)	4.1 (0.6)	626.0 (89.2)	**9.67 (1.42)**	**‡♣^{46}V ($1^+ \rightarrow 2^+$)**
1561.3 (0.3)	5.2 (1.5)	410.5 (121.6)	6.38 (1.90)	∇^{44}Ti (^{44m}V β^+)
1779.5 (0.5)	5.8 (1.2)	521.7 (118.8)	8.73 (2.01)	$*^{28}$Si (n-capture)
1808.3 (0.7)	6.5 (1.7)	422.0 (127.9)	7.13 (2.18)	
1949.1 (0.1)	5.0 (0.1)	5392.8 (132.8)	95.14 (4.07)	
2062.4 (0.4)	5.2 (0.9)	484.3 (94.0)	**8.83 (1.74)**	**‡♣^{46}V ($1^+ \rightarrow 2^+$)**
2168.0 (0.4)	5.2 (1.1)	471.3 (96.5)	8.85 (1.84)	□^{38}Ar (^{38}K β^+)
2186.2 (0.5)	4.2 (0.9)	287.3 (70.3)	5.42 (1.34)	
2459.8 (0.1)	5.0 (0.1)	5392.8 (132.8)	**109.26 (4.68)**	**♣^{46}V (^{46}Cr β^+)**
2466.3 (0.2)	4.3 (0.6)	870.3 (107.2)	**17.66 (2.26)**	**♣^{46}V (^{46}Cr β^+)**
2533.0 (1.1)	7.3 (4.7)	241.4 (250.6)	4.98 (5.17)	?ℵ^{44}Ti (^{44g}V β^+)
2697.4 (0.1)	5.2 (0.2)	3166.3 (100.9)	**67.90 (3.21)**	**♣^{46}V (^{46}Cr β^+)**
2977.8 (0.0)	5.5 (0.1)	7482.6 (120.7)	**170.77 (6.58)**	**♣^{46}V (^{46}Cr β^+)**
3033.0 (0.7)	8.9 (2.9)	472.8 (199.3)	10.92 (4.62)	ℵ^{44}Ti (^{44g}V β^+)
3867.6 (0.4)	5.4 (1.0)	235.4 (45.7)	**6.39 (1.26)**	**♣^{46}V (^{46}Cr β^+)**
4073.5 (0.8)	5.4 (2.0)	98.8 (38.4)	2.78 (1.08)	ℵ^{44}Ti (^{44g}V β^+)
4787.9 (0.9)	7.3 (3.0)	116.5 (54.0)	3.68 (1.71)	
5011.2 (0.8)	5.9 (1.9)	81.5 (27.9)	2.67 (0.92)	
5522.6 (0.4)	5.2 (1.0)	134.1 (25.3)	4.73 (0.91)	ℵ^{44}Ti (^{44g}V β^+)

Table 7.4: Lista de las energías γ vistas en la desintegración del ^{46}Cr en RISING, usando el modo Add-back.

Energía[keV]	fwhm[keV]	Cuentas	I(γ)	
436.8 (0.0)	3.1 (0.0)	18637.6 (200.9)	239.21 (8.76)	$\oplus^{42}$Ca (^{42m}Sc β^+)
510.9 (0.0)	4.1 (0.0)	568233.4 (777.8)	7813.21 (273.67)	$m_e c^2$ (e^+e^-)
595.2 (0.1)	4.0 (0.4)	1496.9 (145.4)	22.11 (2.28)	$*^{74}$Ge (n-capture)
611.0 (0.0)	3.3 (0.0)	66866.5 (271.6)	**1000.00 (35.23)**	**$\clubsuit^{42}$Sc (^{42}Ti β^+)**
833.3 (0.1)	5.0 (0.4)	1380.7 (86.8)	24.12 (1.74)	$*^{72}$Ge (n-capture)
843.8 (0.3)	7.5 (0.9)	1060.2 (111.5)	18.64 (2.07)	$*^{27}$Al (n-capture)
1010.8 (0.4)	2.4 (1.2)	176.1 (68.6)	3.40 (1.33)	
1014.6 (0.2)	2.7 (0.8)	333.1 (80.7)	6.45 (1.58)	$*^{27}$Al (n-capture)
1038.7 (0.2)	4.8 (0.5)	814.2 (82.5)	15.96 (1.71)	$*^{70}$Ge (n-capture)
1122.9 (0.2)	5.0 (0.4)	968.2 (70.3)	19.78 (1.59)	Σ(510.9 + 611.0)
1227.8 (0.0)	3.8 (0.0)	11635.3 (134.6)	249.21 (9.19)	$\oplus^{42}$Ca (^{42m}Sc β^+)
1524.9 (0.0)	4.1 (0.0)	10255.5 (114.8)	246.72 (9.07)	$\oplus^{42}$Ca (^{42m}Sc β^+)
1807.4 (0.7)	6.8 (1.4)	231.8 (61.9)	6.12 (1.65)	
1888.4 (0.2)	3.5 (0.4)	271.6 (37.1)	**7.34 (1.03)**	**$\clubsuit^{42}$Sc (^{42}Ti β^+)**
2036.9 (0.5)	3.2 (1.5)	97.3 (64.3)	2.74 (1.81)	
2167.2 (0.2)	4.4 (0.5)	368.4 (41.5)	10.75 (1.27)	$\square^{38}$Ar (^{38m}K β^+)
2754.3 (0.5)	6.0 (2.1)	147.6 (51.6)	4.95 (1.74)	
3736.6 (0.3)	6.0 (1.0)	218.5 (36.5)	8.94 (1.52)	$\oslash^{40}$Ca (^{40}Sc β+)

Table 7.5: Lista de las energías γ vistas en la desintegración del ^{42}Ti en RISING, usando el modo Add-back.

Las simulaciónes Monte Carlo se hicieron utilizando Geant4, modificando la geometría de RISING en el programa escrito por Dr. Pavel Detistov [Det07] para los anteriores experimentos de RISING (Fast Beam Campaign), añadiendo los 6 detectores DSSSD y simulando una fuente γ monoenergética en el centro del detector M2, que es a su vez, el centro geométrico de RISING.
Los resultados de las 44 eficiencias simuladas y de las eficiencias medidas con las fuentes de calibración, utilizando la rutina de Add-back, se pueden ver en la Fig. D.1 -p.233-. Las Tablas 7.2-7.5 -pp.180 to 183- muestran las energías γ identificadas en las correspondientes medidas de desintegración β, además de la intensidades γ relativas al primer estado excitado en el núcleo hijo.

Resultados: Vida media de la desintegración β de los núcleos ^{54}Ni, ^{50}Fe, ^{46}Cr y ^{42}Ti

Una vez el ión deseado es implantado en un pixel (i,j) del detector de silicio DSSSD, formado por la intersección de las bandas X_i e Y_j en el DSSSD, se espera que se desintegre β. Midiendo la diferencia de tiempo entre la señal de implantación y su posterior señal de desintegración en el mismo pixel, es posible obtener de manera estadística la vida media del núcleo. Si bien un núcleo implantantado se puede identificar mediante su valor de carga Z (energía perdida en las cámaras de ionización) y su valor de A/Q (obtenida a partir del tiempo de vuelo, ToF, y el valor de la rigidez magnética de los dipolos Bρ), el positrón (señal β) no se puede indentificar con un núcleo en particular. Es por ello que en el análisis se utilizaron correlaciones temporales entre una señal de desintegración y todos las implantaciones, en un mismo píxel (i,j), dentro de una ven-

tana temporal de ± 50 segundos. Si pensamos en que cada desintegración corresponde a sólo una implantación anterior, por N correlaciones hechas en la ventana temporal, N-1 de ellas son correlaciones incorrectas (aleatóreas), pero siempre estaremos seguros de incluir la correlación correcta. Si repetimos este procedimiento para cada señal β detectada, estadísticamente obtendremos nuestras correlaciones correctas, sobre un fondo de correlaciones erróneas (aleatóreas) (ver Fig. 7.39, curva roja).
Para determinar, y posteriormente sustraer, el fondo de correlaciones aleatóreas, se correlacionaron implantaciones del píxel (i,j) con desintegraciones en el píxel (j,i) (i $\neq$ j) (ver Fig. 7.39, curva azul).

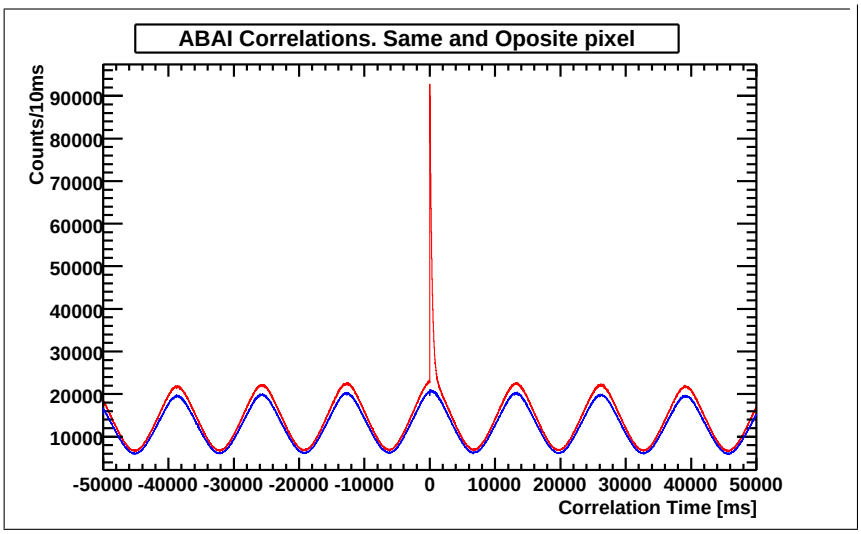

Figure 7.39: Correlaciones temporales de implantación y desintegración en el mismo píxel (en rojo) y en píxeles opuestos (en azul) correspondientes a toda la estadística del ^{54}Ni, en una ventana de correlación de ±50 s

Ahora bien, en los casos estudiados, se espera tener dos desintegraciones β por cada ión implantado, correspondientes a la desintegración del núcleo padre y del núcleo hijo, también radioactivo (ver Fig. 7.3). Las vidas medias del núcleo hijo en cada caso estudiado son bien conocidas y corresponden a las llamadas desintegraciones *super-permitidas* [HT09].

La ecuación 7.5 describe la actividad de un núcleo padre que se desintegra en un núcleo hijo radioactivo (ecuación de Bateman), donde $A(t)$ es la actividad en tiempo t, N_0 es el número de núcleos padres detectados, λ_m es la constante de desintegración del núcleo padre, λ_d es la constante de desintegración del núcleo hijo y C es una constante. Ajustando esta ecuación a la curva de desintegración, con el fondo de correlaciones aleatoreas sustraido, y fijando la vida media del núcleo hijo, se obtiene: (i) la vida media del padre $T^{\beta}_{1/2}$ y (ii)el número de núcleos padres detectados.

$$\begin{aligned} A(t) &= N_0\lambda_m\left(\exp(-\lambda_m t)\right) \\ &\quad + N_0\lambda_m\left(\frac{\lambda_d}{\lambda_d-\lambda_m}\left(\exp(-\lambda_m t)-\exp(-\lambda_d t)\right)\right)+C \end{aligned} \tag{7.5}$$

Este ajuste se hizo utilizando dos métodos de minimización estadística distintos: 1.- Mínimos cuadrados (LS) y 2.- Máxima verosimilitud (ML). Los resultados del ajuste de la vida media $T^{\beta}_{1/2}$, el promedio de los dos metodos de minimización y su comparación con los valores de la literatura, se muestran en la Tabla 7.6 (ver también Figs. 7.40-7.47).

	$T^{\rm LS}_{1/2}$ [ms]	$T^{\rm ML}_{1/2}$ [ms]	$T^{\rm Av}_{1/2}$ [ms]	Lit. $T_{1/2}$ [ms]
^{54}Ni	114.2(3)	114.1(2)	114.2(3)	106(12) [Reu99b]
^{50}Fe	152.1(6)	152.2(6)	152.2(6)	155(11) [Kos97]
^{46}Cr	224.3(13)	223.9(11)	224.1(12)	240(140) [Oni05]
^{42}Ti	211.7(19)	211.2(39)	211.5(29)	208.14(45) [Kur09]

Table 7.6: Resultados de vida media de la desintegración β y su comparación con los valores de la literatura. $T^{\rm LS}_{1/2}$ es la vida media obtenida usando mínimos cuadrados, $T^{\rm ML}_{1/2}$ es la vida media obtenida usando máxima verosimilitud y $T^{\rm Av}_{1/2}$ es el promedio de $T^{\rm LS}_{1/2}$ y $T^{\rm ML}_{1/2}$.

En una publicación reciente por J.C. Hardy et al. [HT09], se hizo una compilación de las vidas medias de los núcleos T_z=0 ("Super-allowed β emitters") promediando los valores de la literatura hasta el momento. En esta publicación, las vidas medias obtenidas analizando los datos sin utilizar el método de minimización por Máxima Verosimilitud, fueron excluidas del promedio. Se sabe que el método de Máxima verosimilitud debe ser usado en casos con poca estadística. En nuestro caso, la estadística es lo suficientemete buena como para confiar en ambos métodos, pero siguiendo la filosofía de Hardy et al., usaremos el valor de la vida media obtenido mediante el método de minimización de máxima verosimilitud, en el cálculo de la $B(GT)$.

También se midió la vida media estudiando la evolución temporal del rayo γ asociado al primer estado excitado en el núcleo hijo. Para ello se hicieron correlaciones temporales de implantación con el evento β-$\gamma^{\rm 1er.estado.excitado}$, de la misma manera que para las correlaciones entre implantación-β. Los resultados obtenidos se encuentran en la Tabla 7.7. Ver también Fig. 7.48.

	$T^{\beta}_{1/2}$ [ms]	$T^{\beta-\gamma}_{1/2}$ [ms]	Lit. $T_{1/2}$ [ms]
^{54}Ni	114.1(2)	114.3(18)	106(12) [Reu99b]
^{50}Fe	152.2(6)	150.1(29)	155(11) [Kos97]
^{46}Cr	223.9(11)	223.9(99)	240(140) [Oni05]
^{42}Ti	211.2(39)	209.5(52)	208.14(45) [Kur09]

Table 7.7: Vidas medias obtenidas mediante correlaciones implantación-β ($T^{\beta}_{1/2}$) y vidas medias obtenidas mediante correlaciones implantación-β-$\gamma^{\text{1er.estado.excitado}}$ ($T_{1/2\beta-\gamma}$) y la comparación con los resultados de la literatura (Lit. $T_{1/2}$).

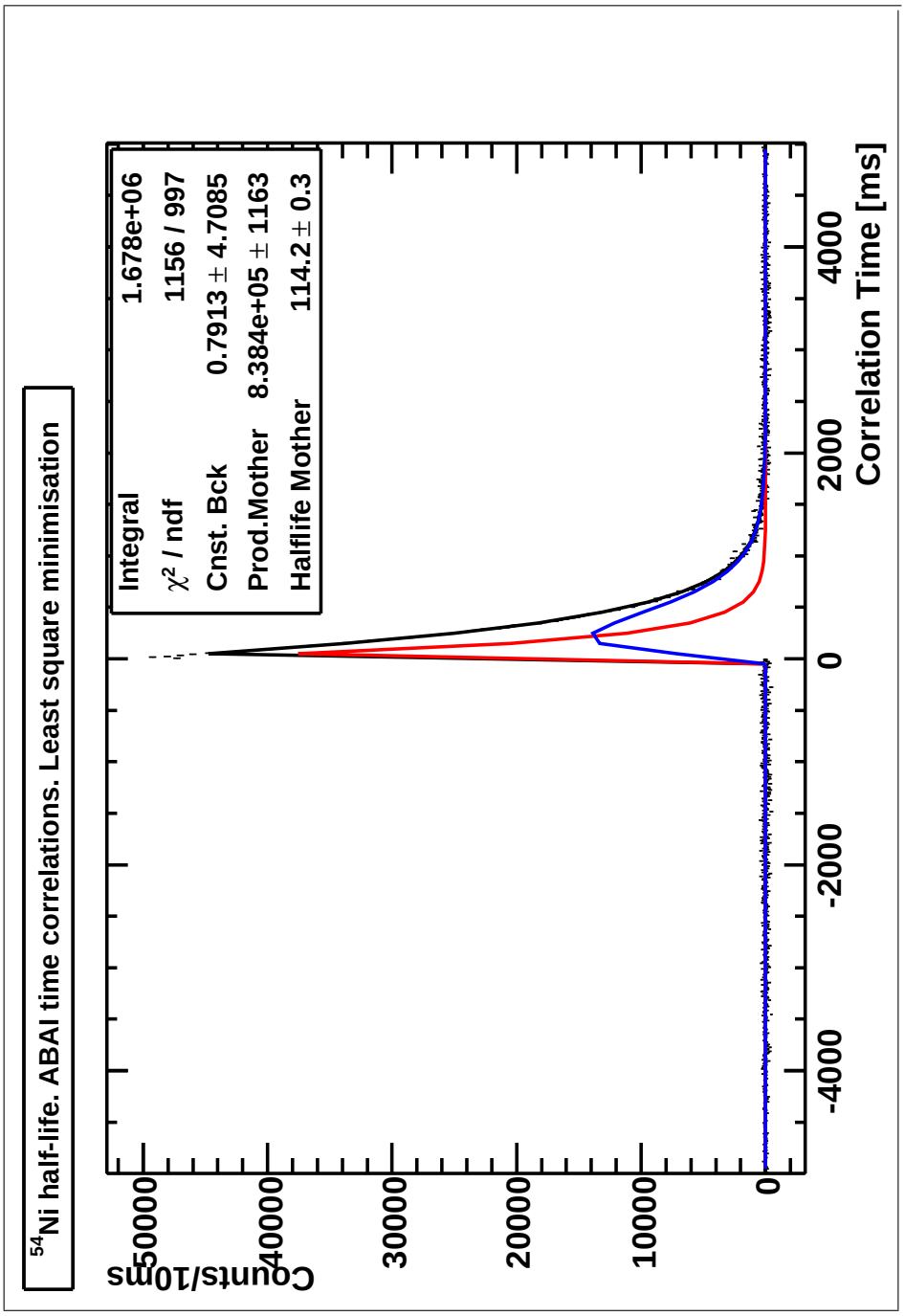

Figure 7.40: Vida media de la desintegración del ^{54}Ni usando minimización por mínimos cuadrados. La curva roja representa la actividad del núcleo padre ^{54}Ni y la curva azul representa la actividad del núcleo hijo ^{54}Co. La vida media del núcleo hijo es $T^d_{1/2}$= 193.271(63) ms [HT09] (parámetro fijo del ajuste).

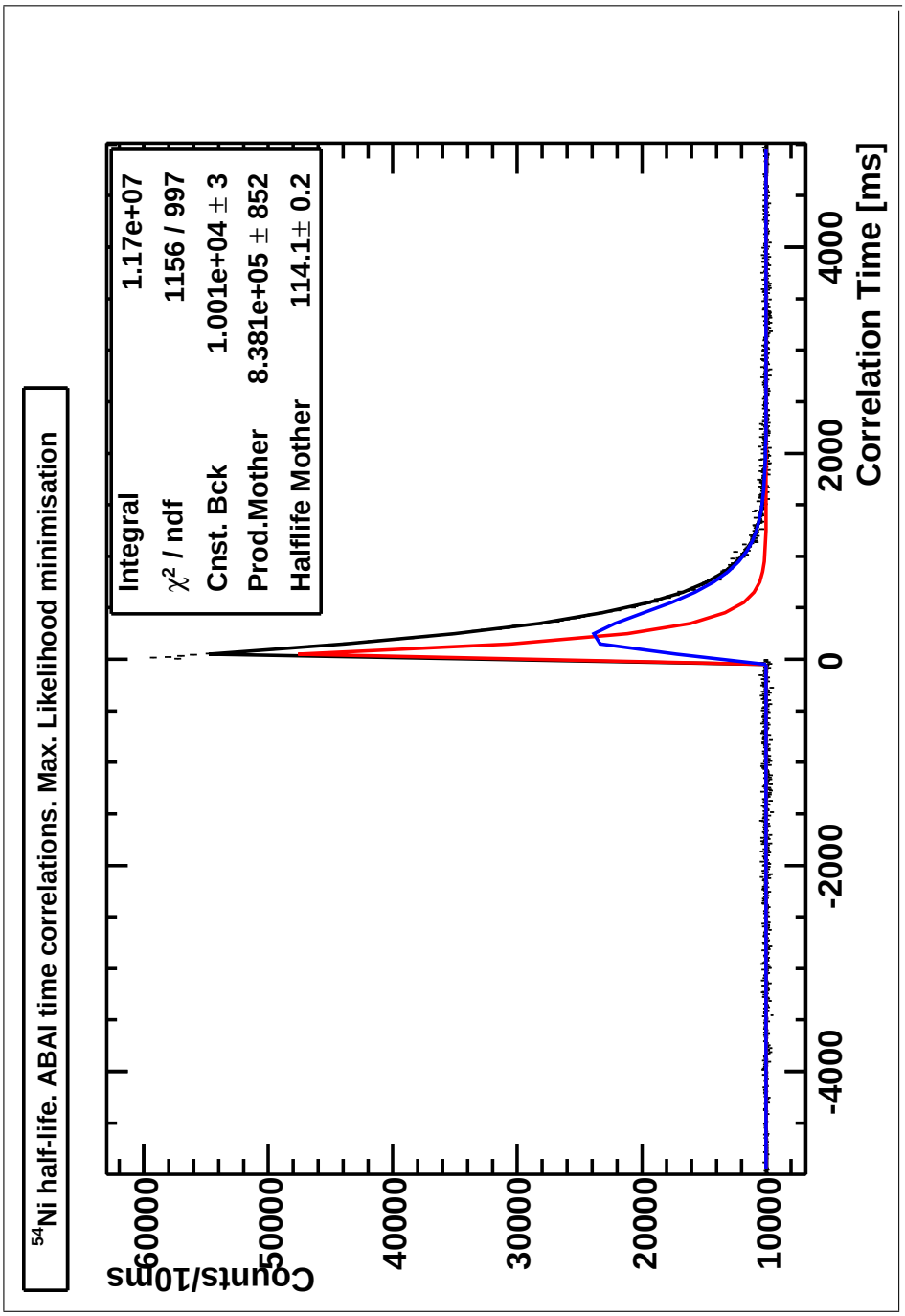

Figure 7.41: Vida media de la desintegración del ^{54}Ni usando minimización por máxima verosimilitud. La curva roja representa la actividad del núcleo padre ^{54}Ni y la curva azul representa la actividad del núcleo hijo ^{54}Co. La vida media del núcleo hijo es $T^d_{1/2}$= 193.271(63) ms [HT09] (parámetro fijo del ajuste).

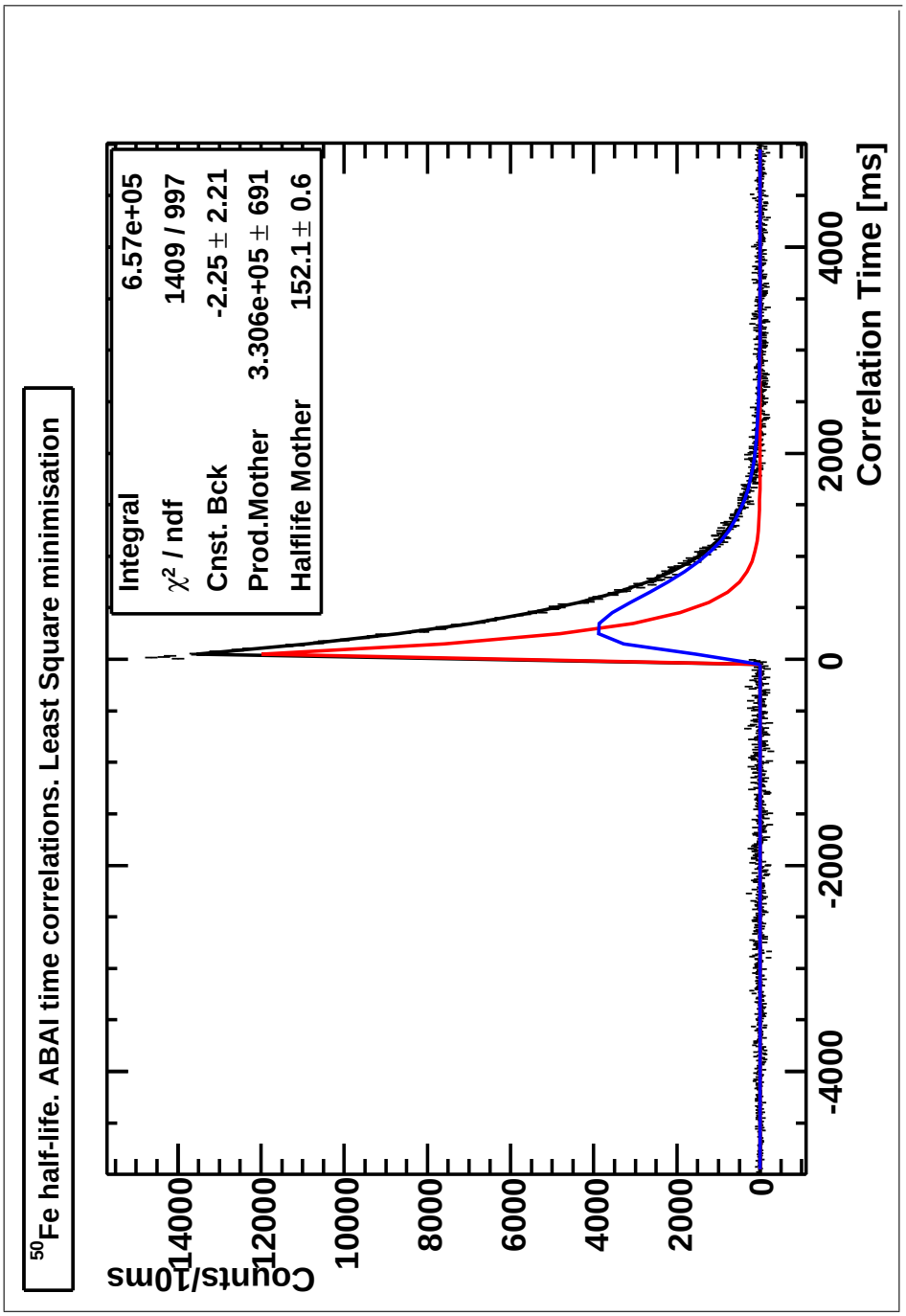

Figure 7.42: Vida media de la desintegración del ^{50}Fe usando minimización por mínimos cuadrados. La curva roja representa la actividad del núcleo padre ^{50}Fe y la curva azul representa la actividad del núcleo hijo ^{50}Mn. La vida media del núcleo hijo es $T^d_{1/2}$= 283.21(11) ms [HT09] (parámetro fijo del ajuste).

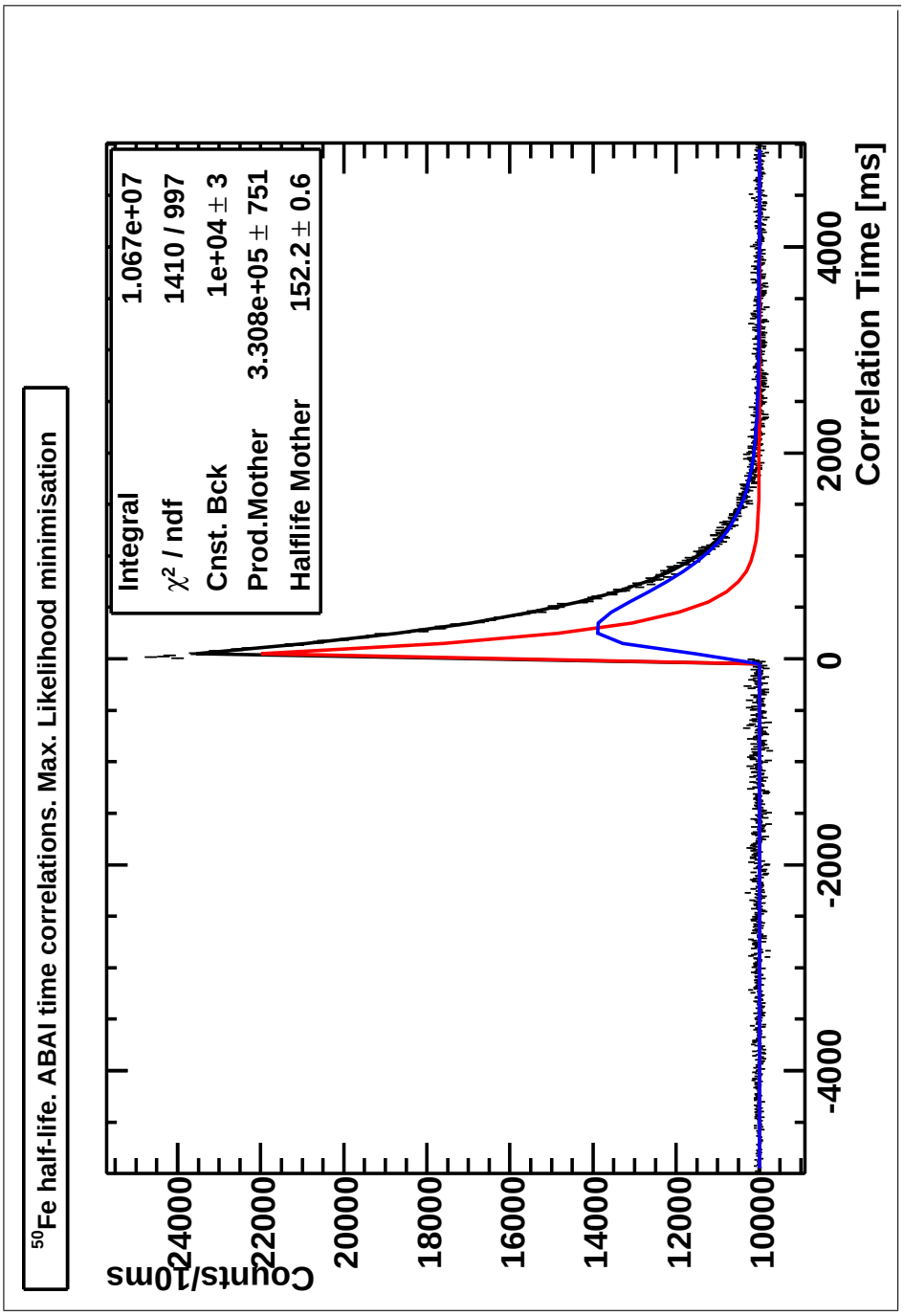

Figure 7.43: Vida media de la desintegración del ^{50}Fe usando minimización por máxima verosimilitud. La curva roja representa la actividad del núcleo padre ^{50}Fe y la curva azul representa la actividad del núcleo hijo ^{50}Mn. La vida media del núcleo hijo es $T^d_{1/2}$= 283.21(11) ms [HT09] (parámetro fijo del ajuste).

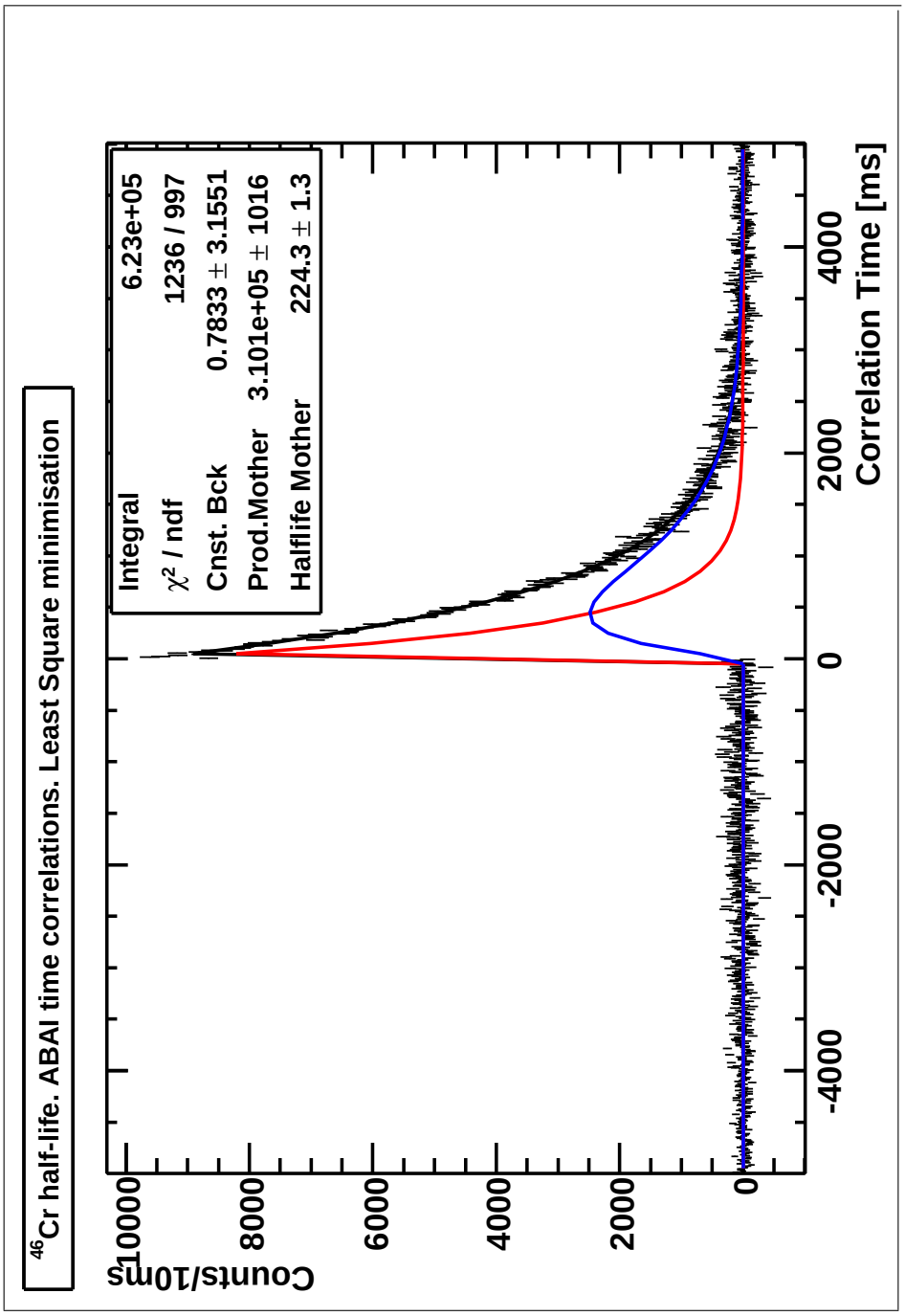

Figure 7.44: Vida media de la desintegración del ^{46}Cr usando minimización por mínimos cuadrados. La curva roja representa la actividad del núcleo padre ^{46}Cr y la curva azul representa la actividad del núcleo hijo ^{46}V. La vida media del núcleo hijo es $T^d_{1/2}$= 422.50(11) ms [HT09] (parámetro fijo del ajuste).

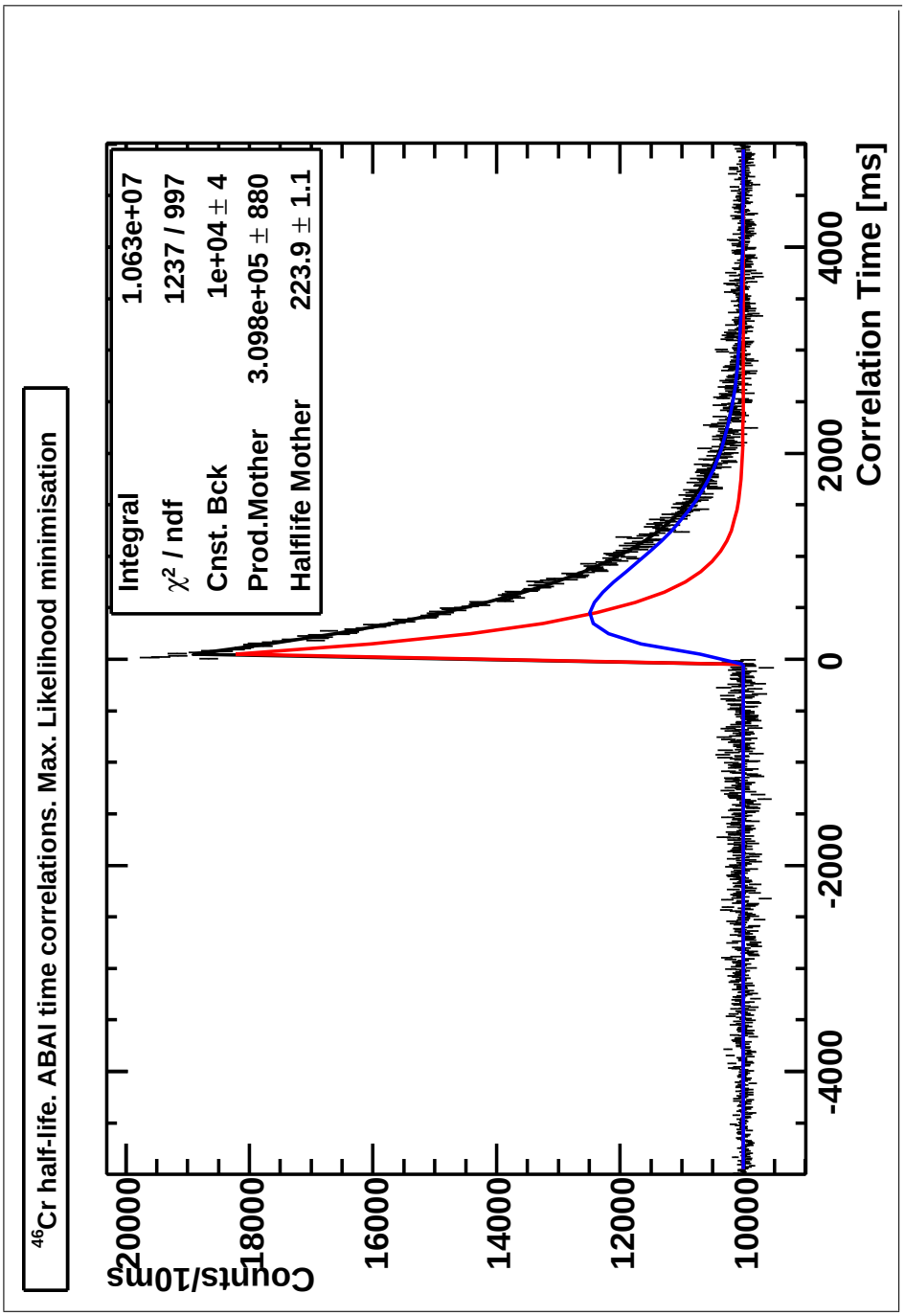

Figure 7.45: Vida media de la desintegración del ^{46}Cr usando minimización por máxima verosimilitud. La curva roja representa la actividad del núcleo padre ^{46}Cr y la curva azul representa la actividad del núcleo hijo ^{46}V. La vida media del núcleo hijo es $T^d_{1/2}$= 422.50(11) ms [HT09] (parámetro fijo del ajuste).

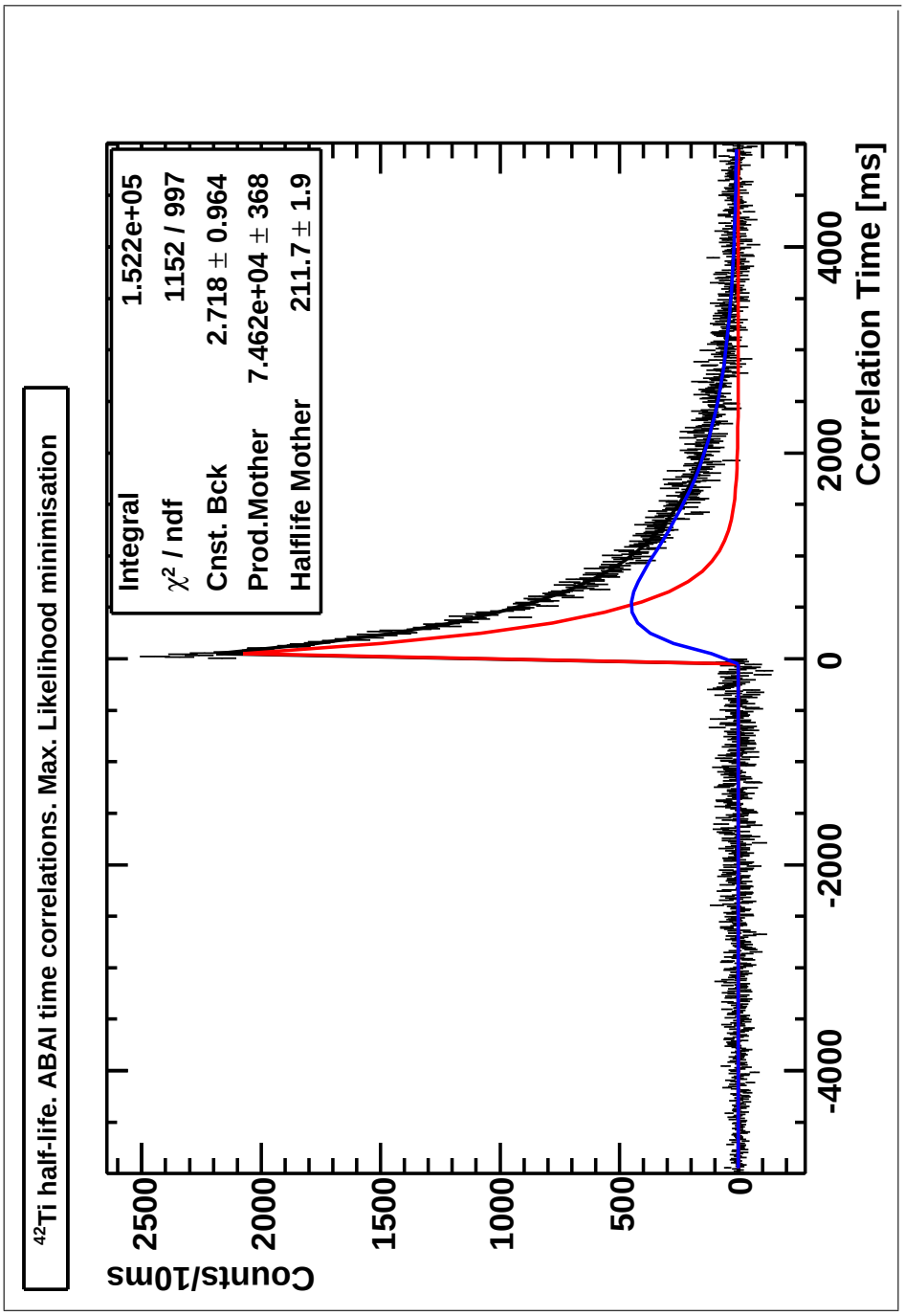

Figure 7.46: Vida media de la desintegración del ^{42}Ti usando minimización por mínimos cuadrados. La curva roja representa la actividad del núcleo padre ^{42}Ti y la curva azul representa la actividad del núcleo hijo ^{42}Sc. La vida media del núcleo hijo es $T^d_{1/2}$= 680.72(26) ms [HT09] (parámetro fijo del ajuste).

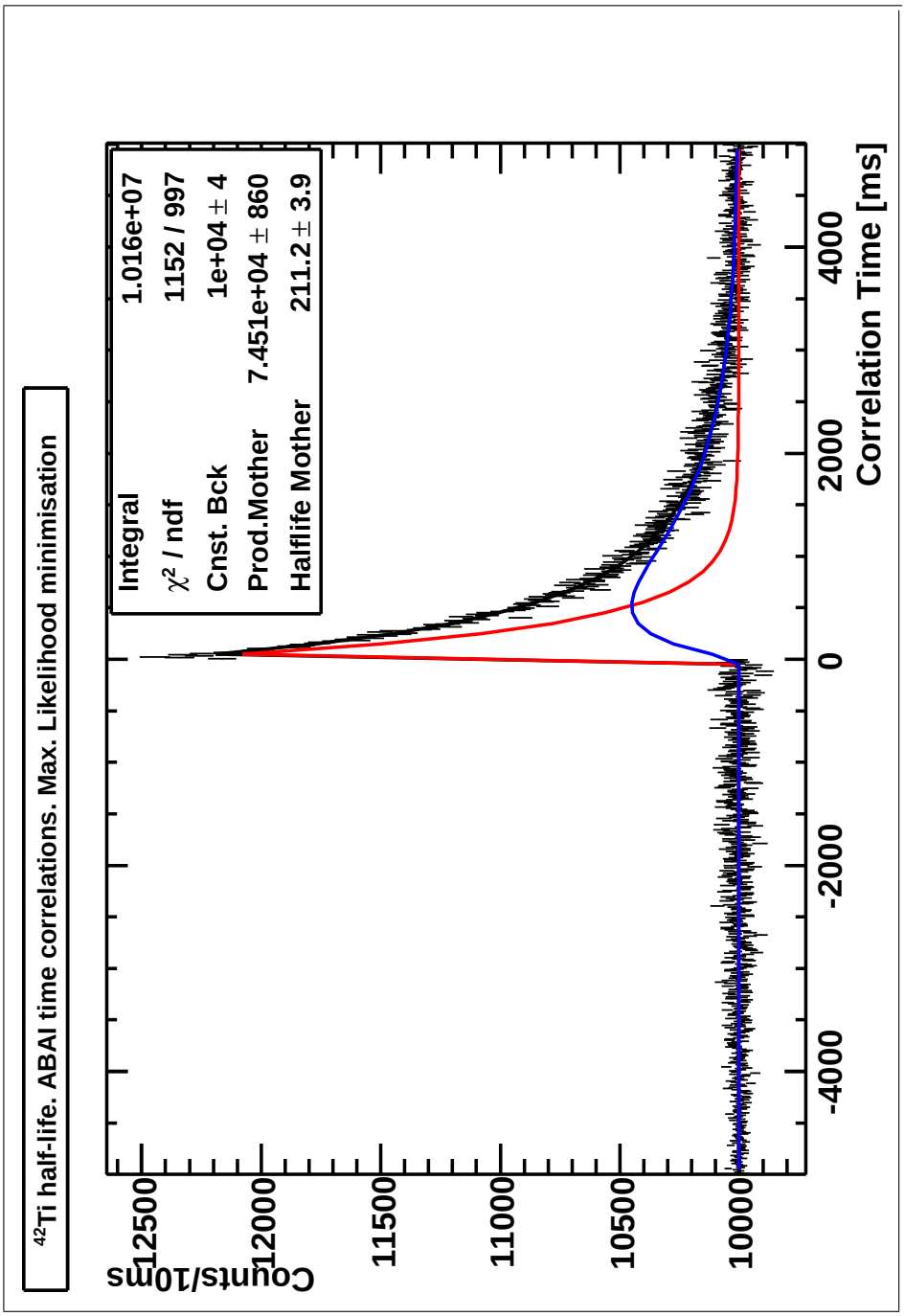

Figure 7.47: Vida media de la desintegración del ^{42}Ti usando minimización por máxima verosimilitud. La curva roja representa la actividad del núcleo padre ^{42}Ti y la curva azul representa la actividad del núcleo hijo ^{42}Sc. La vida media del núcleo hijo es $T^d_{1/2}$= 680.72(26) ms [HT09] (parámetro fijo del ajuste).

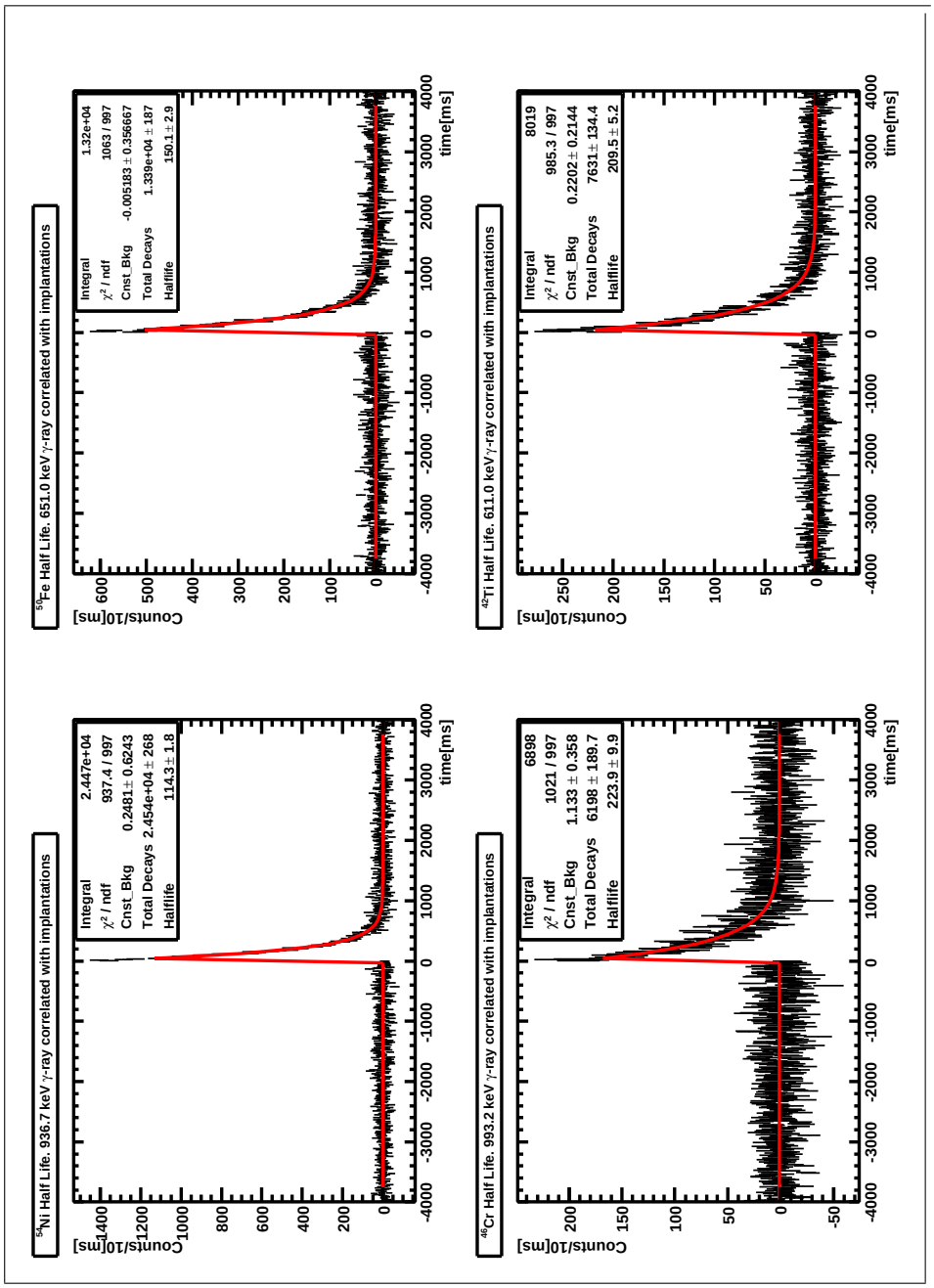

Figure 7.48: Vidas medias de los núcleos ^{54}Ni, ^{50}Fe, ^{46}Cr y ^{42}Ti, evolución temporal del rayo γ asociado al primer estado excitado en los correspondientes núcleos hijos.

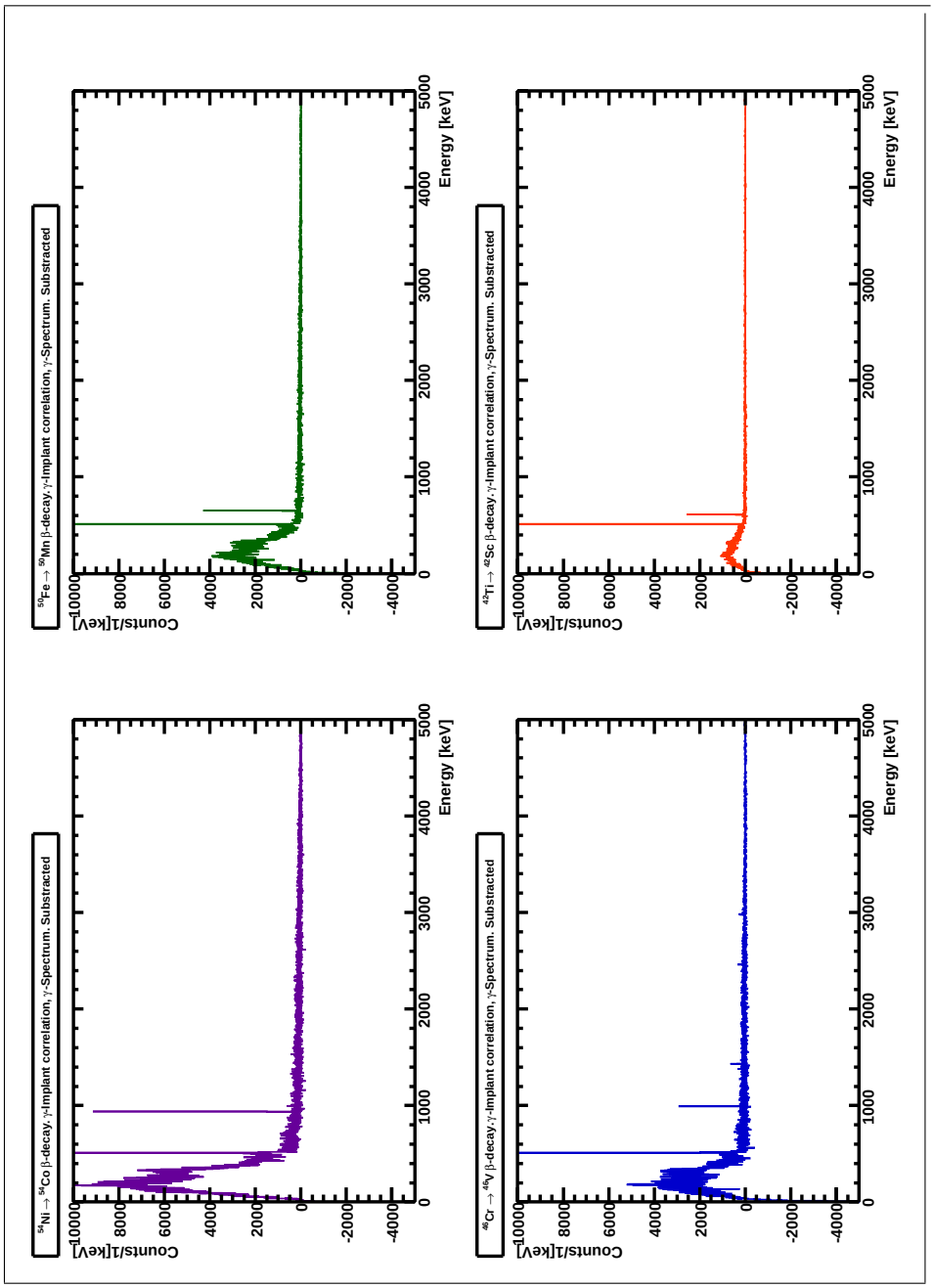

Figure 7.49: ^{54}Ni, ^{50}Fe, ^{46}Cr and ^{42}Ti clean γ-energy spectra, i.e. without contaminants or randoms for correlations in the same pixel.

Resultados en GSI: Población al estado fundamental en el núcleo hijo.

Medir la población del estado fundamental del núcleo padre al estado fundamental del núcleo hijo, es en general una tarea difícil, debido a que se debe conocer el número total de núcleos padre que se desintegran β y todas las desintegraciones β-γ que van a un estado excitado en el núcleo hijo. Así la población al estado fundamental se obtiene mediante sustracción.
El número total de núcleos padre que se desintegran β se obtiene, en general, midiendo los ΔE de los β en un detector de partículas. Esta medida conlleva, pricipalmente, dos dificultades implícitas: (i) La partícula β, puede proceder tanto de la desintegración del núcleo padre como de la actividad del núcleo hijo (o incluso de algún contaminante). (ii) Es necesario conocer la eficiencia de detección β del detector, la cual depende de la energía de la partícula β.
La manera usual de evitar esta última dificultad, es midiendo el número total de partículas β y el número total de coincidencias β-γ. De esta forma las eficiencias β se cancelan. Esto es correcto, siempre y cuando la eficiencia β para la desintegración del estado fundamental del padre al estado fundamental del hijo, no sea distinta de la eficiencia β de la desintegración del estado fundamental del núcleo padre a los estados excitados en el núcleo hijo.

En nuestro experimento contamos con las siguientes ventajas:

- Sabemos exactamente el número de núcleos padres que se han producido, implantado y sobrevivido como padres y que dan una señal ΔE en un pixel (i,j) del DSSSD. Esto se obtiene de la siguiente manera:

  Seleccionamos el valor de Z (energía perdida en las cámaras de ionización) y de A/Q (tiempo de vuelo y rigidez magnética de los dipolos). Del ajuste de la vida media (correlaciones implantación-β, descrito en la sección anterior), podemos obtener el número exacto de núcleos seleccionados que se desintegran β (N_0 de acuerdo a la Ec. 7.5). De esta forma, estamos seguros que no se incluye ningún contaminante como tampoco ningún evento aleatóreo, ya que el fondo de correlaciones aleatóreas ha sido sustraido, a partir de correlaciones temporales de una implantación en el pixel (i,j) con un β en el pixel opuesto (j,i).

- Se midieron las coincidencias β-γ en exactamente las mismas condiciones.
  Esto fue hecho mediante correlaciones temporales implantación-β-en-coincidencia-con-γ para eventos implantación-β que ocurren en un mismo píxel (i,j), sustrayendo las coincidencias aleatóreas obtenidas a partir de correlaciones implantación-β-en-coincidencia-con-γ para eventos implantación-β que ocurren en píxeles opuestos (implantación en píxel (i,j) y evento β-γ en píxel (j,i)). El resultado del espectro γ con las correlaciones aleatóreas normalizadas y sustraidas se encuentra en Fig. 7.49.

Como se puede ver en la Fig. 7.49, la estadística se ve fuertemente reducida en comparación con las Figs. 7.15-7.38 (sin correlación con implantación).
Para obtener la población a los estados excitados en el núcleo hijo, debemos encontrar el factor de normalización para intensidadedes (relativas al primer estado excitado) I_γ^{Rel}

de las respectivas transiciones γ de los espectros β-γ sin correlación.

Del ajuste de la vida media usando correlaciones temporales implantación-β, se obtiene también el número total de núcleos padres N_0^{β} (ver resultados del ajuste en Figs. 7.40 - 7.47). Asimismo, del ajuste de la vida media en la curva de evolución temporal del primer estado excitado en el núcleo hijo, luego de correlacionar implantación-β-$\gamma^{\text{1er.estado.excitado}}$, se obtiene el número total de núcleos padres que se desintegran β, y emiten un γ en coincidencia cuya energía corresponde a la energía del primer estado excitado en el núcleo hijo $N_0^{\gamma_1}$ (ver resultados de los ajustes correspondientes en Fig. 7.48).

Con ello, la población al primer estado excitado $P(\gamma_1)$ queda determinada por

$$P(\gamma_1) = \frac{N_0^{\gamma_1}/(\epsilon_{\gamma_1}\epsilon_{\beta}\epsilon_{\text{surv}})}{N_0^{\beta}/(\epsilon_{\beta}\epsilon_{\text{surv}})} = \frac{N_0^{\gamma_1}}{N_0^{\beta}\epsilon_{\gamma_1}} \tag{7.6}$$

siendo ϵ_{γ_1} la eficiencia de detección γ de RISING a la energía correspondiente a γ_1, ϵ_{β} es la eficiencia de detección β del detector β (DSSSD) y ϵ_{surv} la eficiencia de superviencia de los iones separados, producidos e identificados en el FRS y que se implantan en el DSSSD. En general y ya que tenemos las intesidades γ relativas al primer estado excitado, la población al estado k excitado, se puede escribir como:

$$P(\gamma_k) = \frac{N_0^{\gamma_1}}{N_0^{\beta}\epsilon_{\gamma_1}} I_{\gamma_k}^{\text{Rel}} \tag{7.7}$$

De este modo, la población al estado fundamental P(e.f.) en el núcleo hijo viene dada por:

$$P(\text{e.f.}) = 1 - \frac{N_0^{\gamma_1}}{N_0^{\beta}\epsilon_{\gamma_1}} \sum_k I_{\gamma_k}^{\text{Rel}} \tag{7.8}$$

En las Tablas 7.8-7.11, se encuentran los valores obtenidos de población de los estados excitados en el núcleo hijo, para los cuatro casos estudiados.

Energía [keV]	Intensidad γ Relativa	Población %
936.7	1000.0(35.2)	19.75(122)
2424.6	8.0(1.3)	0.16(3)
3376.1	18.9(1.6)	0.37(4)
3889.6	10.6(1.2)	0.21(3)
4293.4	5.6(5.1)	0.11(10)
4323.0	7.4(2.3)	0.15(5)
4543.8	6.0(1.0)	0.12(2)
4822.8	2.3(0.5)	0.04(1)
5202.4	1.2(0.4)	0.02(1)
e.f		79.07(123)

Table 7.8: Población de los estados excitados del ^{54}Co en la desintegración del ^{54}Ni. El número total de ^{54}Ni implantados que se desintegran β, N_0^{β}, proviene del ajuste de la vida media en las Figs. 7.40 y 7.41, N_0^{β}= 838204.8(686.3). El número de ^{54}Ni implantados que se desintegran β y que además pueblan el primer estado excitado en ^{54}Co, $N_0^{\gamma_1}$, proviene del ajuste de la vida media en la Fig. 7.48, $N_0^{\gamma_1}$ = 24535.1(268.5).

Energía [keV]	Intensidad γ Relativa	Población %
651.0	1000.0(35.2)	22.80(142)
2403.8	55.4(2.6)	1.47(10)
2684.2	27.9(1.9)	0.70(6)
3380.0	37.5(2.2)	0.85(7)
3643.4	6.6(1.2)	0.15(3)
4012.7	1.9(0.9)	0.04(2)
4315.7	3.6(1.4)	0.08(3)
e.f		73.90(143)

Table 7.9: Población de los estados excitados del ^{50}Mn en la desintegración del ^{50}Fe. El número total de ^{50}Fe implantados que se desintegran β, N_0^{β}, proviene del ajuste de la vida media en las Figs. 7.42 y 7.43, N_0^{β}= 330691.7(508.5). El número de ^{50}Fe implantados que se desintegran β y que además pueblan el primer estado excitado en ^{50}Mn, $N_0^{\gamma_1}$, proviene del ajuste de la vida media en la Fig.7.48, $N_0^{\gamma_1}$ = 13391.5(187.0).

Energía [keV]	Intensidad γ Relativa	Población %
915.0	9.9(4.80)	0.14(7)
993.2	1000.0(35.21)	13.90(95)
1432.5	242.0(8.82)	3.36(23)
2459.8	109.3(4.68)	1.52(11)
2466.3	17.7(2.26)	0.38(4)
2697.4	67.9(3.21)	0.94(7)
2977.8	170.8(6.58)	2.50(17)
3867.6	6.4(1.26)	0.09(2)
e.f		77.17(100)

Table 7.10: Población de los estados excitados del ^{46}V en la desintegración del ^{46}Cr. El número total de ^{46}Cr implantados que se desintegran β (N_0^{β}), proviene del ajuste de la vida media en las Figs. 7.44 y 7.45, N_0^{β}=310096.1(1009.3). El número de ^{46}Cr implantados que se desintegran β y que además pueblan el primer estado excitado en ^{46}V, $N_0^{\gamma_1}$, proviene del ajuste de la vida media en la Fig.7.48, $N_0^{\gamma_1}$ = 6198.0(190.0).

Energía [keV]	Intensidad γ Relativa	Población %
611.0	1000.0(35.3)	55.92(355)
1888.4	7.3(1.0)	0.41(6)
e.f		43.66(355)

Table 7.11: Población de los estados excitados del ^{42}Sc en la desintegración del ^{42}Ti. El número total de ^{42}Ti implantados que se desintegran β, N_0^{β}, proviene del ajuste de la vida media en las Figs. 7.46 y 7.47, N_0^{β}=74565.7(250.9). El número de ^{42}Ti implantados que se desintegran β y que además pueblan el primer estado excitado en ^{42}Sc, $N_0^{\gamma_1}$, proviene del ajuste de la vida media en la Fig.7.48, $N_0^{\gamma_1}$ = 7631.3(134.3).

De la Ec. 7.2 se puede calcular la vida media de la transición Fermi,

$$T_F = \frac{K}{(1-\delta_c) f_F B(F)} \tag{7.9}$$

donde K y δ_c son constantes conocidas ([HT09] y [TH02] respectivamente), f_F el factor de Fermi que depende del valor Q_β y de la energía de excitación, y $B(F)$= 2. La razón entre la vida media total $T_{1/2}^{\beta}$ experimental y la vida media de la transición Fermi obtenida de la Ec. 7.9, nos da la población al estado fundamental. En la Tabla 7.12 están resumidos los resultados obtenidos en este trabajo para la vida media total y la población al estado fundamental, y una comparación con el valor esperado utilizando la vida media de la transición Fermi.

	$T_{1/2}^{\mathrm{exp.}\beta}$ [ms]	T_F [ms]	Q-Value [keV]	Pobl.e.f.(Exp.)	Pob.e.f.(Esperada)
^{54}Ni	114.1(1)	139.7(42)	8800(50) [Aud03]	0.791(12)	0.817(25)
^{50}Fe	152.2(2)	204.1(81)	8150(60) [Aud03]	0.739(14)	0.746(30)
^{46}Cr	224.1(7)	288.1(41)	7599(20) [Aud03]	0.772(10)	0.778(11)
$^{42}\mathrm{Ti}_K$	211.7(36)	429.9(1)	7016.8(3) [Kur09]	0.437(36)	0.492(8)
$^{42}\mathrm{Ti}_A$	211.7(36)	435.6(17)	7000(5) [Aud03]	0.437(36)	0.486(9)

Table 7.12: Resultados experimentales: Vida media desintegración β ($T_{1/2}^{\mathrm{exp.}\beta}$), población al estado fundamental del núcleo hijo de nuestro experimento (Pobl.e.f.(Exp.)), valor Q_β según referencias.

Resultados: la fuerza de transición Gamow-Teller B(GT+)

En el análisis de los experimentos de desintegración β, para los cuatro casos estudiados, hemos obtenido: (i) la vida media total de la desintegración $T_{1/2}^{\beta}$ (ii) la población de los estados excitados en el núcleo hijo $P(\gamma_j)$ y (iii) la población al estado fundamental en el núcleo hijo P(e.f.) .

Con estos resultados, se puede obtener la fuerza absoluta $B(GT+)_j$ de cada una de las j transiciónes Gamow-Teller,

$$B(GT+)_j = \frac{K}{\lambda^2}\frac{P(\gamma_j)}{f_j T_{1/2}^{\beta}} \tag{7.10}$$

Energía del estado (β) [keV]	$\mathrm{B(GT^+)}_j^{\beta}$
936.7	0.542(38)
2424.6	0.014(2)
3376.1	0.079(9)
3889.6	0.079(11)
4293.4	0.068(62)
4323.0	0.095(30)
4543.8	0.103(20)
4822.8	0.059(13)
5202.4	0.056(20)

Table 7.13: Resultados de la fuerza de la transición Gamow-Teller a los estados excitados del ^{54}Co en la desintegración β^+ del ^{54}Ni.

Energía del estado (β) [keV]	$B(GT^+)^{\beta}_j$
651.0	0.588(45)
2403.8	0.164(15)
2684.2	0.104(11)
3380.0	0.276(30)
3643.4	0.068(14)
4012.7	0.033(16)
4315.7	0.096(40)

Table 7.14: Resultados de la fuerza de la transición Gamow-Teller a los estados excitados del ^{50}Mn en la desintegración β^+ del ^{50}Fe.

Energía del estado (β) [keV]	$B(GT^+)^{\beta}_j$
993.2	0.472(33)
1432.5	0.167(12)
2459.8	0.210(16)
2466.3	0.053(6)
2697.4	0.172(14)
2977.8	0.639(47)
3867.6	0.082(17)

Table 7.15: Resultados de la fuerza de la transición Gamow-Teller a los estados excitados del ^{46}V en la desintegración β^+ del ^{46}Cr.

Energía del estado (β) [keV]	$B(GT^+)^{\beta}_j$
611.0	2.304(152)
1888.4	0.059(9)

Table 7.16: Resultados de la fuerza de la transición Gamow-Teller a los estados excitados del ^{42}Sc en la desintegración β^+ del ^{42}Ti. Valores calculados usando el valor Q_β [Kur09]

Energía del estado [keV]	$B(GT^+)_\beta$
611.0	2.33(15)
1888.4	0.06(1)

Table 7.17: Resultados de la fuerza de la transición Gamow-Teller a los estados excitados del ^{42}Sc en la desintegración β^+ del ^{42}Ti. Valores calculados usando el valor Q_β [Aud03].

Esquema de Niveles

Con los resultados de los espectros γ, además del análisis de la población a los distintos estados y el cálculo de las fuerzas de transición Gamow-Teller, a partir de nuestros datos experimentales, podemos construir el esquema de niveles para los cuatro núcleos estudiados (ver Figs. 7.50 - 7.53).

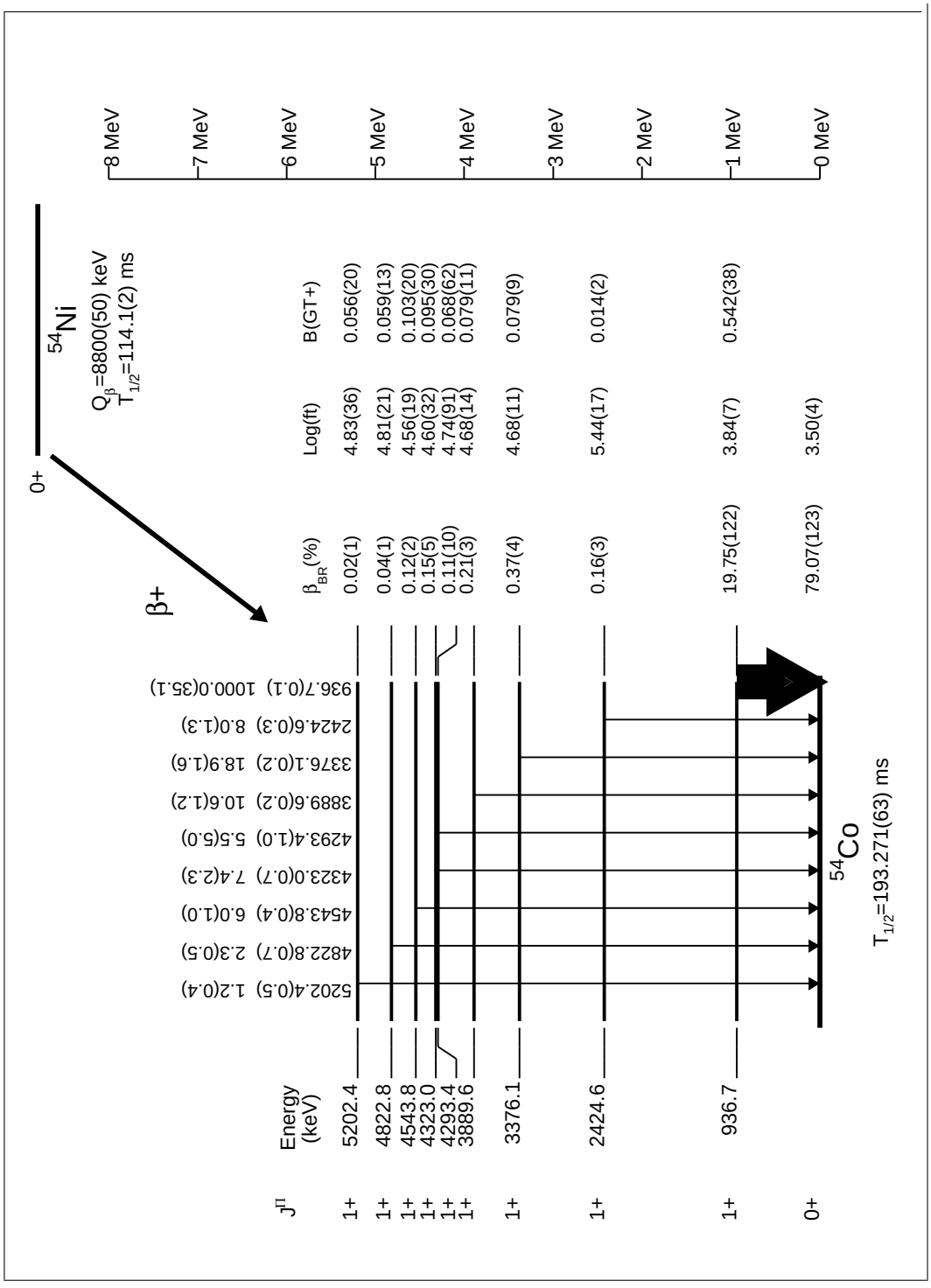

Figure 7.50: Esquema de niveles de la desintegración β del ^{54}Ni. Todos los resultados de esta figura provienen del análisis de nuestro experimento, excepto el valor Q_β [Aud03] y la vida media del núcleo hijo [HT09].

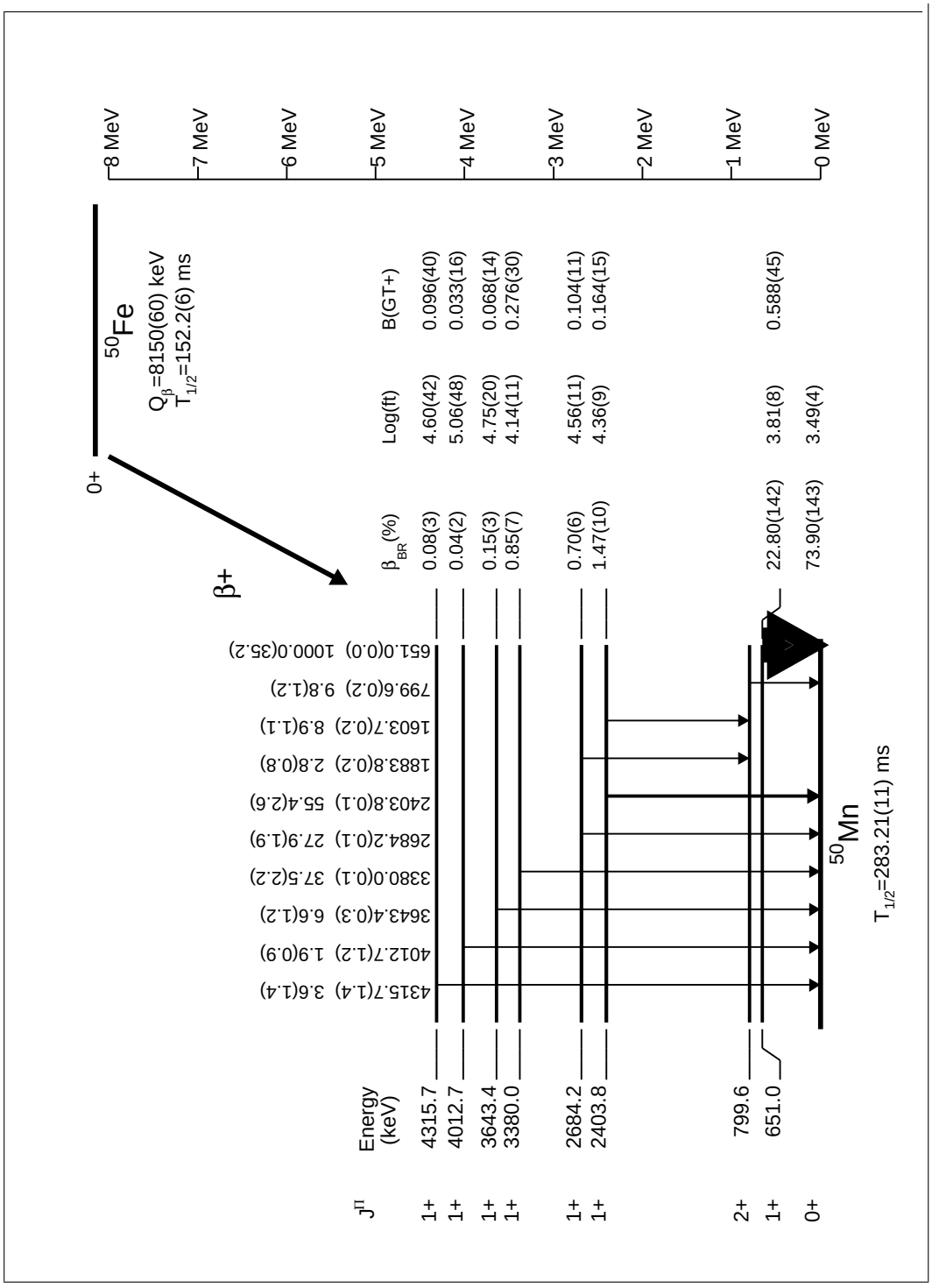

Figure 7.51: Esquema de niveles de la desintegración β del ^{50}Fe. Todos los resultados de esta figura provienen del análisis de nuestro experimento, excepto el valor Q_β [Aud03] y la vida media del núcleo hijo [HT09].

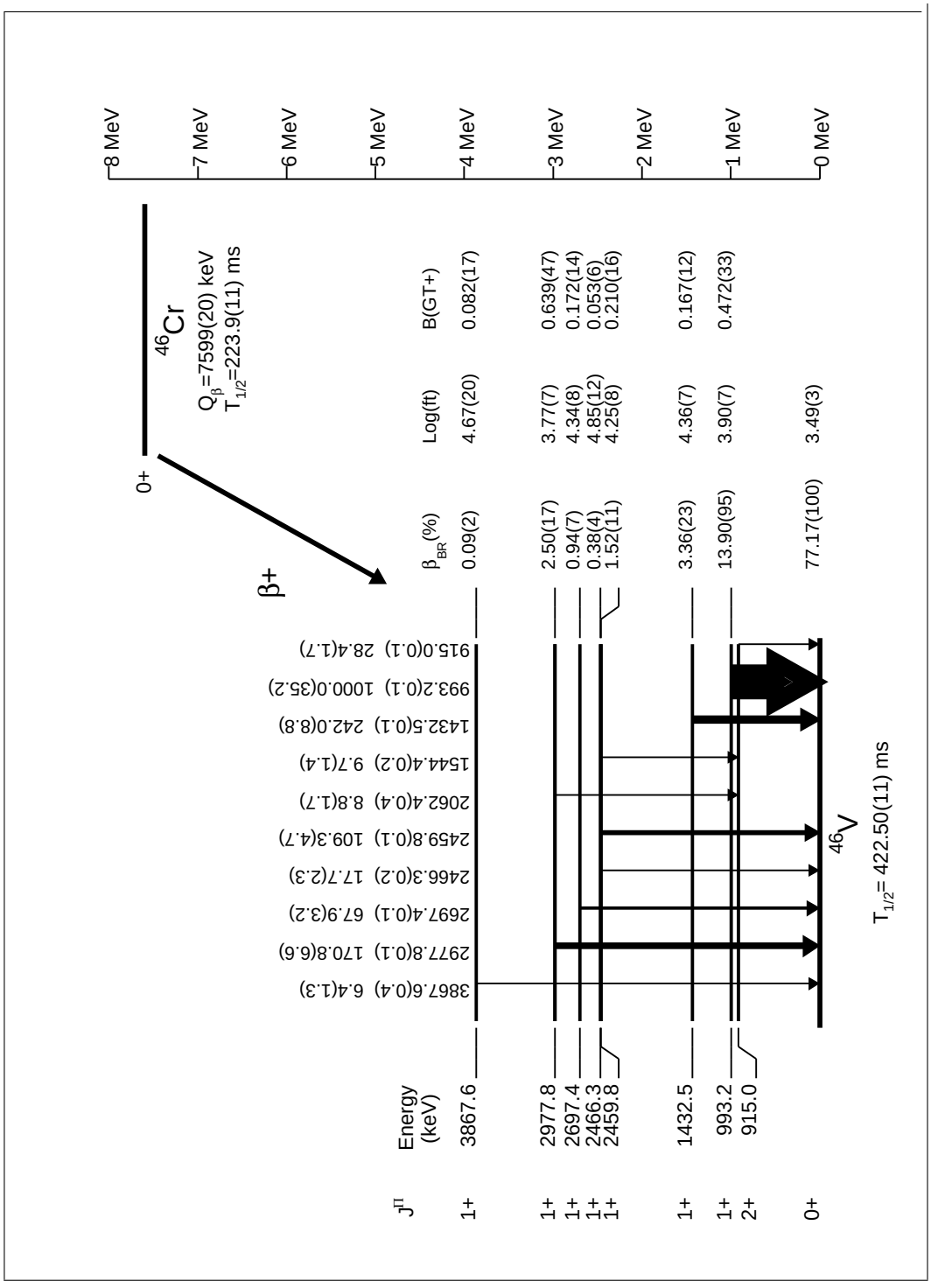

Figure 7.52: Esquema de niveles de la desintegración β del ^{46}Cr. Todos los resultados de esta figura provienen del análisis de nuestro experimento, excepto el valor Q_β [Aud03] y la vida media del núcleo hijo [HT09].

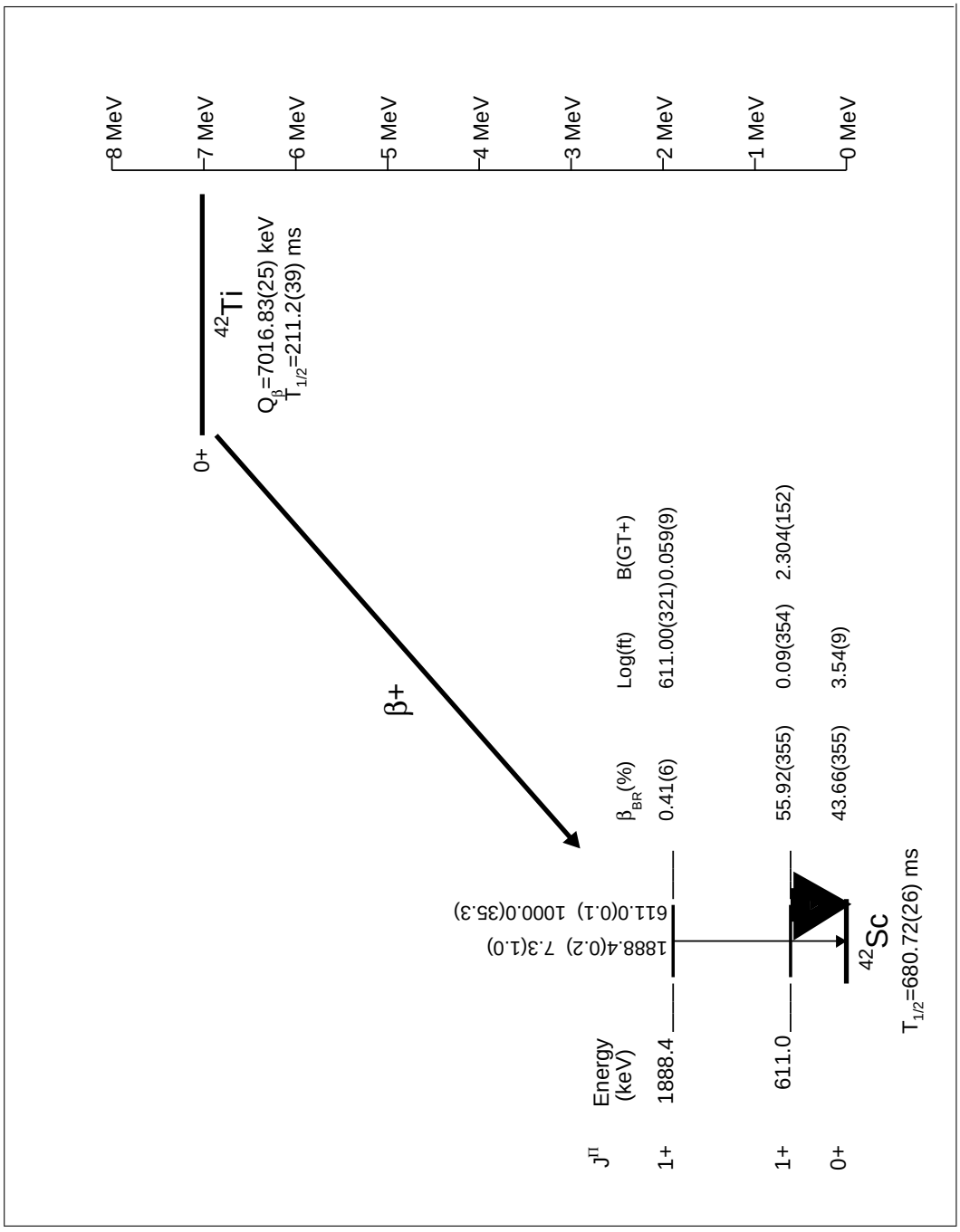

Figure 7.53: Esquema de niveles de la desintegración β del ^{42}Ti. Todos los resultados de esta figura provienen del análisis de nuestro experimento, excepto el valor Q_β [Kur09] y la vida media del núcleo hijo [HT09].

7.5 Discusiones y Conclusiones

7.5.1 Comparación de las fuerzas de transición Gamow-Teller $B(GT)$, obtenidas mediante reacciones de intercambio de carga (CE) y mediante experimentos de desintegración β

En las Tablas 7.22 - 7.19 se encuentra comparación de los resultados experimentales de la $B(GT-)^{\mathrm{CE}}$ y $B(GT+)^{\beta}$ para cada uno de los cuatro casos estudiados.
Como hemos visto la fuerza de la transición Gamow-Teller $B(GT-)$ medido en reacciones de intercambio de carga, debe ser normalizado a (i) un valor de $B(GT+)_i$ o a (ii) el valor de R^2 de la Ec. 7.4. En los casos estudiados se utilizaron los siguientes valores de R^2: $R^2_{^{54}\mathrm{Ni}}$=8.2(9), $R^2_{^{50}\mathrm{Fe}}$=7.6(11), $R^2_{^{46}\mathrm{Cr}}$=7.8(9) y $R^2_{^{42}\mathrm{Ti}}$=5.5(3).

De la comparación de los resultados de los experimentos de reacciones de intercambio de carga y de los experimentos de desintegración β, podemos observar:

(a) que tal y como esperábamos, se observan los mismos estados en los procesos análogos de β^+ e intercambio de carga en núcleos espejo con $\mathrm{T}_z = \pm 1$.

(b) que los valores de la $B(GT)_i$ observados en ambos procesos, coinciden en general, sobre todo para aquellos estados que se pueblan con bastante intensidad. Sin embargo, hay casos en los que se observan diferencias apreciables. Estos casos están marcados con asteríscos en las tablas. Por otro lado parece que la normalización usado en el caso de la masa 46, no es del todo correcta. Las pequeñas diferencias pueden deberse al hecho de que la desintegración β puede ocurrir en cualquier parte del núcleo, mientras que la reacción de intercambio de carga, es específica.

T=1, masa 42

Ex (CE) [keV]	B(GT-)$^{\mathrm{CE}}_j$	Energía del estado (β) [keV]	B(GT$^+$)$^{\beta}_j$
611	2.34(18)	611.0	2.304(152)
1886	0.09(1)	1888.4	0.059(9)
3688	0.16(2)		

Table 7.18: Comparación entre los valores de la fuerza Gamow-Teller obtenidos mediante reacciones de intercambio de carga B(GT-)$^{\mathrm{CE}}$ y experimentos de desintegración β B(GT$^+$)$^{\beta}$ en la masa 42. Usando el valor Q_{β} [Kur09]

Ex (CE) [keV]	B(GT-)$^{\mathrm{CE}}_j$	Energía del estado (β) [keV]	B(GT$^+$)$^{\beta}_j$
611	2.34(18)	611.0	2.33(15)
1886	0.09(1)	1888.4	0.06(1)
3688	0.16(2)		

Table 7.19: Comparación entre los valores de la fuerza Gamow-Teller obtenidos mediante reacciones de intercambio de carga B(GT-)$^{\mathrm{CE}}$ y experimentos de desintegración β B(GT$^+$)$^{\beta}$ en la masa 42, usando el valor Q_{β} [Aud03].

T=1, masa 46

Ex (CE) [keV]	B(GT-)$_j^{\mathrm{CE}}$	Energía del estado (β) [keV]	B(GT$^+$)$_j^{\beta}$
994	0.365(44)	993.2	0.472(33)
1433	0.124(15)	1432.5	0.167(12)
2461	0.195(24)	2459.8	0.210(16)
		2466.3	0.053(6)
2699	0.206(25)	2697.4	0.172(14)
2978	0.604(73)	2977.8	0.639(47)
3535	0.019(3)		
3610	0.025(4)		
3870	0.117(14)	3867.6	0.082(17)
4051	0.043(6)		
4325	0.034(5)		
4378	0.037(5)		

Table 7.20: Comparación entre los valores de la fuerza Gamow-Teller obtenidos mediante reacciones de intercambio de carga B(GT-)$^{\mathrm{CE}}$ y experimentos de desintegración β B(GT$^+$)$^{\beta}$ en la masa 46.

T=1, masa 50

Ex (CE) [keV]	B(GT-)$_j^{\mathrm{CE}}$	Energía del estado (β) [keV]	B(GT$^+$)$_j^{\beta}$
652	0.50(13)	651.0	0.588(45)
2411	0.15(4)	2403.8	0.164(15)
2694	0.11(3)	2684.2	0.104(11)
2790	0.03(1)		
3392	0.35(9)	3380.0	0.276(30)
3654	0.14(4)	3643.4	0.068(14)*
4028	0.07(2)	4012.7	0.033(16)
4333	0.11(3)	4315.7	0.096(40)
4584	0.03(1)		

Table 7.21: Comparación entre los valores de la fuerza Gamow-Teller obtenidos mediante reacciones de intercambio de carga B(GT-)$^{\mathrm{CE}}$ y experimentos de desintegración β B(GT$^+$)$^{\beta}$ en la masa 50.

T=1, masa 54

Ex (CE) [keV]	B(GT-)$_j^{CE}$	Energía del estado (β) [keV]	B(GT$^+$)$_j^{\beta}$
938	0.493(62)	936.7	0.542(38)
2426	0.016(3)	2424.6	0.014(2)
3375	0.079(11)	3376.1	0.079(9)
3506	0.031(5)		
3891	0.103(14)	3889.6	0.079(11)
4092	0.054(8)		
4296	0.023(4)	4293.4	0.068(62)
		4323.0	0.095(30)
4544	0.147(20)	4543.8	0.103(20)
4822	0.101(14)	4822.8	0.059(13)*
5217	0.015(3)	5202.4	0.056(20)*
5464	0.014(2)		
5755	0.013(2)		
5849	0.011(2)		
5909	0.144(19)		
6083	0.048(7)		
6118	0.025(4)		
6362	0.025(4)		
6466	0.018(3)		
6530	0.078(10)		
6792	0.041(6)		
6859	0.038(5)		
7135	0.056(8)		
7388	0.035(5)		
7449	0.047(6)		
7469	0.017(2)		
7542	0.025(4)		
7642	0.022(3)		
7711	0.051(7)		
7858	0.018(3)		
7943	0.151(19)		

Table 7.22: Comparación entre los valores de la fuerza Gamow-Teller obtenidos mediante reacciones de intercambio de carga B(GT-)^{CE} y experimentos de desintegración β B(GT$^+$)$^{\beta}$ en la masa 54.

7.5.2 Ausencia de transiciones M1 $1^+ \rightarrow 1^+$ en l núcleo hijo.

Una observación importante que se puede extraer de los resultados de desintegración beta, es la ausencia de transiciones M1 $1^+ \rightarrow 1^+$ en el núcleo hijo. Si observamos los esquemas de niveles presentados en las Figs. 7.50 - 7.53, vemos que en ninguno de los cuatro casos estudiados se observan transiciones M1 de los estados 1^+ a alta energía de exitación, al primer estado excitado 1^+. Sin embargo sí se observan las transiciones M1 de estos estados al estado fundamental 0^+ e incluso en algún caso las transiciones M1 al

primer estado excitado 2^+. La clave está en el isoespín de los estados considerados. El estado fundamental 0^+ tiene isoespín T=1, esto se debe a que es un núcleo impar con N=Z y la función de ondas total tiene que ser antisimétrica. Por otro lado los estados 1^+ tienen isoespín T=0. En la transición M1 1^+(T=0) $\rightarrow$ 1^+(T=0), sólo puede actuar el término isoescalar, mientras que en las transiciones 1^+(T=0) $\rightarrow$ 0^+(T=1) actúa el término isovectorial que es mucho mayor. Esta regla de selección llamada "Quasi-regla de selección" por Warburton and Weneser [Wil69], ha sido observada por primera vez en núcleos de la capa fp, en este trabajo.

APPENDIX A

FRS CALIBRATION

Once the primary beam is delivered, by the GSI accelerator group at the entrance of the FRS, is centered using two position sensitive current grids. The primary beam is stopped in a Cu material called beam stopper at the entrance of the first dipole. Once the beam is centered in the target position, the intensity is reduced to 10^3 particles per spill. The reduction of the intensity prevents possible damage on the beam line detectors. The previously calculated dipole magnetic fields are set, and the primary beam must be centered till the S4 area.
Using a set of scintillators detector plus slits it is possible to determine if the beam is centered. A slit is a device which stopped part of the beam in the X-direction from the right and the left side. Then, it is possible to place a slit in the middle of the X position, cutting only half of the beam and counting the number of ions with the scintillator and repeat the procedure but cutting the other half. If the number of counts for both sides is the same, then the beam is centered. If both values are different, then small corrections of the dipole magnetic fields can be done. This procedure is repited for every section of the beam line till S4.
Once the beam is centered multi-wire detectors are placed in the beam line. As this detectors are always aligned with the X-position of the beam, any deviation from the center indicates a miss calibration in the analysis software. Then an off-set calibration value is included.
Once the beam is centered, a reference ρ_{ref} value is calculated using the real dipole magnetic fields in Eq.(4.3).

$$B_{real} \times \rho_{ref} = (B\rho)_{primary \quad beam} \tag{A.1}$$

Now a 4000 mg/cm^2 Be target is included on the beam line. The fact of including a material in the primary beam path reduces the energy of the primary beam. MOCADI calculations including the target material are needed in order to correct the magnetics field which are now properly set. Normally at this point the beam is not completely centered, due to small difference between the simulated and the real target thickness. Once the beam is centered, adjusting once more the dipole magnetic fields, a realistic

target thickness value is calculated. For this experiment, the Be target thickness value is 3997 mg/cm^2.
Nuclear reactions are spected once the target is placed in the beam line. Fragment which have similar magetic rigidity respect to the primary beam will remain till all the way long the FRS. But those fragments should not affect the proper calibration of the FRS, because the production of fragment in comparison to the primary beam intesity is several order of magnitudes lower.

A.1 Time of Flight Calibration

The signals coming from the photo-multipliers were treated with a constant-fraction discriminator (CFD) and then used as a start and stop of a time-to-amplitude-converter (TAC). The analog output of the TAC is read by an analog-to-digital-converter(ADC).See Fig4.7. This signals are used to measure the time-of-flight(TOF). The TOF is the difference of the times at which the ion passes through sci41 (at time T_4) and through sci21 (at time T_2) . The delay, T_0, was chosen in such way that $T_0 + T_2 > T_4$. The influence of the light propagation inside the scintillator plates was eliminated by averaging the time difference between the left and right signals. Thus, the measured time-of-flight, TOF^*, was taken from the average of the right and left signals, TOF^*_R and TOF^*_L, opportunely transformed from channel to seconds by a calibration using a pulser giving the calibration factors α_R and α_L,

$$TOF^* = \frac{\alpha_L TOF^*_L + \alpha_R TOF^*_R}{2} = T_2 + T_0 - T_4 \tag{A.2}$$

The real time-of-flight TOF is

$$TOF = \frac{d_0}{v} = T_2 - T_4 \tag{A.3}$$

where d_0 is the flight-path, in our case d_0=37 m, and v is the velocity of the ion. Therefore, using Eq.A.2 and Eq.A.3, the time-of-flight is,

$$TOF = T_0 - TOF^* = \frac{d_0}{v} \tag{A.4}$$

and in terms of d_0 and T_0, we have

$$\frac{1}{v} = \frac{T_0}{d_0} - \frac{TOF^*}{d_0} = a + bTOF^* \tag{A.5}$$

where a and b are the time-of-flight calibration coefficients. To obtain them, different layers of material are introduced into the beam line at the focal plane F2, then the beam is slowed down and different times-of-flight are registered. The velocity of the ion v is calculated using LISE.

APPENDIX B

B(GT) RESULTS FROM CE-REACTION MEASUREMENTS AT RCNP, OSAKA.

Evaluated values [a]		$(^3\mathrm{He}, t)$ [b]		
E_x (MeV)	J^π	E_x (MeV)	L	B(GT)
0.0	0^+	0.0	0	
0.611	1^+	0.611	0	2.34(18)
1.490	3^+	1.490	≥ 1	
1.889	1^+	1.886	0	0.09(1)
2.223	1^+	2.219	≥ 1	
		3.223	≥ 1	
		3.348	≥ 1	
3688	1^+	3688	0	0.16(2)

[a]From Ref. [Wu00].
[b]From Ref. [Ada07b]

Table B.1: States observed in the ^{42}Ca(^{3}He, t)^{42}Sc reaction below 4 MeV excitation energy. For the $L = 0$ states, B(GT) are given.

Evaluated values [a]		$(^3\mathrm{He}, t)$ [b]		
E_x (MeV)	J^π	E_x (MeV)	L	B(GT)
0.0	0^+	0.0	0	
0.801(1)	3^+	0.803	≥ 1	
0.9936(3)	1^+	0.994	0	0.365(44)
1.3761(1)	3^+	1.375	≥ 1	
1.4318(5)	$(1, 2)$	1.433	0	0.124(15)
2.449(15)	$(1^+, 2^+)$	2.461	0	0.195(24)
2.686(15)		2.699	0	0.206(25)
2.8676(12)		2.867	≥ 1	
2.977(15)		2.978	0	0.604(73)
		3.535	0	0.019(3)
3.615(15)		3.610	0	0.025(4)
3.871(15)		3.870	0	0.117(14)
		4.051	0	0.043(6)
		4.325	0	0.034(5)
		4.378	0	0.037(5)

[a]From Ref. [Wu00].
[b]From Ref. [Ada06]

Table B.2: States observed in the $^{46}\mathrm{Ti}(^3\mathrm{He}, t)^{46}\mathrm{V}$ reaction below 4.5 MeV excitation energy. For the $L = 0$ states, except for the $J^\pi = 0^+$ g.s. (IAS), GT transition strengths B(GT) are given.

Evaluated values [a]		$(^3\mathrm{He}, t)$ [b]		
E_x (MeV)	J^π	E_x (MeV)	L	B(GT)
0.0	0^+ [c]	0.0	0	
0.651	1^+	0.652	0	0.50(13)
0.800	2^+	0.800	≥ 1	
1.143	3^+	1.147	≥ 1	
1.802	3	1.805	≥ 1	
		2.411	0	0.15(4)
		2.694	0	0.11(3)
		2.790	0	0.03(1)
		3.177	≥ 1	
		3.392	0	0.35(9)
		3.654	0	0.14(4)
		4.028	0	0.07(2)
		4.333	0	0.11(3)
		4.584	0	0.03(1)

[a]From Refs. [Bor95, Sch00].
[b]From Ref. [Fuj05a]
[c]The IAS with $T = 1$.

Table B.3: States observed in the $^{50}\mathrm{Cr}(^3\mathrm{He}, t)^{50}\mathrm{Mn}$ reaction below $E_x = 4.6$ MeV. For the $L = 0$ states, B(GT) values are given.

Evaluated values [a]		^{54}Fe(^{3}He, t)^{54}Co [b]		
E_x (MeV)	J^π	E_x (MeV)	L	B(GT)
0.0	$0^{+,c}$	0.0	0	
0.9372	1^+	0.938	0	0.493(62)
1.4465	2^+	1.446	≥ 1	
1.8224	3^+	1.823	≥ 1	
		2.292	≥ 1	
		2.426	0	0.016(3)
		3.155	≥ 1	
		3.375	0	0.079(11)
		3.506	0	0.031(5)
		3.891	0	0.103(14)
		4.092	0	0.054(8)
		4.296	0	0.023(4)
		4.544	0	0.147(20)
		4.822	0	0.101(14)
		5.111	≥ 1	
		5.184	≥ 1	
		5.217	0	0.015(3)
		5.289	≥ 1	
		5.464	0	0.014(2)
		5.755	0	0.013(2)
		5.849	0	0.011(2)
		5.909	0	0.144(19)
		6.083	0	0.048(7)
		6.118	0	0.025(4)
		6.362	0	0.025(4)
		6.466	0	0.018(3)
		6.530	0	0.078(10)
		6.792	0	0.041(6)
		6.859	0	0.038(5)
		7.135	0	0.056(8)
		7.388	0	0.035(5)
		7.449	0	0.047(6)
		7.469	0	0.017(2)
		7.542	0	0.025(4)
		7.642	0	0.022(3)
		7.711	0	0.051(7)
		7.858	0	0.018(3)
		7.943	0	0.151(19)

[a] From Ref. [HJQ93].
[b] From Refs. [Ada07a, Ada10]
[c] The IAS with $T = 1$.

Table B.4: States observed in the ^{54}Fe(^{3}He, t)^{54}Co reaction for $E_x \leq 8$ MeV. For the identified $L = 0$ states, GT transition strengths B(GT) are given.

APPENDIX C

APPENDIX A: ADDBACK ROUTINE

When a β-decay occurred in a DSSSD the subsequent γ-decay (if occurred) can also be detected by the RISING Ge array. This γ-ray can deposit its energy in several interactions inside a Ge crystal. If the γ-energy is high enough those interactions can even happen in different crystals and then the energy of a single γ-event is registered in more than one of the 105 crystals of the array. This means we are "losing" efficiency of detection of the single gamma event depending on the energy of the gamma.
To recover the lost efficiency one can think of using the RISING array as a 15 cluster array (with 7 crystals each) simply by adding the energies registered by the 7 crystals. The problem with this method is that we increase unnecessarily the summing probablilty of two simultaneous γ-events which correspond to a single β-event (i.e for the ^{54}Ni case: 937 keV + 511 keV + 511 keV = 1959 keV).
To avoid the summing and the efficiency loss we implemented an 'addback' routine which sums 'simultaneous' γ-events (within a time window of 100 ns after the first detected gamma) from a single β-event *only* if they occurred in *adjacent crystals* of the same cluster.

C.1 Algorithm

The algorithm to adding-back γ-events starts with a loop over all the 15 clusters. For each cluster we construct an Adjacent Matrix A which defines which crystal is adjacent to which. For instance, if we define crystal number 6 at the centre of the cluster, it is adjacent to all the crystals. Then the matrix elements A_{i6} and A_{6j} have the value 1. Then the rest of the crystals will have a cyclic order of adjacency, i.e. crystals 0,1 and 2 are adjacent as well as crystals 5,0 and 1. In summary the element A_{ij} of the Adjacent Matrix A is equal to 1 if crystal i is adjacent to crystal j, and 0 if they are not.

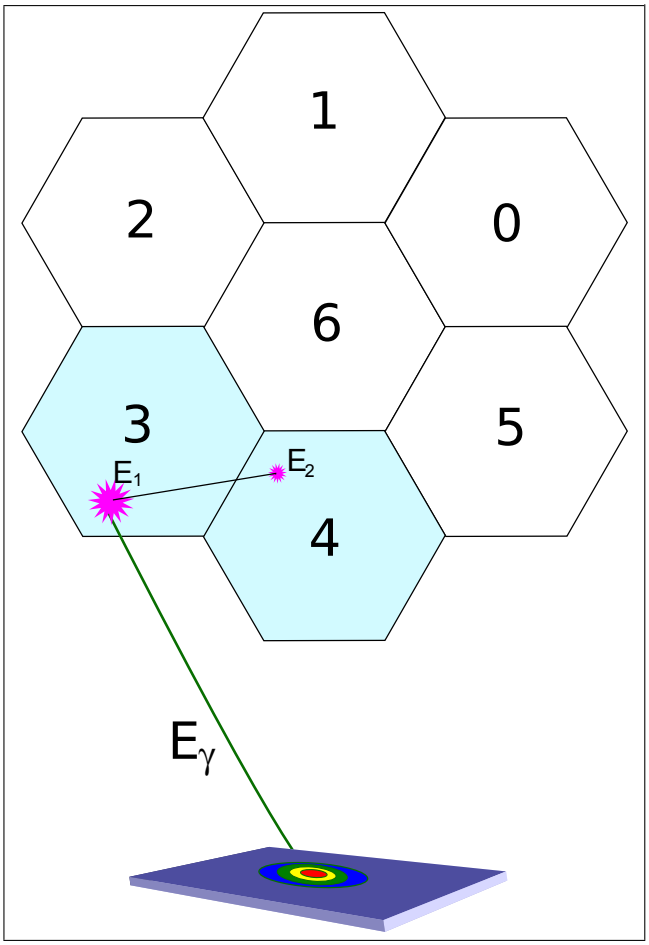

Figure C.1: Drawing of the interaction of a γ-ray with energy E_γ, with two germanium crystals, depositing part of its energy in both of them. $E_\gamma = E_1 + E_2$

$$A = \begin{pmatrix} 1 & 1 & 0 & 0 & 0 & 1 & 1 \\ 1 & 1 & 1 & 0 & 0 & 0 & 1 \\ 0 & 1 & 1 & 1 & 0 & 0 & 1 \\ 0 & 0 & 1 & 1 & 1 & 0 & 1 \\ 0 & 0 & 0 & 1 & 1 & 1 & 1 \\ 1 & 0 & 0 & 0 & 1 & 1 & 1 \\ 1 & 1 & 1 & 1 & 1 & 1 & 1 \end{pmatrix} \tag{C.1}$$

Once the matrix is properly defined according to the real positions of the crystals in a cluster, the value of the calibrated energy for each crystal is read. If the energy is not in the range of (60 keV, 11000 keV), the corresponding A_{ij} value is set to 0. For instance if the energies of crystals 0 and 4 are out of the range, the matrix is

$$A = \begin{pmatrix} 0 & 0 & 0 & 0 & 0 & 0 & 0 \\ 0 & 1 & 1 & 0 & 0 & 0 & 1 \\ 0 & 1 & 1 & 1 & 0 & 0 & 1 \\ 0 & 0 & 1 & 1 & 0 & 0 & 1 \\ 0 & 0 & 0 & 0 & 0 & 0 & 0 \\ 0 & 0 & 0 & 0 & 0 & 1 & 1 \\ 0 & 1 & 1 & 1 & 0 & 1 & 1 \end{pmatrix} \tag{C.2}$$

Now the A matrix also has the information on which crystals can be added. The second filter is the time window of 100 ns between two or more gamma-events which are considered as add-back candidates. In the previous example we can give some numbers for a better understanding of the code.

	Cal. γ-energy	DGF time
Crystal 0	0	0
Crystal 1	1460.2 keV	135 ns
Crystal 2	201.7 keV	251 ns
Crystal 3	535.4 keV	299 ns
Crystal 4	0	0
Crystal 5	235.1 keV	10 ns
Crystal 6	276.0 keV	29 ns

Table C.1: Example of Add-Back procedure

Starting with crystal 6 (because is the central crytal which has more adjacent crystals than others), inside the time window of 100 ns we only have crystal 5, then we add-back both energies (235.1 +276.0 = 511.1 keV) and the sum result is included as an element of the GammaAddback vector. Now the elements A_{i6}, A_{6j}, A_{i5} and A_{5j} are set to 0. The Adjacent Matrix A is now,

$$A = \begin{pmatrix} 0 & 0 & 0 & 0 & 0 & 0 & 0 \\ 0 & 1 & 1 & 0 & 0 & 0 & 0 \\ 0 & 1 & 1 & 1 & 0 & 0 & 0 \\ 0 & 0 & 1 & 1 & 0 & 0 & 0 \\ 0 & 0 & 0 & 0 & 0 & 0 & 0 \\ 0 & 0 & 0 & 0 & 0 & 0 & 0 \\ 0 & 0 & 0 & 0 & 0 & 0 & 0 \end{pmatrix} \tag{C.3}$$

The addback procedure starts now with the highest crystal number available, in this example it is crystal 3. If crystal 3 and crystal 2 energies are inside a 100 ns time window, then both energies are added-back (201.7 + 535.4 = 936.9 keV) and again this value is stored as an element of the GammaAddback vector and the matrix elements A_{i3}, A_{3j}, A_{i2} and A_{2j} are set to 0.

$$A = \begin{pmatrix} 0 & 0 & 0 & 0 & 0 & 0 & 0 \\ 0 & 1 & 0 & 0 & 0 & 0 & 0 \\ 0 & 0 & 0 & 0 & 0 & 0 & 0 \\ 0 & 0 & 0 & 0 & 0 & 0 & 0 \\ 0 & 0 & 0 & 0 & 0 & 0 & 0 \\ 0 & 0 & 0 & 0 & 0 & 0 & 0 \\ 0 & 0 & 0 & 0 & 0 & 0 & 0 \end{pmatrix} \tag{C.4}$$

Finally crystal 1 energy cannot be added with the signal from any other crystal, so it is included as an element of the GammaAddback vector.With this example we can observe the advantage of using this addback routine: from an given event, we could extract three different energies occurring in a cluster: 936.9, 511.1, and 1460.2 keV which is a clear advantage in comparison with the 'Single crystal method' where, following the same example, we will obtain 5 different energies: 1460.2, 201.7,535.4, 235.1 and 276.0 keV, and 'Cluster Method' where we obtain roughly the sum of all energies: 2908.2 keV.

C.2 Addback code

```
for(int m=0;m<15;m++){//start 15 cluster loop
//******Addback*******

//Addback_permision is the A matrix.
int Addback_permision[7][7] = {
//1 means crystal i is adyacent with crystal j; 0 means crystal i is
//not adyacent with crystal j...
 { 1, 1, 0, 0, 0, 1, 1 },  // crystal 0
 { 1, 1, 1, 0, 0, 0, 1 },  // crystal 1
 { 0, 1, 1, 1, 0, 0, 1 },  // crystal 2
 { 0, 0, 1, 1, 1, 0, 1 },  // crystal 3
 { 0, 0, 0, 1, 1, 1, 1 },  // crystal 4
 { 1, 0, 0, 0, 1, 1, 1 },  // crystal 5
 { 1, 1, 1, 1, 1, 1, 1 }   // crystal 6 (at the center of the cluster)
};


for(int j=6;j>-1;j--){
 //start 7 crystals loop beggining for the central crystal.

 gamma_sum= 0;Ncrystal_addbacked=0;
//1.-Elimination of the adjacent crystals which have energies out
// of the following range (60 keV,11000 keV).

if(event.energy_xia_cal[m][j]>11000 || event.energy_xia_cal[m][j]<60){
for(int y=0;y<7;y++){
Addback_permision[j][y]=0; Addback_permision[y][j]=0;
```

```
}}
DGFtime = event.ger_xia_dgf[m][j][0]*0.25+100;
//2.- Add-backing the adjacent crystals which have energies
//in the time range.

if(event.energy_xia_cal[m][j]<11000 && event.energy_xia_cal[m][j]>60 &&
DGFtime<DGFmax && DGFtime>DGFmin){

if(Addback_permision[j][j]!=0)gamma_sum=event.energy_xia_cal[m][j];

for(int y=6;y>-1;y--){
if(Addback_permision[j][y]==1 && j!=y){
DGFtime_adyacent=event.ger_xia_dgf[m][y][0]*0.25+100;

if(TMath::Abs(DGFtime-DGFtime_adyacent)<DGFAddback_time_gate){
gamma_sum= gamma_sum + event.energy_xia_cal[m][y]; //Addback here!!!
//making the corresponding element zero in the
//Addback_permision matrix to avoid double addback counting.
for(int w=0;w<7;w++){
Addback_permision[y][w]=0;
Addback_permision[w][y]=0;
Addback_permision[y][y]=0;}
Ncrystal_addbacked++;
//just to have a statistic about the number of crystals add-backed per cluster
}}}

if(gamma_sum !=0)GammaAddback.push_back(gamma_sum);//
GammaNoAddback.push_back(event.energy_xia_cal[m][j]);
GammaNoAddback_DGFtime.push_back(DGFtime);
}
}//end of crystal loop

}//end of cluster loop
```

APPENDIX D

APPENDIX B: RISING GE ARRAY EFFICIENCY

As explained in Section 4.3.3 -p.67- the efficiency curve was fitted to the experimental and simulated values according to Z.Hu et al. [Hu98].

$$\epsilon(E_\gamma) = \prod_{k=0}^{5} \exp(p_k \ln^k(E_\gamma)) \tag{D.1}$$

The six parameters were obtained for results with and without addback (see Fig.D.1). The result of the evaluation of the Z.Hu [Hu98] curve for energies each 100 keV intervals is given in Tables D.7 and D.8.

Table D.1: ^{133}Ba Single Crystal mode gamma rays

Energy[keV]	FWHM[keV]	Num.Counts
80.8 (0.1)	2.8 (0.1)	61693.0 (294.3)
276.2 (0.1)	2.9 (0.1)	9953.5 (136.9)
302.6 (0.1)	2.9 (0.1)	23501.4 (176.1)
355.7 (0.1)	2.9 (0.1)	72689.5 (279.5)
383.6 (0.1)	2.9 (0.1)	10055.0 (116.4)
661.6 (0.1)	3.0 (0.1)	14767.4 (127.3)
1173.1 (0.1)	3.3 (0.1)	3747.4 (66.4)
1332.4 (0.1)	3.4 (0.1)	3484.2 (61.9)

Table D.2: ^{152}Eu Single Crystal mode gamma rays

Energy[keV]	FWHM[keV]	Num.Counts
121.6 (0.1)	2.7 (0.1)	695273.7(926.1)
244.5 (0.1)	2.8 (0.1)	151912.1(493.0)
344.0 (0.1)	2.9 (0.1)	438255.4(703.4)
410.8 (0.1)	2.9 (0.1)	32535.9(261.0)
443.7 (0.1)	2.9 (0.1)	43454.4(275.8)
778.8 (0.1)	3.1 (0.1)	125895.1(391.1)
867.2 (0.1)	3.1 (0.1)	38681.8(252.0)
963.9 (0.1)	3.2 (0.1)	125696.1(378.0)
1112.0 (0.1)	3.4 (0.1)	108566.9(351.2)
1407.9 (0.1)	3.5 (0.1)	141732.7(380.4)

Table D.3: ^{226}Ra Single Crystal mode gamma rays

Energy[keV]	FWHM[keV]	Num.Counts
186.0 (0.1)	2.8 (0.1)	35773.5 (363.3)
241.8 (0.1)	2.8 (0.1)	63916.7 (360.1)
295.0 (0.1)	2.9 (0.1)	146868.9 (444.2)
351.6 (0.1)	2.9 (0.1)	257206.0 (545.0)
609.1 (0.1)	3.0 (0.1)	229828.1 (494.4)
768.2 (0.1)	3.1 (0.1)	21582.4 (175.5)
933.9 (0.1)	3.2 (0.1)	12350.1 (144.2)
1120.1 (0.1)	3.3 (0.1)	51616.6 (242.7)
1237.9 (0.1)	3.3 (0.1)	19301.8 (157.1)
1377.6 (0.1)	3.1 (0.1)	10937.5 (128.6)
1729.6 (0.1)	3.7 (0.1)	7408.9 (97.0)
1764.5 (0.1)	3.8 (0.1)	39742.3 (205.3)
2118.5 (0.1)	3.9 (0.1)	2573.1 (57.5)
2204.0 (0.1)	4.2 (0.1)	10552.0 (107.1)
2447.6 (0.1)	4.5 (0.1)	3089.7 (57.2)

Table D.4: ^{133}Ba Addback mode

Energy[keV]	FWHM[keV]	Num.Counts
80.8 (0.1)	2.8 (0.1)	60149.9 (285.0)
276.2 (0.1)	3.0 (0.1)	10692.2 (137.3)
302.7 (0.1)	3.0 (0.1)	25855.9 (183.0)
355.8 (0.1)	3.1 (0.1)	82865.1 (299.3)
383.7 (0.1)	3.1 (0.1)	11786.8 (123.8)
661.7 (0.1)	3.4 (0.1)	19022.1 (145.1)
1173.3 (0.1)	3.7 (0.1)	5054.7 (80.4)
1332.6 (0.1)	3.8 (0.1)	4703.7 (73.0)

Table D.5: ^{152}Eu Addback mode

Energy[keV]	FWHM[keV]	Num.Counts
121.7 (0.1)	2.8 (0.1)	718773.6 (840.6)
244.6 (0.1)	3.0 (0.1)	172079.9 (462.4)
344.1 (0.1)	3.1 (0.1)	519317.6 (695.0)
411.0 (0.1)	3.1 (0.1)	38946.4 (255.4)
443.8 (0.1)	3.2 (0.1)	53160.6 (274.4)
778.9 (0.1)	3.5 (0.1)	170387.9 (415.2)
867.4 (0.1)	3.5 (0.1)	52436.6 (270.1)
964.1 (0.1)	3.6 (0.1)	174841.0 (412.2)
1112.1 (0.1)	3.8 (0.1)	152601.0 (386.4)
1408.2 (0.1)	4.0 (0.1)	206280.1 (425.6)

Table D.6: ^{226}Ra Addback mode

Energy[keV]	FWHM[keV]	Num.Counts
186.0 (0.1)	2.9 (0.1)	40340.5 (323.7)
241.8 (0.1)	2.9 (0.1)	75205.6 (338.0)
295.1 (0.1)	3.0 (0.1)	180791.9 (443.3)
351.7 (0.1)	3.1 (0.1)	328486.2 (562.7)
609.3 (0.1)	3.4 (0.1)	318917.7 (540.6)
768.3 (0.1)	3.5 (0.1)	31103.4 (193.1)
934.1 (0.1)	3.5 (0.1)	17680.3 (157.9)
1120.3 (0.1)	3.7 (0.1)	77704.9 (276.5)
1238.1 (0.1)	3.7 (0.1)	28964.9 (178.2)
1377.7 (0.1)	3.5 (0.1)	17008.1 (149.4)
1729.8 (0.1)	4.3 (0.1)	12920.4 (123.9)
1764.7 (0.1)	4.3 (0.1)	64053.8 (243.5)
2118.6 (0.1)	4.6 (0.1)	4567.3 (74.3)
2204.3 (0.1)	4.7 (0.1)	17517.5 (130.7)
2447.9 (0.1)	4.9 (0.1)	5149.4 (80.2)

Energy [keV]	Addback Efficiency	No Addback Efficiency	% Difference
100	0.309338	0.307676	0.5
200	0.275535	0.255479	7.9
300	0.246052	0.214873	14.5
400	0.221214	0.185975	18.9
500	0.201037	0.164584	22.1
600	0.184653	0.148098	24.7
700	0.171204	0.134965	26.9
800	0.160012	0.124223	28.8
900	0.150566	0.115248	30.6
1000	0.142489	0.107617	32.4
1100	0.135497	0.101035	34.1
1200	0.129378	0.095287	35.8
1300	0.123969	0.090216	37.4
1400	0.119145	0.085701	39.0
1500	0.114806	0.081650	40.6
1600	0.110875	0.077991	42.2
1700	0.107288	0.074665	43.7
1800	0.103996	0.071625	45.2
1900	0.100957	0.068835	46.7
2000	0.098136	0.066262	48.1
2100	0.095505	0.063880	49.5
2200	0.093041	0.061666	50.9
2300	0.090724	0.059603	52.2
2400	0.088536	0.057675	53.5
2500	0.086464	0.055867	54.8
2600	0.084495	0.054168	56.0
2700	0.082618	0.052568	57.2
2800	0.080825	0.051058	58.3
2900	0.079108	0.049629	59.4
3000	0.077459	0.048275	60.5

Table D.7: List of Addback and Single Crystal efficiencies each 100[keV], from the evaluation of Z.Hu [Hu98] efficiency curve. First Part.

Energy [keV]	Addback Efficiency	No Addback Efficiency	% Difference
3100	0.075873	0.046990	61.5
3200	0.074344	0.045768	62.4
3300	0.072867	0.044605	63.4
3400	0.071439	0.043496	64.2
3500	0.070056	0.042436	65.1
3600	0.068714	0.041424	65.9
3700	0.067411	0.040454	66.6
3800	0.066144	0.039525	67.3
3900	0.064911	0.038634	68.0
4000	0.063710	0.037778	68.6
4100	0.062538	0.036956	69.2
4200	0.061395	0.036165	69.8
4300	0.060278	0.035403	70.3
4400	0.059187	0.034668	70.7
4500	0.058120	0.033960	71.1
4600	0.057075	0.033277	71.5
4700	0.056053	0.032617	71.9
4800	0.055052	0.031979	72.2
4900	0.054070	0.031362	72.4
5000	0.053108	0.030765	72.6
5100	0.052165	0.030187	72.8
5200	0.051240	0.029627	73.0
5300	0.050331	0.029084	73.1
5400	0.049440	0.028557	73.1
5500	0.048565	0.028046	73.2
5600	0.047706	0.027550	73.2
5700	0.046862	0.027068	73.1
5800	0.046032	0.026600	73.1
5900	0.045218	0.026144	73.0
6000	0.044417	0.025702	72.8

Table D.8: List of Addback and Single Crystal efficiencies each 100[keV], from the evaluation of Z.Hu [Hu98] efficiency curve. Second Part.

En.[keV]	219.4mm	229.4mm	239.4mm	249.4mm	(1-2)%	(2-3)%	(3-4)%
100	0.388	0.358	0.333	0.302	8.4	7.5	10.4
200	0.357	0.329	0.306	0.283	8.4	7.8	7.9
300	0.310	0.286	0.264	0.246	8.3	8.3	7.3
400	0.276	0.254	0.235	0.219	8.3	8.4	7.1
500	0.251	0.232	0.214	0.200	8.3	8.3	7.1
600	0.232	0.214	0.198	0.185	8.3	8.2	7.1
700	0.216	0.200	0.185	0.173	8.3	8.1	7.1
800	0.204	0.188	0.174	0.163	8.3	7.9	7.1
900	0.193	0.178	0.165	0.154	8.3	7.8	7.2
1000	0.183	0.169	0.157	0.147	8.3	7.7	7.2
1100	0.175	0.162	0.150	0.140	8.3	7.6	7.2
1200	0.168	0.155	0.144	0.134	8.2	7.6	7.2
1300	0.161	0.149	0.138	0.129	8.2	7.5	7.2
1400	0.155	0.143	0.133	0.124	8.2	7.5	7.2
1500	0.149	0.138	0.128	0.120	8.2	7.5	7.2
1600	0.144	0.133	0.124	0.116	8.2	7.5	7.2
1700	0.139	0.129	0.120	0.112	8.1	7.5	7.2
1800	0.135	0.125	0.116	0.108	8.1	7.5	7.1
1900	0.131	0.121	0.112	0.105	8.1	7.6	7.1
2000	0.127	0.117	0.109	0.102	8.1	7.6	7.1
2100	0.123	0.114	0.106	0.099	8.1	7.6	7.1
2200	0.120	0.111	0.103	0.096	8.0	7.7	7.0
2300	0.116	0.108	0.100	0.093	8.0	7.7	7.0
2400	0.113	0.105	0.097	0.091	8.0	7.8	7.0
2500	0.110	0.102	0.095	0.089	8.0	7.8	7.0
2600	0.107	0.100	0.092	0.086	8.0	7.9	6.9
2700	0.105	0.097	0.090	0.084	7.9	8.0	6.9
2800	0.102	0.095	0.088	0.082	7.9	8.0	6.9
2900	0.100	0.093	0.086	0.080	7.9	8.1	6.8
3000	0.098	0.091	0.084	0.078	7.9	8.1	6.8

Table D.9: Evaluation of the efficiency curve for the addback simulation for different radii of the RISING array. Columns 2-5 shows the efficiency value for the different simulated radii. Columns 6-8 shows the percentage difference between two simulated radii with 1cm difference. First Part

En.[keV]	219.4mm	229.4mm	239.4mm	249.4mm	(1-2)%	(2-3)%	(3-4)%
3100	0.095	0.089	0.082	0.077	7.9	8.2	6.7
3200	0.093	0.087	0.080	0.075	7.8	8.3	6.7
3300	0.091	0.085	0.078	0.073	7.8	8.3	6.7
3400	0.089	0.083	0.077	0.072	7.8	8.4	6.6
3500	0.088	0.081	0.075	0.070	7.8	8.4	6.6
3600	0.086	0.080	0.073	0.069	7.8	8.5	6.6
3700	0.084	0.078	0.072	0.068	7.7	8.5	6.5
3800	0.083	0.077	0.071	0.066	7.7	8.6	6.5
3900	0.081	0.075	0.069	0.065	7.7	8.6	6.4
4000	0.079	0.074	0.068	0.064	7.7	8.7	6.4
4100	0.078	0.072	0.067	0.063	7.7	8.7	6.3
4200	0.077	0.071	0.065	0.062	7.7	8.7	6.3
4300	0.075	0.070	0.064	0.060	7.6	8.8	6.3
4400	0.074	0.069	0.063	0.059	7.6	8.8	6.2
4500	0.073	0.068	0.062	0.058	7.6	8.8	6.2
4600	0.071	0.066	0.061	0.057	7.6	8.9	6.1
4700	0.070	0.065	0.060	0.057	7.6	8.9	6.1
4800	0.069	0.064	0.059	0.056	7.5	8.9	6.1
4900	0.068	0.063	0.058	0.055	7.5	8.9	6.0
5000	0.067	0.062	0.057	0.054	7.5	8.9	6.0
5100	0.066	0.061	0.056	0.053	7.5	9.0	5.9
5200	0.065	0.060	0.055	0.052	7.5	9.0	5.9
5300	0.064	0.060	0.055	0.052	7.4	9.0	5.8
5400	0.063	0.059	0.054	0.051	7.4	9.0	5.8
5500	0.062	0.058	0.053	0.050	7.4	9.0	5.8
5600	0.061	0.057	0.052	0.050	7.4	9.0	5.7
5700	0.060	0.056	0.052	0.049	7.4	9.0	5.7
5800	0.060	0.056	0.051	0.048	7.4	9.0	5.6
5900	0.059	0.055	0.050	0.048	7.3	9.0	5.6

Table D.10: Evaluation of the efficiency curve for the addback simulation for different radii of the RISING array. Columns 2-5 show the efficiency value for the different simulated radii. Columns 6-8 shows the percentage difference between two simulated radii with 1cm difference. Second Part.

En.[keV]	219.4mm	229.4mm	239.4mm	249.4mm	(1-2)%	(2-3)%	(3-4)%
100	0.406	0.355	0.332	0.300	14.4	6.9	10.5
200	0.330	0.307	0.285	0.264	7.5	7.9	7.8
300	0.268	0.248	0.230	0.214	8.0	8.1	7.3
400	0.228	0.210	0.194	0.181	8.7	8.1	7.2
500	0.201	0.184	0.170	0.159	9.2	8.1	7.2
600	0.181	0.165	0.153	0.142	9.4	8.0	7.3
700	0.165	0.151	0.140	0.130	9.5	7.9	7.3
800	0.153	0.140	0.129	0.121	9.4	7.9	7.3
900	0.142	0.130	0.121	0.113	9.2	7.8	7.3
1000	0.134	0.122	0.114	0.106	9.0	7.7	7.3
1100	0.126	0.116	0.107	0.100	8.8	7.7	7.3
1200	0.119	0.110	0.102	0.095	8.6	7.6	7.3
1300	0.113	0.105	0.097	0.091	8.3	7.6	7.3
1400	0.108	0.100	0.093	0.087	8.1	7.6	7.3
1500	0.103	0.096	0.089	0.083	7.9	7.5	7.3
1600	0.099	0.092	0.085	0.080	7.7	7.5	7.3
1700	0.095	0.088	0.082	0.077	7.5	7.5	7.2
1800	0.091	0.085	0.079	0.074	7.3	7.5	7.2
1900	0.088	0.082	0.076	0.071	7.2	7.5	7.2
2000	0.085	0.079	0.073	0.069	7.0	7.5	7.2
2100	0.082	0.076	0.071	0.066	6.9	7.5	7.1
2200	0.079	0.074	0.069	0.064	6.8	7.5	7.1
2300	0.076	0.071	0.066	0.062	6.8	7.5	7.1
2400	0.074	0.069	0.064	0.060	6.7	7.6	7.1
2500	0.072	0.067	0.062	0.058	6.7	7.6	7.0
2600	0.069	0.065	0.060	0.056	6.7	7.6	7.0
2700	0.067	0.063	0.059	0.055	6.7	7.6	7.0
2800	0.065	0.061	0.057	0.053	6.7	7.7	7.0
2900	0.064	0.060	0.055	0.052	6.7	7.7	6.9
3000	0.062	0.058	0.054	0.050	6.8	7.7	6.9

Table D.11: Evaluation of the efficiency curve for the single crystal simulation for different radii of the RISING array. Columns 2-5 shows the efficiency value for the different simulated radii. Columns 6-8 shows the percentage difference between two simulated radii with 1cm difference. First Part.

En.[keV]	219.4mm	229.4mm	239.4mm	249.4mm	(1-2)%	(2-3)%	(3-4)%
3100	0.060	0.056	0.052	0.049	6.9	7.8	6.9
3200	0.059	0.055	0.051	0.048	6.9	7.8	6.9
3300	0.057	0.053	0.049	0.046	7.0	7.8	6.9
3400	0.056	0.052	0.048	0.045	7.1	7.9	6.9
3500	0.054	0.051	0.047	0.044	7.3	7.9	6.8
3600	0.053	0.049	0.046	0.043	7.4	8.0	6.8
3700	0.052	0.048	0.045	0.042	7.5	8.0	6.8
3800	0.050	0.047	0.043	0.041	7.7	8.0	6.8
3900	0.049	0.046	0.042	0.040	7.9	8.1	6.8
4000	0.048	0.045	0.041	0.039	8.0	8.1	6.8
4100	0.047	0.044	0.040	0.038	8.2	8.2	6.8
4200	0.046	0.043	0.039	0.037	8.4	8.2	6.8
4300	0.045	0.042	0.038	0.036	8.6	8.3	6.8
4400	0.044	0.041	0.038	0.035	8.8	8.3	6.8
4500	0.043	0.040	0.037	0.034	9.1	8.4	6.8
4600	0.042	0.039	0.036	0.034	9.3	8.5	6.8
4700	0.042	0.038	0.035	0.033	9.6	8.5	6.8
4800	0.041	0.037	0.034	0.032	9.8	8.6	6.8
4900	0.040	0.036	0.033	0.031	10.1	8.6	6.8
5000	0.039	0.036	0.033	0.031	10.3	8.7	6.8
5100	0.039	0.035	0.032	0.030	10.6	8.7	6.8
5200	0.038	0.034	0.031	0.029	10.9	8.8	6.8
5300	0.037	0.033	0.031	0.029	11.2	8.9	6.8
5400	0.036	0.033	0.030	0.028	11.5	8.9	6.8
5500	0.036	0.032	0.029	0.028	11.8	9.0	6.8
5600	0.035	0.031	0.029	0.027	12.1	9.0	6.8
5700	0.035	0.031	0.028	0.026	12.4	9.1	6.8
5800	0.034	0.030	0.028	0.026	12.8	9.2	6.8
5900	0.033	0.030	0.027	0.025	13.1	9.2	6.8

Table D.12: Evaluation of the efficiency curve for the single crystal simulation for different radii of the RISING array. Columns 2-5 shows the efficiency value for the different simulated radii. Columns 6-8 shows the percentage difference between two simulated radii with 1cm difference. Second Part.

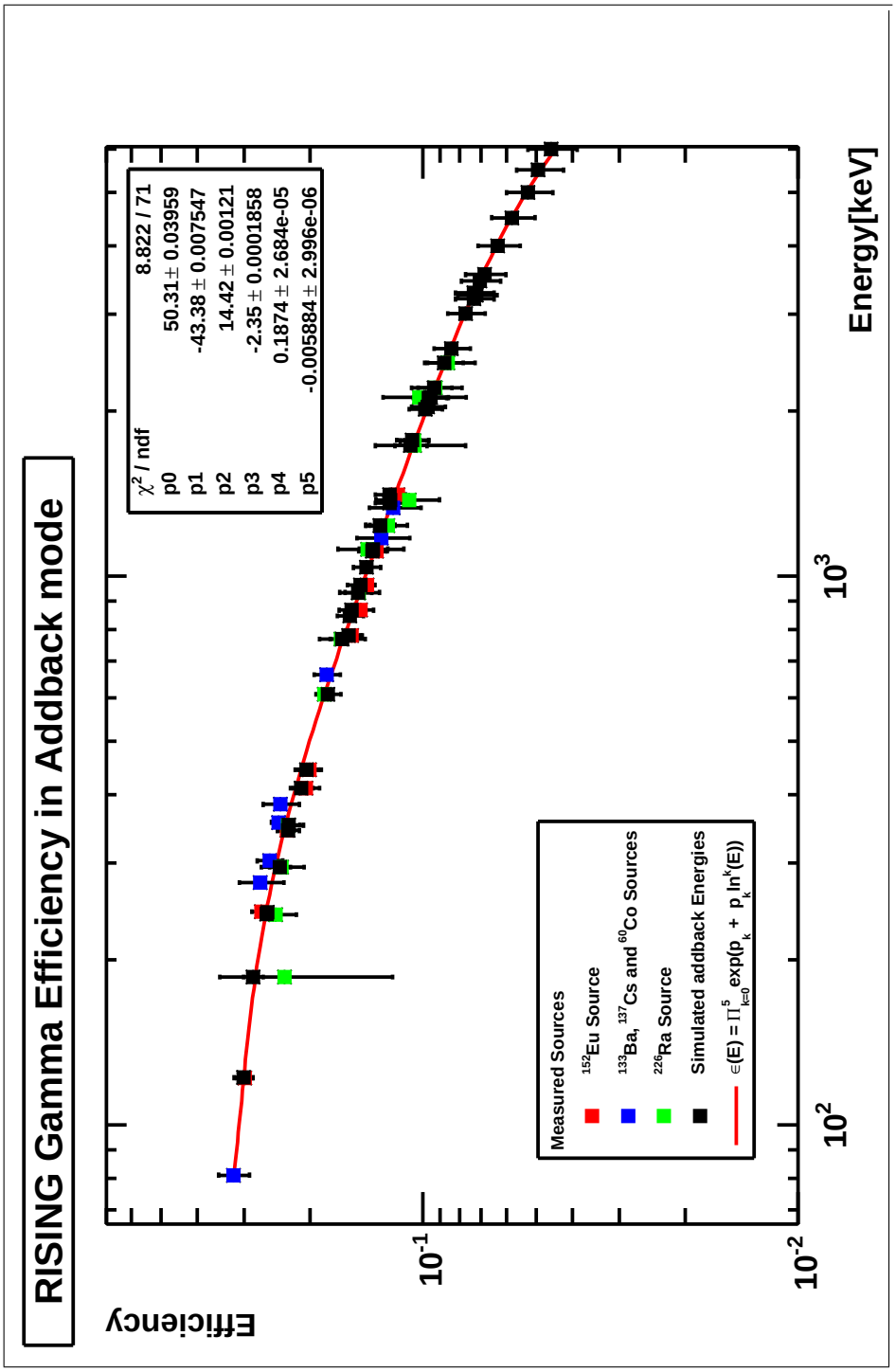

Figure D.1: RISING efficiency curve using the Addback routine

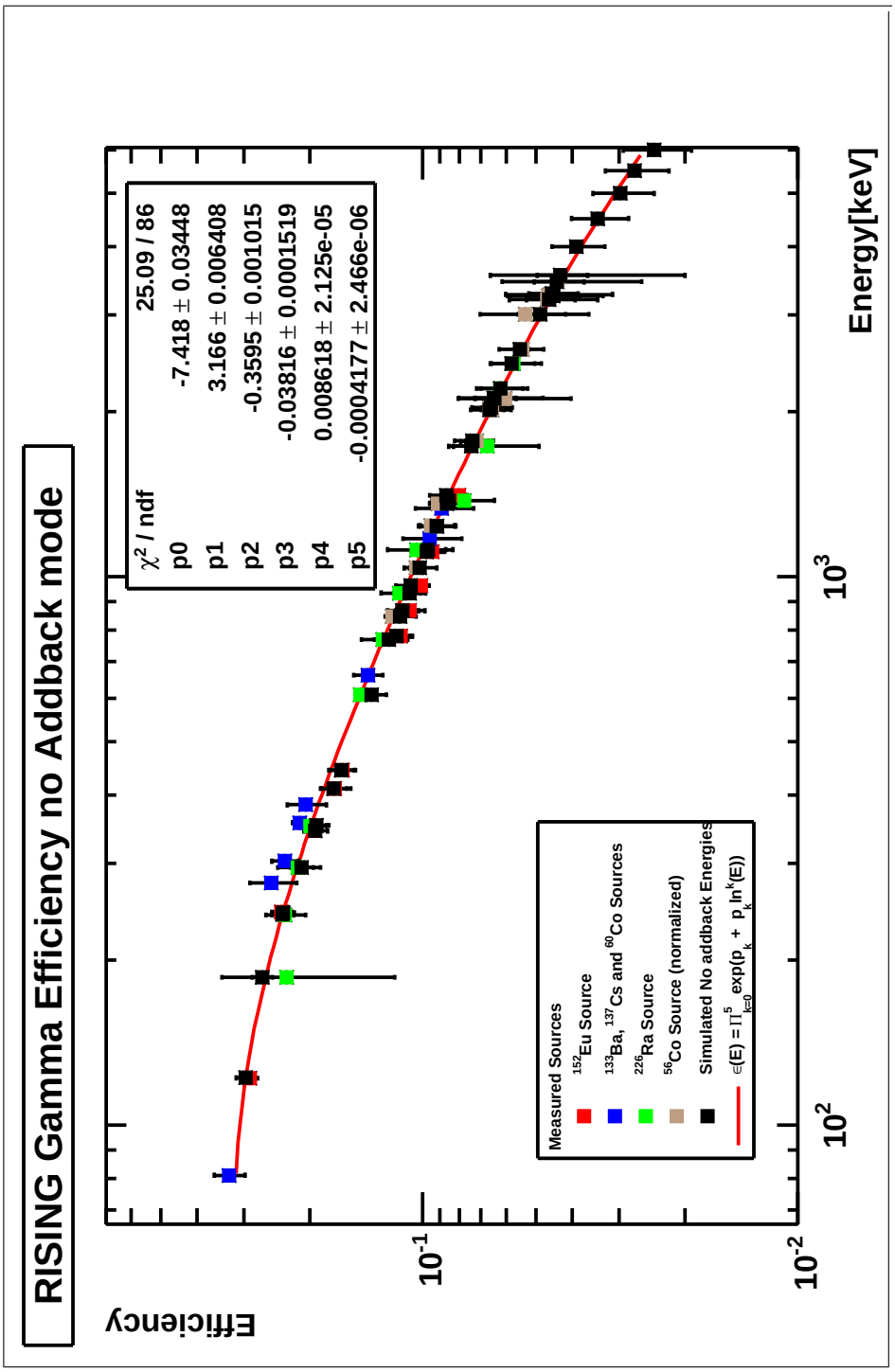

Figure D.2: Efficiency curve using the sum of single crystals

APPENDIX E

APPENDIX C: SIMULATION OF THE BACKGROUND OF WRONG CORRELATIONS

One important result of our experiments was to understand the shape of the wrongly correlated β-Implantation events in the ABAI correlations.
This sinusoidal like shape came as a surprise at the beginsing and we wondered if we were analysing the data correctly. The only way to clarify that was simulate the experiment.

E.1 Simulation uniformly-distributed random implantations

We simulated, using ROOT the classes TTimeStamp and TRandom, randomly uniform distributed implantation events in a spill period (13 sec distributed in 10 sec synchrotron ON and 3 sec OFF). Secondly, when an implantation-simulated-event is created, another beta-simulated-event is created following an exponential distribution $\exp(-\lambda t)$ with $\lambda = \frac{\ln(2)}{114.1}$. The event global time was retrieved from the real simulation time, with a possible maximum precision of ns, using the ROOT class TTimeStamp. The implantation and decay time are stored in different vectors. Then time differences between a decay and all the past and future implantations in a time window of $\pm$ 50 s are shown in Figure E.2 (10 min of simulation) and Figure E.2 (1 h of simulation). From these figures it is possible to see the correlation dependence of the spill period, since: 1) the background peaks correspond to the total spill period of 13 s, and 2) the 'rise-time' of the background peak is 3 s which corresponds to the synchrotron OFF time in a spill period.
Now if we simulate implantation events uniformly distributed in the complete spill period of 13 sec, see Figure E.3 (10 min of simulation) we can observe that the correlation spill period dependence disappears. Instead, we obtain a background with a slope which is related to the probability of correlation of a beta with an implantation occurring in the time window of correlation t_w after/before in comparison with the time of measurement t_m. In this case t_m=10 min and t_w=$\pm$50 s. If $t_m \rightarrow \infty$ then the slope might be

completely flat. See Figure E.4.

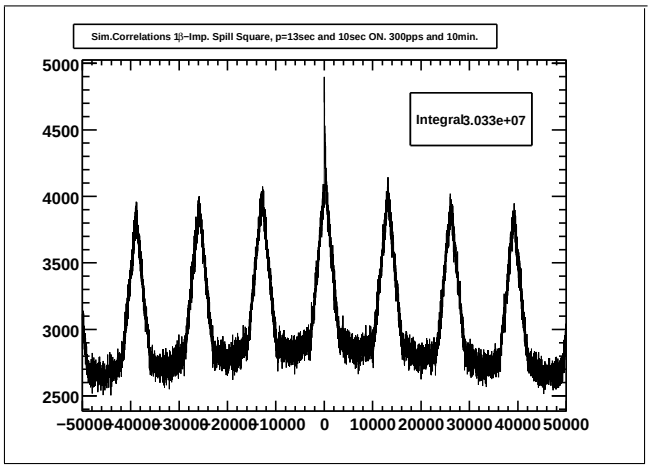

Figure E.1: ABAI correlations using simulated implantation and beta events in a ±50s time window. The implantations were obtained using a uniform random distribution in the first 10 s of the spill period of 13 s. The beta-events were simulated using an exponential distribution with $T_{1/2}$= 114.1 ms (experimental ^{54}Ni half-life). We simulated 300 implantations per spill and the total simulation time was 10 min.

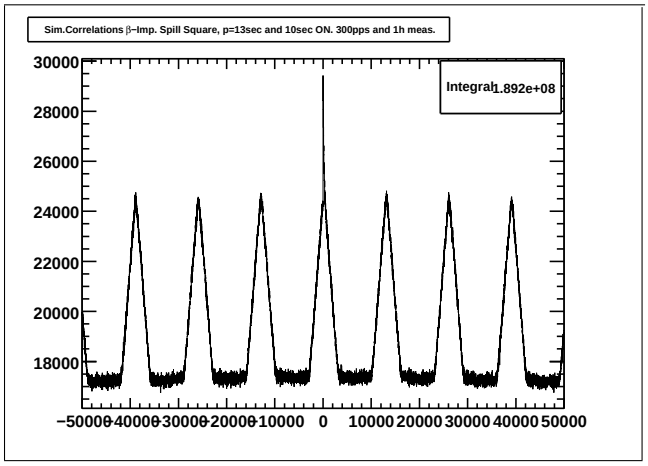

Figure E.2: ABAI correlations using simulated implantation and beta events in a ±50s time window. The implantations were obtained using a uniform random distribution in the first 10 s of the spill period of 13 s.The beta-events were simulated using an exponential distribution with $T_{1/2}$= 114.1 ms (experimental ^{54}Ni half-life). We simulated 300 implantations per spill and the total simulation time was 1 h.

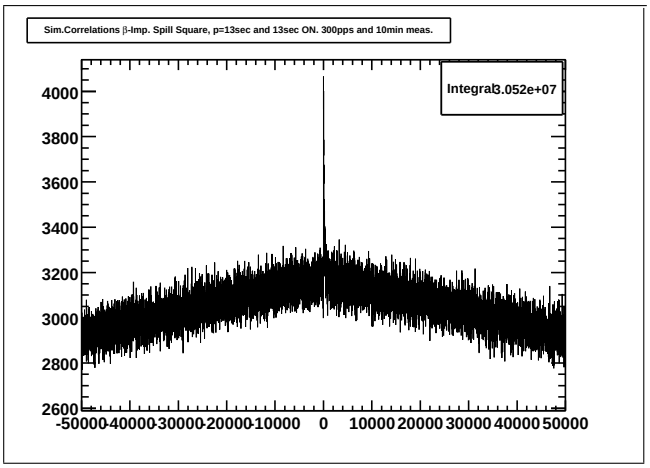

Figure E.3: ABAI correlations using simulated implantation and beta events in a ±50s time window. The implantations were obtained using a uniform random distribution in the complete spill period of 13 s. The beta-events were simulated using an exponential distribution with $T_{1/2}$= 114.1 ms (experimental ^{54}Ni half-life). We simulated 300 implantations per spill and the total simulation time was 10 min.

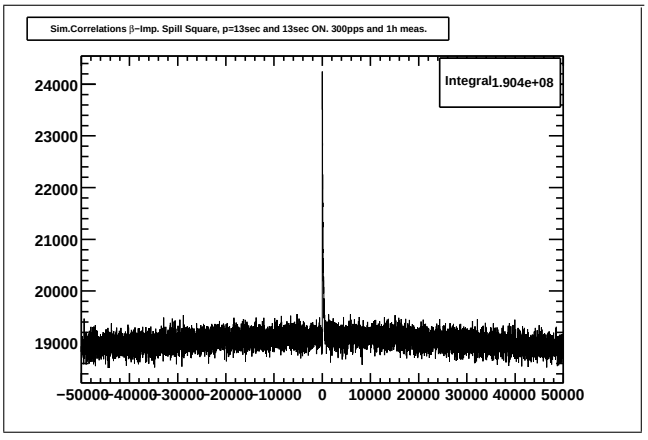

Figure E.4: ABAI correlations using simulated implantation and beta events in a ±50s time window. The implantations were obtained using a uniform random distribution in the complete spill period of 13 s. The beta-events were simulated using an exponential distribution with $T_{1/2}$= 114.1 ms (experimental ^{54}Ni half-life). We simulated 300 implantations per spill and the total simulation time was 1 h.

E.2 Simulation Gaussian-distributed random implantations

As shown in Section 5.2.3, the implantation events do not have an uniform distribution during a spill period. In order to perform an accurate simulation we assume a Gaussian distribution centred in the middle of the synchrotron ON time period, 5 sec, and with variance σ= 2sec.
In Figure E.5 and Figure E.6 we can see the simulation results for measurements of 10 min and 1h respectively. In Figure E.5 we can appreciate a smoothing of the background shape in comparison with Figure . This change in the shape is only related with the distribution function of the implantation events. Nevertheless, the period of the background is again the period of the spill.

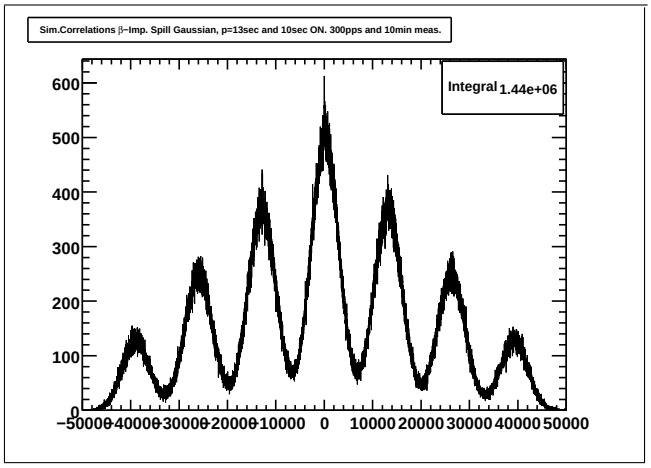

Figure E.5: ABAI correlations using simulated implantation and beta events in a ±50s time window. The implantations were obtained using a Gaussian random distribution in the first 10sec of the spill period. The beta-events were simulated using an exponential distribution with $T_{1/2}$= 114.1 ms (experimental ^{54}Ni half-life). We simulated 300 implantations per spill and the total simulation time was 10 min.

Figure E.6 shows a 1h simulation including wrong correlations created using a different random source for the implantation events, but with the same Gaussian distribution. Now the "rise-time" is half of the spill period, which is what we can observe in the real experiment when we perform correlations with no condition on the spill range. See Figure 5.28.

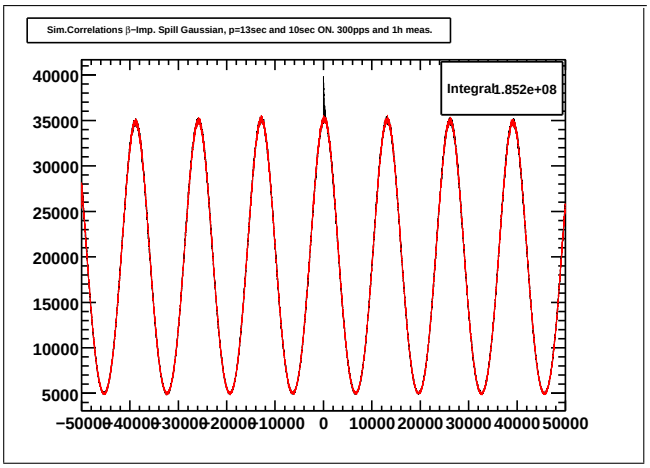

Figure E.6: ABAI correlations using simulated implantation and beta events in a ±50s time window. The implantations were obtained using a Gaussian random distribution in the first 10sec of the spill period. The beta-events were simulated using an exponential distribution with $T_{1/2}$= 114.1 ms (experimental ^{54}Ni half-life). We simulated 300 implantations per spill and the total simulation time was 1 h.

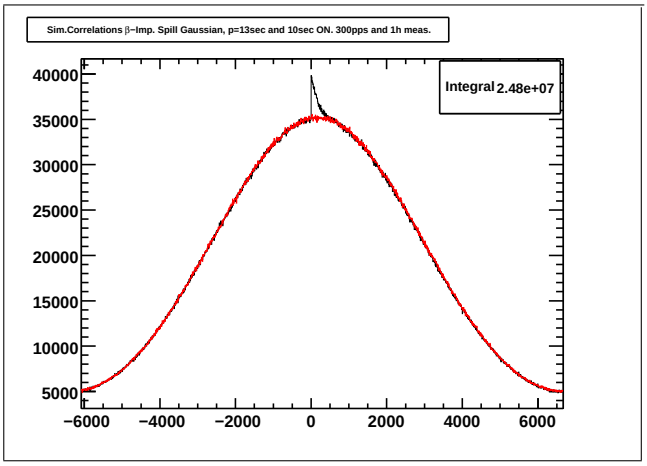

Figure E.7: Expansion of Figure E.6.

Finally, using a more realistic implantation rate of 20 implantation per spill period and a larger simulation time of 10 hours we can almost reproduce the shapes shown in a real experiment (see Fig E.8). Comparing simulations in Figs E.5 and E.8 we can see the difference in peak-to-background. The lower the rate of implantation the better peak-to-background value.

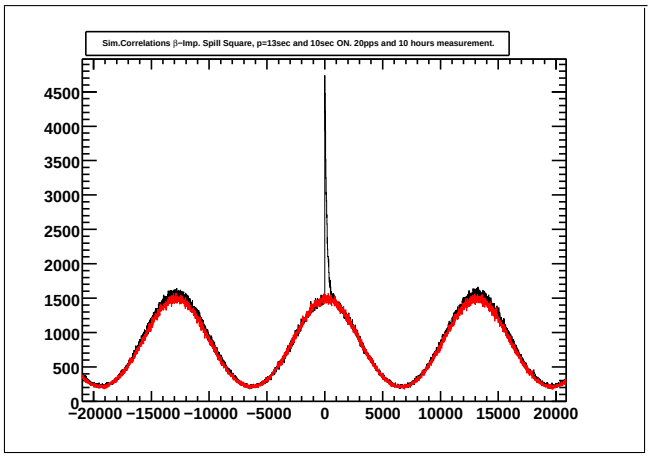

Figure E.8: ABAI correlations using simulated implantation and beta events in a ± 20s time window. The implantations were obtained using a Gaussian random distribution in the first 10sec of the spill period. The beta-events were simulated using an exponential distribution with $T_{1/2}$= 114.1 ms (experimental ^{54}Ni half-life). We simulated 20 implantations per spill and the total simulation time was 10 h.

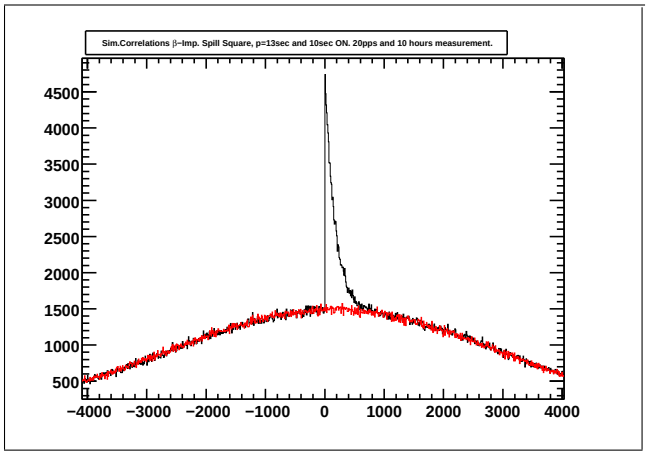

Figure E.9: Expansion of Figure E.8.

BIBLIOGRAPHY

[Ada06] T. Adachi. *Phys. Rev. C*, 73:024311, 2006.

[Ada07a] T. Adachi. PhD thesis, Osaka University, Departament of Physics, 2007.

[Ada07b] T. Adachi. *Nucl. Phys. A*, 788:70–75, 2007.

[Ada07c] T. Adachi. *Nucl. Phys. A*, 788:70c, 2007.

[Ada10] T. Adachi, 2010. Private communication.

[Aud03] G. Audi. *Nucl. Phys. A*, 729:337–676, 2003.

[Bec96] H. Becquerel. *Compt. Rend. Acad. Sc. Paris*, 122:501, 1896.

[Bet32] H. Bethe. *Z.Phys*, 76:293, 1932.

[Bla75] J.N. Black. *Phys. Rev. C*, 11:939–951, 1975.

[BM98] A. Bohr and B.R. Mottelson. *Nuclear Structure. Vol 1: Single Particle Motion*. World Scientific Publishing Co.Pte.Ltd. 2^{nd} Edtion, 1998.

[Bor95] T.W. Borrows. *Nucl. Data Sheets*, 75:1, 1995.

[Cac09] L. Caceres. *Phys. Rev. C*, 79:011301(R), 2009.

[Cha14] J. Chadwick. *Verhandl. Dtsch. phys. Ges*, 16:383, 1914.

[CM76] G. Coleman and R.A. Meyer. *Phys. Rev. C*, 13:847–858, 1976.

[dB97] P. Van den Berg. *Nucl. Inst. and Meth. B*, 126:194–197, 1997.

[Det07] P. Detistov. *Acta Physica Polonica B*, 38:1287–1292, 2007.

[Dos07] C. Dossat. *Nucl. Phys. A*, 792:18–86, 2007.

[DWI06] M.A. Bentley D.D. Warner and P. Van Isacker. *Nature Physics*, (2):311–318, 2006.

[Ebe92] J. Eberth. *Prog. Part. Nucl. Phys.*, 28:495–504, 1992.

[EW27] C.D. Ellis and W.A. Wooster. *Nature*, 119:563–564, 1927.

[Fuj01] Y. Fujita. *Nucl. Phys*, A687:311c–320c, 2001.

[Fuj03] Y. Fujita. *Phys.Rev. C*, 67:064312, 2003.

[Fuj05a] Y. Fujita. *Phys. Rev. Lett.*, 95:212501, 2005.

[Fuj05b] Y. Fujita. *Journal of Physics: Conference Series*, 20:107–112, 2005.

[Fuj06] Y. Fujita. *Journal of Physics: Conference Series*, 49:29–34, 2006.

[Fuj07a] H. Fujita. *Phys. Rev. C*, 75:034310, 2007.

[Fuj07b] Y. Fujita, 2007. Private communication.

[Fuj07c] Y. Fujita. *Phys. Rev. C*, 75:057305, 2007.

[Gal69] A. Gallmann. *Phys.Rev.*, 186:1160–1166, 1969.

[Gar08] A.B. Garnsworthy. *Physics Letters B*, 660:326–330, 2008.

[GdAW01] H. Grawe P. Regan P.Reiter G. de Angelis, J. Gerl and H.-J. Wollersheim. The rising project, letter of intent. `http://www-linux.gsi.de/~wolle/EB_at_GSI/RISING/rising.htm`, 2001.

[Gei92] H. Geissel. *Nucl. Inst. and Meth. B*, 70:286–297, 1992.

[GFN82] W.A. Fower G.M. Fuller and M.J. Newman. *The Astrophysical Journal*, 252:715–740, 1982.

[Goo80] C.D. Goodman. *Phys. Rev. Lett.*, 44:1755, 1980.

[Gre07] J. Grebosz. *Computer Physics Communications*, 176:251–265, 2007.

[Hag94] E. Hagberg. *Phys. Rev. Lett.*, 73:396–399, 1994.

[Hag97] E. Hagberg. *Nucl. Phys. A*, 613:183–198, 1997.

[HJQ93] Z. Weizhong H. Junde, S. Huibin and Z. Qing. *Nucl. Data Sheets*, 68:887, 1993.

[Hon89] J. Honkanen. *Nucl. Phys. A*, 496:462–476, 1989.

[HT06] J.C. Hardy and I.S. Towner. *Nucl. Phys. News*, 16:11, 2006.

[HT09] J.C. Hardy and I.S. Towner. *Phys. Rev. C*, 79:055502, 2009.

[Hu98] Z. Hu. *Nucl. Inst. and Meth. A*, 419:121–131, 1998.

[Iva07] O. Ivanov. PhD thesis, Katholieke Universiteit Leuven, 2007.

[Jac75] S.V. Jackson. *Phys. Rev. C*, 12:2094–2096, 1975.

[JH06] M. Richter J. Hoffman, N. Hurz. Titris, time stamp synchronizing system. `http://www.gsi.de/informationen/wti/ee/elekt_entwicklung/titris_e.html`, 2006.

[Jun07] A. Jungclaus. *Phys. Rev. Lett.*, 99:132501, 2007.

[Kos97] V.T. Koslowsky. *Nucl. Phys. A*, 624:293–298, 1997.

[Kra88] K.S. Krane. *Introductory Nuclear Physics.* John Wiley & Sons, INC. 2^{nd} Edition, 1988.

[Kud01] Y. Kudryavtsev. *Nucl. Inst. and Meth. B*, 179:412–435, 2001.

[Kum09] R. Kumar. *Nucl. Inst. and Meth. A*, 598:754, 2009.

[Kur09] T. Kurtukian. *Phys. Rev. C*, 80:035502, 2009.

[LLC] Xia LLC. Dgf-4c user's manual. `http://www.xia.com/DGF-4C_Download.html`.

[LMP00] K. Langanke and G. Martínez-Pinedo. *Nucl. Phys. A*, 673:481, 2000.

[LMP02] K. Langanke and G. Martínez-Pinedo. *Nucl. Phys. A*, 704:154c, 2002.

[LMP03] K. Langanke and G. Martínez-Pinedo. *Rev. Mod. Phys.*, 75:819, 2003.

[Loz08] R.L. Lozeva. *Phys. Rev. C*, 77:064313, 2008.

[ltd] MICRON Semiconductor ltd. Double sided silicon strip detector w1 datasheet. `http://www.micronsemiconductor.co.uk/pdf/w1.pdf`.

[M̈92] G. Münzenberg. *Nucl. Inst. and Meth. B*, 70:265–275, 1992.

[Man76] F.M. Mann. *Nucl. Phys. A*, 258:341–349, 1976.

[mGcKa] mesytec GmbH and co. KG. Logaritmic preamplifier datasheet. `http://www.mesytec.com/datasheets/MPR16_LOG.pdf`.

[mGcKb] mesytec GmbH and co. KG. Stm-16 datasheet v2.4. `http://www.mesytec.com/datasheets/STM-16.pdf`.

[Oni05] T.K. Onishi. *Phys. Rev. C*, 72:024308, 2005.

[Pau33] W. Pauli. *Rapports du Septieme Conseil de Physique Solvay. Brussels*, 1933.

[Pau09] D. Pauwels. PhD thesis, Katholieke Universiteit Leuven, 2009.

[Pie07a] S. Pietri. *Eur. Phys. J. Special Topics*, 150:319–320, 2007.

[Pie07b] S. Pietri. *Nucl. Inst. and Meth. B*, 261:1079–1083, 2007.

[Ram72] S. Raman. *Nucl. Phys. A*, 184:138–156, 1972.

[Reg07] P. Regan. *Nuclear Physics A*, 787:491c–498c, 2007.

[Reu99a] I. Reusen. PhD thesis, Katholieke Universiteit Leuven, 1999.

[Reu99b] I. Reusen. *Phys. Rev. C*, 59:2416–2421, 1999.

[Ric04] V. Ricciardi. PhD thesis, Universidad de Santiago de Compostella, 2004.

[RN67] R.R. Roy and B.P. Nigam. *Nuclear Physics: Theory and Experiment.* John Wiley & Sons, INC., 1967.

[roo] ftp://root.cern.ch/root/doc/12Trees.pdf.

[RR88] C.E. Rolfs and W.S. Rodney. *Cauldrons in the Cosmos.* The University of Chicago Press, 1988.

[RS94] J. Rapaport and E. Sugarbaker. *Annu. Rev. Nucl. Part. Sci.*, 44:1755, 1994.

[Rud08a] D. Rudolph. *Eur. Phys. J. A*, 36:131–138, 2008.

[Rud08b] D. Rudolph. *Phys. Rev. C*, 78:021301(R), 2008.

[Sch00] A. Schmidt. *Phys. Rev. C*, 62:044319, 2000.

[Sek87] T. Sekine. *Nucl. Phys. A*, 467:93–114, 1987.

[sis] `http://www.gsi.de/beschleuniger/sis18/sis_e.html`.

[S.p] CAEN S.p.A. Adc v785 documentation. `http://www.caen.it/nuclear/product.php?mod=V785`.

[SS00] R. Schneider and A. Stolz. Technical manual ionization chamber music80, 2000.

[Sta63] H.H. Heckman & P.W. Starring. *Nuclear Physics and the Fundamental Particles.* Holt, Rinehart and Winston, INC., 1963.

[Ste91] H. Stelzer. *Nucl. Inst. and Meth. A*, 310:103–106, 1991.

[Ste08] S.J. Steer. *Phys. Rev. C*, 78:061302(R), 2008.

[Tad87] T.N. Taddeucci. *Nucl. Phys. A*, 469:125–172, 1987.

[TH02] I.S. Towner and J.C. Hardy. *Phys. Rev. C*, 66:35501, 2002.

[unia] `http://www-inj.gsi.de/`.

[unib] `http://www.gsi.de/portrait/Broschueren/Wunderland/10_e.html`.

[Uoz94] Y. Uozumi. *Phys.Rev. C*, 52:263–274, 1994.

[Uzu94] J.L Uzureau. *Phys. Lett. B*, 331:280–284, 1994.

[WB74] D.H. Wilkinson and B.E.F.Macefield. *Nucl. Phys. A*, 232:58–92, 1974.

[Wil69] D.H. Wilkinson. *Isospin in Nuclear Physics.* SBN 7204 0155 0, 1969.

[Wil96] M. Wilhelm. *Nucl. Inst. and Meth. A*, 381:462–465, 1996.

[Wu00] S.C. Wu. *Nucl. Data Sheets*, 91:1, 2000.

[Yaf77] R. P. Yaffe. *Phys. Rev. C*, 16:1581–1589, 1977.

[YFG11] B. Rubio Y. Fujita and W. Gelletly. *Progress in Particle and Nucleus Physics, in print*, 2011.

[You70] D.H. Youngblood. *Phys.Rev. C*, 2:477–487, 1970.

[Zeg06] R.G.T. Zegers. *Phys.Rev. C*, 74:024309, 2006.

AGRADECIMIENTOS

Son muchísimas las personas a las cuales debo agradecer por estos increibles años en Valencia. Es imposible recordar a todos en estos agradecimientos, pero intentaré ser lo mas sincero posible y, en lo posible, sin caer en la "salamería".
Primero que nada le agradezco a Berta Rubio, mi directora de tesis, por su paciencia infinita en todas las discusiones respecto a este trabajo, por no dejar ni un cabo sin atar, por apoyarme cuando lo necesité y confiar en mi desde el el primer momento; sin duda que de su ejemplo como profesional y como persona he aprendido mucho. A José Luis Taín, por darme la oportunidad de trabajar en el Grupo de Espectroscopía Gamma. A Alejandro Algora por todos los grandes momentos compartidos, las discusiones con pasión latina, los cafés reflexivos, las ideas revolucionarias (aunque tampoco tanto), el gran viaje desde Ginebra, nuestro anti-san Valentín en Venecia, las decenas de experimentos en que trabajamos juntos. A vosotros tres: **muchísimas gracias**. Todo lo que he aprendido en estos años os lo debo.

I would like to thank to two important persons related with my formation: Prof. William Gelletly and Prof. Yoshitaka Fujita. Bill and Yoshi: thanks a lot for these patient (the former)/with passion (the last) but always enjoyable discussions and of course thanks for your continuous encourage. I also may acknowledge to all those great young physicist that I have the pleasure to meet and enjoy during the different experiments: Dieter Powels and Oleg Ivanov from Louven; Plamen Boutachkov, Stephane Pietri, Namita Goel, Robert Hoischen and Cesar Domingo from GSI; Tatsuya Adachi, Hiro Fujita and Hiroaki Matsubara from Osaka. My most sincere thanks to the senior physicists which help me from one way or another during these years: Andrés Gadea, Jurek Grebosz, Hans-Jürgen Wollersheim, Rakesh Kumar, Jürgen Gerl, Magda Groska, Jerome Giovinazzo and Bertram Blank.

También quiero agradecer a mis compañeros de trabajo y amigos: A Loli Jordán, Giuseppe Giubrone, Ebhelixes Valencia y Levent Kucuk, con ellos he vivido grandes momentos tanto dentro como fuera del trabajo. Mención especial, medalla al mérito, *copa, recopa y mundial* merece Jorge Agramunt, mi segunda línea, compañero, colega y amigo. Jorgito, son muchas las batallas que hemos librado juntos, más aún las horas

sin dormir durante un experimento, por la tontería de hacer los turnos de ambos. Pero como bien dices: "compañero: el que acompaña" y ante tan abrumante lógica, infinitas birras han caído. Solo me queda agregar *sin razón ni conocimiento*: "que sean infinitas más la penúltima!". Muchas gracias por estar ahí, acompañandome siempre.

Grandes personas con las que he tenido oportunidad de compartir en el IFIC: Carlos, Emma, Joan, Tito, Neus, Regina, Santi, Ricardo y Pablito. Muchas gracias a todos. La segunda mención especial es para Mercedes. Querida Mer: simplemente gracias por todo tu apoyo.

No puedo dejar de agradecer al único verdadero equipo de rugby de toda la Comunidad: Ciencias RC. En particular quiero agradecer a Suso por alentarme. Siempre teniendo la palabra precisa en el momento adecuado, y esto no solo en el campo. A Alex17, Mati y Jorge (otra vez), tres grandes compañeros y amigos; no olvidaré los grandes momentos que vivimos y lo mucho que aprendí de vosotros (de la vida en general, porque de rugby...). Al resto del equipo: muchas gracias por todo, hipochicos. Ule-Ule.

Especialmente le agradezco a mi familia en Chile, a mis Hermanas: Marce, Pauli y Lori, con extención a mis cuñados, a mis sobrinos (ahora en plural): Elías y Loretito y, por supuesto, a mis viejitos queridos: Kiko y Laly. Han sido cinco años largos, larguísimos quizás, donde en ningún momento he dejado de sentir el apoyo de ustedes. No ha sido fácil para nadie, pero todos hemos aprendido cosas que de otra manera no hubiesemos podido (yo el primero). A todos ustedes: MUCHAS GRACIAS.